



University
of Glasgow

Scheurich, Frank (2011) *Modelling the aerodynamics of vertical-axis wind turbines*.

PhD thesis.

<http://theses.gla.ac.uk/2897/>

Copyright and moral rights for this thesis are retained by the author

A copy can be downloaded for personal non-commercial research or study, without prior permission or charge

This thesis cannot be reproduced or quoted extensively from without first obtaining permission in writing from the Author

The content must not be changed in any way or sold commercially in any format or medium without the formal permission of the Author

When referring to this work, full bibliographic details including the author, title, awarding institution and date of the thesis must be given

Modelling the Aerodynamics of Vertical-Axis Wind Turbines

Frank Scheurich



School of Engineering
College of Science and Engineering
University of Glasgow

Submitted in fulfilment of the requirements for the degree of
Doctor of Philosophy

September 2011

© 2011 F. Scheurich

Abstract

The current generation of wind turbines that are being deployed around the world features, almost exclusively, a three-bladed rotor with a horizontal-axis configuration. In recent years, however, a resurgence of interest in the vertical-axis wind turbine configuration has been prompted by some of its inherent advantages over horizontal-axis rotors, particularly in flow conditions that are typical of the urban environment.

The accurate modelling of the aerodynamics of vertical-axis wind turbines poses a significant challenge. The cyclic motion of the turbine induces large variations in the angle of attack on the blades during each rotor revolution that result in significant unsteadiness in their aerodynamic loading. In addition, aerodynamic interactions occur between the blades of the turbine and the wake that is generated by the rotor. Interactions between the blades of the turbine and, in particular, tip vortices that were trailed in previous revolutions produce impulsive variations in the blade aerodynamic loading, but these interactions are notoriously difficult to simulate accurately.

This dissertation describes the application of a simulation tool, the Vorticity Transport Model (VTM), to the prediction of the aerodynamic performance of three different vertical-axis wind turbines - one with straight blades, another with curved blades and a third with a helically twisted blade configuration - when their rotors are operated in three different conditions. These operating conditions were chosen to be representative of the flow conditions that a vertical-axis wind turbine is likely to encounter in the urban environment. Results of simulations are shown for each of the three different turbine configurations when the rotor is operated in oblique flow, in other words when the wind vector is non-perpendicular to the axis of rotation of the rotor, and also when subjected to unsteady wind. The performance of the straight-bladed turbine when it is influenced by the wake of another rotor is also discussed. The capability of the VTM to simulate the flow surrounding vertical-axis wind turbines has been enhanced by a dynamic stall model that was implemented in the course of this research in order to account for the effects of large, transient variations of the angle of attack on the aerodynamic loading on the turbine blades.

It is demonstrated that helical blade twist reduces the oscillation of the power coefficient that is an inherent feature of turbines with non-twisted blades. It is also found that the variation in the blade aerodynamic loading that is caused by the continuous variation of the angle of attack on the blades during each revolution is much larger, and thus far more significant, than that which is induced by an unsteady wind or by an interaction with the wake that is produced by another rotor. Furthermore, it is shown that a vertical-axis turbine that is operated in oblique flow can, potentially, produce a higher power coefficient compared to the operation in conditions in which the wind vector is perpendicular to the axis of rotation, when the ratio between the height of the turbine and the radius of the rotor is sufficiently low.

Acknowledgements

First and foremost, I would like to thank my supervisor, Professor Richard Brown, for his advice and encouragement throughout this project and for the freedom he gave me to pursue my own ideas. I have thoroughly enjoyed my research experience and his support has been greatly appreciated. Furthermore, I would like to thank Dr Timothy Fletcher for the many fruitful discussions that contributed to the success of this study - and for his companionship on several occasions, such as the exchange visits to South Korea.

Several persons from academia and industry deserve my thanks. Professor Roderick Galbraith and Dr Giangi Gobbi provided experimental measurements of a dynamic stall test, that were used in this project, and insightful comments on the phenomenon of dynamic stall. Dr Tamás Bertényi from *Quiet Revolution Ltd.* provided the geometry and the experimental measurements of the performance of the qr5 vertical-axis wind turbine that were also used in this study. Furthermore, I would like to thank Carlos Simão Ferreira from TU Delft for the fruitful discussions about the aerodynamics of vertical-axis wind turbines during the time he was a visiting researcher at Glasgow University. Dr Marco Vezza became my official supervisor in the final year of my doctoral research, after Professor Richard Brown had changed over to Strathclyde University, and his help contributed to a smooth continuation of this project.

This research has been enriched by the support and assistance of the other members of the former Rotorcraft Aeromechanics Laboratory: Dr Mary Kelly, Dr Hyo Won Kim, Dr Catriona Phillips, Alasdair Thom and Dr Karthik Duraisamy. I would especially like to thank Alasdair for sharing the office with me the entire three years and for giving me so many ‘words of the day’ that truly helped me to extend my knowledge of the (Scottish) English language.

Finally, but as importantly, I would like to thank my family for the support and encouragement throughout the years and, particularly, Anja for her love and understanding and for taking part in this journey.

Declaration

The work that is described in this dissertation was carried out in the former Rotorcraft Aeromechanics Laboratory, and in the School of Engineering, at the University of Glasgow between October 2008 and July 2011. I hereby declare that this thesis is my own work and that it has not been submitted for a degree at this or any other university.

Frank Scheurich

Glasgow, September 2011

Contents

Abstract	2
Acknowledgements	3
Declaration	4
Table of Contents	5
List of Figures	8
List of Tables	15
Acronyms	16
1 Introduction	17
1.1 Research Objectives	21
1.2 Synopsis	22
1.3 Publications	23
2 Computational Aerodynamics	26
2.1 The Vorticity Transport Model	28
2.1.1 Governing Equations	28
2.1.2 Computational Grid	29
2.1.3 Numerical Implementation	31
2.1.3.1 Discretisation of the Governing Equations	31
2.1.3.2 Advection Routine	32
2.1.3.3 Velocity Field	35

2.1.3.4	Vorticity Source	40
2.1.4	Ground Plane	41
2.2	Summary	42
2.3	Chapter Nomenclature	43
3	Blade Aerodynamic Model	45
3.1	Lifting-Line Model	45
3.2	Modelling of Dynamic Stall	47
3.2.1	The Dynamic Stall Phenomenon	47
3.2.2	Implementation of a Dynamic Stall Model into the VTM	51
3.2.2.1	Non-Linear Quasi-Steady Aerofoil Model	52
3.2.2.2	Unsteady Attached Flow	54
3.2.2.3	Unsteady Separated Flow	55
3.2.2.4	Dynamic Stall Vortex	57
3.3	Model Validation	59
3.4	Summary	68
3.5	Chapter Nomenclature	68
4	Blade Aerodynamic Loading and Turbine Performance	71
4.1	Blade Aerodynamic Loading - Comparison with Experiment	71
4.1.1	Experimental Set-up and Turbine Model	72
4.1.2	Blade Loading and Angle of Attack	74
4.1.3	Blade-Wake Interaction	81
4.1.4	Effect of Grid Resolution	88
4.2	Turbine Performance - Comparison with Experiment	92
4.3	Summary	97
4.4	Chapter Nomenclature	97
5	Influence of Rotor Configuration on Turbine Performance	99
5.1	Turbine Configurations	100
5.2	Variation of Power and Rotor Forces with Tip Speed Ratio	102
5.3	Angle of Attack and Blade Loading	105
5.4	Variation of Torque and Power with Azimuth	111
5.5	Wake Structure	116

5.6	Summary	122
5.7	Chapter Nomenclature	123
6	Influence of Operating Condition on Turbine Performance	124
6.1	Oblique Flow	126
6.1.1	Height-to-Radius Ratio	127
6.1.2	Blade Geometry	133
6.2	Unsteady Flow	135
6.2.1	Power Coefficient	137
6.2.2	Blade Aerodynamic Loading	142
6.2.3	Wake Structure	144
6.3	Turbine-Turbine-Interaction	149
6.3.1	Parallel Arrangement	152
6.3.2	Upwind-Downwind Arrangement	157
6.4	Summary	167
6.5	Chapter Nomenclature	168
7	Conclusions and Outlook	170
7.1	Conclusions	170
7.2	Outlook	175
	References	178
	Appendices	188
A	Coefficients of Dynamic Stall Model	188
B	Rotor Parameters	189
C	Grid Parameters	191

List of Figures

1.1	<i>Novel Offshore Vertical Axis (NOVA) wind turbine concept</i>	19
1.2	<i>Different lift-driven vertical-axis wind turbine designs</i>	20
2.1	<i>Nested grid structure with overlap of the boundaries of adjacent grid levels</i>	30
2.2	<i>Computed vorticity in nested grid boxes that contain cells of different size</i>	30
2.3	<i>Schematic showing the calculation of vorticity across cell faces</i>	33
2.4	<i>Schematic showing the interaction between target and source clusters using the multipole method to calculate the velocity field</i>	37
2.5	<i>Representation of the velocity field of cluster i and the velocity-inducing clusters in the near field, in the intermediate field and in the far field .</i>	39
2.6	<i>Ground plane formed using the method of images</i>	42
3.1	<i>Blade aerodynamic model and inner wake model</i>	46
3.2	<i>Schematic showing the essential flow morphology and the aerodynamic coefficients during the dynamic stall process on an oscillating aerofoil .</i>	50
3.3	<i>Experimental measurements of the normal and tangential force coeffi- cients produced by the NACA 0015 aerofoil when operated under quasi- steady conditions</i>	60
3.4	<i>Sinusoidal variation of the angle of attack with Ωt in comparison to the variation of the geometric angle of attack that is experienced by the blades of a vertical-axis wind turbine at different tip speed ratios</i>	61

3.5	<i>VTM-predicted normal and tangential force coefficients based on static aerofoil data and in conjunction with its dynamic stall model compared to experimental measurements of dynamic stall. A skewed sinusoidal variation of angle of attack (with amplitude 11.90°) was used in order to represent vertical-axis wind turbine conditions at $\lambda = 4.85$</i>	64
3.6	<i>VTM-predicted normal and tangential force coefficients based on static aerofoil data and in conjunction with its dynamic stall model compared to experimental measurements of dynamic stall. A skewed sinusoidal variation of angle of attack (with amplitude 17.10°) was used in order to represent vertical-axis wind turbine conditions at $\lambda = 3.40$</i>	65
3.7	<i>VTM-predicted normal and tangential force coefficients based on static aerofoil data and in conjunction with its dynamic stall model compared to experimental measurements of dynamic stall. A skewed sinusoidal variation of angle of attack (with amplitude 21.80°) was used in order to represent vertical-axis wind turbine conditions at $\lambda = 2.70$</i>	66
3.8	<i>VTM-predicted normal and tangential force coefficients based on static aerofoil data and in conjunction with its dynamic stall model compared to experimental measurements of dynamic stall. A skewed sinusoidal variation of angle of attack (with amplitude 29.00°) was used in order to represent vertical-axis wind turbine conditions at $\lambda = 2.05$</i>	67
4.1	<i>Orientation of the blades and specification of the azimuth angle</i>	73
4.2	<i>Experimental arrangement and its computational representation</i>	74
4.3	<i>VTM-predicted variation of non-dimensional normal and tangential forces with blade azimuth for the section at mid-span of the blade compared to simulations of the 2D aerodynamics of the same aerofoil in a planar cyclic motion at $\lambda = 5.0$.</i>	76
4.4	<i>Comparison between the variation in VTM-predicted aerodynamic loading and experimental measurements for $\lambda = 7.5$, $\lambda = 5.0$ and $\lambda = 2.5$</i>	78
4.5	<i>VTM-predicted variation with azimuth of the angle of attack at three different blade sections for $\lambda = 7.5$, $\lambda = 5.0$ and $\lambda = 2.5$</i>	79

LIST OF FIGURES

4.6	<i>Computed vorticity field surrounding the turbine, represented using contours of vorticity on a vertical plane that contains the axis of rotation of the turbine</i>	82
4.7	<i>VTM-predicted variation with azimuth of the non-dimensional normal force along the blade span at $\lambda = 7.5$</i>	84
4.8	<i>VTM-predicted variation with azimuth of the non-dimensional normal force along the blade span at $\lambda = 5.0$</i>	85
4.9	<i>VTM-predicted variation with azimuth of the non-dimensional normal force along the blade span at $\lambda = 2.5$</i>	86
4.10	<i>Flow field when the rotor is operated at $\lambda = 5.0$, visualised by plotting an isosurface of vorticity with colouring allocated to the vorticity developed by blade 1 and blade 2</i>	87
4.11	<i>Comparison between experimental measurements and the variation in VTM-predicted aerodynamic loading using two different grid resolutions when the rotor is operated at $\lambda = 5.0$</i>	89
4.12	<i>Computed vorticity field surrounding the turbine using a coarse grid and a fine grid when the rotor is operated at $\lambda = 5.0$</i>	90
4.13	<i>VTM-predicted sectional normal and tangential forces at four different locations along the blade using a coarse grid and a fine grid when the rotor is operated at $\lambda = 5.0$</i>	91
4.14	<i>The Quiet Revolution qr5 vertical-axis wind turbine and the VTM-predicted flow field of the turbine visualised by plotting an isosurface of vorticity .</i>	93
4.15	<i>VTM-predicted power coefficient based on static airfoil data and in conjunction with its dynamic stall model in comparison to experimental measurements for the qr5 vertical-axis wind turbine manufactured by Quiet Revolution Ltd.</i>	94
4.16	<i>VTM-predicted variation with azimuth of the aerodynamic angle of attack at three sections along the length of the blade of the qr5 turbine. .</i>	95
5.1	<i>Geometry of the vertical-axis wind turbines with straight, curved and helically twisted blades</i>	100

LIST OF FIGURES

5.2	<i>Diagram showing the wind direction, the definition of rotor azimuth and direction of positive normal and tangential forces, as well as the relative positions of the rotor blades</i>	101
5.3	<i>VTM-predicted variation with tip speed ratio of the power coefficients of the straight- and curved-bladed turbines and the turbine with helically twisted blades</i>	102
5.4	<i>VTM-predicted variation with tip speed ratio of the forces on the rotor of the straight- and curved-bladed turbines and the turbine with helically twisted blades</i>	104
5.5	<i>VTM-predicted forces and angle of attack distribution over one complete rotor revolution at four different spanwise stations along the blade of the straight-bladed turbine</i>	106
5.6	<i>VTM-predicted forces and angle of attack distribution over one complete rotor revolution at four different spanwise stations along the blade of the curved-bladed turbine</i>	107
5.7	<i>VTM-predicted forces and angle of attack distribution over one complete rotor revolution at four different spanwise stations along the lower portion of the blade of the turbine with helically twisted blades</i>	109
5.8	<i>VTM-predicted forces and angle of attack distribution over one complete rotor revolution at four different spanwise stations along the upper portion of the blade of the turbine with helically twisted blades</i>	110
5.9	<i>VTM-predicted variation with azimuth of the sectional non-dimensional torque at different blade sections for the three turbine configurations that were investigated</i>	112
5.10	<i>VTM-predicted variation with azimuth of the non-dimensional sectional torque along the blade spans of the straight- and curved-bladed turbines and the turbine with helically twisted blades</i>	113
5.11	<i>VTM-predicted variation of the power coefficients of the straight- and curved-bladed turbines and the turbine with helically twisted blades . . .</i>	115
5.12	<i>VTM-predicted variation with azimuth of the forces on the rotor of the straight- and curved-bladed turbines and the turbine with helically twisted blades when the rotors are operated at $\lambda = 3.5$</i>	116

5.13	<i>Three-dimensional graphical representation of the computed flow fields surrounding the turbine configurations with straight blades, curved blades and helically twisted blades. The wake geometry is visualised by rendering a surface on which the vorticity has constant magnitude</i>	119
5.14	<i>Computed vorticity fields surrounding the straight-bladed, curved-bladed, and helically twisted turbine, represented using contours of the component of vorticity that is perpendicular to a vertical plane that contains the axis of rotation of the turbine, and that is aligned with the wind direction</i>	120
5.15	<i>Computed vorticity fields surrounding the straight-bladed, curved-bladed, and helically twisted turbine, represented using contours of vorticity magnitude on horizontal planes that intersect with the mid-spans of the rotor blades</i>	121
6.1	<i>Arrangement of vertical-axis wind turbines at four different urban sites.</i>	125
6.2	<i>VTM-predicted flow field of the vertical-axis wind turbine with helically twisted blades at an oblique flow angle, visualised by plotting an isosurface of vorticity</i>	126
6.3	<i>Influence of turbine height-to-radius ratio on the VTM-predicted power coefficient of a straight-bladed vertical-axis wind turbine in normal flow</i>	128
6.4	<i>Influence of turbine height-to-radius ratio on the VTM-predicted power coefficient of a straight-bladed vertical-axis wind turbine at different oblique flow angles and at different tip speed ratios</i>	130
6.5	<i>Computed vorticity field surrounding the straight-bladed vertical-axis wind turbine with $H/R = 1.2$, represented using contours of the vorticity component that is perpendicular to a vertical plane that contains the axis of rotation of the turbine</i>	131
6.6	<i>VTM-predicted variation with azimuth of the non-dimensional tangential force along the blade span of the straight-bladed vertical-axis wind turbine in normal flow and in oblique flow</i>	132
6.7	<i>Influence of rotor geometry on the unsteady component of the VTM-predicted power coefficient of three different turbine configurations with $H/R = 3.0$ in normal flow and in oblique flow</i>	134

LIST OF FIGURES

6.8	<i>VTM-predicted variation of the power coefficients of three different turbine configurations when the rotors are operated at $R_g = 14$</i>	138
6.9	<i>VTM-predicted variation of the power coefficients of three different turbine configurations when the rotors are operated at $R_g = 1.5$</i>	139
6.10	<i>VTM-predicted variation of the power coefficients for the straight-bladed and curved-bladed turbines and the turbine with helically twisted blades when the rotors are operated in unsteady wind conditions with $\Delta V/V_\infty = \pm 0.3$ and $R_g = 1.5$</i>	141
6.11	<i>Mean power coefficient produced by the turbine configurations in unsteady wind conditions - as a percentage of that generated by an ‘ideal’ turbine with constant tip speed ratio</i>	142
6.12	<i>VTM-predicted aerodynamic angle of attack and sectional forces in steady and unsteady wind conditions over three complete rotor revolutions at two different spanwise locations along the reference blade of the straight-bladed turbine</i>	143
6.13	<i>Computed vorticity field surrounding the straight-bladed turbine in unsteady wind conditions, represented using contours of vorticity on a vertical plane that contains the axis of rotation of the turbine and that is aligned with the wind direction</i>	146
6.14	<i>Computed vorticity field surrounding the straight-bladed turbine in unsteady wind conditions, represented using contours of vorticity on a horizontal plane that intersects with the mid-spans of the rotor blades . . .</i>	147
6.15	<i>Computed vorticity field surrounding the straight-bladed turbine in unsteady wind conditions, represented by an isosurface of vorticity</i>	148
6.16	<i>Relative locations of the straight-bladed vertical-axis wind turbines in a parallel and in an upwind-downwind arrangement</i>	151
6.17	<i>VTM-predicted ratio of the power coefficient that is produced by each of the rotors in a parallel arrangement to the power coefficient that is produced by one of the rotors in isolation</i>	153
6.18	<i>VTM-predicted variation with azimuth of the power coefficient that is produced by the reference rotor and those produced by the rotors in a parallel arrangement at two different crosswind separations</i>	154

LIST OF FIGURES

6.19	<i>VTM-predicted flow fields surrounding the straight-bladed turbines when they are operated in a parallel arrangement at two different crosswind separations, represented using contours of vorticity on a horizontal plane that intersects with the mid-spans of the rotor blades</i>	154
6.20	<i>VTM-predicted flow fields surrounding the straight-bladed turbines when they are operated in a parallel arrangement at two different crosswind separations, visualised by plotting an isosurface of vorticity</i>	155
6.21	<i>VTM-predicted variation with azimuth of the aerodynamic angle of attack and the loading at the mid-span of the blade of the reference rotor and those produced by the rotors in a parallel arrangement</i>	156
6.22	<i>VTM-predicted ratio of the power coefficient that is produced by the downwind rotor in an upwind-downwind arrangement to the power coefficient that is produced by one of the rotors when operated in isolation .</i>	159
6.23	<i>VTM-predicted flow fields surrounding the straight-bladed turbines when they are operated at different streamwise and crosswind separations from each other, visualised by plotting an isosurface of vorticity.</i>	160
6.24	<i>VTM-predicted flow fields surrounding the straight-bladed turbines when they are operated at a streamwise separation of $7R$, represented using contours of vorticity on a horizontal plane that intersects with the mid-spans of the rotor blades</i>	161
6.25	<i>VTM-predicted flow fields surrounding the straight-bladed turbines when they are operated at a streamwise separation of $12R$, represented using contours of vorticity on a horizontal plane that intersects with the mid-spans of the rotor blades</i>	162
6.26	<i>VTM-predicted variations with azimuth of aerodynamic angle of attack and tangential force at two different spanwise locations along the blades of the reference rotor and the downwind rotors, when the turbines are operated in an upwind-downwind arrangement with a streamwise separation of $7R$</i>	163
6.27	<i>VTM-predicted variation with time (in rotor revolutions) of the power coefficient that is produced by the reference rotor and those which are produced by the downwind rotors in an upwind-downwind arrangement .</i>	166

List of Tables

A.1	<i>Coefficients that are used within the dynamic stall model and that are deduced from static aerofoil data for the NACA 0015 aerofoil</i>	188
A.2	<i>Time constants used in the dynamic stall model</i>	188
B.1	<i>Rotor parameters of the straight-bladed turbine used in Strickland's experiment</i>	189
B.2	<i>Geometric properties of the straight-bladed, the curved-bladed and the helically twisted turbine configurations</i>	190
B.3	<i>Rotor parameters of the straight-bladed, the curved-bladed and the helically twisted turbine configurations</i>	190
C.1	<i>Grid parameters used within the study of the effect of grid resolution . .</i>	191

Acronyms

CFD	Computational Fluid Dynamics
CFL	Courant-Friedrichs-Lewy (number)
DES	Detached-Eddy Simulation
ETI	Energy Technologies Institute
FMM	Fast Multipole Method
GWEC	Global Wind Energy Council
IEA	International Energy Agency
IPCC	Intergovernmental Panel on Climate Change
LES	Large-Eddy Simulation
NACA	National Advisory Committee for Aeronautics
NASA	National Aeronautics and Space Administration
NOVA	Novel Offshore Vertical Axis Wind Turbine Concept
PIV	Particle Image Velocimetry
TVD	Total Variation Diminishing
URANS	Unsteady Reynolds-Averaged Navier-Stokes
VAWT	Vertical-Axis Wind Turbine
VTM	Vorticity Transport Model
WAF	Weighted Average Flux

Chapter 1

Introduction

In recent years, the number of wind turbines that have been deployed all over the world has increased considerably. According to the Global Wind Energy Council [1], more than 38GW of new wind power capacity was installed worldwide in the year 2009, bringing the total installed capacity, by the end of 2009, to 160GW. The development and deployment of devices that generate useful energy from the kinetic energy contained in the wind are motivated largely by two objectives. Firstly, there is a perceived need to reduce emissions of carbon dioxide and other pollutants by replacing fossil fuel-fired power plants with renewable energy technologies. Secondly, there is a perceived demand to establish an alternative to fossil fuels in the light of the finite nature and unequal global distribution of the known coal, oil and gas resources.

The energy company *BP plc* [2] estimates that the generation of electricity by wind turbines in 2009 was over 260TWh which corresponds to merely 1.3% of the amount of electricity generated globally, but the share of wind energy in the electricity that is generated worldwide is expected to increase substantially in the coming decades. The contribution of wind power to the future electric energy supply will be highly dependent on governmental policies, however. Indeed, the International Energy Agency [3] predicts, in a *baseline scenario* which assumes that governments introduce no new energy and climate policies, that the share of wind energy in the global electricity generation will be only 5% in the year 2050. In contrast, the most ambitious scheme, the so-called *BLUE Map scenario* that includes the target of halving global energy-related emissions of carbon dioxide by the year 2050 compared to the levels in the year 2005, projects up to 22% of the worldwide electricity demand to be provided by wind energy in the year

2050. The target setting of the *BLUE Map scenario* is motivated by the findings of the studies that were carried out by the Intergovernmental Panel on Climate Change [4; 5]. According to these investigations, substantial changes in structure and function of the worldwide ecosystems are very likely to occur when global warming, associated with increased atmospheric concentration of carbon dioxide, exceeds 2°C compared to the pre-industrial level (Ref. 4, p. 213ff.). Furthermore, it is concluded that the reduction of the emissions of carbon dioxide by 50% by the year 2050 compared to the levels in the year 2005 is necessary if global warming is to be confined to 2°C (Ref. 5, p. 197ff).

The current generation of wind turbines that are being deployed around the world features, almost exclusively, a three-bladed rotor with a *horizontal-axis* configuration. In recent years, however, there has been a resurgence of interest in both large-scale and small-scale *vertical-axis* wind turbines. The development of *large-scale* vertical-axis wind turbines is a response to the apparent exhaustion of the potential for significant improvement of horizontal-axis turbine configurations in the near future. For instance, the UK Energy Technologies Institute is conducting the Novel Offshore Vertical Axis (NOVA) project [6] with the aim of installing a prototype large offshore vertical-axis wind turbine by the year 2020. The study hopes to demonstrate that such devices have improved stability and simpler maintenance access compared to horizontal-axis designs. The proposed configuration is depicted in Figure 1.1.

In contrast to current plans for providing electricity at the scale of the national grid by concentrating *large-scale* wind turbines in on- and offshore wind farms, another potentially effective strategy for harvesting wind energy, particularly in the urban environment, relies on using *small-scale* wind turbines, with rotor diameters of only several metres. These devices can be distributed within cities and thus contribute to a decentralised energy supply in which the urban energy requirement is provided by on-site energy production equipment. The design of a wind turbine that operates efficiently within an urban area poses a significant challenge, however, since the wind in the built environment is characterised by frequent and often rapid changes in direction and speed, as described by McIntosh [7] amongst others. In these wind conditions, vertical-axis wind turbines might offer several advantages over horizontal-axis wind turbines. This is because vertical-axis turbines do not require a yaw control system, whereas horizontal-axis wind turbines have to be rotated in order to track changes in wind direction. In addition, the gearbox and the generator of a vertical-axis turbine

can be situated at the base of the turbine, thereby reducing the loads on the tower under unsteady wind conditions, and facilitating the maintenance of the system. The principal advantage of these features of a vertical-axis configuration is to enable a somewhat more compact design that alleviates the material stress on the tower and requires fewer mechanical components compared to a horizontal-axis turbine.

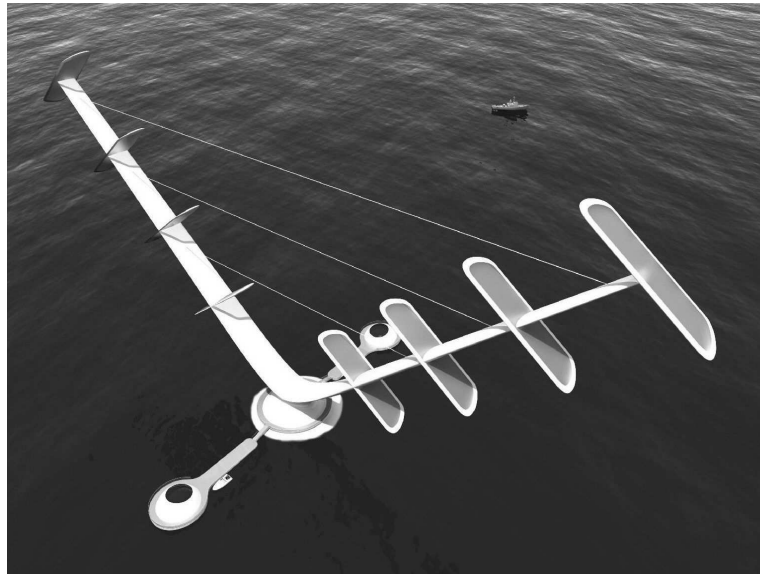


Figure 1.1: *NOVA Offshore Aerogenerator concept developed by Wind Power Limited, rotor invented by David Sharpe. Courtesy of GRIMSHAW Architects. © 2009.*

A vertical-axis wind turbine is called a Darrieus turbine when it is driven by aerodynamic lift. The concept was patented in the United States by the Frenchman Georges Darrieus [8] in 1931. The patent includes both straight- and curved-bladed configurations in which the blades are supported using plates located at the top and the bottom of the turbine to provide structural strength. By curving the blades to yield the so-called troposkien shape, which is equivalent to the shape of a spinning rope that is constrained at its ends, the high bending moments that are encountered on straight-bladed turbines can, to some extent, be alleviated. Both straight-bladed and curved-bladed vertical-axis wind turbines suffer, however, from a marked azimuthal variation in the aerodynamic loading on their blades. These variations in loading manifest as oscillations in the torque and power that is output from the turbine. The oscillating torque that is developed by straight- and curved-bladed turbines contributes

significantly to the vibration that is transmitted to the tower and the foundations of the system. In addition, the oscillations in the loading on the blades can lead to increased fatigue of the rotor structure. For these reasons, several commercial vertical-axis wind turbines feature a design that incorporates blades that are twisted helically around the rotational axis of the turbine. The torque, and consequently the power output, of vertical-axis wind turbines with helically twisted blades is relatively steady, thus alleviating the stress on the turbine system, reducing the vibration transmitted into its supporting structure, and thereby increasing the design life of the turbine. Figure 1.2 shows examples of a straight-bladed and a curved-bladed vertical-axis wind turbine and a turbine with helically twisted blades.

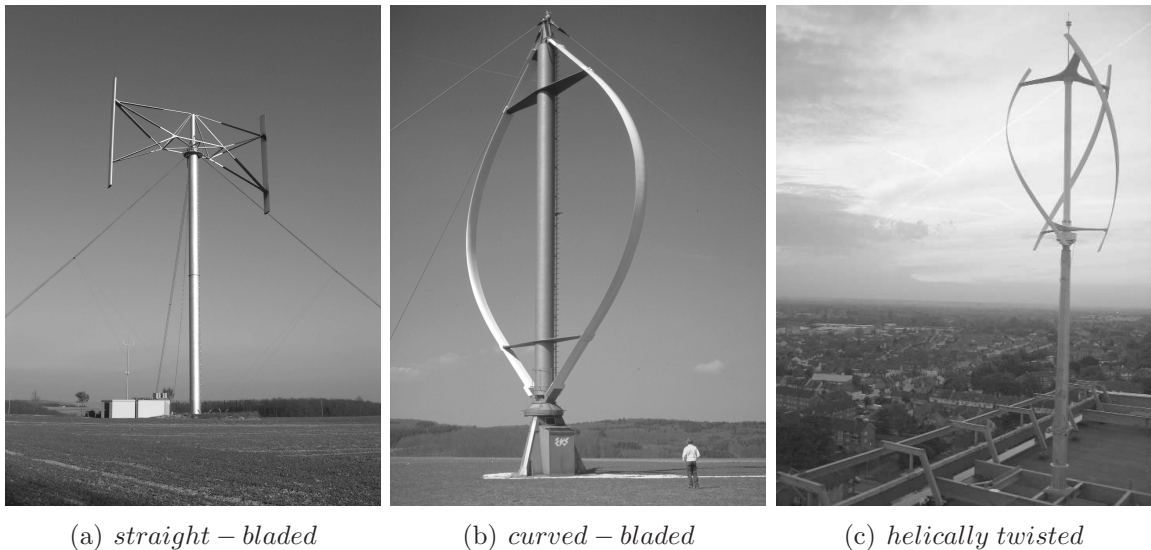


Figure 1.2: *Different lift-driven vertical-axis wind turbine designs. Photographs by courtesy of a) Michael Schelker, b) Bundesverband WindEnergie e.V. and c) Quiet Revolution Ltd.*

It should be noted that there is a second class of vertical-axis wind turbines, called Savonius turbines, that are driven by aerodynamic drag rather than lift. The design was proposed by the Finn Sigurd Savonius [9] in the 1920s. It can easily be shown, however, that the efficiency of a device that is driven solely by aerodynamic drag is very low compared to a lift-driven wind turbine configuration¹. Savonius rotors are thus only sparsely used for the generation of electricity, and they are not addressed in

¹see Gasch and Twele (Ref. 10, p. 37ff.) for a detailed comparison

this dissertation. Hemispherical cup anemometers work on the aerodynamic principles of a Savonius-type rotor, however, since the design of a drag-driven device is more robust and somewhat simpler than that of a lift-driven configuration.

1.1 Research Objectives

The accurate aerodynamic modelling of vertical-axis wind turbines poses a significant challenge. The cyclic motion of the turbine induces large variations in the angle of attack on the blades during each revolution of the rotor that result in significant unsteadiness in their aerodynamic loading. In addition, an aerodynamic interaction occurs between the blades of the turbine and the wake that is generated by the rotor. Interactions between the blades of the turbine and, in particular, tip vortices that were trailed in previous revolutions produce impulsive variations in the blade aerodynamic loading, but these interactions are notoriously difficult to simulate accurately. The aerodynamic characteristics of vertical-axis wind turbines are thus somewhat more complex compared to those of horizontal-axis configurations, and are partially responsible for the fact that industrial and academic research has focused primarily on horizontal-axis turbines in the past decades. This has had the result that vertical-axis wind turbines are devices that are still relatively poorly understood.

Given the recent resurgence of interest in academia and industry in vertical-axis wind turbines, a simulation tool that can predict accurately the aerodynamic performance of vertical-axis rotors would be of significant benefit to the designers of these devices. The research described in this dissertation aims to increase the understanding of the flow field surrounding vertical-axis turbines and to understand some of the aerodynamic factors that influence the performance of different vertical-axis turbine configurations under different operating conditions. A numerical method, the Vorticity Transport Model (VTM) that will be described in detail in Chapter 2 of this dissertation, has been used to carry out a computational study in order to achieve these objectives. The capability of the VTM to simulate the flow surrounding vertical-axis wind turbines has been enhanced by a dynamic stall model that was implemented in the course of this research in order to account for the effects of large, transient variations of the angle of attack on the aerodynamic loading on the turbine blades. The results from the investigation that is described in this dissertation should provide valuable information that may be considered when designing vertical-axis wind turbines.

1.2 Synopsis

The structure of this dissertation is arranged as follows.

Chapter 2 presents a comprehensive description of the Vorticity Transport Model. This model is the computational method that was used to carry out all the simulations that are presented in this dissertation.

In Chapter 3, the blade aerodynamic model that is used within the VTM is presented and the strategy that was used to model the effect of dynamic stall on the blades of vertical-axis wind turbines is described. Subsequently, the implementation of a dynamic stall model within the Vorticity Transport Model is documented. Comparisons are shown between VTM simulations of dynamic stall and experimental measurements in order to verify the approach.

In Chapter 4, comparisons between VTM simulations and experimental measurements are shown for two different vertical-axis wind turbines. Firstly, the VTM-predicted aerodynamic loading on the blades of a straight-bladed vertical-axis wind turbine is compared to experimental measurements on the same turbine when operated at three different tip speed ratios. Secondly, the VTM-predicted variation of the power coefficient with tip speed ratio of a commercial vertical-axis wind turbine with helically twisted blades is compared to experimental measurements of the same turbine. The comparisons were carried out in order to establish confidence in the ability of the method to simulate accurately the aerodynamic performance of vertical-axis wind turbines.

In Chapter 5, the influence of blade curvature and helical blade twist on the aerodynamic performance of a vertical-axis wind turbine is discussed in detail. This was done by analysing the performance, at various tip speed ratios, of three different vertical-axis wind turbine configurations: one with a straight-bladed configuration, another with a curved-bladed configuration and another with a helically twisted configuration.

In Chapter 6, each of the three different turbine configurations, that are introduced in Chapter 5, is investigated when its rotor is operated in several different operating conditions that are relevant to full-scale practice. Indeed, the behaviour of the turbines is analysed in unsteady wind conditions and also in oblique flow, in other words in conditions in which the wind vector is non-perpendicular to the axis of rotation of the turbine. In addition, the influence of the wake that is generated by a vertical-axis

turbine on the performance of another vertical-axis turbine is described. Simulations of these turbine-turbine interactions are relevant to understand the aerodynamic behaviour of several vertical-axis wind turbines when they are arranged in a cluster.

Finally, in Chapter 7, the dissertation concludes with a summary of all chapters and suggestions for future work.

The relevant nomenclature is tabulated in the last section of the each chapter.

1.3 Publications

Several components of this dissertation have been published during the course of the research.

Preliminary research results that showed, for the first time, the application of the VTM to the prediction of the aerodynamics of vertical-axis wind turbines were presented at the 22nd Scottish Fluid Mechanics Meeting in Oban, Scotland, in May 2009. This work was significantly modified and extended, particularly by the inclusion of a dynamic stall model within the simulation, and published in *Wind Energy* in March 2011 (Ref. 11). In the paper, the VTM-predicted blade aerodynamic loading on a straight-bladed vertical-axis wind turbine is compared with experimental measurements of the performance of the same turbine. It is shown that the interaction between the blades of the rotor and the vortices that are shed and trailed in previous revolutions has a significant effect on the distribution of aerodynamic loading on the blade. It was also suggested that the disagreement between experimental and numerical data that has been presented in previous studies was most likely a result of the interactions between the blades of the rotor and the wake that is developed by the turbine having not been modelled with sufficient fidelity. Furthermore, it was shown that dynamic stall, induced by the interaction of the blades and the wake of the turbine, may occur near to the tips of the blades even during operation at tip speed ratios that have historically been considered to be too low to cause the blades to stall dynamically. Chapter 4 of the present dissertation is based on the study published in this paper.

In January 2010, a paper that described the influence of blade curvature and helical blade twist on the aerodynamic performance of a vertical-axis wind turbine was presented at the 48th AIAA Aerospace Sciences Meeting in Orlando, USA (Ref. 12). An improved and extended version of this paper was published in the *Journal of Power*

and Energy in May 2011 (Ref. 13). This work showed that the variation with azimuth of the torque coefficient, that is an inherent feature of vertical-axis wind turbines with non-twisted blades, can be reduced considerably if azimuthal twist and local radius are carefully chosen for each blade section within a helically twisted configuration. Chapter 5 of the present dissertation comprises the findings that were presented in this paper. A short extract of this work was also presented at the Universitas 21 interdisciplinary conference for research students in Melbourne and Brisbane, Australia, in December 2009 (Ref. 14).

In March 2011, a paper was presented at the Annual Conference of the European Wind Energy Association (EWEA) in Brussels, Belgium (Ref. 15). In this study, the behaviour of different vertical-axis wind turbine configurations was investigated when the rotors were operated in oblique flow, in other words in conditions in which the wind vector is non-perpendicular to the axis of rotation of the turbine. The paper showed that a vertical-axis turbine that is operated in oblique flow can, potentially, produce a higher power coefficient compared to operation in conditions in which the wind vector is perpendicular to the axis of rotation, when the ratio between the height of the turbine and the radius of the rotor is sufficiently low. Preliminary results of this work were also presented at the 6th PhD Seminar on Wind Energy in Europe, organised by the European Academy of Wind Energy (EAWE), in Trondheim, Norway, in October 2010 (Ref. 16). The research results presented in these papers are part of Chapter 6.

A paper that described the performance of different vertical-axis wind turbines in *unsteady* wind conditions has been accepted for publication in *Wind Energy* and is currently in print (Ref. 17). In *steady* wind conditions, the power coefficients that are produced by both straight- and curved-bladed turbines vary considerably within one rotor revolution because of the continuously varying angle of attack on the blades, as described in Refs. 12 and 13. The present paper shows that the variation in the blade aerodynamic loading that is caused by the continuous variation of the angle of attack on the blades during the cyclic motion of the turbine is much larger, and thus far more significant, than that which is induced by the unsteadiness in the wind conditions. These findings are part of Chapter 6 of this dissertation.

In June 2011, a paper that showed simulation results for the aerodynamic interactions between two straight-bladed vertical-axis wind turbines was presented at the Wake Conference in Visby, Sweden (Ref. 18). This work showed that a vertical-axis

turbine that is operated downwind of another turbine can produce a higher power coefficient, than that which is produced by a single, isolated turbine, when the crosswind separation between the two turbines is sufficiently large to avoid direct impingement on the downwind turbine of the wake that is produced by the upwind rotor. Not surprisingly, the downwind rotor was shown to produce a much lower power coefficient, than that of a turbine that is operated in the undisturbed free stream, when it is fully immersed within the wake that is generated by the upwind rotor. Chapter 6 of this dissertation comprises the research results that were presented in this paper.

Also in June 2011, a paper that described the effect of dynamic stall on the aerodynamics of vertical-axis wind turbines was presented at the 29th AIAA Applied Aerodynamics Conference in Honolulu, USA (Ref. 19). This paper has also been accepted for publication in the *AIAA Journal* and is currently in print (Ref. 20). In these papers, detailed comparisons were made between VTM predictions and experimental measurements of the loading on an aerofoil in conditions of dynamic stall. Furthermore, the VTM-predicted performance of a commercial vertical-axis wind turbine with helically twisted blades was compared with experimental measurements of the performance of the same turbine. It was demonstrated that the VTM is able to model accurately the aerodynamics of vertical-axis wind turbines when its dynamic stall model is employed in the simulation. In addition, it was shown that the design of the turbine that was analysed in this work could, potentially, be improved if the aim is to reduce the variations with azimuth of the power coefficient that is produced by the rotor. Chapter 3 and Chapter 4 of the present dissertation contain elements of the validation, between VTM simulations and experimental measurements, that was carried out in the scope of this study.

Chapter 2

Computational Aerodynamics

The flow field surrounding vertical-axis wind turbines is highly unsteady. The rotation of the turbine induces large variations in the angle of attack of its blades that can manifest as dynamic stall. The continuous variation of the angle of attack on the blades of the rotor results in the generation of vorticity that is trailed and shed from the blades into the wake. Interactions between the blades of the turbine and the vorticity in the wake can exacerbate dynamic stall and result in impulsive changes to the blade aerodynamic loading. These interactions are notoriously difficult to simulate accurately, however. According to Klimas [21], the interaction between the blades and the wake of the turbine is considered to be one of the most critical problems in the numerical modelling of the aerodynamics of vertical-axis wind turbines. The accurate prediction of the aerodynamics of vertical-axis wind turbines thus poses a significant challenge, but is essential if the design of such devices is to be improved.

Historically, a range of theoretical and computational aerodynamic methods has been used to model the flow environment around vertical-axis wind turbines. Based on the actuator disk momentum theory that was elaborated by Glauert [22] in the context of propeller aerodynamics, Templin [23] developed the single streamtube model and applied it to the analysis of vertical-axis wind turbines. The streamtube concept was developed further and extended by Strickland [24] and Paraschivoiu [25], amongst others, and resulted in double, multiple and double-multiple streamtube models. The double-multiple streamtube model allowed the local induced velocities in the upwind and downwind regions of the turbine to be determined more accurately compared to the original single streamtube approach, and thus offered an improvement in the simulation of the loading on the blades. The need for higher accuracy in the calculation of

the blade aerodynamic loading and the dynamics of the wake that is generated by the rotor resulted in the development of several vortex models. Indeed, Strickland *et al.* [26] proposed a free vortex model that provided an improved representation of the wake by using a vortex lattice method. Coton *et al.* [27] applied a *prescribed* wake model in order to reduce the computational costs that were associated with *free* wake models and thus, because of the low performance of computers in the past decades, restricted the use of these modelling techniques. In recent years, however, increased availability of high-performance computing has allowed the aerodynamics of vertical-axis wind turbines to be computed from first principles using the Navier-Stokes equations. Hansen and Sørensen [28] and Simão Ferreira *et al.* [29] used various CFD methods including URANS approaches, DES and LES to simulate the two-dimensional aerodynamics of an aerofoil while in a planar, cyclic motion designed to emulate that of the blades of a vertical-axis wind turbine. Detached-eddy simulations of a similar aerofoil configuration have also been performed by Horiuchi *et al.* [30]. Although these conventional CFD methods have yielded, to some extent, reasonable predictions of the behaviour of simple aerofoil and rotor geometries, there have been no publications in the literature, to the author's knowledge, in which the full three-dimensional flow field of a complex rotor system with curved, helically twisted blades has accurately been modelled from first principles.

In most CFD methods, the Navier-Stokes equations are cast into primitive variable form, in which velocity is coupled with pressure and density, and then advanced through time numerically. This approach is known to suffer from numerical dissipation of the vorticity in the wake that is produced by the blades of the rotor. Numerical dissipation in these computations can be reduced by refining the computational grid or, arguably, by using higher-order discretisation of the governing equations. The number of cells that is necessary to model reliably the wake that is produced by vertical-axis wind turbines usually results in very high computational costs, however, since the accurate prediction of the blade aerodynamic loading requires the wake to be captured, and thus vorticity to be conserved, for many rotor revolutions.

An alternative method that can overcome the problem of excessive numerical dissipation that is associated with the primitive variable formulation of the Navier-Stokes equations is to conserve vorticity explicitly after casting the Navier-Stokes equations in vorticity-velocity form. This approach represents the basis of the Vorticity Transport

Model (VTM) that has been used to carry out all the simulations that are presented in this dissertation. The strategy that is implemented within the VTM to solve the governing equations numerically is described in detail in the present chapter.

2.1 The Vorticity Transport Model

The Vorticity Transport Model developed by Brown [31], and extended by Brown and Line [32], enables the simulation of wind turbine aerodynamics and performance by providing a high-fidelity representation of the dynamics of the wake that is generated by the turbine rotor. The VTM was originally developed for simulating the flow field surrounding helicopters, but is an aerodynamic tool that is applicable also to the study of wind turbines. The VTM consists of an outer model in which the dynamics of the wake that is generated by the rotor are calculated based on basic fluid dynamics principles and an inner, lifting-line-type, blade aerodynamic model in which the aerodynamic loads on the blades of the rotor are determined. The outer model is described in the present chapter, whereas the inner model is described in Chapter 3 of this dissertation.

2.1.1 Governing Equations

The motion of any Newtonian fluid can be described by the Navier-Stokes equations. These are derived from the basic physical principles of mass, momentum and energy interchange. Since vertical-axis wind turbines typically operate at low Mach numbers where compressibility effects are negligible, it is assumed that the flow field that surrounds the turbine is incompressible. Consequently, the unsteady incompressible Navier-Stokes equations can be written in primitive variable formulation as

$$\frac{\partial}{\partial t}u + u \cdot \nabla u = -\frac{1}{\rho}\nabla p + \nu\nabla^2 u \quad (2.1)$$

where u is the velocity vector, ρ is density, p is pressure and ν is the kinematic viscosity. The continuity equation, that accounts for the conservation of mass, reads

$$\nabla \cdot u = 0 \quad (2.2)$$

2.1 The Vorticity Transport Model

The wakes that are generated by the rotating blades of vertical-axis wind turbines are characterised by compact vortical structures. An efficient approach to model the aerodynamics of vertical-axis wind turbines is therefore via the explicit conservation of vorticity after casting the unsteady, incompressible Navier-Stokes equations in vorticity-velocity form. Taking the curl² of Equation 2.1, the Navier-Stokes equations become the vorticity transport equation

$$\frac{\partial}{\partial t}\omega + u \cdot \nabla\omega - \omega \cdot \nabla u = \nu\nabla^2\omega \quad (2.3)$$

where the vorticity $\omega = \nabla \times u$. The advection, stretching, and diffusion terms within the vorticity transport equation describe the changes in the vorticity field with time at any point in space, as a function of the velocity field, u , and the viscosity, ν .

An assumption is made that the Reynolds number of the flow that surrounds the wind turbine is sufficiently high so that the flow field can be considered as inviscid, with the exception of within the boundary layer on any solid surface that is immersed within the fluid. The vorticity transport equation can thus be written in inviscid form as

$$\frac{\partial}{\partial t}\omega + u \cdot \nabla\omega - \omega \cdot \nabla u = S \quad (2.4)$$

where the vorticity source term, S , is used to account for the creation of vorticity at any solid surfaces that move through the fluid, for instance the surfaces of the blades of the wind turbine.

2.1.2 Computational Grid

In the VTM, Equation 2.4 is discretised in finite-volume form using a structured Cartesian mesh within the fluid domain surrounding the turbine rotor, and then advanced through time. The computational grid is formed within an underlying three-dimensional Cartesian background stencil that consists of cubes with a edge-length of Δ_0 . The VTM allows grid levels of different cell size to be specified. Coarser grids are used with increasing distance from the turbine centre in order to reduce the computational costs of the simulations and to focus resources closer to where the wake needs

²see Currie (Ref. 33, p. 56) for a complete derivation

to be most highly resolved. The configuration of the overlap between different grid levels is sketched in Figure 2.1, whereas Figure 2.2 shows an example of the computed vorticity that is developed by a vertical-axis wind turbine with two straight blades after seven rotor revolutions have elapsed. At this point in the computation, the wake is contained within a series of grids with four different levels of refinement.

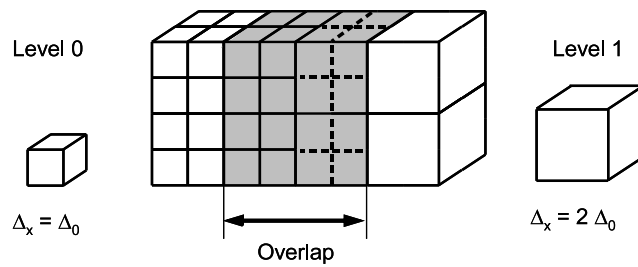


Figure 2.1: Nested grid structure with overlap of the boundaries of adjacent grid levels.

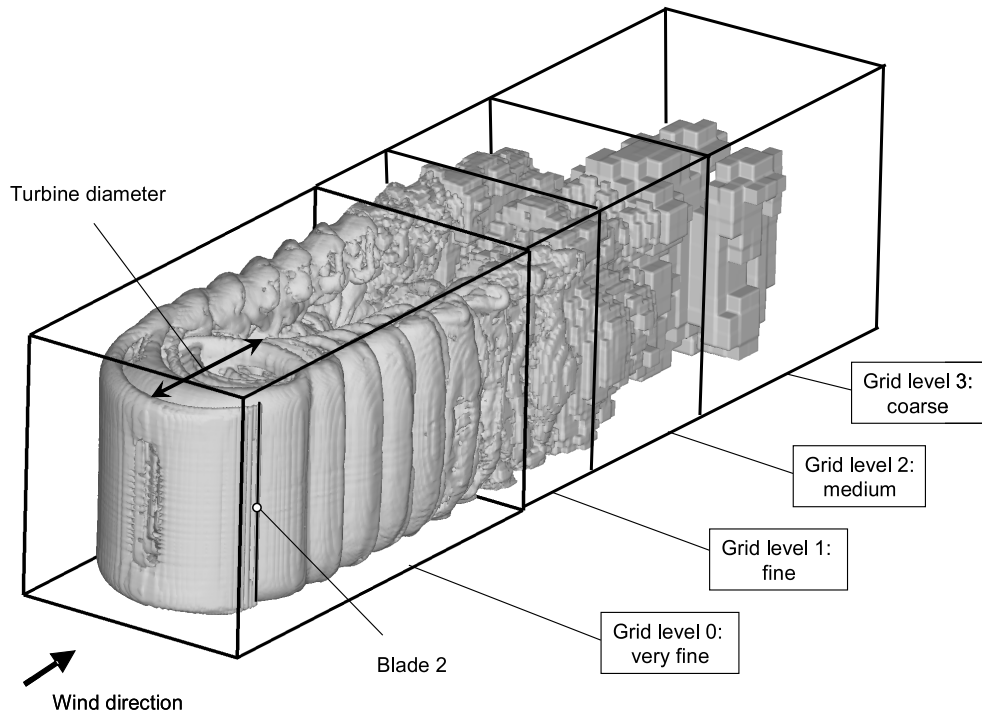


Figure 2.2: Computed vorticity in nested grid boxes that contain cells of different size.

As the vorticity moves to a new location, new cells are created and any cells that no longer contain vorticity are destroyed. Thus, the grid structure is free to follow the evolution of the wake, eliminating the requirement for explicit numerical boundary conditions at the edge of the computational domain and increasing the computational efficiency of the method.

2.1.3 Numerical Implementation

The following section describes the numerical techniques that are employed within the VTM to solve the governing equations.

2.1.3.1 Discretisation of the Governing Equations

The vorticity transport equation that governs the flow around vertical-axis wind turbines was introduced in Equation 2.4. Within the VTM, the governing equations are discretised in finite-volume formulation and then solved in the computational domain by advancing the flow field in discretised time intervals, Δt . The grid is generated by dividing the solution domain into a finite number of control volumes that represent the grid cells. The distribution of vorticity that is calculated for each cell is assumed to be uniform within the cell. Thus, any flow variable $q(x, t)$ can be defined at the current time step, n , by the spatial and temporal integration over the cell volume, V , and the time step, Δt , as

$$[q]^n = \int_V q(x, n\Delta t) dV \quad (2.5)$$

and

$$[q]_{\Delta t}^n = \int_{(n)\Delta t}^{(n+1)\Delta t} [q]^n dt \quad (2.6)$$

Consequently, the governing equation, that was presented in Equation 2.4, can be written in discretised form as

$$[\omega]^{n+1} - [\omega]^n = [\omega \cdot \nabla u]_{\Delta t}^n - [u \cdot \nabla \omega]_{\Delta t}^n + [S]_{\Delta t}^n \quad (2.7)$$

2.1 The Vorticity Transport Model

The velocity field $u^n = u([\omega]^n)$ is determined at the beginning of the n^{th} time step, i.e. at $t = n\Delta t$, from the vorticity distribution in the flow field using the Biot-Savart law that is introduced in Section 2.1.3.3 of this dissertation. Subsequently, the vorticity field at the time $t = (n + 1)\Delta t$ is calculated using an operator-splitting technique such that

$$\begin{aligned}
 [\omega]^* &= [\omega]^n + [S]_{\Delta t}^n \\
 [\omega]** &= [\omega]^* + [\omega \cdot \nabla u]_{\Delta t}^n \\
 [\omega]^{n+1} &= [\omega]** - [u \cdot \nabla \omega]_{\Delta t}^n
 \end{aligned} \tag{2.8}$$

where the stretching operator, $[\omega \cdot \nabla u]_{\Delta t}^n$, is calculated using Runge-Kutta integration and the advection operator, $[u \cdot \nabla \omega]_{\Delta t}^n$, is evaluated using the Weighted-Average-Flux (WAF) scheme, introduced by Toro [34], and described in more detail in the following section.

2.1.3.2 Advection Routine

An accurate representation of the vortical structures within the wake that is produced by a vertical-axis wind turbine is crucial if interactions between the blades of the rotor and their wakes are to be resolved with highest fidelity. Numerical diffusion is an inherent feature of many CFD methods and can often result in spatial smearing of the vorticity distribution in the flow field. Toro's Weighted-Average-Flux method is therefore employed within the VTM in order to represent the flux of vorticity through the interface between two adjacent cells and thus to evaluate the advection operator in Equation 2.8. The WAF scheme is a second order accurate Riemann solver for hyperbolic conservation laws and was originally developed in order to capture discontinuities introduced by shock waves in compressible gas dynamics problems. The capability of the method to accurately resolve steep gradients in flow properties in the vicinity of shock waves renders the approach also applicable to calculate the steep gradients that can occur in the vorticity distribution in the wake of wind turbines.

2.1 The Vorticity Transport Model

The three-dimensional advection operator is broken down into three one-dimensional operators by a space-operator splitting technique, as suggested by Strang [35]. The inter-cell flux of vorticity in one grid direction can therefore be calculated as

$$[\omega_i]^{n+1} = [\omega_i]^n - \frac{\Delta t}{\Delta x} \left(F_{i+\frac{1}{2}} - F_{i-\frac{1}{2}} \right) \quad (2.9)$$

The flux of vorticity through the left face, $F_{i-\frac{1}{2}}$, and the right face, $F_{i+\frac{1}{2}}$, of a cell i is shown schematically in Figure 2.3.

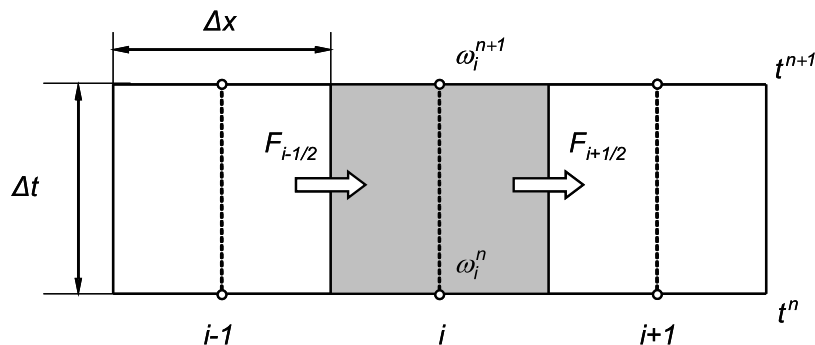


Figure 2.3: Schematic showing the calculation of vorticity across cell faces. Adapted from Toro [34].

Since the value of $[\omega_i]^n$ varies discontinuously across each cell interface, the inter-cell flux can be calculated using the solution to a piece-wise constant Riemann problem. The WAF method constructs the flux of vorticity by considering it as a wave of vorticity that arises at position $i + \frac{1}{2}$ and travels at the local flow speed $u_{i+\frac{1}{2}}$. The weighted-average flux of vorticity across the cell-interface

$$F_{i+\frac{1}{2}} = W_1 F_{i+\frac{1}{2}}^{(1)} + W_2 F_{i+\frac{1}{2}}^{(2)} \quad (2.10)$$

is composed of the two partial fluxes

$$F_{i+\frac{1}{2}}^{(1)} = u_{i+\frac{1}{2}}^n [\omega_i]^n \quad (2.11)$$

$$F_{i+\frac{1}{2}}^{(2)} = u_{i+\frac{1}{2}}^n [\omega_{i+1}]^n \quad (2.12)$$

2.1 The Vorticity Transport Model

These partial fluxes are weighted by the functions W_1 and W_2 that are defined by

$$W_1 = \frac{1}{2} \left(1 + \lambda_{i+\frac{1}{2}} \phi_{i+\frac{1}{2}} \right) \quad (2.13)$$

$$W_2 = \frac{1}{2} \left(1 - \lambda_{i+\frac{1}{2}} \phi_{i+\frac{1}{2}} \right) \quad (2.14)$$

where ϕ is the local Courant-Friedrichs-Lewy (CFL) number

$$\phi_{i+\frac{1}{2}}^n = \frac{u_{i+\frac{1}{2}}^n \Delta t}{\Delta x} \quad (2.15)$$

and λ is a wave-amplifier that is a function of the CFL number, ϕ , and the vorticity distribution ratio, r , which is calculated by

$$r_{i+\frac{1}{2}}^n = \frac{\omega_i^n - \omega_{i-1}^n}{\omega_{i+1}^n - \omega_i^n} \quad (2.16)$$

The amplifier functions that are used within the VTM are based on the SUPERA amplifier function that was suggested by Toro [36].

Godunov [37] showed that only first-order linear schemes preserve monotonicity. As a second order scheme, the WAF method, in contrast, is susceptible to spurious oscillations in the region of large vorticity gradients. The wave-amplifiers are therefore selected to maintain monotonicity of the solution by rendering the scheme Total Variation Diminishing (TVD). The Total Variation of the vorticity field at timestep n is defined as

$$TV^n(\omega) = \sum_{i=-\infty}^{\infty} |[\omega_{i+1}]^n - [\omega_i]^n| \quad (2.17)$$

and a fully TVD scheme must satisfy the condition

$$TV^{n+1}(\omega) \leq TV^n(\omega) \quad (2.18)$$

This simply imposes geometric bounds on the relationship between the wave-amplifier and the vorticity distribution ratio, as explained by Toro (Ref. 38, p. 456ff.).

2.1.3.3 Velocity Field

Before the inter-cell vorticity flux can be calculated using the WAF method, the velocities at the cell faces have to be determined. Within the VTM, the local velocities in the flow field are calculated using the Biot-Savart law as described below.

The well-justified assumption that the flow field surrounding wind turbines is incompressible results in the velocity field having zero divergence. Consequently, the velocity field is entirely defined by the vorticity field, and can be calculated through a vector identity. Since $\omega = \nabla \times u$, the curl of vorticity can also be written as

$$\nabla \times \omega = \nabla(\nabla \cdot u) - \nabla^2 u \quad (2.19)$$

Using the continuity equation for incompressible flow, introduced in Equation 2.2, the relationship that is presented in Equation 2.19 results in a Poisson equation that is sometimes referred to as the differential form of the Biot-Savart law

$$\nabla^2 u = -\nabla \times \omega \quad (2.20)$$

The solution to Equation 2.20 can be found using Green's theorem³, so that the Biot-Savart law can be written in integral form as

$$u(x) = \int_V K(x, y) \times \omega(y) dy \quad (2.21)$$

where the Biot-Savart kernel K is given by

$$K(x, y) = -\frac{1}{4\pi} \frac{(x - y)}{|x - y|^3} \quad (2.22)$$

Within the VTM, the regularised kernel, as suggested by Rosenhead [40] and Moore [41],

$$K_\delta(x, y) = -\frac{1}{4\pi} \left(\frac{(x - y)}{(|x - y|^2 + \delta^2)^{3/2}} \right) \quad (2.23)$$

³see Karamcheti (Ref. 39, p. 532ff.) for a complete derivation

2.1 The Vorticity Transport Model

is used to approximate the Biot-Savart kernel in order to overcome the singularity that occurs if $x = y$. The value of the artificial smoothing parameter, δ , is chosen in order to ensure that the maximum velocity induced by the vorticity within a cell is found at the faces of the cell, as explained by Line [42].

Using the methodology described above, the velocity field that is induced by the vorticity field can then be approximated by

$$u(x) \approx \int_V K_\delta(x, y) \times \omega(y) dy \quad (2.24)$$

The local velocity that is induced at the location x_0 can be calculated by a summation over all the individual cells, i , located at y_c and containing the vorticity ω_i

$$u(x_0) \approx \sum_{i=1}^N K_\delta(x_0, y_c) \times \omega_i \quad (2.25)$$

A direct summation over all the cells that contain vorticity would result in high computational costs, however, since the number of mathematical operations that have to be carried out in order to solve the Biot-Savart relationship increases in proportion to N^2 , where N is the number of cells. The computational costs can be reduced to have a linear dependency on the number of cells by the use of the Fast Multipole Method (FMM), developed by Greengard and Rokhlin [43]. Within the FMM, clusters are formed by grouping together individual vorticity-containing cells. The Biot-Savart interactions are then modelled as interactions between these clusters rather than interactions between individual cells. The interaction between two clusters can then be determined assuming that the second cluster is well separated from the first. Figure 2.4 shows a schematic of the interaction between clusters with the vorticity weighted centre of the cluster being located at y_σ and the centre of each individual vorticity containing cell being located at y_j .

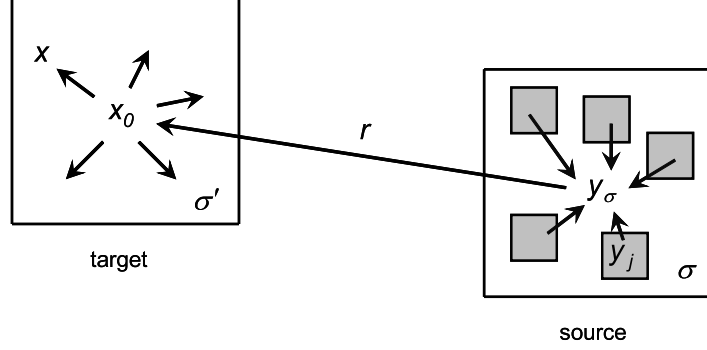


Figure 2.4: Schematic showing the interaction between target and source clusters using the multipole method to calculate the velocity field.

The vorticity within the cluster σ induces the velocity

$$u(x_0) \approx \sum_{j \in \sigma} K_\delta(x_0, y_j) \times \omega_j \quad (2.26)$$

at the centre of the second cluster σ' . Equation 2.26 can be expanded about the centre of the source cluster using a three-dimensional Taylor series so that

$$\begin{aligned} u(x_0) &\approx \sum_{j \in \sigma} K_\delta(x_0, y_\sigma + (y_j - y_\sigma)) \times \omega_j \\ &\approx \sum_{j \in \sigma} \sum_k \frac{1}{k!} D_y^k K_\delta(x_0, y_\sigma) (y_j - y_\sigma)^k \times \omega_j \end{aligned} \quad (2.27)$$

with the vectors $k = (k_1, k_2, k_3)$, $k! = (k_1!, k_2!, k_3!)$, $D_y^k = (\partial/\partial y_1^{k_1}, \partial/\partial y_2^{k_2}, \partial/\partial y_3^{k_3})$, and $x^k = (x_1^{k_1}, x_2^{k_2}, x_3^{k_3})$ for $k_i \geq 0$. The subscripts 1, 2 and 3 refer to the Cartesian directions x , y and z . Truncating the series at the p th term yields the approximation for the induced velocity

$$u(x_0) \approx \sum_{k=0}^p a_k(x_0, y_\sigma) \times m_k(\sigma) \quad (2.28)$$

2.1 The Vorticity Transport Model

where a_k is a tensor that expresses the range of the interactions in cluster σ and is given by

$$a_k(x_0, y_\sigma) = \frac{1}{k!} D_y^k K_\sigma(x_0, y_\sigma) \quad (2.29)$$

and the moment of vorticity, m_k , describes the local distribution of vorticity within the cluster and is given by

$$m_k(\sigma) = \sum_{j \in \sigma} (y_j - y_\sigma)^k \omega_j \quad (2.30)$$

The discrete velocities in the target cluster are calculated by using a truncated Taylor series expansion about the centre of the cluster x_0 . The velocities at other positions, x , within the target cluster can then be approximated by using a series expansion about x_0 . This requires the spatial derivative of the velocity at this location. Differentiating Equation 2.28 with respect to x_0 gives the spatial derivative

$$D_x^n u(x_0) = (-1)^n \sum_{k=n}^p \frac{k!}{(k-n)!} a_k(x_0, y_\sigma) \times m_{k-n}(\sigma) \quad (2.31)$$

A Taylor expansion may be used to extrapolate from the velocity at location x_0 to the velocity at a nearby point x in the target cluster such that

$$u(x) \approx u(x_0) + \sum_{k=n}^p \frac{1}{k!} D_x^k u(x_0) (x - x_0)^k \quad (2.32)$$

The derivatives of the velocity field at the location x can also be obtained in a similar fashion.

Within the VTM, the computational cells are clustered in an octree data structure that allows the storage of the velocity field and the vorticity field on levels similar to those used to construct the adaptive grid that was described earlier. Eight individual ‘child’ cells are grouped together at the lowest level of the structure and allocated to a ‘parent’ cluster on the next octree level. Eight of these clusters, that are now considered as the ‘children’, are grouped together to form a further parent cluster. This process

is repeated throughout the grid until the entire domain is embedded in one ‘parent’ cluster.

At the start of the velocity calculation, the FMM determines the moments of vorticity, as given in Equation 2.30, in a sweep up through the octree structure from the individual cells to the overall parent cluster. Subsequently, the velocity on each level is calculated by a sweep back down through the octree structure. Hereby, the velocity at cluster i on level n is composed of contributions from far field, intermediate field and near field velocities. The near field consists of the clusters that directly neighbour the cluster i . The intermediate field is defined within the next hierarchical level as the set of parent clusters neighbouring the particular parent cluster that contains i . The far field consists of the remaining clusters. This structure is depicted in Figure 2.5.

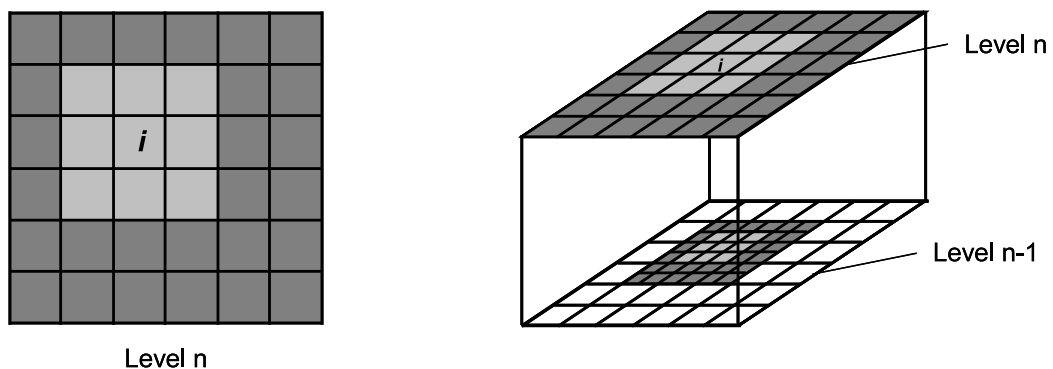


Figure 2.5: Representation of the velocity field of cluster i and the velocity-inducing clusters in the near field (light grey), in the intermediate field (dark grey) and in the far field (white).

The velocity for a cluster i , located on level n , that is induced by the vorticity in the intermediate field is calculated by Equation 2.28, thereby taking into account all cluster-cluster interactions on that level. The velocity thus determined is added to the velocity contribution from the far field that is calculated on level $n + 1$ and then transferred to the children of i on level $n - 1$ using Equation 2.32. The far and the intermediate fields of i then become the far field of the children of i , whereas the near field of i becomes the intermediate field of the children. This process is repeated for all clusters on level n before a downward sweep is carried out through the octree to level $n - 1$. Once the lowest level of the octree structure is reached, the far field component is determined

for each cell. The Biot-Savart relationship, given in Equation 2.26, is then used to calculate directly the components of the velocity from the near and intermediate field. The summation of the velocity components from the far, intermediate and near field yields the overall velocity field from which the advection of the vorticity field can be evaluated.

2.1.3.4 Vorticity Source

In the derivation of the Vorticity Transport Equation, presented in Equation 2.4, it was assumed that the flow field surrounding the wind turbine is inviscid. Viscosity exists, however, in the thin boundary layer on the surface of the rotating blades of the wind turbine. The vorticity source term, S in Equation 2.4, is used to account for the creation of vorticity at the rotor blades, and at any other solid surfaces that are immersed within the fluid. The vorticity source term is calculated as the sum of the temporal and spatial variations in the bound vorticity, ω_b , on the rotor blades so that

$$S = -\frac{d}{dt}\omega_b + u_b\nabla \cdot \omega_b \quad (2.33)$$

where u_b is the local velocity that comprises contributions from the circumferential velocity of the blade, the free stream velocity and the velocity component induced by the wake. The first term in Equation 2.33 represents the shed vorticity and the second term represents the trailed vorticity from the blade. Most importantly in the present context, the shed vorticity distribution behind the blade is fully resolved within the approach. The influence of the shed vorticity on the unsteady aerodynamic response of the system is thus captured directly in the simulations without the need for empirical modeling of the response of the blade. The implication of this inherent feature of the VTM on the coupling between the wake and blade models will be discussed in Chapter 3 of this dissertation.

Various methods can be used to calculate the vorticity that is generated by the blades, including conventional CFD methods, as demonstrated by Whitehouse *et al.* [44]. The blade aerodynamic model that is implemented within the version of the VTM used to generate the results that are presented in this dissertation is based on an approach, however, that is informed by lifting-line theory, as introduced by Prandtl [45, 46]. This

model, which is somewhat simpler to implement into a simulation tool and to apply in the engineering context than a CFD method, is described in more detail in Chapter 3 of this dissertation.

The timescales at which the wake of a wind turbine evolves are typically many times larger than those that must be resolved in order to capture the unsteady aerodynamics of the rotor. A substepping approach is thus implemented in the VTM in order to account for the different time scales of the outer and inner wake. Thereby, the global timestep Δt is divided into M substeps, Δt_i . A partial contribution, $[S]_{\Delta t_i}^{n+i/M}$, of the source term, $[S]_{\Delta t_i}$, is calculated within the blade aerodynamic model at each substep i . This partial contribution represents the vorticity that is created in close vicinity to the rotor blade from time $n\Delta t + i\Delta t_i$ to $n\Delta t + (i + 1)\Delta t_i$. The vorticity source term that is passed to the wake solution at each global timestep, Δt , is then simply the sum of the vorticity at each substep

$$[S]_{\Delta t}^n = \sum_{i=0}^{M-1} [S]_{\Delta t_i}^{n+i/M} \quad (2.34)$$

2.1.4 Ground Plane

The VTM-predicted variation with azimuth of the blade aerodynamic loading on a straight-bladed vertical-axis wind turbine is compared to experimental measurements made by Strickland *et al.* [47] in Chapter 4 of this dissertation. The particular design of the experiment resulted in rotor blades that operate very close to a horizontal solid surface that was part of the test facility. In VTM simulations of this experiment, a ground plane was modelled using the method of images in order to mimic the effects of this solid surface on the flow around the turbine. The method of images is based on the creation of a mirror image of the rotor and the wake that is generated by its blades. The component of vorticity parallel to the ground plane in the mirrored wake is equal in strength but opposite in direction to that within the original rotor wake. The component of vorticity normal to the ground plane, however, is equal both in strength and direction to that within the original wake. The ground plane is, consequently, located half way between the original and the mirrored wake, as depicted in Figure 2.6. The component normal to the ground plane of the induced velocity in the wake above and the wake below the ground plane cancel out so that zero flow through the ground

plane is achieved. It should be noted that the method of images represents an inviscid ground plane. In other words, any flow features, such as the secondary ground vortices that were described by Harvey and Perry [48], that may be found if a true no-slip condition on the ground plane was accounted for, are not captured using the present approach.

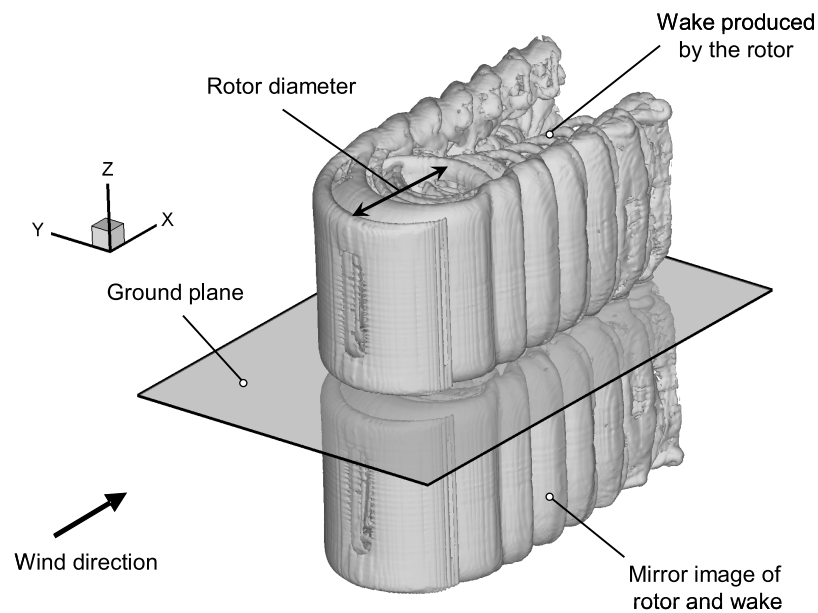


Figure 2.6: *Ground plane formed using the method of images. Adapted from Whitehouse [49].*

2.2 Summary

The numerical methods that are used within the VTM to solve the governing equations and thus to calculate the flow field surrounding vertical-axis wind turbines have been presented. The governing equations are discretised in a finite-volume formulation and then solved on a structured Cartesian grid that surrounds the rotor. The fast multipole method is used, in conjunction with an adaptive grid in which cells are only present within the calculation when the vorticity within them is non-zero, to reduce considerably the computational cost of each simulation when compared to an equivalent calculation performed on a fixed grid. As the vorticity moves to a new location, new

cells are created and any cells that no longer contain vorticity are destroyed. Thus, the grid structure is free to follow the evolution of the wake, eliminating the requirement for explicit numerical boundary conditions at the edge of the computational domain and increasing the computational efficiency of the method. The numerical diffusion of vorticity within the flow field surrounding the wind turbine is kept at a very low level by using a Riemann problem technique based on Toro's Weighted Average Flux method. This approach permits many rotor revolutions to be captured without significant spatial smearing of the wake structure. This is in contrast to the performance of more conventional CFD techniques based on the pressure-velocity-density formulation of the Navier-Stokes equations. These features render the VTM applicable to the study of the performance and wake dynamics of vertical-axis wind turbines.

2.3 Chapter Nomenclature

a_k	k^{th} Taylor coefficient of K_δ
F	intercell vorticity flux
i, j	indices
K	Biot-Savart kernel
K_δ	Rosenhead-Moore kernel
m_k	k^{th} moment of vorticity
M	number of substeps
n	current time step
p	pressure
q	any flow variable
r	vorticity distribution ratio
S	vorticity source
t	time
u	flow velocity
u_b	local velocity at a blade section
V	cell volume
W	weighting function
δ	artificial smoothing parameter
Δ_0	cell edge-length of the underlying Cartesian stencil

2.3 Chapter Nomenclature

Δt	global (outer) time step
Δx	cell edge-length
λ	wave-amplifier function
ν	kinematic viscosity
ρ	density
σ	source cluster
ϕ	local cell CFL number
ω	vorticity
ω_b	vorticity bound to rotor blades

Chapter 3

Blade Aerodynamic Model

The VTM consists of an outer model, in which the dynamics of the wake that is generated by the rotor are calculated based on basic fluid dynamics principles, and an inner model, in which the aerodynamic loads on the blades of the rotor are determined. Various methods can be used to calculate the bound vorticity on the blades, thereby coupling the outer wake model with the inner model for the blade aerodynamic loading within the VTM. The blade aerodynamic model, that is employed within the version of the VTM used to generate the results that are documented in this dissertation, is outlined in the present chapter. In addition, the phenomenon of dynamic stall and the strategies used to model its effect on the aerodynamic characteristics of an aerofoil are described, since dynamic stall plays an important role in the aerodynamics of vertical-axis wind turbines. Subsequently, the implementation of a dynamic stall model into the blade aerodynamic model within VTM is documented, and comparisons are shown between VTM simulations of dynamic stall and experimental measurements in order to verify the approach.

3.1 Lifting-Line Model

A modified version of the Weissinger lifting-line model [50] is employed within the VTM to calculate the blade aerodynamic loading for all the simulations that are presented in this dissertation. Within the Weissinger-L model, each rotor blade is represented by a number of panels, as depicted in Figure 3.1. A bound vortex and a collocation point are located at the quarter-chord and at the three-quarter chord of each panel,

respectively. The strength of the bound vortex, ω_b , is determined by the condition that the component of the local flow velocity, u_b , normal to the panel is zero at all collocation points. The trailed and shed vorticity form a vortex lattice that detaches from the blade at the separation line and convects freely with the local velocity behind the blade. The vortex lattice structure is interpolated into the computational grid, and thus transformed to cell-based vorticity, when the panels reach a pre-defined age.

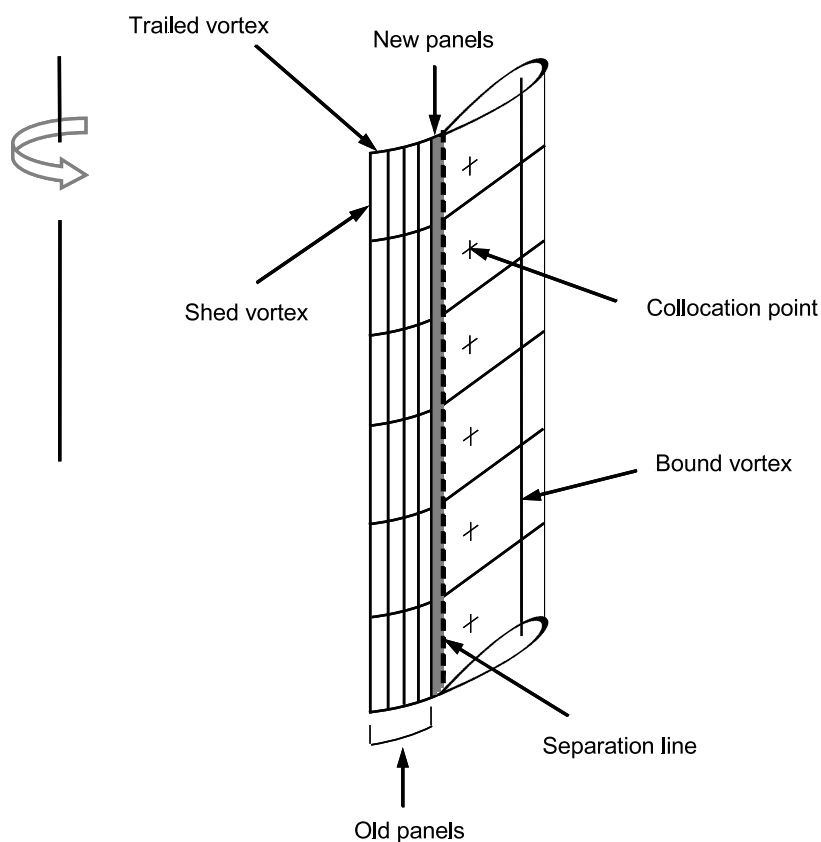


Figure 3.1: *Blade aerodynamic model and inner wake model.*

Classical lifting-line theory predicts the derivative of the lift coefficient with respect to the angle of attack for a panel with infinite aspect ratio to be 2π . Although this is an accurate approximation for most aerofoils that are operated at very low angles of attack, as shown by Abbott and von Doenhoff [51], amongst others, this derivative diverges significantly from 2π at moderate incidences. The angle of attack of the

blades of vertical-axis wind turbines can easily exceed 25° , particularly at low tip speed ratios. The non-linear variation of lift with angle of attack, and in particular the occurrence of dynamic stall, has thus to be accounted for in the blade aerodynamic model if the aerodynamics of vertical-axis wind turbines are to be predicted accurately. Consequently, The Weissinger-L method has been modified within the VTM by using two-dimensional experimental aerofoil data in order to represent the real performance of any given aerofoil. The modification is carried out by scaling the strength of the bound circulation by the ‘real’ lift coefficient at the specific angle of attack. The ‘real’ lift coefficient is provided either by look-up tables that contain the experimentally measured static two-dimensional characteristics of the rotor blade sections or by a dynamic stall model. In this dissertation it is shown that the inclusion of an accurate representation of dynamic stall is crucial if the aerodynamics of vertical-axis wind turbines are to be predicted reliably.

3.2 Modelling of Dynamic Stall

The geometric angle of attack on the blades of a vertical-axis wind turbine varies cyclically with azimuth due to the continuously changing geometric relationship between the free stream velocity and the rotational velocity of the blade. Dynamic stall can occur when the angle of attack transiently exceeds the static stall angle of the aerofoil sections of the rotor blade. Since the maximum angle of attack experienced by the blades *increases* when the tip speed ratio of the turbine *decreases*, dynamic stall becomes increasingly important at lower tip speed ratios. As will be shown later in this dissertation, dynamic stall can also occur at high tip speed ratios when the angle of attack on the blade is locally increased by interactions between the blades of the rotor and the vortices within the wake that is generated by the turbine.

3.2.1 The Dynamic Stall Phenomenon

The phenomenon of dynamic stall is still not fully understood although it has been the subject of intensive study in past decades using both experimental and numerical methods. The understanding of the mechanisms that trigger dynamic stall and the ability to predict the influence of the associated unsteady aerodynamic conditions on

the behaviour of an aerofoil is of particular interest in the context of helicopter aerodynamics. This is because dynamic stall is an essential factor that limits the flight envelope of helicopters. Not surprisingly, most studies of dynamic stall in the past were therefore carried out for operating conditions, in terms of Reynolds and Mach numbers, that are comparable to those encountered in the flow environment around helicopter rotor blades.

A selection of relevant publications concerning the phenomenon of dynamic stall is given below. McCroskey *et al.* [52] took pressure, hot-film and hot-wire measurements of the flow around various aerofoil sections under dynamic stall conditions in order to investigate the influence of dynamic stall on forces and pitching moments, and boundary-layer separation and reattachment characteristics. In addition to hot-wire and pressure measurements, Carr *et al.* [53] used smoke visualisation techniques to study the influence of reduced frequency, Reynolds number and oscillation amplitude on the dynamic stall characteristics of an oscillating aerofoil, whereas Chandrasekhara and Carr [54] employed a stroboscopic schlieren system to visualise the formation and convection of dynamic stall vortices along the upper surface of an oscillating aerofoil. In recent years, increased availability of high-performance computing has allowed the phenomenon of dynamic stall to be studied using the Navier-Stokes equations. The influence of reduced frequency, mean angle of attack and Reynolds number on the dynamic stall characteristics of an aerofoil were investigated numerically by Akbari and Price [55] who solved the two-dimensional Navier-Stokes equations in streamfunction-vorticity formulation. Spentzos *et al.* [56] carried out a CFD study of the three-dimensional flow field around wings with various planform shapes in dynamic stall conditions. Simão Ferreira *et al.* [29] used a URANS approach, DES and LES in order to investigate dynamic stall on an aerofoil while in a planar, cyclic motion designed to emulate that of the blades of a vertical-axis wind turbine. They compared their findings to the results of an experimental study in which they used PIV measurements to visualise the flow field surrounding a straight-bladed vertical-axis wind turbine under dynamic stall conditions.

According to McCroskey *et al.* [52], dynamic stall will occur on any lifting surface when it is subjected to any type of unsteady motion, such as pitching, plunging or vertical translation, that takes the effective angle of attack above its static stall angle. As the angle of attack increases, the flow stays attached on the upper surface of

an oscillating aerofoil much longer, and thus produces higher values of the lift coefficient, compared to an aerofoil under quasi-steady conditions. As the angle of attack subsequently decreases, the lift coefficient is significantly smaller than that obtained in a static aerofoil test, however. For these reasons, the variation of the lift, drag and moment coefficients of an aerofoil under dynamic stall conditions is characterised by marked hysteresis and thus differs significantly from the performance of the same aerofoil under quasi-steady conditions.

Leishman (Ref. 57, p. 527) identified three principal unsteady phenomena to be responsible for the delay in the onset of stall under unsteady conditions. Firstly, an increase in the angle of attack causes vorticity to be shed into the wake which results in a reduction in lift and a less adverse pressure gradient compared to that at the same angle of attack under quasi-steady conditions. Secondly, a positive pitch rate results in a decrease in the leading edge pressure gradient due to the kinematically induced camber effect. Thirdly, unsteady effects in the boundary layer, such as flow reversal without significant flow separation, contribute to a delay in stall onset. The strong adverse pressure gradient that finally builds up at the leading edge of the aerofoil, if the angle of attack is increased under dynamic conditions, results ultimately in the formation of a free shear layer at the leading edge. Subsequent to the formation and roll up of the shear layer to form a vortical disturbance, this dynamic stall vortex convects over the upper surface of the aerofoil and is finally shed at the trailing edge into the wake. A schematic of the flow morphology at various stages of the dynamic stall process, and the concomitant effect on the aerodynamic coefficients of the aerofoil, is presented in Figure 3.2. According to Leishman (Ref. 57, p. 528f.), the process of dynamic stall can be described by a sequence of events:

1. The onset of flow separation is delayed due to a reduction in the adverse pressure gradient as a result of the influence of the shed wake, the induced camber effect and the unsteady boundary layer response, as described above (*Stage 1*).

2. Vortex formation at the leading edge of the aerofoil at the beginning of *Stage 2* results in additional lift but a break in the moment coefficient. This stage is therefore also called moment stall.

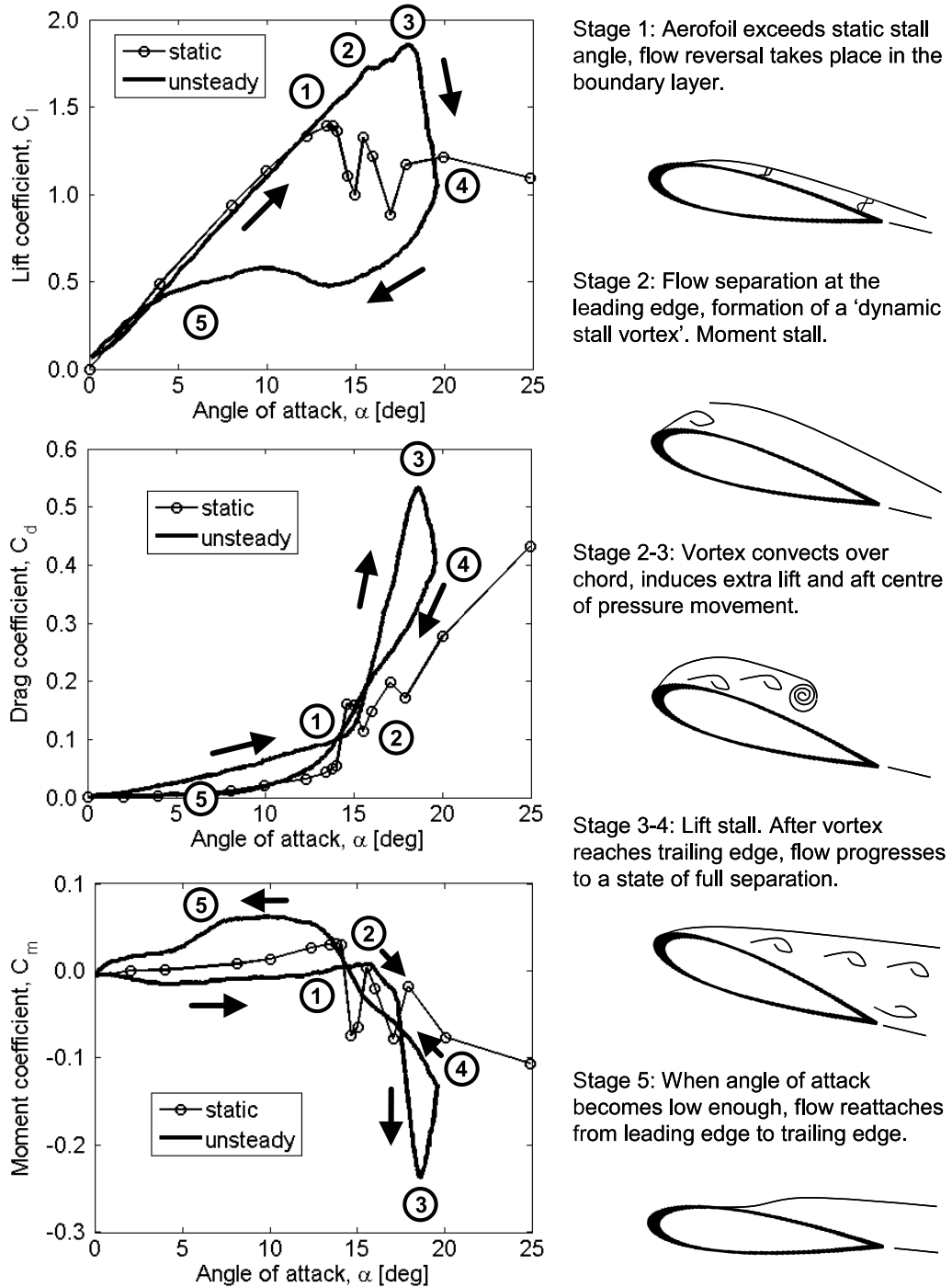


Figure 3.2: Schematic showing the essential flow morphology and the aerodynamic coefficients during the dynamic stall process on an oscillating aerofoil. Adapted from Leishman [57].

3. The vortex convects over the upper surface of the aerofoil between *Stage 2* and *Stage 3*. This process is associated with a further increase in lift but a significant nose-down pitching moment since the centre of pressure moves towards the trailing edge of the aerofoil. Green *et al.* [58] showed in experimental measurements that the convection speed of the dynamic stall vortex is between one half and one third of the free stream velocity.

4. The vortex reaches the trailing edge of the aerofoil and is shed into the wake between *Stage 3* and *Stage 4*. As a consequence, lift, pressure drag and nose-down pitching moment reach their maxima. The sudden drop of the lift coefficient after having reached its maximum is referred to as lift stall.

5. Subsequent to the state of fully separated flow, in which the aerodynamic loading is approximately the same as in quasi-steady conditions, flow reattachment takes place when the angle of attack becomes low enough (*Stage 5*). The time that is required for the disturbance in the flow to convect far enough downstream in order for flow attachment to take place, and the reverse kinematically induced camber effect on the leading edge pressure gradient that results from the negative pitch rate, result in a marked delay in the attachment process, however.

3.2.2 Implementation of a Dynamic Stall Model into the VTM

The unsteady loads that are produced on the blades of a wind turbine during dynamic stall can exceed considerably the loading that might be predicted by an analysis in which a quasi-steady flow state is assumed. The accurate prediction of unsteady aerodynamic effects, and in particular dynamic stall, is therefore vital in the design process for wind turbines in order to predict reliably the performance of the turbine and thus to avoid either material fatigue or unnecessary safety margins. The accurate numerical simulation of the dynamic stall phenomenon poses a significant challenge, however, since the underlying physics are characterised by complex and non-linear flow phenomena that include unsteady attached and separated flow, boundary layer separation, flow reattachment and vortex shedding. The approaches that were adopted in the past in order to simulate the effect of dynamic stall on the performance of rotor blades of wind turbines and helicopters were therefore mostly based on semi-empirical

models. A description of the various different modelling techniques used in the past is given by Leishman (Ref. 57, p. 537ff.).

The Weissinger-L method that is used within the VTM to model the blade aerodynamic loading, as described in Section 3.1 of this dissertation, has been modified to incorporate a semi-empirical dynamic stall model to account for the effect of dynamic stall on the aerodynamic performance of any given aerofoil. The dynamic stall model that was implemented in the VTM follows the approach suggested by Leishman and Beddoes [59] but was modified in order to couple the model to the VTM, as explained in the following section. The Leishman-Beddoes model was originally developed to simulate the effect of dynamic stall on the blades of a helicopter. Gupta and Leishman [60] demonstrated, however, that a modified version of the original Leishman-Beddoes model can be used to represent the dynamic stall of aerofoils that are comparable to those used for horizontal-axis wind turbines.

The Leishman-Beddoes dynamic stall model is based on classical unsteady thin aerofoil theory that was first described by Theodorsen [61] and by von Kármán and Sears [62], but includes empirical parameters that are deduced from experimental measurements. The model that was proposed by Leishman and Beddoes consists of three subroutines. The first and second account for the unsteady airloads in attached flow and in separated flow, respectively, and the third represents the airloads that are induced if a dynamic stall vortex forms near the leading edge and convects over the chord of the aerofoil.

3.2.2.1 Non-Linear Quasi-Steady Aerofoil Model

The approach that was proposed by Leishman and Beddoes to model both attached and separated flow follows directly from the Kirchhoff-Helmholtz theory that is described by Thwaites [63], amongst others. Hereby, the trailing edge separation phenomenon in the stall and post-stall region of a lifting body is considered as specific case of the Kirchhoff flow so that the sectional normal force coefficient, C_n , and the sectional tangential force coefficient, C_t , can be approximated as a function of the chordwise location of the separation point using

$$C_n = C_{n_\alpha} \left(\frac{1 + \sqrt{f}}{2} \right)^2 \alpha \quad (3.1)$$

$$C_t = C_{n_\alpha} \alpha^2 \sqrt{f} \quad (3.2)$$

where α is the angle of attack and C_{n_α} is the derivative of the normal force coefficient with respect to the angle of attack. The parameter f is the chordwise position at which the flow separates from the upper surface of the aerofoil, non-dimensionalised by the aerofoil chord. The relationship between the angle of attack, α , and the parameter f is given empirically by the functions

$$f = \begin{cases} 1.00 - 0.40 \exp\left(\frac{\alpha - \alpha_1}{S_1}\right) & \text{if } \alpha \leq \alpha_1 \\ 0.02 + 0.58 \exp\left(\frac{\alpha_1 - \alpha}{S_2}\right) & \text{if } \alpha > \alpha_1 \end{cases} \quad (3.3)$$

where the angle α_1 and the coefficients S_1 and S_2 are empirical parameters that describe the behaviour of the aerofoil in question under quasi-steady conditions.

Experimental measurements made by Angell *et al.* [64] revealed that the tangential force can become negative under deep stall conditions. This observation conflicts with the Kirchhoff theory since the tangential force coefficient, based on this theory, is always greater than or equal to zero irrespective of the flow state. Sheng *et al.* [65] thus suggested a modification to the model. The modification includes an additional parameter, here defined as K , that accounts for negative tangential forces at low Mach numbers in deep dynamic stall. Consequently, the sectional normal and tangential force coefficients are written as

$$C_n = C_{n_\alpha} \left(\frac{1 + \sqrt{f}}{2} \right)^2 \sin \alpha \quad (3.4)$$

$$C_t = C_{n_\alpha} \alpha \sin \alpha \left(\sqrt{f} - K \right) \quad (3.5)$$

The onset of flow separation at the leading edge is defined by a criterion that is based on the study carried out by Evans and Mort [66]. They showed that the peak velocity on the upper surface of an aerofoil, that was operated at stall incidence in quasi-steady conditions, can be related to the distance between the location at which the peak velocity occurs and the laminar separation point. Beddoes [67, 68] showed that the variation with pitch rate of this correlation is small for a given aerofoil at given Mach and Reynolds numbers and suggested to use the Evans-Mort correlation to define a critical value of the normal force coefficient, C_{n_1} , in order to indicate the onset of dynamic stall.

3.2.2.2 Unsteady Attached Flow

The aerofoil performance under unsteady (but attached) flow conditions is calculated by a superposition of indicial aerodynamic response functions derived from a finite-difference approximation to Duhamel's integral. The indicial response, or in other words, the response to a step change in forcing, can be expressed as the steady state response added to which is a deficiency function that decays exponentially with time. Consequently, the normal force coefficient due to circulation, $C_{n_k}^C$, that arises from a step change in angle of attack, α , is expressed by

$$C_{n_k}^C = C_{n_\alpha} (\alpha_k - X_k - Y_k) = C_{n_\alpha} \alpha_{e_k} \quad (3.6)$$

where k is the current time sample, α_e is the equivalent angle of attack in quasi-steady conditions and X and Y are deficiency functions that are given by

$$X_k = X_{k-1} \exp\left(\frac{-\Delta s}{T_1}\right) + A_1 (\alpha_k - \alpha_{k-1}) \exp\left(\frac{-\Delta s}{2 T_1}\right) \quad (3.7)$$

$$Y_k = Y_{k-1} \exp\left(\frac{-\Delta s}{T_2}\right) + A_2 (\alpha_k - \alpha_{k-1}) \exp\left(\frac{-\Delta s}{2 T_2}\right) \quad (3.8)$$

where Δs is the distance travelled by the aerofoil in semi-chords, A_1 and A_2 are empirical coefficients and T_1 and T_2 are empirical time constants.

The induced velocity due to vortex shedding in unsteady attached flow is already accounted for in the VTM, however, through its model of the shed wake, as described in Section 2.1.3.4 of this dissertation. In other words, the angle of attack in unsteady

attached flow that is calculated within the VTM for each time step is identical to the equivalent angle of attack, α_{e_k} , in Equation 3.6. Consequently, the deficiency functions that are presented in Equations 3.7 and 3.8 were not included in the dynamic stall model that is implemented within the VTM.

It should be noted that the total normal force coefficient under attached flow conditions, C_n , is calculated in the original Leishman-Beddoes model as the sum of the circulatory and impulsive components

$$C_{n_k} = C_{n_k}^C + C_{n_k}^I \quad (3.9)$$

The impulsive component, $C_{n_k}^I$, of the normal force was not included in the dynamic stall model that is implemented in the VTM, however, since any non-circulatory contribution to the loading is calculated within the VTM independently of the Weissinger-L blade model, as described by Line [42].

3.2.2.3 Unsteady Separated Flow

In unsteady flow conditions, changes in angle of attack cause a lag in the leading edge pressure response that results in a lag in the normal force coefficient. Thus, the critical pressure at which leading edge separation occurs in unsteady conditions is achieved at much higher angles of attack when compared to quasi-steady flow conditions, and consequently results in a delay in the onset of dynamic stall. This delay is accounted for in the model by a first-order lag that is applied to the normal force coefficient, C_{n_k} , to give

$$C'_{n_k} = C_{n_k} - D_k^p \quad (3.10)$$

where the deficiency function

$$D_k^p = D_{k-1}^p \exp\left(\frac{-\Delta s}{T_p}\right) + (C_{n_k} - C_{n_{k-1}}) \exp\left(\frac{-\Delta s}{2 T_p}\right) \quad (3.11)$$

T_p is a time constant that is obtained from experimental measurements. Niven and Galbraith [69] showed that this time lag is insufficient to model the behaviour of an aerofoil when it is operated at low Mach numbers, however. They thus suggested a modification to the model in order to improve the performance of the model at low

Mach numbers. In the modified model an additional lag is applied to the normal force coefficient to account for the finite time between initial boundary layer perturbation and vortex formation. The lag can be written in numerical form as

$$C''_{n_k} = C'_{n_k} - D_k^b \quad (3.12)$$

with the deficiency function

$$D_k^b = D_{k-1}^b \exp\left(\frac{-\Delta s}{T_b}\right) + \left(C'_{n_k} - C'_{n_{k-1}}\right) \exp\left(\frac{-\Delta s}{2 T_b}\right) \quad (3.13)$$

and a time constant T_b that is also obtained from experimental measurements.

An effective angle of attack, α_f , can then be calculated as

$$\alpha_{f_k} = \frac{C''_{n_k}}{C_{n_\alpha}} \quad (3.14)$$

Consequently, a parameter that describes the location of the effective separation point, f' , is obtained by using the effective angle of attack in the relationship

$$f'_k = \begin{cases} 1.00 - 0.40 \exp\left(\frac{\alpha_{f_k} - \alpha_1}{S_1}\right) & \text{if } \alpha_{f_k} \leq \alpha_1 \\ 0.02 + 0.58 \exp\left(\frac{\alpha_1 - \alpha_{f_k}}{S_2}\right) & \text{if } \alpha_{f_k} > \alpha_1 \end{cases} \quad (3.15)$$

Equation 3.15 is equivalent to Equation 3.3 under quasi-steady flow conditions. A further first-order lag is applied to the parameter f' in order to account for additional effects of the unsteady boundary layer response so that a parameter that describes the location of the trailing edge separation point, f'' , under unsteady flow conditions, is obtained as

$$f''_k = f'_k - D_k^f \quad (3.16)$$

where the deficiency function

$$D_k^f = D_{k-1}^f \exp\left(\frac{-\Delta s}{T_f}\right) + \left(f'_k - f'_{k-1}\right) \exp\left(\frac{-\Delta s}{2 T_f}\right) \quad (3.17)$$

with the time constant T_f that is, again, obtained empirically.

3.2.2.4 Dynamic Stall Vortex

The formation and shedding of a dynamic stall vortex results in an additional contribution to the normal force coefficient. The presence of the dynamic stall vortex results in a marked overshoot of the normal force. Following the method that was suggested by Beddoes [70] and adapted by Sheng *et al.* [65], the added overshoot due to the dynamic stall vortex can be expressed as

$$C_{nV_k} = V_{x_k} (f_k'' - f_k') \quad (3.18)$$

and added to the normal force coefficient. V_{x_k} is a function of the normal force due to the dynamic stall vortex and is defined as

$$V_{x_k} = \begin{cases} \sin^{3/2} \left[\frac{\pi \tau_k}{2 T_v} \right] & \text{if } 0 < \tau_k < T_v \\ \cos^2 \left[\pi \left(\frac{\tau_k - T_v}{T_{VL}} \right) \right] & \text{if } \tau_k \geq T_v \end{cases} \quad (3.19)$$

where τ_k represents the non-dimensional time since the initiation of vortex shedding, T_v is the non-dimensional period of the initial vortex formation, and T_{VL} is the vortex passage time constant. The time constants T_v and T_{VL} are obtained from experimental measurements.

In the Leishman-Beddoes model the overshoot in the normal force coefficient is triggered, and subsequently accounted for, as soon as the critical normal force coefficient, C_{n1} , is reached. The influence of the dynamic stall vortex can be expressed as a modification of the parameter f'' so that

$$f_k^{tot} = \begin{cases} f_k'' + V_{x_k} (f_k'' - f_k') & \text{if } C_{n_k}'' \geq C_{n1} \\ f_k'' & \text{if } C_{n_k}'' < C_{n1} \end{cases} \quad (3.20)$$

Finally, the instantaneous total normal force, $C_{n_k}^{tot}$, and the tangential force coefficient, C_{t_k} , under either unsteady attached or separated flow conditions are determined by

$$C_{n_k}^{tot} = C_{n_\alpha} \left(\frac{1 + \sqrt{f_k^{tot}}}{2} \right)^2 \sin \alpha_{e_k} \quad (3.21)$$

$$C_{t_k} = \eta C_{n_\alpha} \alpha_{e_k} \sin \alpha_{e_k} \left(\sqrt{f_k''} - K \right) \quad (3.22)$$

The recovery factor η accounts for the inability of the aerofoil to attain 100% suction at the leading edge as a result of viscous effects that influence the chordwise pressure distribution on a real aerofoil, even when the flow is fully attached.

The instantaneous sectional lift and drag coefficients can then be calculated as

$$C_{l_k} = C_{n_k}^{tot} \cos \alpha_{e_k} + C_{t_k} \sin \alpha_{e_k} \quad (3.23)$$

$$C_{d_k} = C_{n_k}^{tot} \sin \alpha_{e_k} - C_{t_k} \cos \alpha_{e_k} + C_{d_0} \quad (3.24)$$

For each inner time step in the VTM, the aerofoil coefficients C_l and C_d are obtained from Equations 3.6 to 3.24 and used within the blade aerodynamic model that was described in Section 3.1 in order to represent a more realistic aerofoil behaviour than is obtained using static aerofoil data. The approach that is outlined above describes the calculation of the normal and tangential force coefficients. The moment coefficient can be calculated within the dynamic stall model by following a similar procedure.

It should be noted that further development of Leishman-Beddoes-type semi-empirical dynamic stall models is ongoing. Recent improvements in availability and quality of experimental measurements have resulted in an enhancement of the accuracy and capability of the models. Indeed, Gobbi [71] has suggested the replacement of several time constants that are used in Beddoes's *third generation dynamic stall model* [70] by a single coefficient in order to reduce the number of constants that have to be derived from experimental measurements, thereby simplifying the application of the model. Larsen *et al.* [72] suggested the mapping of the separation point parameter, f , from the physical aerofoil profile to a unit circle, as performed in traditional aerofoil theory,

in order to increase the accuracy of the model when full flow separation occurs. Using this approach they showed improved predictions in the context of horizontal-axis wind turbines compared to the original model proposed by Leishman and Beddoes [59].

3.3 Model Validation

Before the VTM and its dynamic stall model is applied to model the aerodynamics of vertical-axis wind turbines, it is essential to establish first that the effect of dynamic stall on the blade aerodynamic loading is correctly simulated by the approach. The variation of the VTM-predicted normal and tangential force coefficients of a NACA 0015 aerofoil in a dynamic stall test is shown below in comparison to experimental measurements that were made by Angell *et al.* [64] for a Reynolds number of 800,000, a Mach number of 0.064 and a reduced frequency of 0.05. The parameters were chosen by the experimentalists to mimic a flow environment that is typical of that which surrounds a vertical-axis wind turbine. End plates were attached to the tips of the blade in the experiment in order to minimise those three-dimensional effects that would be induced by the finite blade span. Pressure measurements were taken only at the mid-span of the blade and, consequently, the normal and tangential force coefficients were presented as two-dimensional aerofoil data. Within the VTM, such an aerofoil is best modelled by a blade with a very high aspect ratio so that the influence of the finite blade span on the aerodynamics at the mid-span of the blade is small.

Figure 3.3 shows the variation of the normal force coefficient, C_n , and the tangential force coefficient, C_t , with angle of attack, α , in a static aerofoil test (in this case experimental measurements made by Angell *et al.* [64]), in other words under quasi-steady conditions, in order to provide a reference case for the test of dynamic stall that will be described below.

The *geometric* angle of attack, α , of the blade of a rotating vertical-axis wind turbine is a function only of the tip speed ratio, λ , and the azimuth angle, ψ , such that

$$\alpha = \arctan \left(\frac{\sin \psi}{\lambda + \cos \psi} \right) \quad (3.25)$$

By oscillating a fixed blade according to the skewed sinusoidal function that is given in Equation 3.25, the experiment conducted by Angell *et al.* [64] was designed to emulate

the time histories of the angle of attack encountered by the blades of a vertical-axis wind turbine. The maximum amplitude of the angle of attack was varied between different test runs in order to simulate the time histories of the angle of attack at different tip speed ratios.

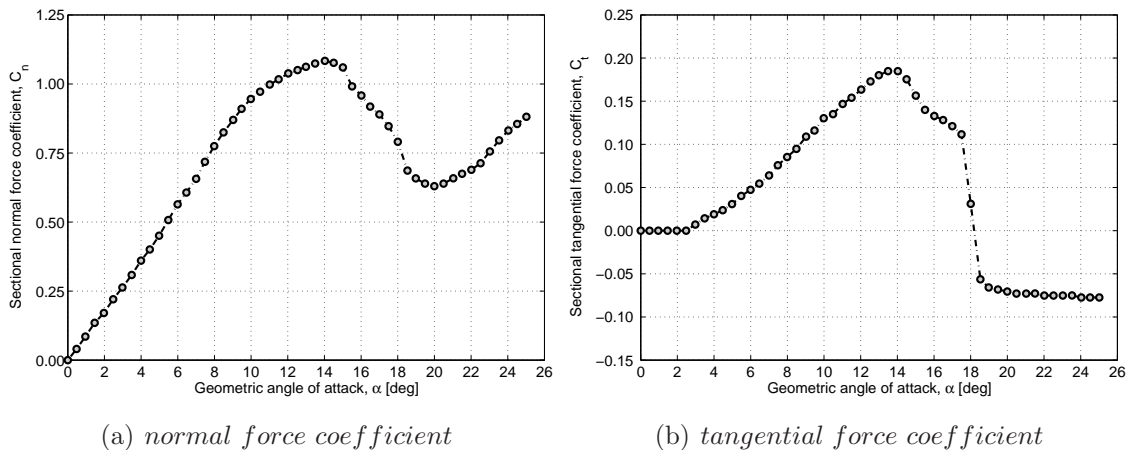


Figure 3.3: Experimental measurements made by Angell *et al.* [64] of the normal and tangential force coefficients produced by the NACA 0015 aerofoil when operated under quasi-steady conditions at a Mach number of 0.064 and a Reynolds number of 800,000.

Figure 3.4 shows the variation of the angle of attack as a pure sinusoidal function in comparison to the VAWT function that is mathematically described by Equation 3.25, for the tip speed ratios 4.85, 3.40, 2.70 and 2.05. These tip speed ratios represent, respectively, high, moderate and low tip speed ratios within the range at which lift-driven vertical-axis wind turbines typically operate. Figures 3.5, 3.6, 3.7 and 3.8 show the comparisons between VTM predictions and the experimental measurements made by Angell *et al.* [64] for these four tip speed ratios. VTM simulations have been carried out with its dynamic stall model and also with a simple quasi-steady representation of aerofoil behaviour in order to evaluate the effect of dynamic stall on the accuracy with which the behaviour of the aerofoil is modelled.

The parameters that are used within the dynamic stall model to describe the quasi-steady behaviour of the NACA 0015 aerofoil were deduced from the static experimental measurements that were made by Angell *et al.* [64] (see Figure 3.3) and are summarised in Table A.1, whereas the time constants that are used in the model are given in Table A.2 in the Appendix. The constants are informed by the values given by

Sheng *et al.* [65], Beddoes [70] and Leishman [73], respectively, but are adapted to best represent the behaviour of the aerofoil that was observed in the experiments carried out by Angell *et al.* [64].

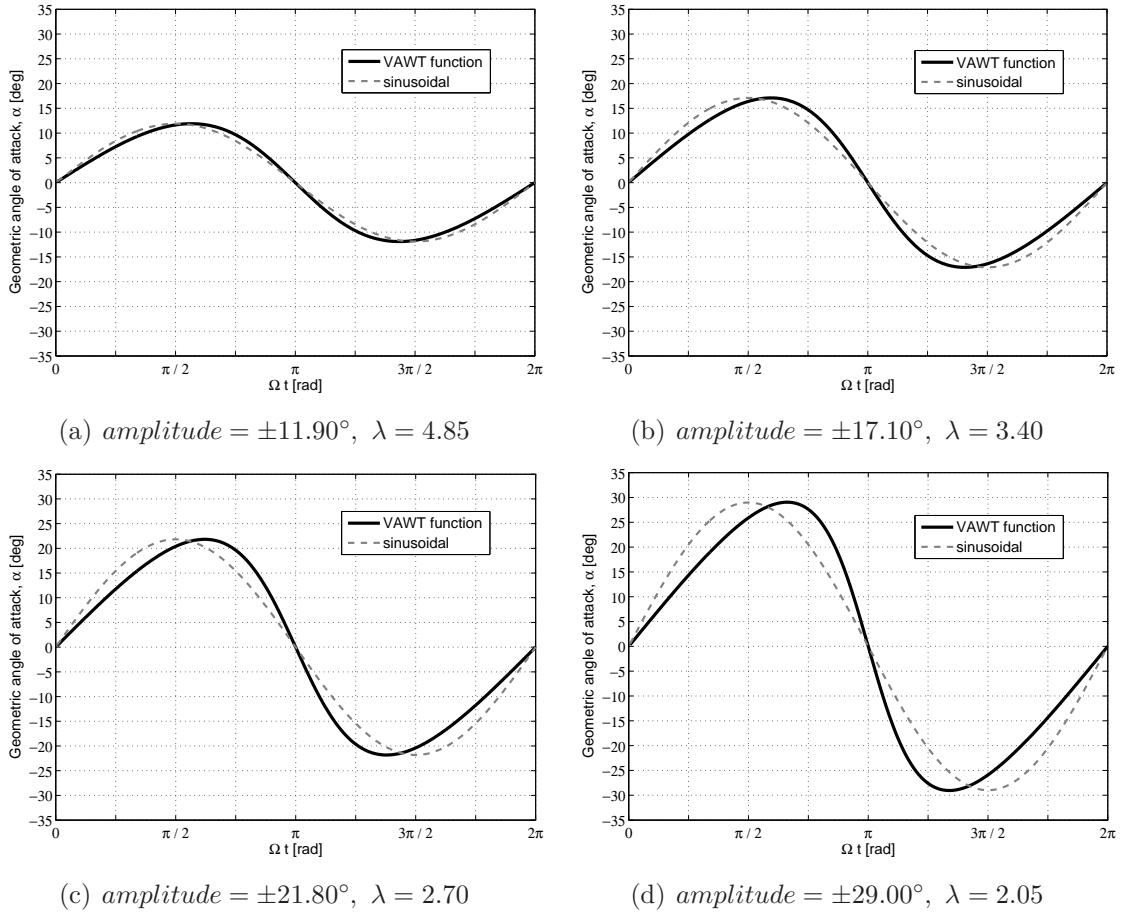


Figure 3.4: Sinusoidal variation of the angle of attack with Ωt in comparison to the variation of the geometric angle of attack that is experienced by the blades of a vertical-axis wind turbine (according to the VAWT function given in Equation 3.25) at different tip speed ratios.

Figure 3.5 shows that, at a high tip speed ratio, the normal and tangential force coefficients that are predicted by the VTM when quasi-steady aerofoil data is used are almost identical to the VTM prediction in conjunction with its dynamic stall model. This is a simple consequence of the variation of the angle of attack at high tip speed ratios being predominantly confined to the regime in which the aerodynamic behaviour of the aerofoil is linear.

At a moderate tip speed ratio, it is clear that the use of static aerofoil data is inadequate to model the behaviour of the aerofoil, as shown in Figures 3.6(a) and (c). The hysteresis that occurs in the experiment is not captured and the peaks in the measured aerodynamic coefficients are considerably under-predicted by the VTM simulations that are based on static aerofoil data. The aerofoil behaviour is represented much more accurately when the dynamic stall model is used within the VTM, as demonstrated in Figures 3.6(b) and (d). Although the experimental measurements are not perfectly matched, the VTM simulations that include the dynamic stall model reproduce reasonably well the magnitudes and shapes of the hysteresis loops in both the measured normal and tangential force coefficients. According to the measurements made by Angell *et al.* [64] the static stall angle of the NACA 0015 airfoil is 14° if the chord Reynolds number is 800,000. Interestingly, Figure 3.6 shows the normal and tangential force coefficients and the drag coefficient to be influenced significantly by unsteady aerodynamic effects even in conditions in which the static stall angle of the NACA 0015 aerofoil is only exceeded by a small amount.

The deficiencies of the model when static aerofoil data is used become even more apparent at low tip speed ratio, as shown in Figures 3.7(a) and (c) and Figures 3.8(a) and (c). Figures 3.7(b) and (d) and Figures 3.8(b) and (d) reveal, however, that, as in the case of a moderate tip speed ratio, the VTM predictions are improved considerably when a dynamic stall model is used in the analysis.

The variation in the angle of attack deviates more from a pure sinusoidal function as the tip speed ratio is decreased, as shown in Figure 3.4. Although the maximum angle of attack is similar in both the negative and positive range, the skewed sinusoidal variation of the angle of attack in the experiment results in an asymmetry of the aerodynamic coefficients with respect to the y-axis that is simply due to the difference in pitch rate in the upstroke and downstroke of the aerofoil. This asymmetry, and the maximum value of the tangential force coefficient, is well predicted by the VTM simulation that includes the dynamic stall model, as shown in Figures 3.7(d) and 3.8(d). The asymmetry is not captured as well in the simulation of the normal force coefficient as it is for the tangential force coefficient, however. The impulsive changes to the variation of the measured normal force coefficient at both high positive and high negative angles of attack, as shown in Figure 3.8(b), suggest that a strong dynamic stall vortex was created during the experiment. Although the development

and motion of the dynamic stall vortex is accounted for in the Leishman-Beddoes-type dynamic stall model that is employed within the VTM, the use of a critical normal force coefficient to define the onset of dynamic stall would appear to be the origin of the under-prediction of the force that is generated on the aerofoil. Indeed, Sheng *et al.* [74] showed that the Evans-Mort correlation that is used in the Leishman-Beddoes model might be imprecise if the Mach number is low, and suggested a criterion for the onset of flow separation at the leading edge that is based on the angle of attack instead. Further discrepancies are also observed between the predicted normal force coefficient and the experimental measurements during the downstroke of the aerofoil, as shown in Figures 3.7(b) and 3.8(b). This corresponds to the part of the dynamic stall hysteresis loop during which recovery from a separated to a fully attached flow state takes place. Based on the experimental measurements made by Green and Galbraith [75, 76], a modification of the Leishman-Beddoes model has been developed by Sheng *et al.* [77] in order to simulate the recovery to fully attached flow with higher accuracy.

The modifications to the original Leishman-Beddoes dynamic stall model that have been proposed by Sheng *et al.* [74, 77] introduce additional semi-empirical coefficients that require extensive experimental measurements, however. Indeed, these parameters change, to some extent, with aerofoil shape, and with both Reynolds and Mach number. The predictive capability of such a modified model for aerofoil performance at operating conditions that differ from the test conditions can thus be called into question in the absence of comprehensive data for these coefficients. The suggestions made by Sheng *et al.* [74, 77] regarding the dynamic stall onset criterion and the improved modelling of flow re-attachment were therefore not incorporated into the dynamic stall model that is used within the VTM. This was done primarily to increase the generality and robustness of the model by limiting the number of empirical model parameters that need to be determined before the model can be used.

Interestingly, even at a very low tip speed ratio, the tangential force coefficient is predicted very satisfactorily by the VTM in conjunction with its dynamic stall model. The accurate simulation of the tangential force coefficient is somewhat more important than the simulation of the normal force coefficient in the context of vertical-axis wind turbines. This is because reliable prediction of torque, and thus the power, that is produced by the turbine depends directly on accurate prediction of the tangential force that is generated along the length of the blade.

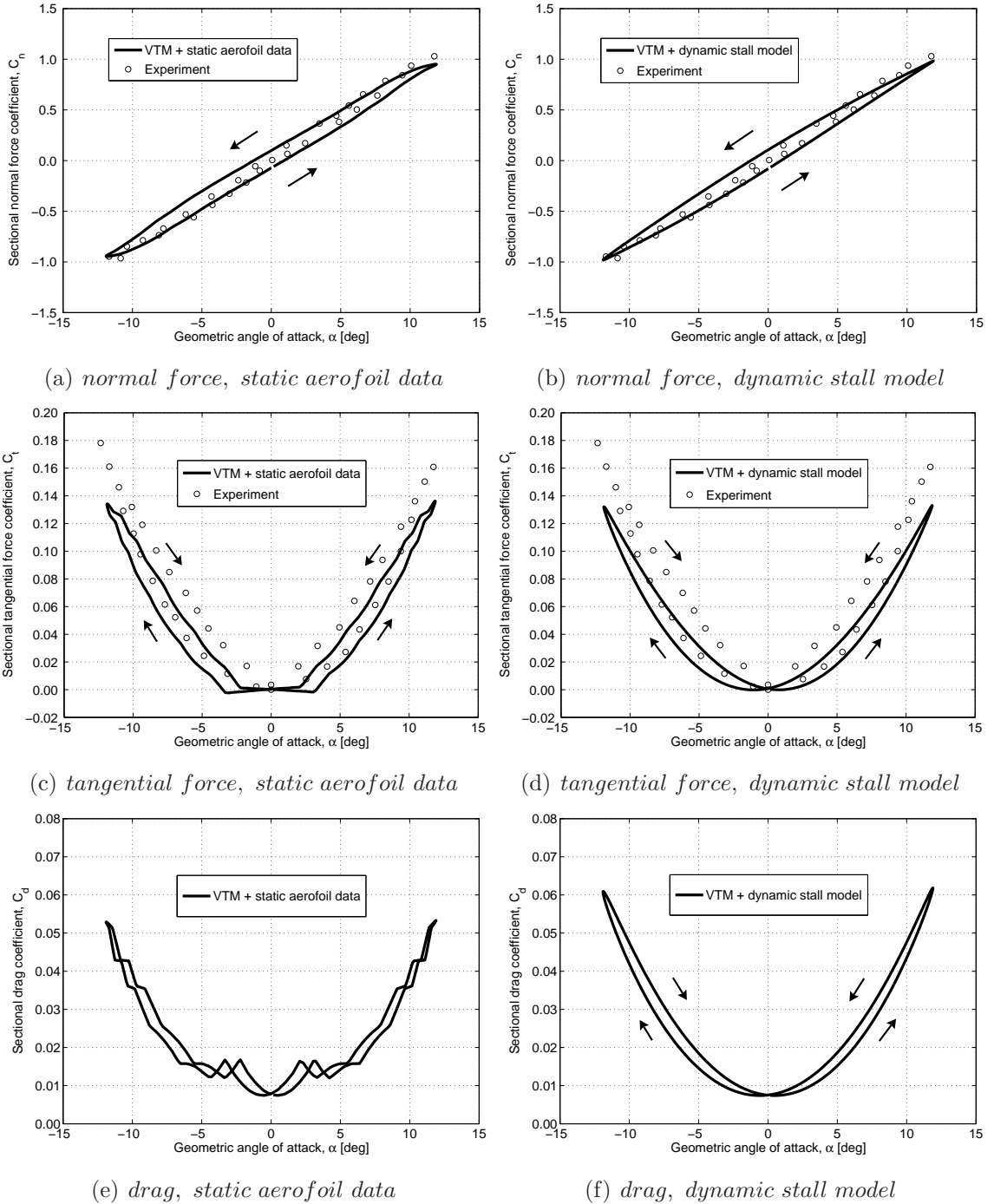


Figure 3.5: VTM-predicted normal and tangential force coefficients based on static aerofoil data (left) and in conjunction with its dynamic stall model (right) compared to experimental measurements of dynamic stall made by Angell et al. [64]. A skewed sinusoidal variation of angle of attack (with amplitude 11.90°) was used in order to represent vertical-axis wind turbine conditions at $\lambda = 4.85$.

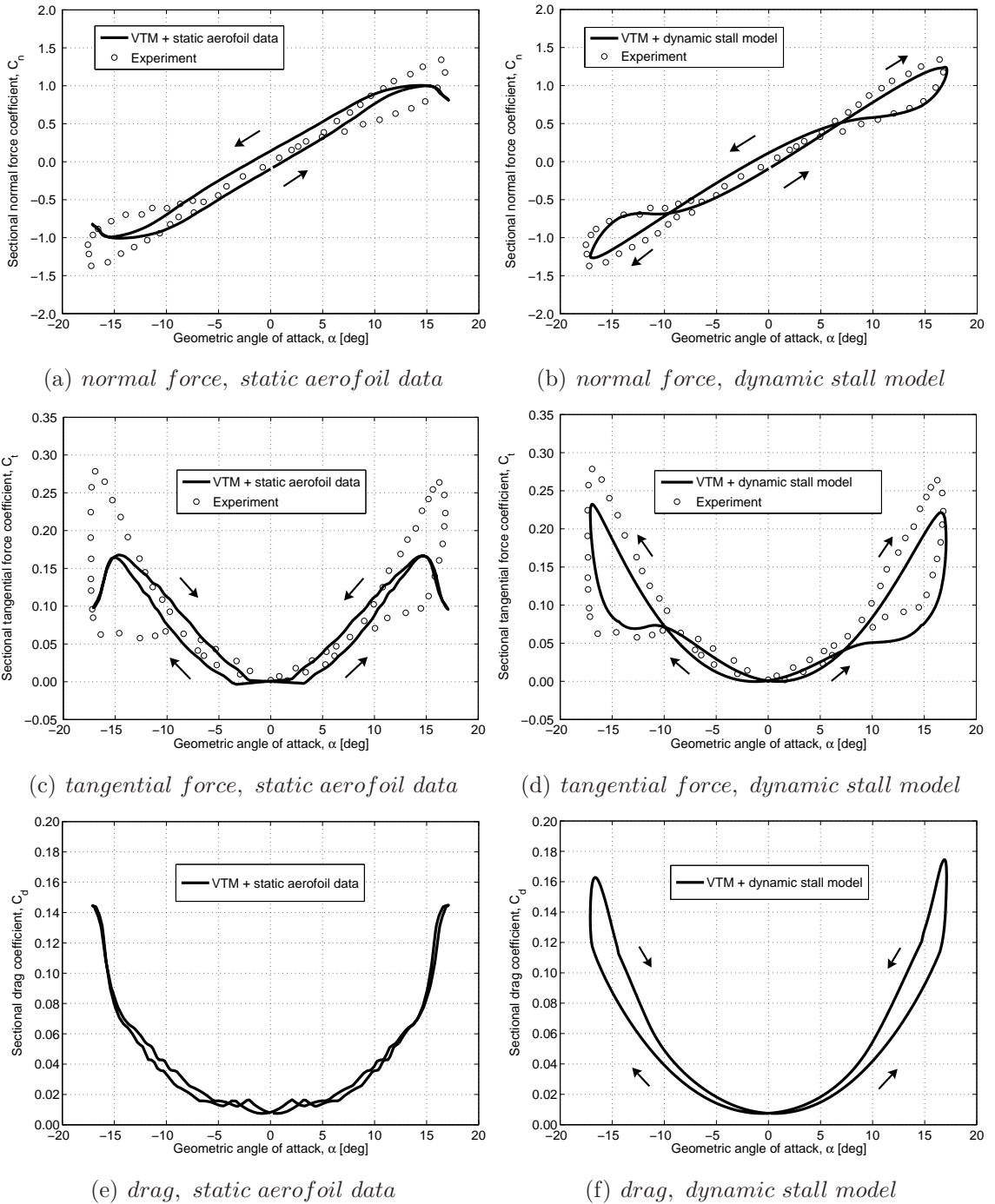


Figure 3.6: VTM-predicted normal and tangential force coefficients based on static aerofoil data (left) and in conjunction with its dynamic stall model (right) compared to experimental measurements of dynamic stall made by Angell et al. [64]. A skewed sinusoidal variation of angle of attack (with amplitude 17.10°) was used in order to represent vertical-axis wind turbine conditions at $\lambda = 3.40$.

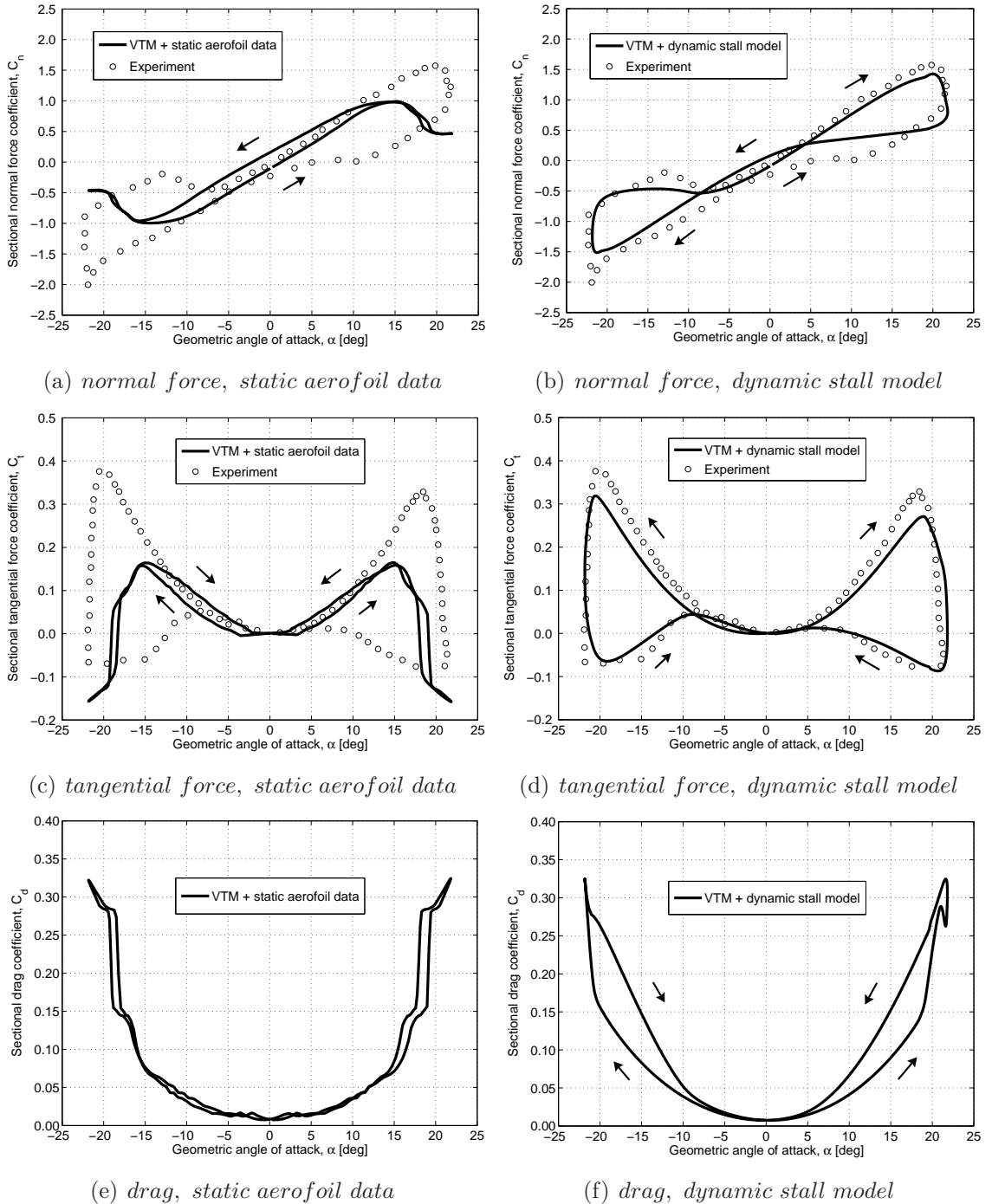


Figure 3.7: VTM-predicted normal and tangential force coefficients based on static aerofoil data (left) and in conjunction with its dynamic stall model (right) compared to experimental measurements of dynamic stall made by Angell et al. [64]. A skewed sinusoidal variation of angle of attack (with amplitude 21.80°) was used in order to represent vertical-axis wind turbine conditions at $\lambda = 2.70$.

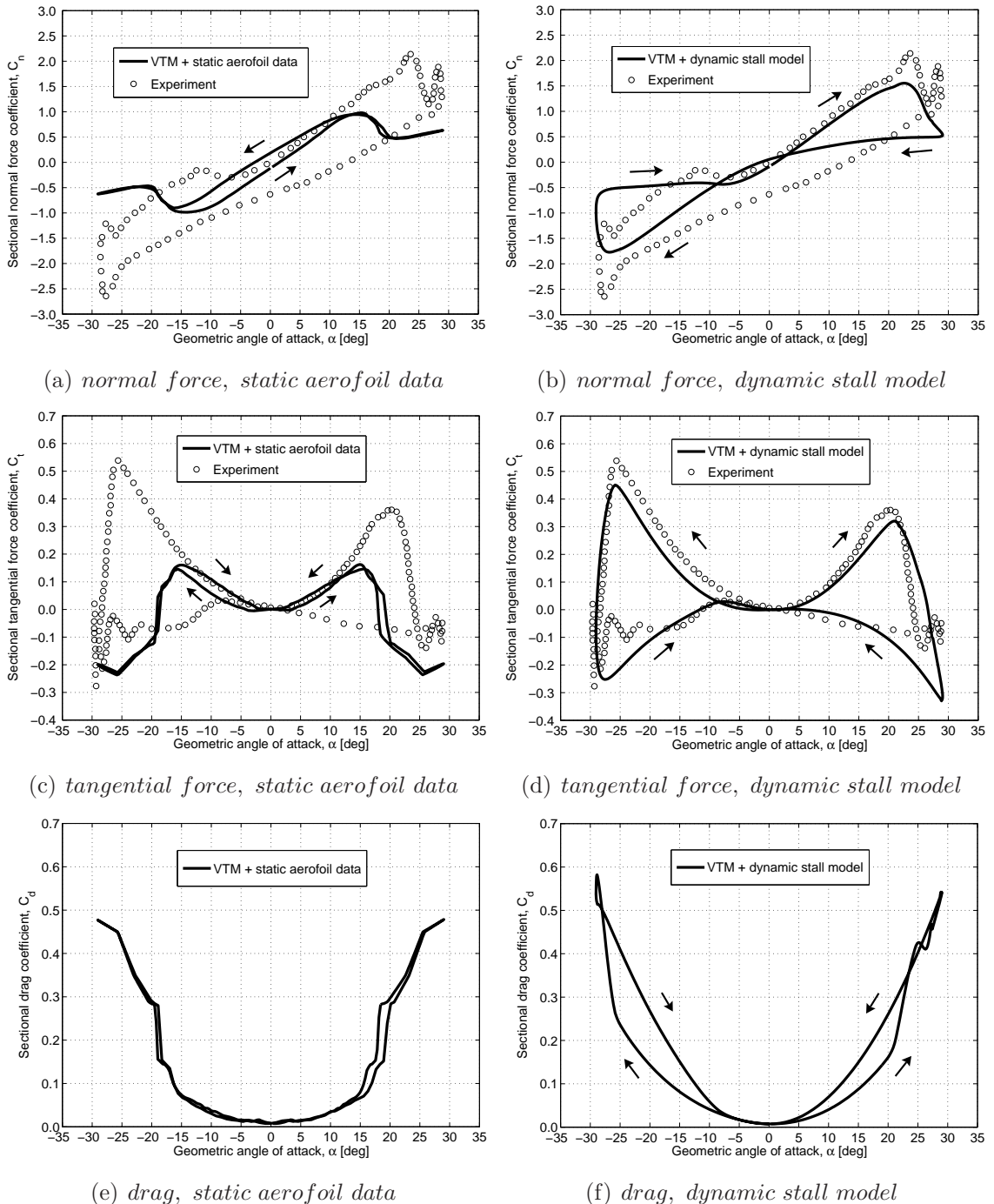


Figure 3.8: VTM-predicted normal and tangential force coefficients based on static aerofoil data (left) and in conjunction with its dynamic stall model (right) compared to experimental measurements of dynamic stall made by Angell et al. [64]. A skewed sinusoidal variation of angle of attack (with amplitude 29.00°) was used in order to represent vertical-axis wind turbine conditions at $\lambda = 2.05$.

3.4 Summary

A Weissinger lifting-line model is used within the VTM to determine the blade aerodynamic loading. The model has been modified by the implementation of a Leishman-Beddoes-type semi-empirical dynamic stall model in order to account more realistically for the effect of dynamic stall on the aerodynamic characteristics of any given aerofoil. VTM simulations have been carried out with its dynamic stall model and compared with a quasi-steady representation of aerofoil behaviour in order to evaluate the effect of dynamic stall on the accuracy with which the behaviour of the aerofoil under dynamic conditions can be simulated by the Vorticity Transport Model. The VTM-predicted variations of the normal and tangential force coefficients agree reasonably well with experimental measurements of dynamic stall when the VTM is used in conjunction with its dynamic stall model. Not surprisingly, large discrepancies occur between the experimental measurements and VTM predictions that are based on static aerofoil data, particularly at low tip speed ratios. This indicates that the use of a model that is based on static aerofoil data is insufficient to predict reliably the aerodynamics of vertical-axis wind turbines. Although some discrepancies between experimental measurements and the VTM predictions that include the dynamic stall model are apparent, the variations with angle of attack of the VTM-predicted coefficients agree reasonably well, overall, with experimental measurements in terms of the shapes and sizes of the hysteresis loops. These comparisons provide confidence that the effect of dynamic stall is satisfactorily accounted for in the VTM when its dynamic stall model is used to represent the blade aerodynamics.

3.5 Chapter Nomenclature

A_1, A_2	coefficients of indicial response functions
c	aerofoil chord length
C_d	sectional drag coefficient, $F_d/\frac{1}{2}\rho cV_\infty^2$
C_{d_0}	sectional zero-lift drag coefficient
C_l	sectional lift coefficient, $F_l/\frac{1}{2}\rho cV_\infty^2$
C_n	sectional normal force coefficient, $F_n/\frac{1}{2}\rho cV_\infty^2$
C_{n_1}	critical normal force coefficient delimiting attached flow

C_{nV}	normal force component due to dynamic stall vortex
C_n^C	circulatory normal force coefficient
C_n^I	non-circulatory (impulsive) normal force coefficient
C_n^{tot}	total normal force coefficient in unsteady conditions
C_n', C_n''	normal force coefficients including lags
$C_{n\alpha}$	derivative of the normal force coefficient with respect to α
C_t	sectional tangential force coefficient, $F_t/\frac{1}{2}\rho cV_\infty^2$
D^f, D^b, D^p	deficiency functions in the unsteady model
f	flow separation point with respect to the aerofoil chord length
f', f'', f^{tot}	delayed separation points of f
F_d	sectional drag
F_l	sectional lift
F_n	sectional force acting normal to the aerofoil chord
F_t	sectional force acting tangential to the aerofoil chord
k	current time sample
K	constant to account for negative values of C_t in deep (dynamic) stall
Ma	Mach number
Re	Reynolds number, $V_\infty c/\nu$
s	distance travelled by aerofoil in semi-chords, $2V_\infty t/c$
S_1, S_2	coefficients of separation point curve fit
T_1, T_2	time constants of the indicial response functions
T_b, T_f, T_p, T_v	time constants
T_{VL}	vortex passage time constant
u_b	local velocity at a blade section
V_∞	free stream velocity
V_x	function of normal force due to dynamic stall vortex
X, Y	circulatory deficiency functions
α	angle of attack
α_1	angle of attack at separation point $f = 0.6$
α_e	equivalent angle of attack in steady flow
α_f	effective angle of attack
η	recovery factor
λ	tip speed ratio

3.5 Chapter Nomenclature

ν	kinematic viscosity
τ	non-dimensional time
ψ	azimuth angle
ω_b	vorticity bound to rotor blades
Ω	angular frequency

Chapter 4

Blade Aerodynamic Loading and Turbine Performance

Before the Vorticity Transport Model is used to investigate the influence of rotor geometry and operating conditions on the performance of vertical-axis wind turbines, it is essential to establish first that the aerodynamics of vertical-axis turbines are predicted accurately by the method. In the present chapter, VTM predictions are therefore compared against experimental measurements of the blade aerodynamic loading of a straight-bladed vertical-axis turbine that were made by Strickland *et al.* [47]. The influence of grid resolution on the simulated blade loading and wake structure is also investigated. In addition, the VTM-predicted variation with tip speed ratio of the power coefficient that is produced by a commercial vertical-axis wind turbine with blades that are twisted helically around its rotational axis is compared to experimental measurements made by Penna [78] in order to further validate the approach.

4.1 Blade Aerodynamic Loading - Comparison with Experiment

The VTM has been used to predict the normal and tangential forces acting on the blades of a straight-bladed turbine that has been configured to be geometrically analogous to the experimental device used by Strickland *et al.* [47]. It is shown that the interaction between the blades and the vortices that are shed and trailed in previous revolutions has a significant effect on the distribution of aerodynamic loading on the blade. Furthermore, it is suggested that the disagreement between experimental and

4.1 Blade Aerodynamic Loading - Comparison with Experiment

numerical data that has been presented in previous studies that were carried out by Strickland *et al.* [47] and Ponta and Jacovkis [79] was most likely a result of the interactions between the blades of the turbine and the wake that is developed by the rotor having not been modelled with sufficient fidelity.

4.1.1 Experimental Set-up and Turbine Model

The performance of a straight-bladed vertical-axis rotor was predicted using the VTM and compared with data that was obtained from experiments carried out by Strickland *et al.* [47] in water in a tow tank. The properties of the turbine that has been investigated are summarised in Table B.1 in the Appendix. The average blade Reynolds number, based on the circumferential velocity, ΩR , was 40,000. Unfortunately, aerofoil performance data, particularly when the aerofoil is operated in dynamic stall, for such a low Reynolds number is scarce within the published literature.

The VTM allows grid levels of different cell size to be specified in the computational domain surrounding the rotor. Coarser grids are used with increasing distance from the turbine centre in order to reduce the computational costs of the simulations and to focus resources closer to where the wake needs to be most highly resolved. This nested grid structure was shown in Figure 2.2 and described in more detail in Section 2.1.2 of this dissertation. The influence of grid resolution on the predicted blade aerodynamic loading and wake structure is analysed in Section 4.1.4. For the simulation of the blade aerodynamics, the surface of the blade was discretised into 32 panels. Panels were concentrated at the blade tips in order to resolve accurately the formation of the tip vortices. The orientation of the blades and specification of the azimuth angle of the turbine with respect to the reference blade ('blade 1') is shown in Figure 4.1.

In the experiment, strain gauges were used to record the variation with azimuth of the normal and tangential forces on the blades of the turbine. As shown in Figure 4.2(a), one end of the blade pierced the water surface while the other end of the blade operated close to the bottom of the tow tank. The gap between the blade tip and the bottom of the tank was stated as being less than 15cm. In their analysis, however, Strickland *et al.* [47] compared their experimental data with numerical results for the non-dimensional tangential and normal forces for a *two-dimensional* rotor under the assumption that the presence of the tank bottom and the free surface would reduce three-dimensional effects. This assumption is open to some doubt given the configuration of the turbine within the tow tank, however. As shown in this dissertation, the

4.1 Blade Aerodynamic Loading - Comparison with Experiment

gap between the blade and the bottom of the tow tank leads to the formation of tip vortices that convect downstream and interact with the blades of the turbine. These blade-vortex interactions are simply not present in a strictly two-dimensional flow field.

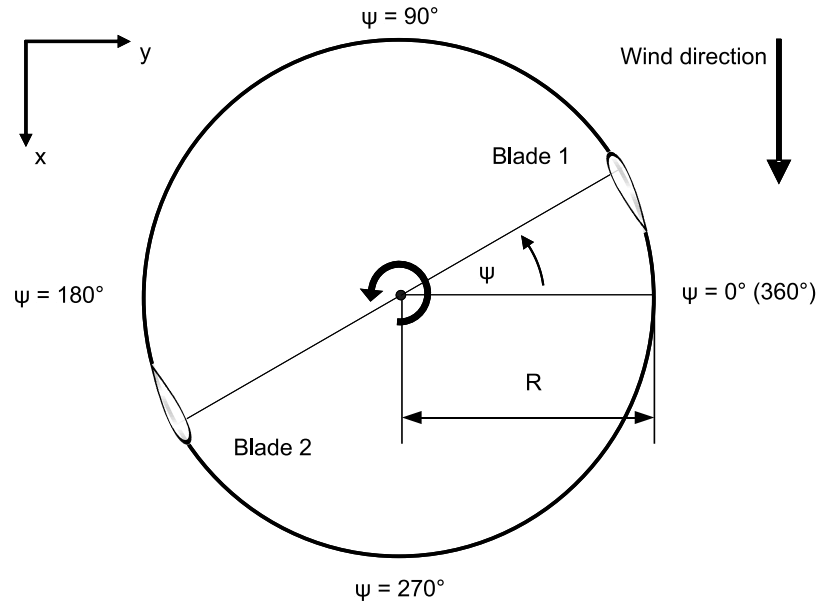


Figure 4.1: Orientation of the blades and specification of the azimuth angle.

In the numerical study presented in this dissertation, the bottom of the tow tank is represented by a ground plane. This plane was set at a distance of 10cm from the blade tip in order to simulate the gap between the bottom of the tow tank and the end of the blade, as depicted in Figure 4.2(b). In the experiment, the aspect ratio of the submerged portion of the blade was five. In the numerical study, the water surface was not modelled, however. Instead, the blade span was increased to yield an aspect ratio of 15 in order to prevent any interaction between the lower portion of the blade and the vortices trailed from the upper tip of the blade. Consequently, when comparing the predicted forces with the experimental measurements, the VTM-calculated aerodynamic forces acting only on the lower portion of the blade, in other words, only on that part of the blade which is equivalent to the submerged portion of the blade in the experiment, has been presented in order to provide a more realistic comparison of the two systems.

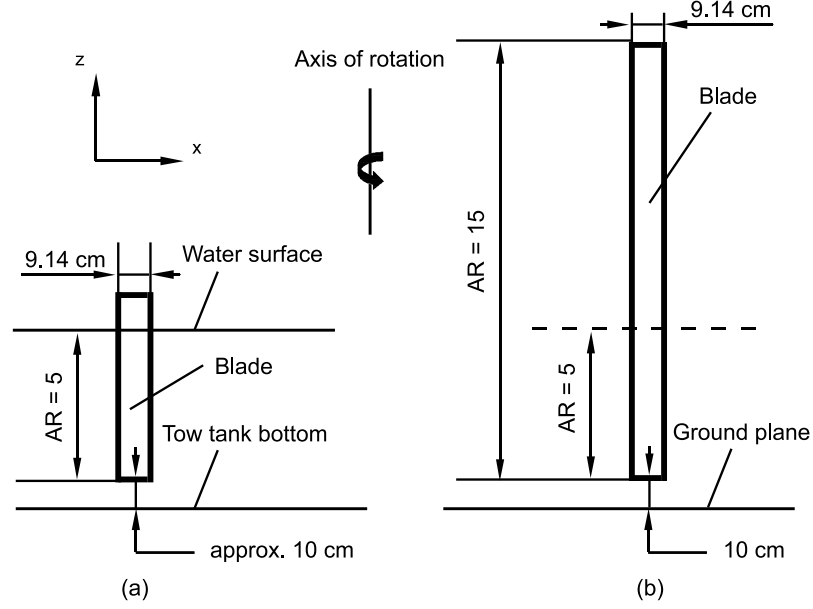


Figure 4.2: *Experimental arrangement (a) and its computational representation (b).*

4.1.2 Blade Loading and Angle of Attack

By adopting the notation that was used by Strickland *et al.* [47], the normal and tangential forces that act on a blade section can be written in terms of the sectional non-dimensional normal force, F_n^* , and the sectional non-dimensional tangential force, F_t^* . The sectional non-dimensional forces are related to the sectional normal and tangential force coefficients C_n and C_t by

$$F_n^* = \frac{F_n}{1/2\rho cV_\infty^2} = C_n \left(\frac{u_b}{V_\infty} \right)^2 \quad (4.1)$$

$$F_t^* = \frac{F_t}{1/2\rho cV_\infty^2} = C_t \left(\frac{u_b}{V_\infty} \right)^2 \quad (4.2)$$

where F_n and F_t are the sectional normal and tangential forces, V_∞ is the free stream velocity, and u_b is the local velocity at the blade section. This velocity u_b comprises contributions from the circumferential velocity of the blade, the free stream velocity and the velocity component that is induced by the wake. The non-dimensional forces

4.1 Blade Aerodynamic Loading - Comparison with Experiment

acting on the entire lower portion of the blade, in other words the portion that is equivalent to the submerged portion of the blade in the experiment, are denoted as F_N^* and F_T^* .

The flow at the mid-span of the blade is least affected by three-dimensional aerodynamic effects, and thus the behaviour of the aerodynamic loading at this blade section provides the closest approximation to the two-dimensional aerodynamic performance of the blade aerofoil. Previous computations of the two-dimensional aerodynamics of the aerofoil in a planar, cyclic motion designed to emulate that of the mid-section of the blade have been conducted by Strickland *et al.* [47] and by Ponta and Jacovkis [79] and comparison with this data provides the opportunity to verify, to some extent, the predictions of the VTM. In Figure 4.3, the VTM-predicted variation of the sectional non-dimensional normal force, F_n^* , and the sectional non-dimensional tangential force, F_t^* , with azimuth angle, ψ , for the section at mid-span of the blade is compared to similar data obtained during these previous simulations. The local blade velocity of a vertical-axis turbine varies cyclically with azimuth. This is simply due to the sinusoidal variation in the component of free stream velocity relative to the blade chord. The free stream velocity vector is orthogonal to the blade chord close to 90° azimuth resulting in a high angle of attack and an associated peak in the blade loading. As the blade passes toward the leeward side of the turbine, between 180° and 360° azimuth, the flow that is induced by the wake of the turbine results in a reduction in the aerodynamic loading on the blades. Generally, the VTM-predicted forces for the section at the mid-span of the blade are in very good agreement with the earlier numerical predictions, particularly with those obtained by Ponta and Jacovkis, lending confidence in the predictive capabilities of the VTM.

Further confirmation of the predictions of the VTM may be obtained by comparing the integrated load on the lower part of the simulated blade to the loads on the submerged portion of the blade that were measured in the experiment conducted by Strickland *et al.* [47]. This comparison is presented in Figure 4.4 for the non-dimensional normal force, F_N^* , and the non-dimensional tangential force, F_T^* , for three different tip speed ratios. Results of VTM simulations with a quasi-steady representation of aerofoil behaviour and with the dynamic stall model that was described in Chapter 3 of this dissertation, are presented in order to allow the effect of dynamic stall on the blade loading to be evaluated.

4.1 Blade Aerodynamic Loading - Comparison with Experiment

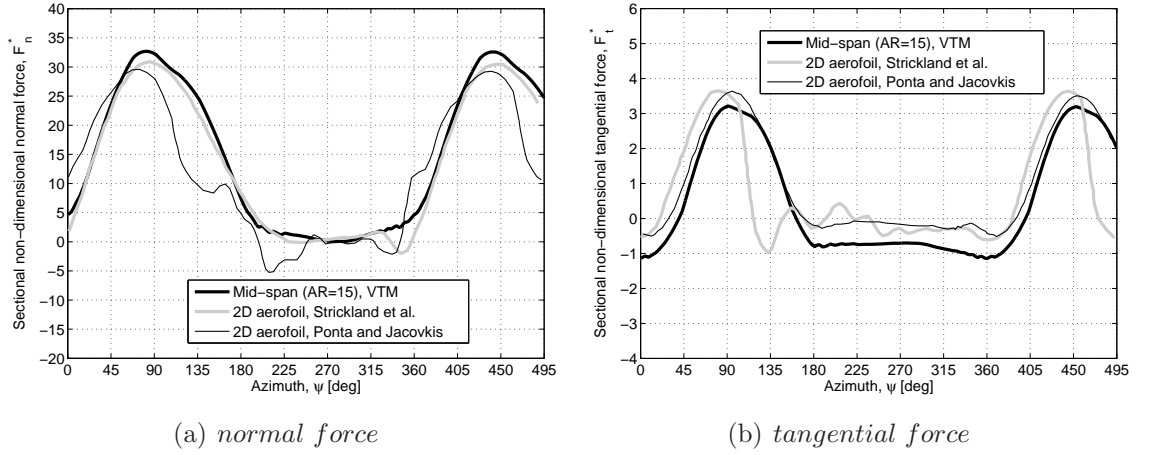


Figure 4.3: VTM-predicted variation with blade azimuth of (a) non-dimensional normal force and (b) non-dimensional tangential force for the section at mid-span of the blade compared to simulations made by Strickland et al. [47] and by Ponta and Jacovkis [79] of the 2D aerodynamics of the same aerofoil in a planar cyclic motion at $\lambda = 5.0$.

Figure 4.4(a) shows the measured and computed normal forces on the blade when the rotor was operated at the highest tip speed ratio. Very satisfactory agreement between the measured and VTM-predicted non-dimensional *normal force* is obtained irrespective of which blade aerodynamic model is used in the analysis. The VTM predictions of the tangential force that are based on static aerofoil data are very similar to the VTM predictions that include the dynamic stall model, as shown in Figure 4.4(b). The variation with azimuth of the VTM-predicted tangential force agrees with the experimental measurements in terms of the curve shape. The computed tangential force under-predicts the peak of the measured tangential force, however. The reason for this discrepancy in the variation of tangential force is currently unknown, in particular since good agreement is obtained for the variation of the normal force. Some suggestions that might explain the difference between the predicted and measured tangential forces are made later in this section.

Figures 4.4(c) and 4.4(d) show the VTM-predicted normal and tangential forces in comparison to experimental measurements for a tip speed ratio of five. Very satisfactory agreement between the experimental measurements of both the normal and tangential force and the VTM predictions that are made in conjunction with a dynamic stall model is obtained for the entire rotor revolution. The measured tangential force is

4.1 Blade Aerodynamic Loading - Comparison with Experiment

only marginally under-predicted close to 90° and 270° azimuth. The VTM predictions that are based on static aerofoil data agree well with the experiments, except between 225° and 300° azimuth. It is suggested that the reason for this discrepancy between the experimental measurements and the VTM-predicted force that is based on static aerofoil data is the interaction between the blades of the turbine and the vortices in the wake. Indeed, Figure 4.5(b) reveals that the angle of attack locally exceeds the static stall angle of the aerofoil between 225° and 300° azimuth. It is thus not surprising that a simulation that is based on static aerofoil data results in inaccuracies when the static stall angle is exceeded.

At the lowest tip speed ratio, the normal force that is predicted by the VTM in conjunction with its dynamic stall model agrees satisfactorily with the experimental measurements in terms of curve shape and magnitude, as shown in Figure 4.4(e), whereas it is clear that the VTM simulation that is based on static aerofoil data cannot predict the blade loading accurately. Indeed, the experimental measurements are largely under-predicted when static aerofoil data is used in the analysis. This is simply because at a tip speed ratio of 2.5 the static stall angle of the aerofoil is exceeded considerably during the cyclic motion of the blades around the azimuth, as indicated in Figure 4.5(c).

The variation of the non-dimensional normal force features negative values close to 270° azimuth for all three tip speed ratios that were investigated. Interestingly, in the computational analysis of the two-dimensional aerodynamics of the aerofoil in a planar, cyclic motion that was carried out by Strickland *et al.* [47] and Ponta and Jacovkis [79], the normal force is predicted to be close to zero at 270° , as shown in Figure 4.3. Strickland *et al.* [47] suggested, therefore, that the ‘hump’ that is observed close to 270° azimuth in the variation of the measured normal force - but not in their computed force - may have been partially due to alignment errors in the blade mounting. The VTM-predicted variation of the angle of attack, shown in Figure 4.5, and the detailed analysis of the flow field surrounding the rotor that is presented in the following section of this dissertation strongly suggest, however, that this ‘hump’ is caused by interactions between the blade of the rotor and vortices that were trailed and shed into the wake in previous turbine revolutions. These blade-vortex interactions are simply not present in a strictly two-dimensional flow field and are, consequently, not accurately modelled when a simplistic analysis tool is used that neglects three-dimensional effects on the blade loading.

4.1 Blade Aerodynamic Loading - Comparison with Experiment

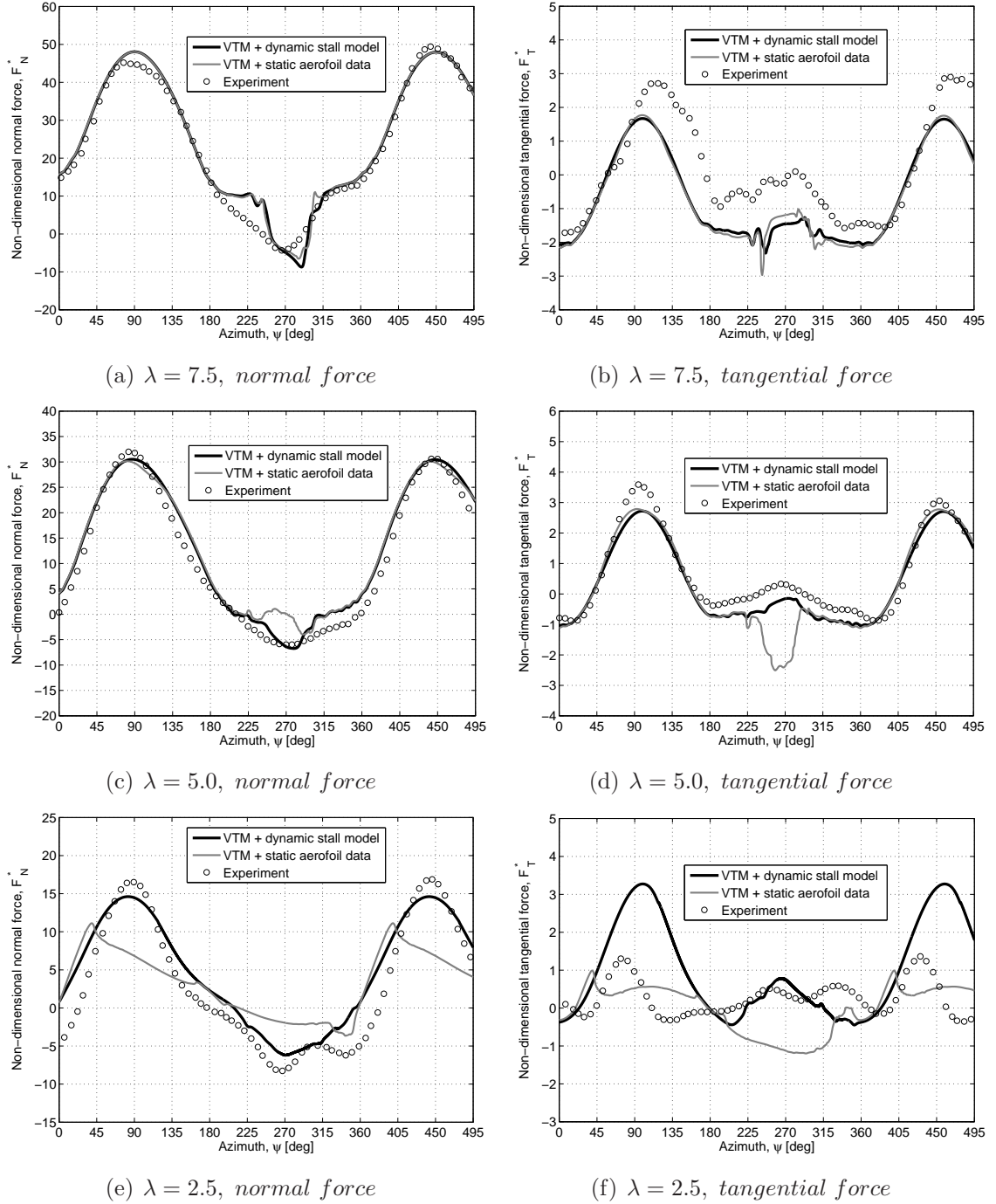


Figure 4.4: Comparison between the variation in VTM-predicted aerodynamic loading and experimental measurements made by Strickland et al. [47] for $\lambda = 7.5$, $\lambda = 5.0$ and $\lambda = 2.5$. Note: the sign convention for the normal force is opposite to that used in Ref. 47.

4.1 Blade Aerodynamic Loading - Comparison with Experiment

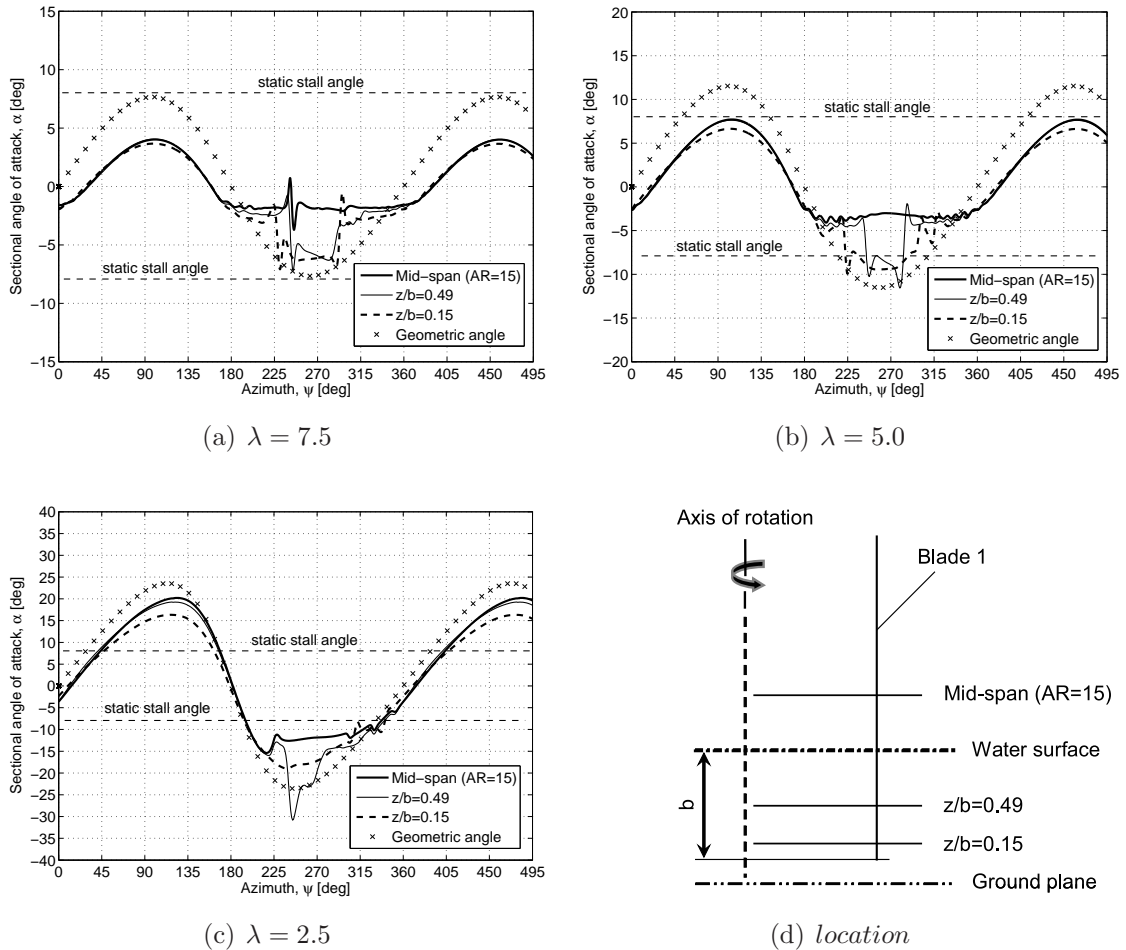


Figure 4.5: VTM-predicted variation with azimuth of the angle of attack at three different blade sections for $\lambda = 7.5$, $\lambda = 5.0$ and $\lambda = 2.5$.

Evaluation of the local angle of attack allows a more detailed assessment of the importance of dynamic stall during the operation of a vertical-axis turbine. Figure 4.5 shows the variation with azimuth of the aerodynamic angle of attack that is predicted by the VTM in conjunction with its dynamic stall model at three different locations along the length of the blade when the rotor is operated at three different tip speed ratios. The figure also shows the geometric angle of attack that is calculated based on Equation 3.25 for each tip speed ratio. The aerodynamic angle of attack is significantly lower than the geometric angle of attack because of the flow that is induced by the wake of the turbine. Close to 90° azimuth, the free stream velocity vector is almost

4.1 Blade Aerodynamic Loading - Comparison with Experiment

orthogonal to the blade chord, resulting in a high angle of attack. The variation of the aerodynamic angle of attack is very small when the turbine is operated at the highest tip speed ratio. Indeed, the aerodynamic angle of attack does not exceed the static stall angle of the aerofoil anywhere over the entire azimuth range. At a tip speed ratio of five, the variation of the aerodynamic angle of attack is predominantly within the regime in which the lift coefficient varies linearly with incidence. The static stall angle of the aerofoil is only exceeded close to 270° azimuth and then only marginally. At the lowest tip speed ratio, the variation of the aerodynamic angle of attack is large by comparison, indicating that the aerodynamics of the blades are characterised by dynamic stall for most of the azimuth range. Irrespective of the tip speed ratio, a series of sharp, localised perturbations to the aerodynamic angle of attack of the blade are seen to extend a considerable distance from the tip of the blade towards its mid-span, most notably as the blade passes downstream of the axis of rotation. The origin of these perturbations is investigated further in the following section.

The measured *normal* forces at three different tip speed ratios are, with marginal discrepancies, well predicted by the VTM simulation when the dynamic stall model is used. Discrepancies between the experimental measurements and the predictions of the VTM in conjunction with the dynamic stall model are largest for the *tangential* forces, particularly at the lowest and highest tip speed ratios that were simulated. The origin of the discrepancy between the predicted and measured tangential force is presently not entirely clear since the normal force is generally well predicted by the VTM simulation when the dynamic stall model is used in the simulation. In addition, comparisons between VTM predictions and experimental measurements of dynamic stall that were presented in the previous chapter of this dissertation showed good agreement in terms of curve shape and magnitude of the blade aerodynamic loading, in particular for the tangential force. The reason for the discrepancy between the VTM predictions that include a dynamic stall model and the measurements that were made by Strickland *et al.* [47] for the tangential force on the blades of the vertical-axis rotor is most likely two-fold. Firstly, the experimental measurements of the tangential force are likely to be associated with a much higher uncertainty than the normal force. Indeed, Vittecoq and Laneville [80] carried out a comparable experiment to the one made by Strickland *et al.* [47], investigating turbine performance for a range of tip speed ratios between 1.5 and 5. They compared their measured forces to those measured by

4.1 Blade Aerodynamic Loading - Comparison with Experiment

Strickland *et al.* [47] for a tip speed ratio of 2.5, and found good agreement for the normal force but discrepancies in phase and magnitude for the tangential force. They concluded that these discrepancies might have arisen because the tangential force is an order of magnitude smaller than the normal force and thus might be more susceptible to uncertainties in the measurements. Secondly, inaccuracies might be introduced simply through the difference between the set-up of the experiment and the model used in the present study - particularly in terms of the different aspect ratio of the blades of the turbine and the presence of the free water surface in the experiment. Although the influence of the differences between the two systems is considered to be small and would affect both the normal and the tangential forces, it might have a greater effect on the tangential force. This is, again, because the tangential force is an order of magnitude smaller than the normal force and therefore more susceptible to any discrepancies, even if they are small, between the configurations of the two systems.

4.1.3 Blade-Wake Interaction

The localised perturbations to the angle of attack of the blade close to 270° azimuth, that are seen in Figure 4.5, appear to be caused directly by aerodynamic interaction between the blades of the rotor and the vorticity that is trailed from their lower tips during previous revolutions. These blade-vortex interactions are visualised in Figure 4.6 by showing the vorticity distribution that is produced by the rotor on a plane oriented perpendicular to the ground, so that it contains the axis of rotation of the turbine and is aligned with the free stream velocity vector, at the instant of time when the reference blade ('blade 1') is located at 270° azimuth. The flow field is represented using contours of the component of vorticity perpendicular to the plane in order to emphasise the vorticity that is trailed from the blades. The dark rendering corresponds to vorticity with clockwise sense, and the light rendering to vorticity with counter-clockwise sense of rotation.

4.1 Blade Aerodynamic Loading - Comparison with Experiment

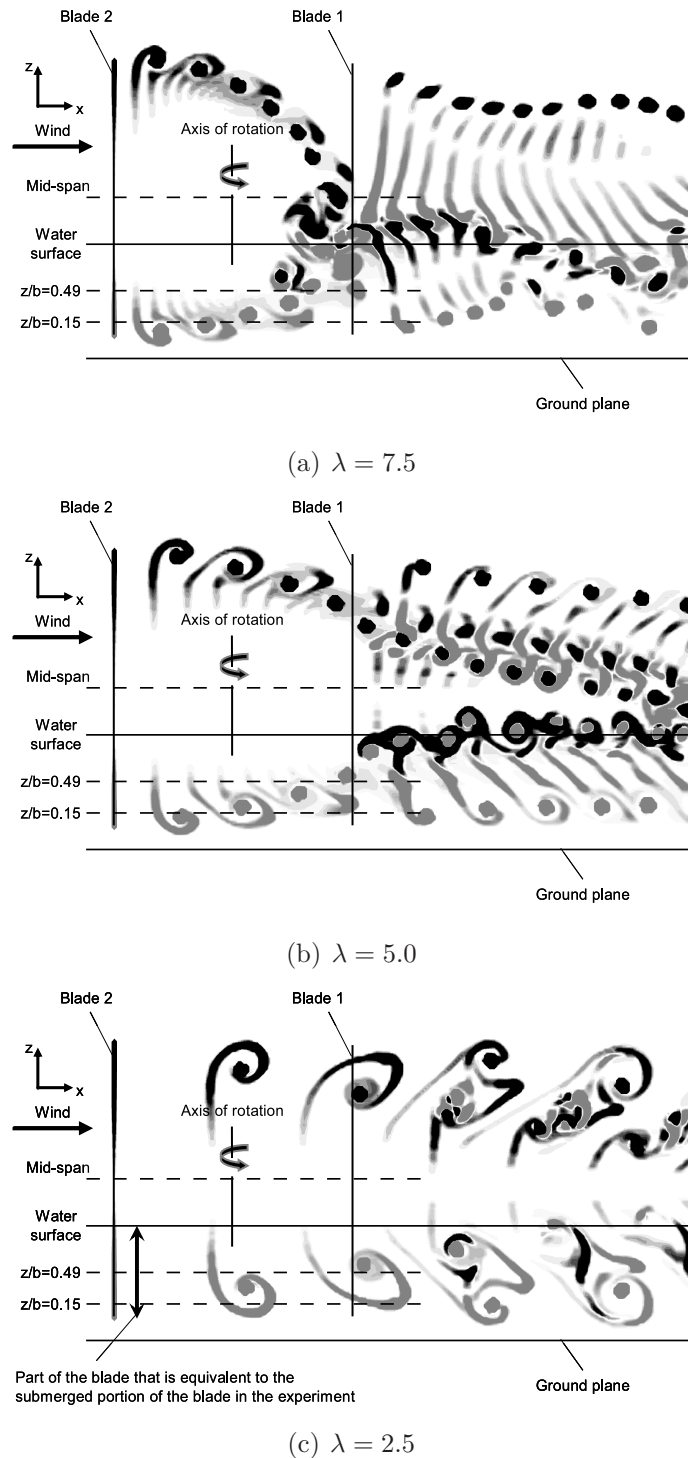


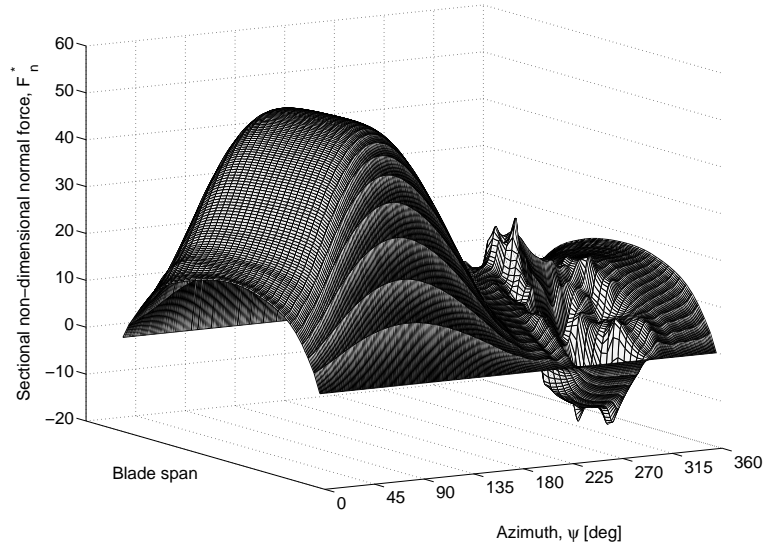
Figure 4.6: Computed vorticity field surrounding the turbine, represented using contours of vorticity on a vertical plane that contains the axis of rotation of the turbine. Blade 1 is located at $\psi = 270^\circ$.

4.1 Blade Aerodynamic Loading - Comparison with Experiment

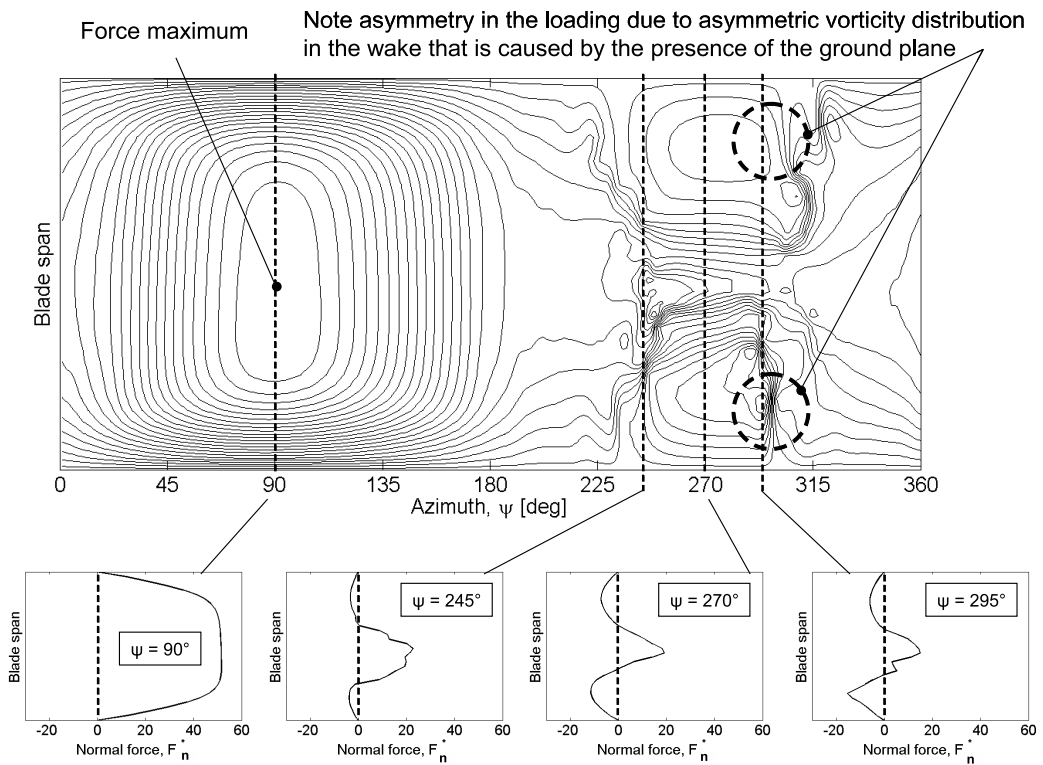
Figure 4.6(a) shows the flow field that surrounds the turbine when the rotor is operated at a tip speed ratio of 7.5. At this tip speed ratio, the low free stream velocity compared to the rotational velocity results in a dense distribution of the tip vortices between the blades of the turbine in comparison to the situation at lower tip speed ratios, as shown in Figures 4.6(b) and 4.6(c). On the side of the rotor where the ground plane is modelled, the angle between the vortex trajectory and the ground plane is smaller compared to the corresponding angle of the trajectory of the vortices trailed from the upper blade tip. Furthermore, it is apparent that self-induction causes the vortices on the side of the rotor where the ground plane is present to travel more quickly downstream than the vortices that are trailed from the upper blade tip. This effect becomes weaker with decreasing tip speed ratio. As a result of the skewing of the wake, the equivalent tip vortices interact earlier with the lower tip of the blade than with the upper tip, as shown in Figure 4.6(b). The effect of the ground plane, and thus the asymmetry in the distribution of vorticity with respect to the horizontal centreline, is weakest when the rotor is operated at the lowest tip speed ratio, as shown in Figure 4.6(c).

The distributions of the non-dimensional normal forces along the blade span and the variation of the loading with azimuth for tip speed ratios of 7.5, 5 and 2.5 are presented in Figures 4.7, Figures 4.8 and Figures 4.9, respectively. The distribution of the loading along the blade between 0° and 180° azimuth differs significantly to that between 180° and 360° . The blade aerodynamic loading is characterized by a smooth and uniform distribution of the aerodynamic forces between 0° and 180° azimuth. The loading decreases steadily in magnitude towards the tip of the blades, simply due to the flow that is induced by the tip vortices. The blade aerodynamic loading between 180° and 360° , in contrast, is characterised by a series of impulsive and abrupt localised perturbations. When the turbine is operated at tip speed ratios of 7.5 and 5.0, a marked asymmetry with respect to the horizontal centreline occurs in the blade loading between 180° and 360° azimuth, as revealed in Figures 4.7(b) and 4.8(b). In contrast, the blade loading is fairly symmetric with respect to the horizontal centreline when the turbine is operated at the lowest tip speed ratio, as shown in Figure 4.9(b). This observation is entirely consistent with the wake structure that was shown in Figure 4.6 and is simply due to the weaker effect of the ground plane on the wake that is developed by the rotor when the tip speed ratio decreases.

4.1 Blade Aerodynamic Loading - Comparison with Experiment



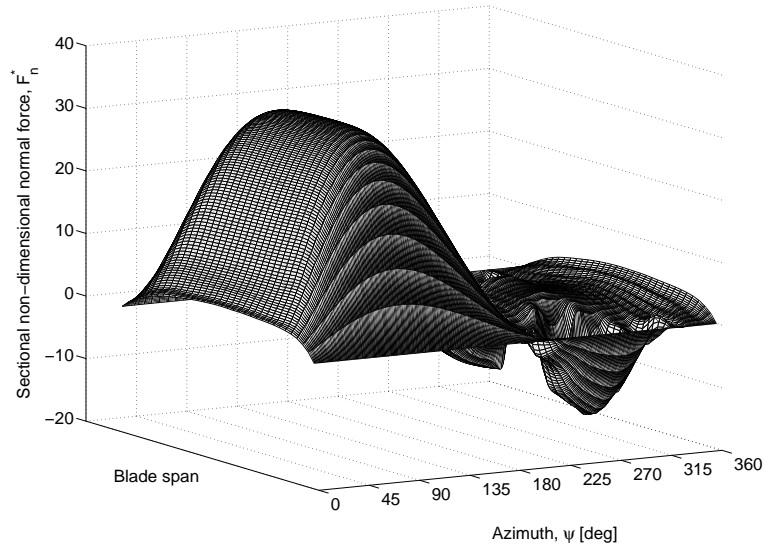
(a)



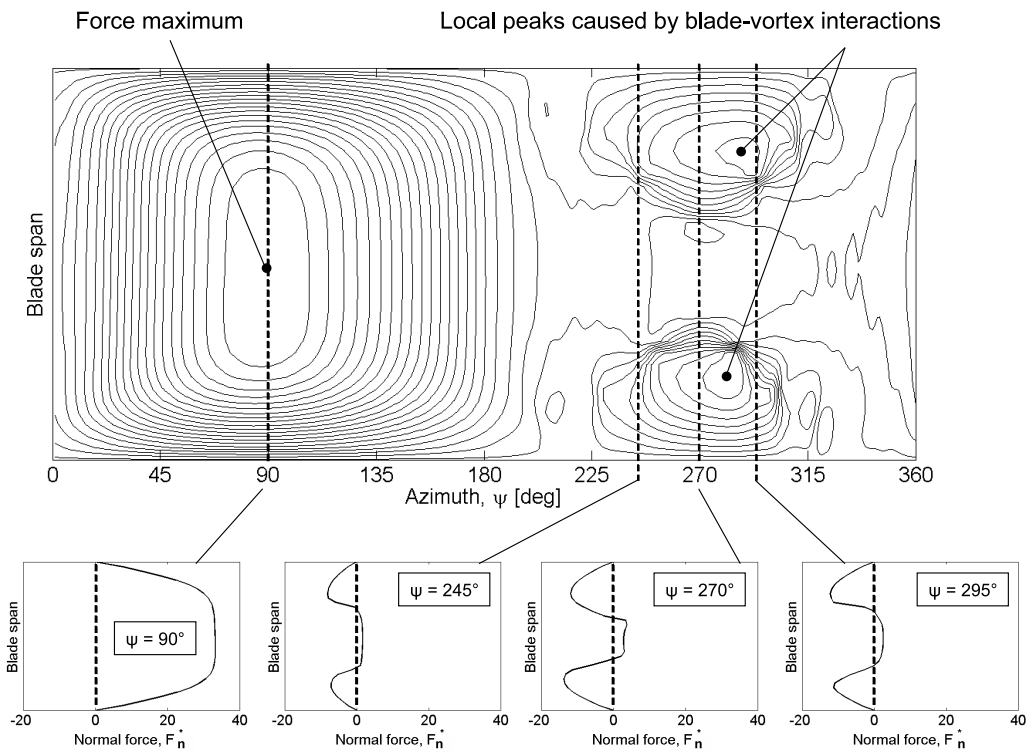
(b)

Figure 4.7: *VTM-predicted variation with azimuth of the non-dimensional normal force along the blade span at $\lambda = 7.5$.*

4.1 Blade Aerodynamic Loading - Comparison with Experiment



(a)



(b)

Figure 4.8: VTM-predicted variation with azimuth of the non-dimensional normal force along the blade span at $\lambda = 5.0$.

4.1 Blade Aerodynamic Loading - Comparison with Experiment

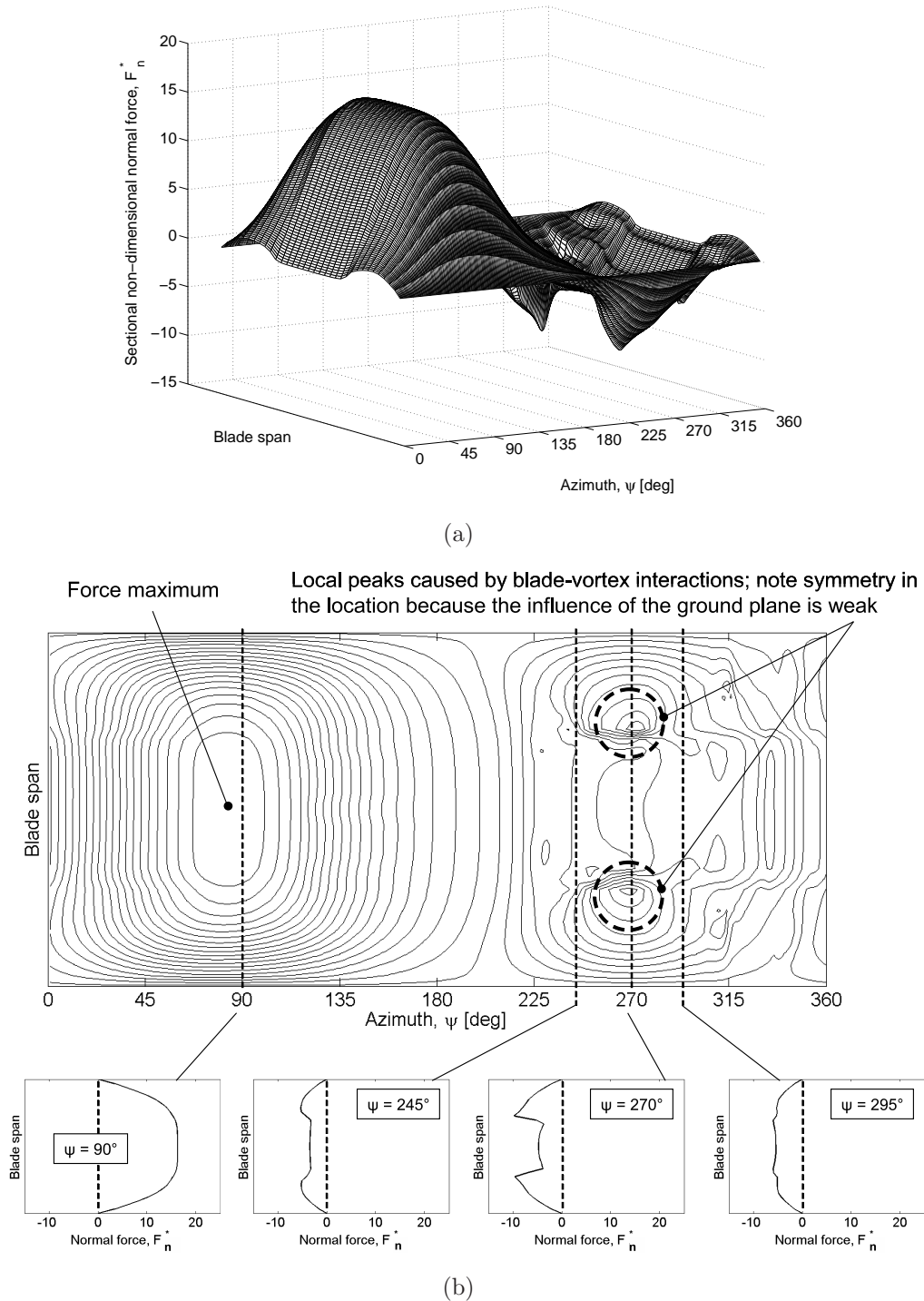


Figure 4.9: *VTM-predicted variation with azimuth of the non-dimensional normal force along the blade span at $\lambda = 2.5$.*

4.1 Blade Aerodynamic Loading - Comparison with Experiment

Figure 4.10 shows a rendition of the overall, three-dimensional structure of the wake, visualised as a surface within the flow on which the vorticity in the wake has constant magnitude. The vorticity from each blade is rendered in a separate shade. The figure shows the complexity of the evolution of the wake downstream of the turbine - the essentially cycloidal structure of the initial sections of the wake is seen to break down relatively rapidly as the self-induced velocity of both the shed and trailed vorticity produced by the blades acts to distort and disorder the wake into a complicated tangle of individual vortical filaments. The interaction between the lower tip of blade 1 and the vorticity in the wake is shown in detail in the inset to Figure 4.10, and reveals that two different types of blade-vortex interactions are present within the system. Indeed, a complex, intermeshed system of vorticity is revealed in which interactions between the reference blade and its own tip vortex trailed in a previous revolution of the turbine as well as an interaction between the reference blade and the tip vortex trailed by the other blade of the turbine are both present.

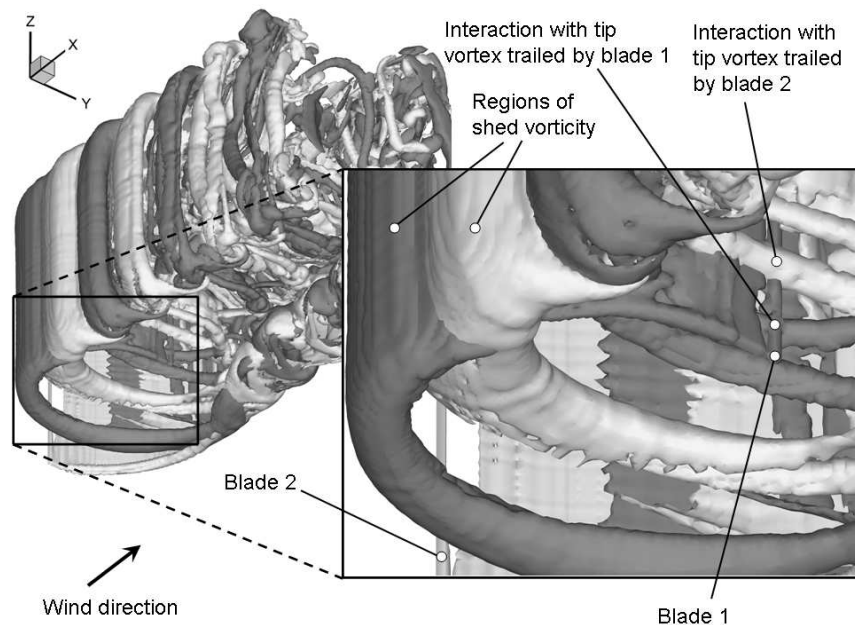


Figure 4.10: Flow field when the rotor is operated at $\lambda = 5.0$ visualised by plotting an isosurface of vorticity with colouring allocated to the vorticity developed by blade 1 and blade 2. Blade 1 is located at $\psi = 270^\circ$.

4.1.4 Effect of Grid Resolution

VTM simulations have been carried out with two grids of cells with different sizes in order to assess the influence of grid resolution on the predicted blade loading and wake structure. The fine grid resolution has twice the number of cells per rotor radius than the coarse grid. Table C.1 in the Appendix summarises the detailed characteristics of the fine and the coarse grids used in the study.

Figure 4.11 shows a comparison between experimental measurements made by Strickland *et al.* [47] and the VTM-predicted normal and tangential forces obtained using the coarse and the fine grids. The computed blade aerodynamic loading is very similar, irrespective of the grid resolution that was used, for almost the entire azimuth, except close to 270° azimuth. The reason for the discrepancy between the simulations that are based on different grid resolutions is revealed in Figures and 4.12(e) and (f) that show the distribution of vorticity that is produced by the rotor on a plane oriented perpendicular to the ground. The plane contains the axis of rotation of the turbine and is aligned with the free stream velocity vector. The vorticity is smeared, in particular immediately downstream of blade 1, when a coarse grid is used in the analysis. The simulation that is based on a fine grid resolution, in contrast, captures much of the finer structure of the tip vortices and, indeed, the break-up of these vortices as they convect further downstream.

Interestingly, the trajectories of the tip vortices are predicted to be somewhat different depending on the grid that is used within the analysis. Indeed, the simulation that is based on the fine grid predicts the interactions between the tip vortices and blade 1 to extend over a fairly broad portion of the blade, whereas these blade-vortex interactions are predicted to occur in a more confined region of the blade when the coarse grid is used in the simulation. The effect on the blade aerodynamic loading of these differences in the predictions of the blade-vortex interactions is shown in Figure 4.13. The figure shows the normal and tangential forces that are predicted by the VTM, for both the coarse and the fine grid resolution, at four different locations close to the lower tip of the blade, as indicated in Figures 4.12(e) and (f). Impulsive perturbations are predicted to occur due to blade-vortex interactions at the two blade sections that are closest to the tip, irrespective of the grid resolution that is used within the analysis. Only the simulation that is based on the fine grid, however, predicts impulsive

4.1 Blade Aerodynamic Loading - Comparison with Experiment

perturbations to be present for the two blade sections that are located closer to the mid-span of the blade. The integrated blade loading along the portion of the blade that is equivalent to the submerged portion of the blade in the experiment that was carried out by Strickland *et al.* [47] consequently depends on whether the coarse or the fine grid is employed, particularly close to 270° azimuth, as shown in Figure 4.11.

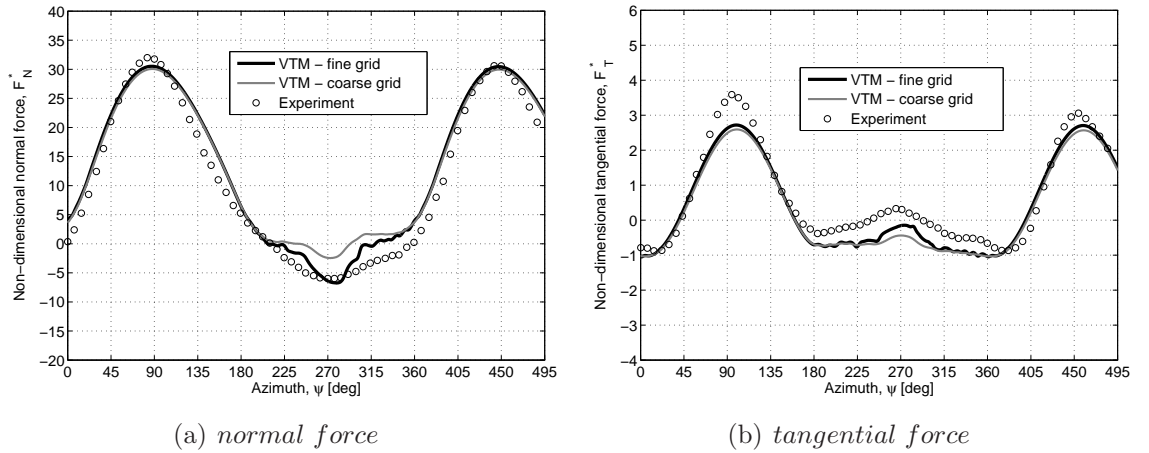


Figure 4.11: Comparison between experimental measurements and the variation in VTM-predicted aerodynamic loading using two different grid resolutions when the rotor is operated at $\lambda = 5.0$.

Figures 4.12(a) and (b) show the three-dimensional flow field that surrounds the turbine rotor as predicted by the simulations that are based on the coarse and the fine grids, respectively. Figures 4.12(c) and (d) depict the vorticity distribution on a horizontal plane that is located at the mid-span of the blade, visualised by contours of vorticity magnitude. The visualisations of both the three-dimensional flow field and the vorticity distribution on the horizontal plane show characteristic smearing of the regions of vorticity that occurs when the coarse grid is used in the simulation. Not surprisingly, the finer structure of the vorticity in the wake can be resolved when the fine grid is employed in the analysis.

4.1 Blade Aerodynamic Loading - Comparison with Experiment

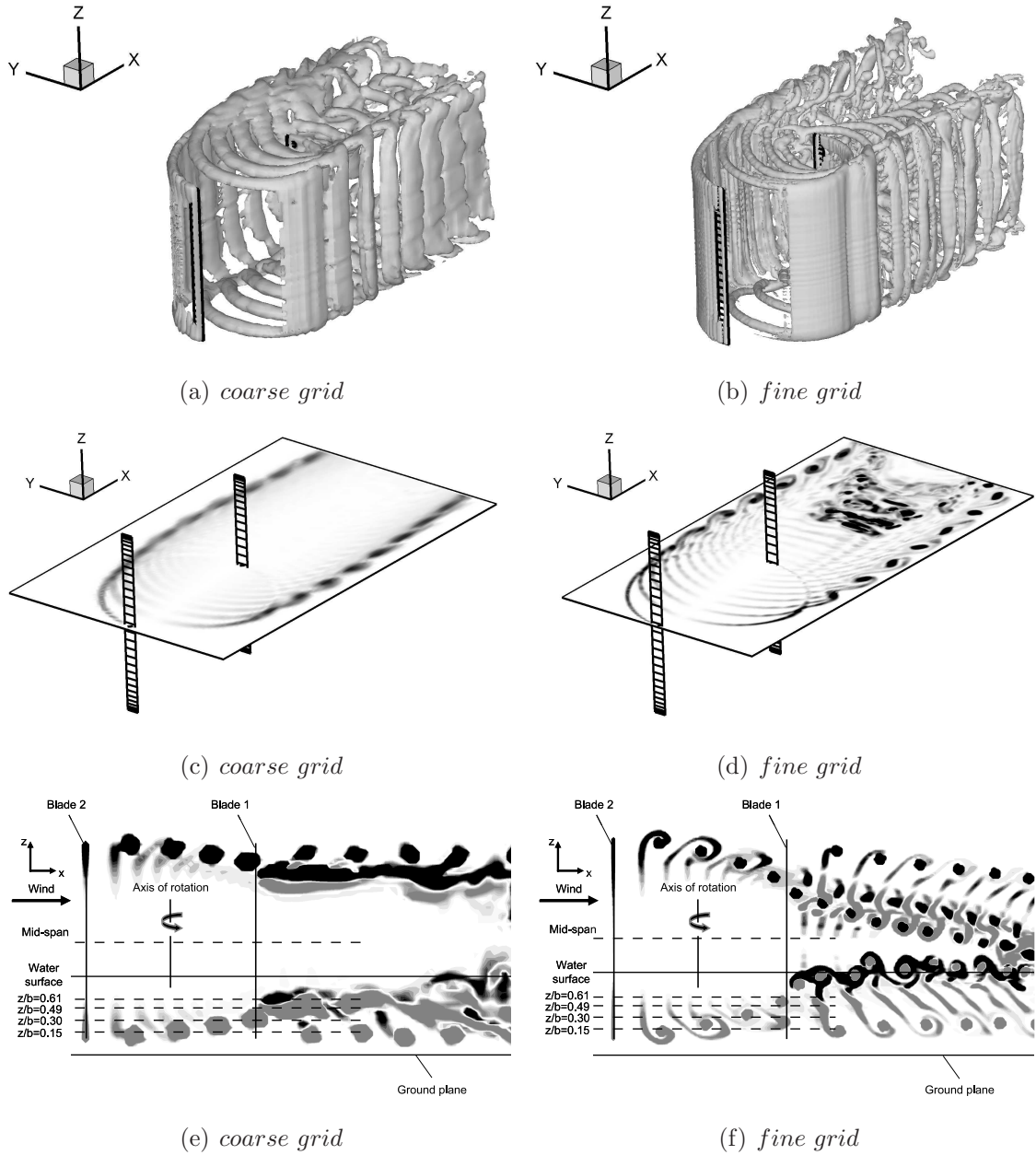


Figure 4.12: Computed vorticity field surrounding the turbine using a coarse grid (left) and a fine grid (right) when the rotor is operated at $\lambda = 5.0$.

4.1 Blade Aerodynamic Loading - Comparison with Experiment

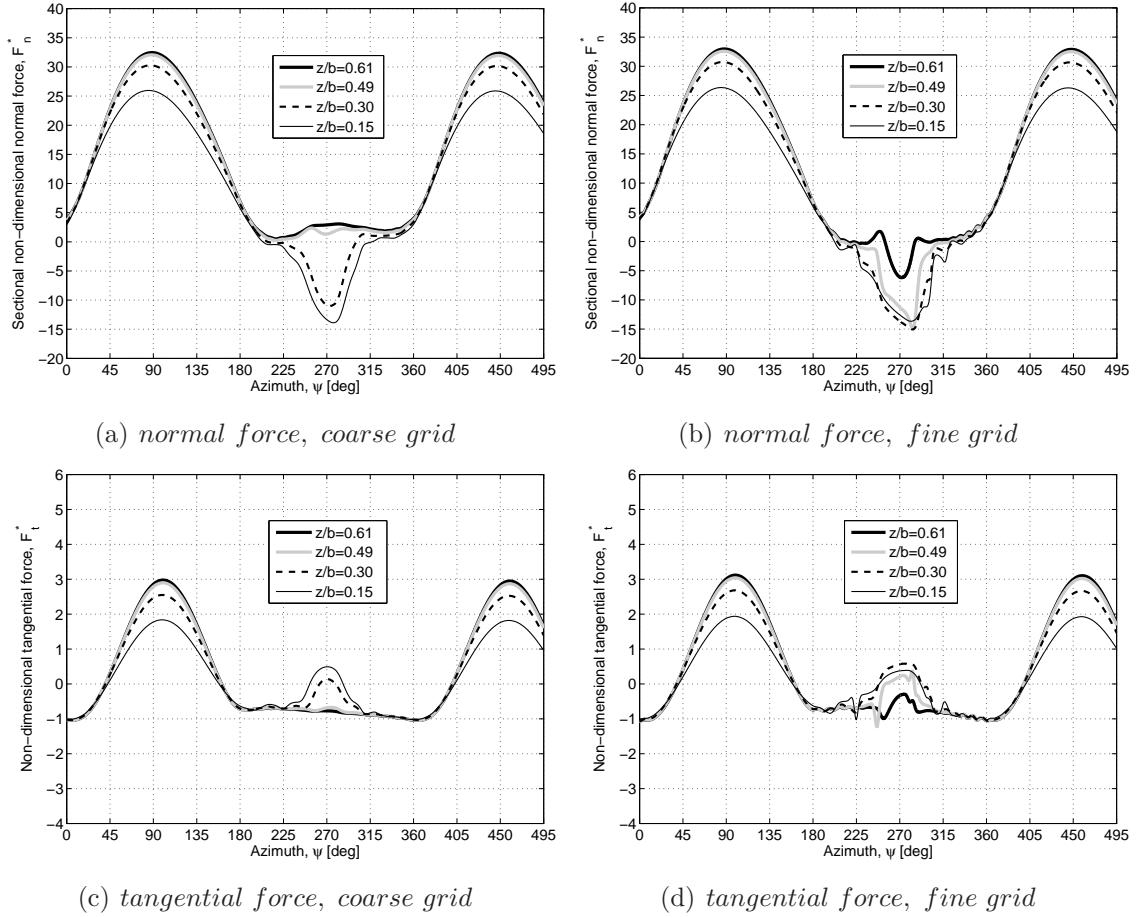


Figure 4.13: VTM-predicted sectional normal and tangential forces at four different locations along the blade using a coarse grid (left) and a fine grid (right) when the rotor is operated at $\lambda = 5.0$.

The VTM-predicted loading agrees reasonably well with experimental measurements when a coarse grid is used within the simulation. The coarse grid resolution is not sufficient to predict accurately some of the more subtle features of the aerodynamics and wake dynamics of a vertical-axis rotor, however. Better agreement between the VTM predictions and the experimental measurements is apparent when the fine grid is employed in the analysis. All the simulations that are presented in the remainder of this dissertation were thus carried out with the fine grid resolution.

4.2 Turbine Performance - Comparison with Experiment

The VTM has been used to model the aerodynamics of the qr5 commercial vertical-axis wind turbine that is produced by *Quiet Revolution Ltd.*, a UK-based manufacturer. The turbine consists of three blades with NACA four-digit aerofoil sections that are helically twisted around the rotational axis of the rotor, as shown in figure 4.14(a). The radius of each blade section, in other words the distance between the rotational axis and each individual section, varies along the blade span. The turbine height and the reference radius, R , are 5m and 1.5m, respectively. The blades of the turbine are inclined so that the blade tip at the top of the turbine, defined such that $z/b = 1$, precedes the tip at the bottom of the turbine, defined such that $z/b = 0$, by 120° in azimuth. The definition is made that the reference blade is located at 0° azimuth when the blade tip at the top of the rotor, thus the blade section at $z/b = 1$, is aligned with the free stream velocity vector and its leading edge faces the wind. The turbine has support struts close to the top and the bottom that connect the blades to the shaft of the rotor. For simplicity, these support struts were not modelled within the numerical simulation. The influence of the struts on the turbine performance would appear to become important, however, at higher tip speed ratios, as will be discussed later in this section. The flow field that is predicted by the VTM to surround the turbine is visualised in figure 4.14(b) by plotting an isosurface of vorticity.

Figure 4.15 shows the VTM-predicted variation of power coefficient, C_P , with tip speed ratio, λ , as compared with experimental measurements that were made by Penna [78] on a full scale qr5 turbine in the 9m by 9m wind tunnel of the Canadian National Research Council. Blockage effects in the wind tunnel were accounted for by estimating analytically the interference of the wind tunnel walls on the measurements. This estimation was applied as a correction to the measurements and included in the presented data. The experiment was carried out with a constant free stream velocity of 9m/s. The average blade Reynolds number, based on the circumferential velocity, ΩR , was thus approximately 400,000 for tip speed ratios near the centre of the turbine's operating range. Figure 4.15(a) shows significant discrepancies between the experimental measurements and VTM simulations when static airfoil data is used in the simulation;

4.2 Turbine Performance - Comparison with Experiment

indeed, the trend of the power coefficient with tip speed ratio is completely mispredicted. Interestingly, the measured power coefficients are over-predicted when the tip speed ratio is greater than or equal to four, whereas they are under-predicted at low tip speed ratios. This characteristic behaviour of the predictions that are based on static airfoil data is a result of the tangential force coefficient being largely under-predicted at low tip speed ratios, as shown in Figures 3.7(c) and 3.8(c). The over-prediction of the power coefficient at high tip speed ratios, in contrast, is a result of the hysteresis loop that is associated with dynamic stall on the blades not being captured, and thus the net tangential force coefficient being over-predicted by the simulation, as indicated in Figure 3.6(c). It is thus not surprising that an analysis that is based on static airfoil data over-predicts the power coefficient of the qr5 at high tip speed ratios since the distribution of the angle of attack along the blade span, as shown in Figure 4.16(a), suggests that the blade of the qr5, and in particular its lower tip, is subject to unsteady aerodynamic effects even when the turbine is operated at high tip speed ratios.

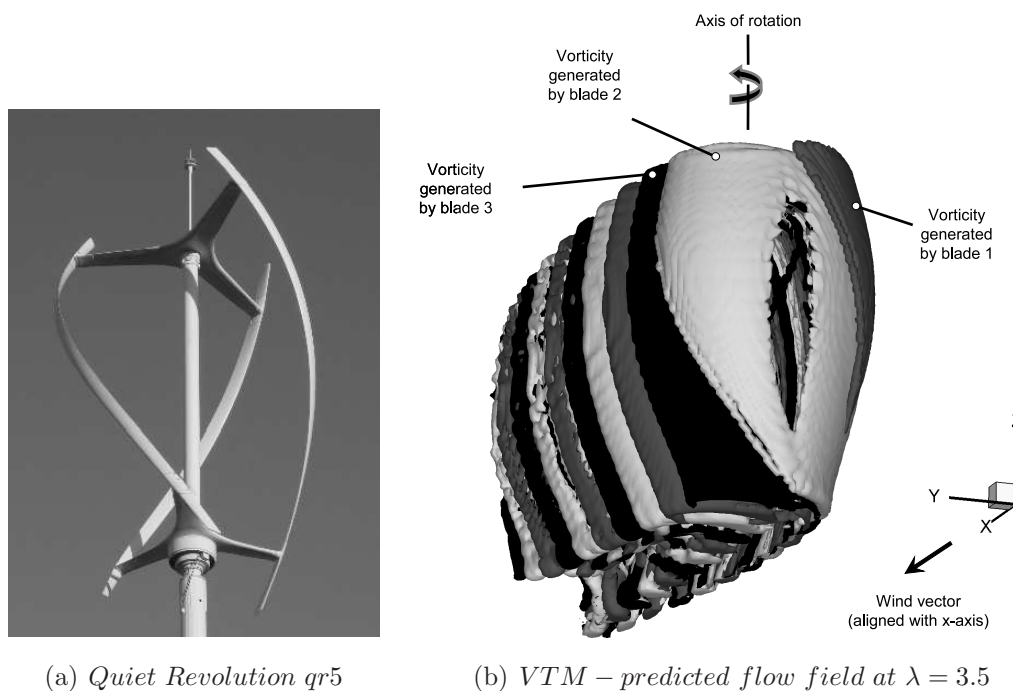
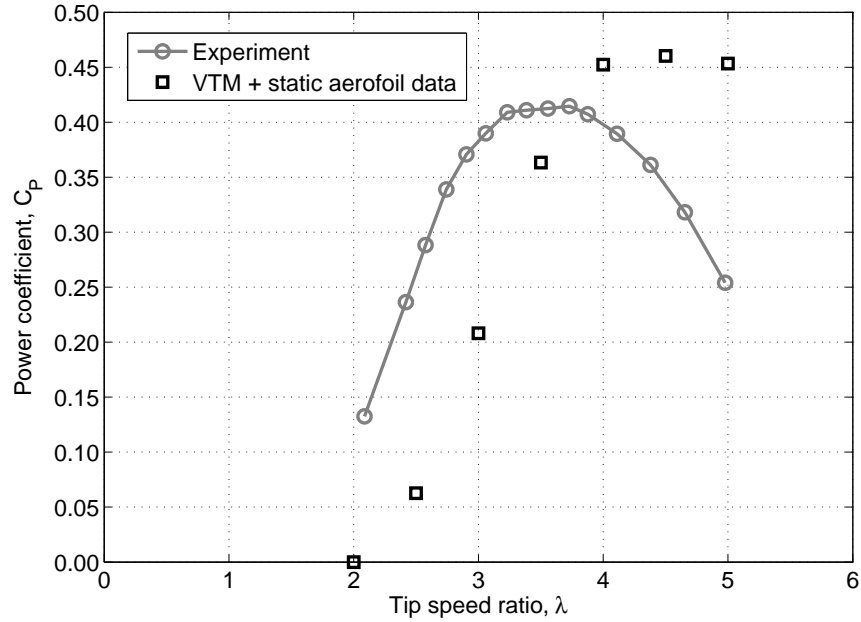
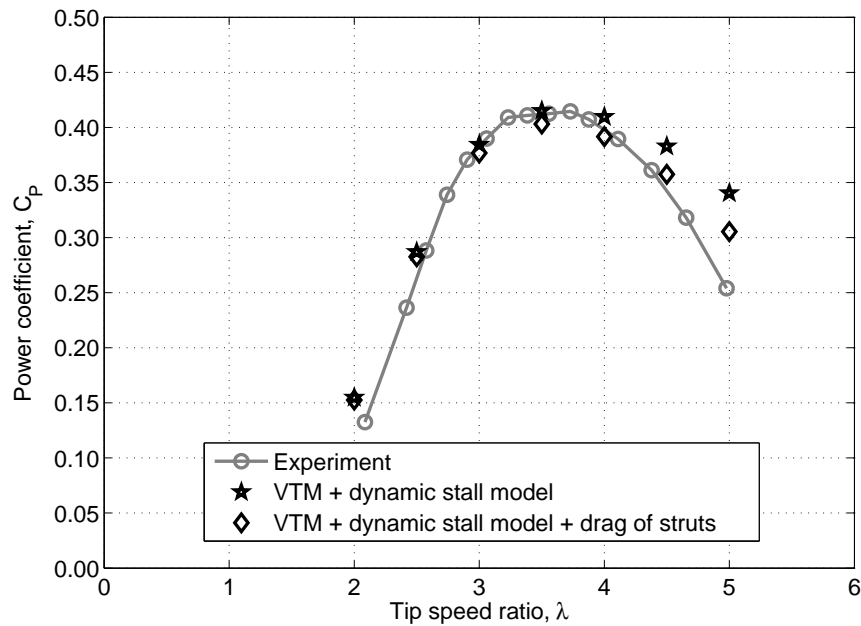


Figure 4.14: The Quiet Revolution qr5 vertical-axis wind turbine (courtesy of Quiet Revolution Ltd.) (left) and the VTM-predicted flow field of the turbine visualised by plotting an isosurface of vorticity (right).

4.2 Turbine Performance - Comparison with Experiment



(a) VTM simulations based on static airfoil data



(b) VTM simulations in conjunction with its dynamic stall model

Figure 4.15: VTM-predicted power coefficient based on static airfoil data (a) and in conjunction with its dynamic stall model (b) in comparison to experimental measurements made by Penna [78] for the qr5 vertical-axis wind turbine manufactured by Quiet Revolution Ltd.

4.2 Turbine Performance - Comparison with Experiment

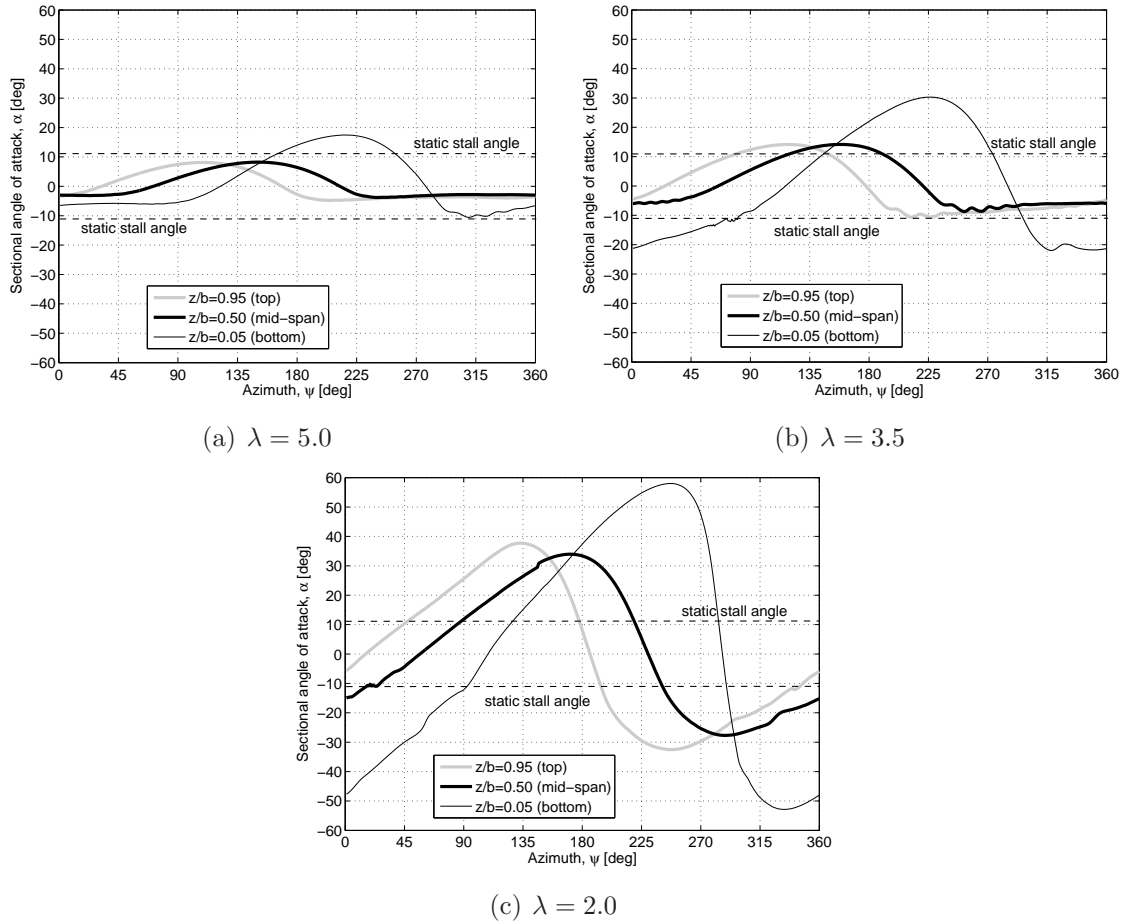


Figure 4.16: VTM-predicted variation with azimuth of the aerodynamic angle of attack at three sections along the length of the blade of the qr5 turbine.

Very satisfactory agreement between experimental measurements and simulation is obtained, in contrast, when the VTM is employed in conjunction with its dynamic stall model, as shown in figure 4.15(b). The VTM simulations (‘stars’ in figure 4.15(b)) agree very well with the experimental measurements when the tip speed ratio is less than that for the maximum power coefficient, whereas they over-predict the measured power coefficients at higher tip speed ratios. In particular, the tip speed ratio at which the maximum power coefficient is obtained and the maximum power coefficient itself are very well predicted - arguably better than has previously been possible using any other numerical technique. The reason for the disagreement between VTM simulations and experimental measurements at higher tip speed ratios is most likely the additional

4.2 Turbine Performance - Comparison with Experiment

drag that is due to the support struts that connect the rotor blades with the shaft of the turbine (see figure 4.14(a)). These struts were not modelled within the simulation.

An estimation of the drag that is caused by the struts, and thus the loss in overall power of the qr5 turbine is given below. The loss of power that is due to the parasite drag of one support strut, $C_{P_{st}}$, can be estimated as

$$C_{P_{st}} = \frac{1}{2} \rho \int_0^{2\pi} \int_0^{R_{st}} C_{d0,st} (\Omega r + V_\infty \cos \psi)^2 c_{st} r \Omega \, dr d\psi \quad (4.3)$$

where ρ is the air density, $C_{d0,st}$ is the drag coefficient of the strut at zero lift, R_{st} is the maximum radius of the strut, Ωr is the local circumferential velocity, V_∞ is the wind speed, ψ is the azimuth and c_{st} is the local chord of the strut.

By integrating equation (4.3) for each strut, the total loss of power due to the support structure can be expressed as a non-dimensionalised power coefficient

$$C_{P_{st,total}} = \sum_{i=1}^N \frac{1}{4} C_{d0,st} \frac{A_{st}^i}{A} \left(\frac{R_{st}^i}{R} \lambda + \left(\frac{R_{st}^i}{R} \right)^3 \lambda^3 \right) \quad (4.4)$$

where N is the number of support struts, A_{st}^i is the area of strut i and A is the swept area of the turbine. The power loss that is caused by the drag generated by the support struts is a function of the tip speed ratio cubed, as indicated by the last term in Equation 4.4. The power coefficients of the qr5 that are predicted by the VTM when the estimated drag generated by the struts is included ('diamonds' in figure 4.15(b)), are in better agreement with the experimental measurements at high tip speed ratio, although the measured power coefficient is still over-predicted by the numerical simulations. This indicates that there are larger, as yet unresolved power losses within the system that can not be accounted for solely by this simplistic model for the parasite drag of the struts. For instance, the struts, as well as the vertical shaft of the turbine, do not only generate parasite drag but also shed vorticity that interferes with the aerodynamic performance of the portions of the blades that are closest to the support structure. These secondary effects are not accounted for by the calculation of the parasite drag. Nevertheless, the simple drag estimation shows that at least some of the discrepancy between VTM simulation and experimental measurements at the highest tip speed ratios could quite feasibly be caused by the struts not being included in the numerical model.

4.3 Summary

VTM simulations have been compared to two sets of independent experimental measurements of the performance of vertical-axis turbines. The VTM-predicted sectional forces for an aerofoil at the mid-span of a straight blade of a vertical-axis rotor compare very well with previous computations of the two-dimensional aerodynamics of the same aerofoil in an equivalent planar, cyclic motion. In the downstream part of the revolution of the turbine, aerodynamic interactions occur between the blades of the rotor and vortices in the wake. These blade-wake interactions cause transient excursions in the angle of attack on the blade beyond the static stall angle, leading to localised dynamic stall near the tips of the blades. Indeed, the conclusion that local dynamic stall is induced by blade-wake interactions is supported by the improved correlation between experimental measurements and VTM predictions that results when the dynamic stall model is incorporated into the VTM to represent the blade aerodynamics compared to when only a quasi-steady model was used. It is suggested, thus, that the disagreement between experimental measurements and computational data that has been presented in previous studies arises because three-dimensional aerodynamic effects, such as interactions between the blades of the turbine and the vortices in the wake, were not modelled with sufficient fidelity.

The VTM has further been used to simulate the three-dimensional flow field surrounding a commercial vertical-axis wind turbine. This turbine consists of three blades that are helically twisted around the rotational axis of the rotor. The predicted variation of the power coefficient agrees very favourably with experimental measurements of the rotor performance. It was demonstrated that an appropriate implementation of a dynamic stall model is essential if the performance of the turbine is to be predicted reliably over its entire operating range.

When these results are taken together, they provide significant confidence in the ability of the VTM to predict accurately the aerodynamics of vertical-axis wind turbines.

4.4 Chapter Nomenclature

A	swept area
A_{st}	area of the support struts, $R_{st}c_{st}$
AR	aspect ratio, b/c

b	blade span
c	aerofoil chord length
c_{st}	chord length of the support strut, $c_{st} = c(r)$
$C_{d0,st}$	zero drag coefficient of the support strut
C_d	sectional drag coefficient, $F_d/\frac{1}{2}\rho cu_b^2$
C_l	sectional lift coefficient, $F_l/\frac{1}{2}\rho cu_b^2$
C_n	sectional normal force coefficient, $F_n/\frac{1}{2}\rho cu_b^2$
C_t	sectional tangential force coefficient, $F_t/\frac{1}{2}\rho cu_b^2$
C_P	power coefficient, $P/\frac{1}{2}\rho AV_\infty^3$
$C_{P_{st,total}}$	total power loss due to the support struts
F_d	sectional drag
F_l	sectional lift
F_n	sectional force acting normal to the aerofoil chord
F_n^*	sectional non-dimensional normal force, $F_n/\frac{1}{2}\rho cV_\infty^2$
F_N	force acting normal to the blade chord
F_N^*	non-dimensional normal force, $F_N/\frac{1}{2}\rho bcV_\infty^2$
F_t	sectional force acting tangential to the aerofoil chord
F_t^*	sectional non-dimensional tangential force, $F_t/\frac{1}{2}\rho cV_\infty^2$
F_T	force acting tangential to the blade chord
F_T^*	non-dimensional tangential force, $F_T/\frac{1}{2}\rho bcV_\infty^2$
H	turbine height
P	power
R	reference radius of the rotor
R_{st}	maximum radius of the support strut, $R_{st} = R_{st}(z)$
Re_b	blade Reynolds number, $\Omega Rc/\nu$
u_b	local velocity at a blade section
V_∞	wind speed
x, y, z	coordinates
α	angle of attack
λ	tip speed ratio, $\Omega R/V_\infty$
ψ	azimuth angle
ρ	air density
Ω	angular velocity of the rotor

Chapter 5

Influence of Rotor Configuration on Turbine Performance

In order to investigate the influence of blade curvature and helical blade twist on the aerodynamic performance and wake dynamics of vertical-axis wind turbines, the Vorticity Transport Model has been used to model the flow fields surrounding three different turbines: one with a straight-bladed configuration, another with a curved-bladed configuration and another with a helically twisted configuration. The influence of geometry on the aerodynamic performance of a vertical-axis wind turbine is described in the present chapter, whereas the behaviour of each turbine configuration in a set of more practically relevant operating conditions is analysed in Chapter 6.

The geometry of each turbine is described in Section 5.1 of this dissertation. An exploration of the aerodynamic characteristics of the turbines has been conducted over their entire range of operational tip speed ratios. The variations with tip speed ratio of the power coefficient that is produced by each turbine and the forces that act on each rotor are analysed in Section 5.2, whereas the variations with azimuth of the blade aerodynamic loading and of the power coefficient that is generated by each turbine are discussed in Sections 5.3 and 5.4. The structures of the wakes that are produced by the blades of each configuration are compared in Section 5.5.

5.1 Turbine Configurations

The geometry of each of the three vertical-axis wind turbines that have been investigated is illustrated in Figure 5.1. The blades of each turbine are separated by 120° azimuth. Starting from the straight-bladed configuration, shown in Figure 5.1(a), the radial location of each blade section was displaced using a hyperbolic cosine distribution in order to yield the troposkien shape of the curved-bladed configuration shown in Figure 5.1(b). The helically twisted configuration, shown in Figure 5.1(c), was then obtained by twisting the blades around the rotor axis. The blades of the straight- and curved-bladed configuration, and each individual section of the blades of the helically twisted configuration, are designed to have zero geometric pitch angle. In other words, the chord of each blade section is tangential to the local segment of the circle that is described by the trajectory of the blades. The geometric properties of the three turbines that are investigated are listed in Table B.2, whereas the key parameters of the rotors are summarised in Table B.3 in the Appendix.

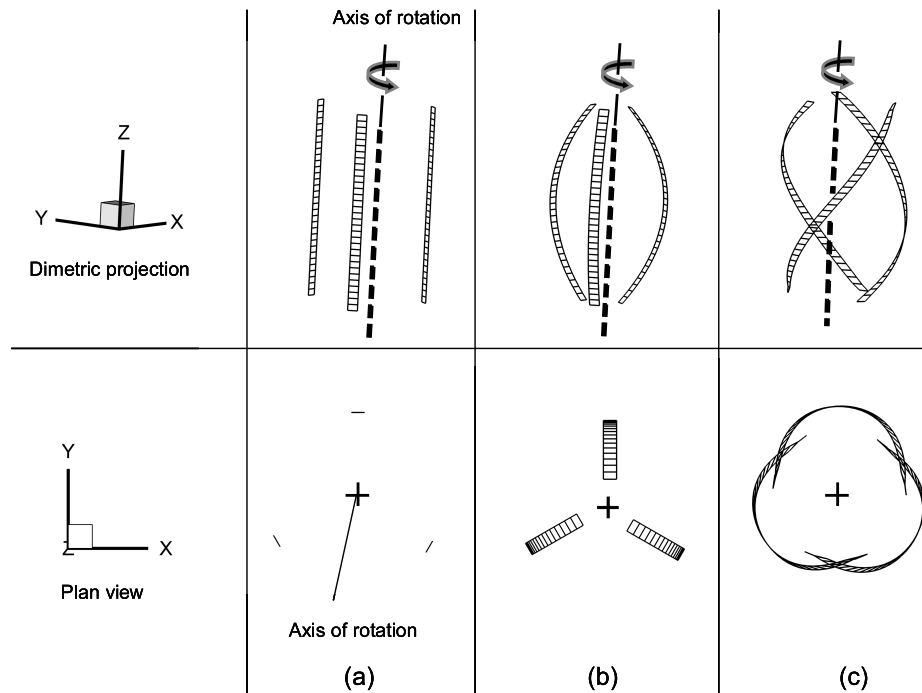


Figure 5.1: Geometry of the vertical-axis wind turbines with (a) straight, (b) curved and (c) helically twisted blades.

The maximum radius, R , of each rotor is at the mid-span of the reference blade ('blade 1') of the turbine, and is identical for each of the three different configurations. This radius is used as the reference radius of the rotor when presenting non-dimensional data for the performance of the rotor. The tip speed ratio, λ , is defined as the ratio between the circumferential velocity at the mid-span of the blade, ΩR , and the wind speed, V_∞ . The orientation of the blades and the specification of the azimuth angle of the turbine with respect to the mid-span of blade 1 are shown in Figure 5.2.

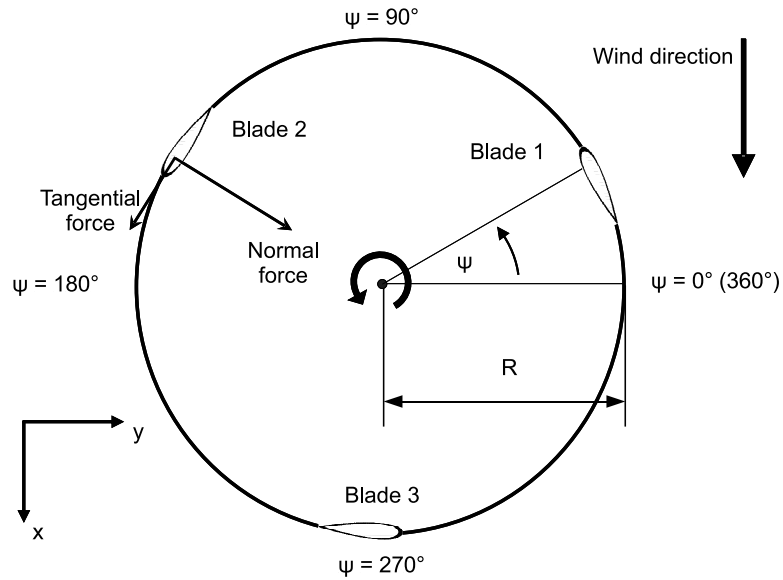


Figure 5.2: Diagram showing the wind direction, the definition of rotor azimuth and direction of positive normal and tangential forces, as well as the relative positions of the rotor blades.

The simulations that are discussed in the present chapter were carried out under the assumption that the turbine is operated in steady and uniform wind conditions. This was done in order to isolate the unsteady blade aerodynamic loading that is caused simply by the rotation of the turbine from the unsteady loading that would be induced by non-uniform or unsteady wind conditions in the real operating environment. The influence of the operating conditions on the performance of each turbine will be discussed in depth in Chapter 6 of this dissertation.

5.2 Variation of Power and Rotor Forces with Tip Speed Ratio

Figure 5.3 shows the variation with tip speed ratio of the power coefficients that are produced by the straight- and curved-bladed turbines and the turbine with helically twisted blades. Although the key rotor parameters of the three different wind turbines are identical, the difference in their aerodynamic design leads, naturally, to different absolute values of their power coefficients even if they are operated at the same tip speed ratio.

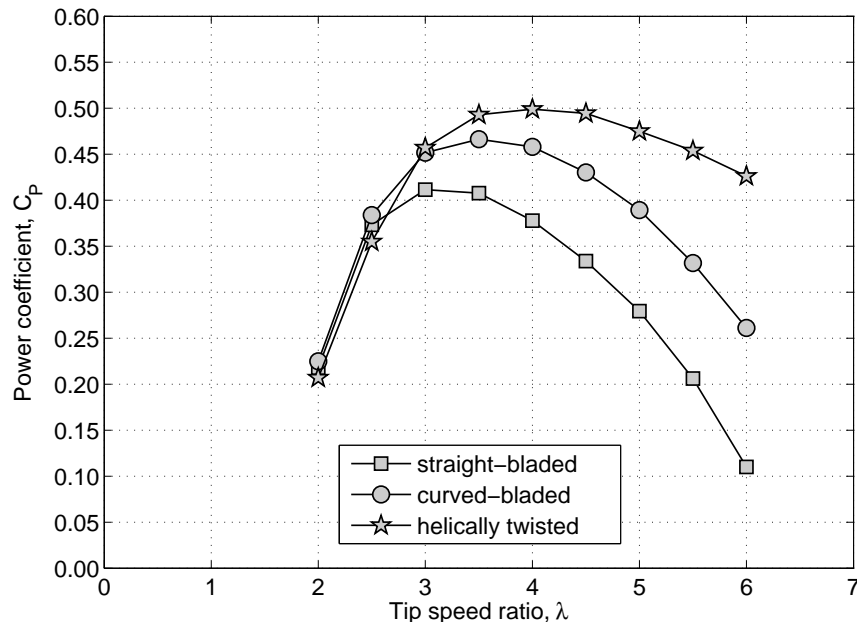


Figure 5.3: VTM-predicted variation with tip speed ratio of the power coefficients of the straight- and curved-bladed turbines and the turbine with helically twisted blades.

Interestingly, the curved and helically twisted configurations produce higher power coefficients than the straight-bladed configuration over almost the entire operating range, in fact except for very low tip speed ratios. The differences in the power coefficients that are produced are most pronounced at high tip speed ratios. This can be explained by the very low angle of attack, and thus aerodynamic loading, that is experienced by the blades of the straight-bladed turbine at high tip speed ratios.

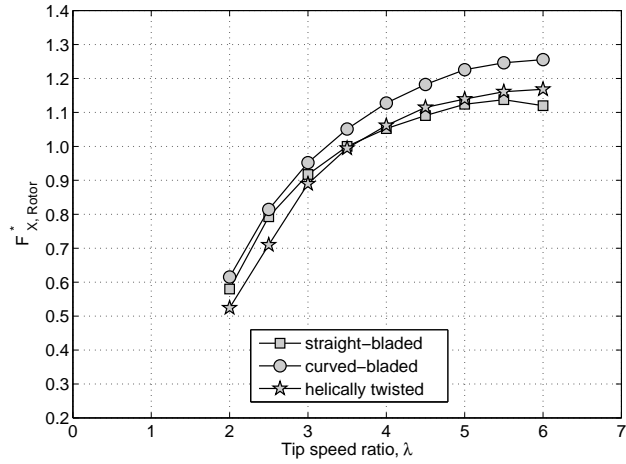
5.2 Variation of Power and Rotor Forces with Tip Speed Ratio

The variation with tip speed ratio of the power coefficient that is produced by the helically twisted configuration has a smaller gradient in the mid-operating range compared to that of the non-twisted configurations. This is because each individual section of the curved, twisted blade achieves its highest individual aerodynamic performance at a slightly different tip speed ratio, thereby avoiding the sudden drop in power that is observed for the non-twisted configurations when the tip speed ratio is different from that at which the turbine achieves its maximum efficiency. A shallow gradient in the $C_p - \lambda$ curve is beneficial since it enables the turbine to operate with comparatively high efficiency over a broad range of off-design operating conditions.

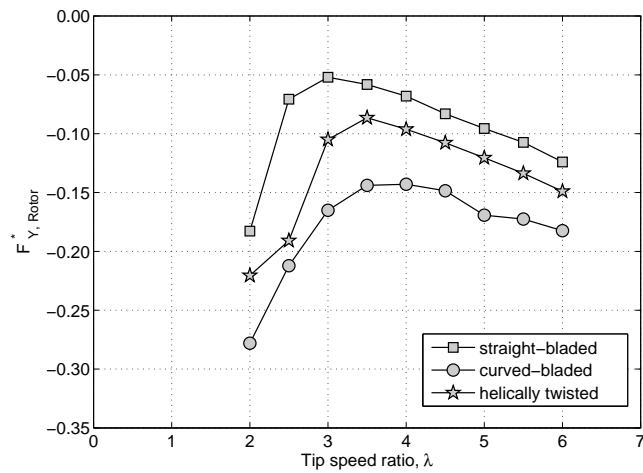
It should be noted that the maximum efficiency achieved by a vertical-axis wind turbine, and the shape of the $C_p - \lambda$ curve, depends on various parameters, such as the ratio between the blade chord and the rotor radius, as shown by Paraschivoiu (Ref. 81, p. 71ff.) amongst others. It thus can not be concluded that the supremacy of the helically twisted design shown in the results presented here exists for all meaningful rotor parameters. In other words, it is conceivable that a turbine with suitably designed non-twisted blades could achieve a maximum power coefficient that is equal or higher than that produced by the helically twisted configuration. Indeed, Raciti Castelli and Benini [82] showed in a numerical study that the power coefficient of a vertical-axis turbine that comprised one blade which was twisted helically, and which had a constant radius along its span, was slightly lower than that of another similar rotor with one non-twisted blade. Interestingly, however, the non-twisted configuration in their study also exhibited a slightly steeper gradient in the mid-range of the $C_p - \lambda$ curve than the twisted configuration. A parametric study with the aim of optimising the design was beyond the scope of the present investigation, however, given that the objective was simply to analyse the fundamental, and thus somewhat qualitative, differences in performance between straight- and curved-bladed turbines and helically twisted configurations.

Figure 5.4 shows the variation with tip speed ratio of the forces that act on the rotor of each configuration. The variations with tip speed ratio of the x- and the y-components of the forces (see Figure 4.1 for the definition of the force direction) are comparable for each configuration, in terms of the overall trend, with slight differences in magnitude. This is consistent with the variations with azimuth of the power coefficients produced by the turbines and simply reflects the differences in the aerodynamic design of the rotors.

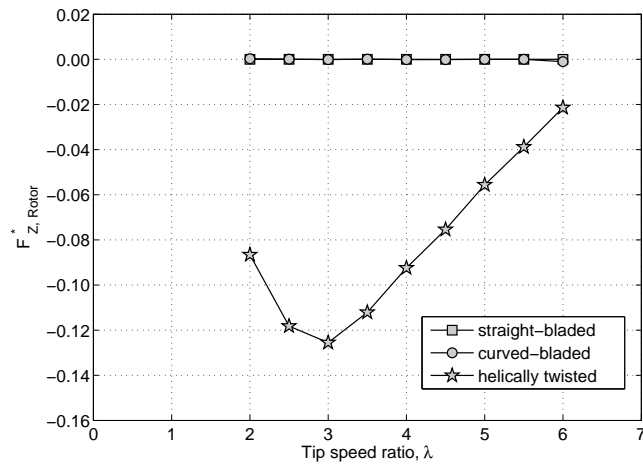
5.2 Variation of Power and Rotor Forces with Tip Speed Ratio



(a) x – component (streamwise force)



(b) y – component (crosswind side force)



(c) z – component (axial force)

Figure 5.4: VTM-predicted variation with tip speed ratio of the forces on the rotor of the straight- and curved-bladed turbines and the turbine with helically twisted blades.

The variations with tip speed ratio of the z-component of the rotor forces differ significantly between the twisted and the non-twisted configurations, however. Indeed, the helically twisted configuration produces an axial force that varies with tip speed ratio and, more importantly, is always non-zero for the entire operating range of the turbine that was investigated. Not surprisingly, the straight- and the curved-bladed turbines do not produce significant axial forces, irrespective of the tip speed ratio at which they are operated. The helically twisted configuration produces an axial force because of the effect of blade sweep that is induced when the blade is twisted helically around the rotational axis of the turbine. A swept blade produces a tangential force component that is non-parallel to the direction of the free stream. If a swept blade is orientated to operate in a vertical-axis wind turbine configuration, it consequently produces a force component that acts in the direction of the rotor axis.

5.3 Angle of Attack and Blade Loading

An exploration of the aerodynamic characteristics of the three turbines has been conducted over their entire range of operational tip speed ratios. As the tip speed ratio is varied, the relative contribution of dynamic stall, blade-vortex interaction and other wake related effects on the loading on the blades of each turbine does change. The associated relative changes in aerodynamic performance between the three rotor configurations are marginal, however. Only those results for a tip speed ratio of 3.5, in other words for a tip speed ratio somewhat near the mid-range of operationally-relevant tip speed ratios, are therefore presented in the following.

Figure 5.5(a) shows the variation with azimuth of the angle of attack at four span-wise locations along the reference blade of the *straight-bladed* turbine, as defined in Figure 5.5(b). The variation with azimuth of the sectional non-dimensional normal and tangential forces is presented in Figures 5.5(c) and 5.5(d).

A peak occurs in the variation of the angle of attack, and consequently in the blade aerodynamic loading, close to 90° azimuth. The behaviour of this turbine is thus very similar to that of the two-bladed turbine for which the blade loading was analysed in Section 4.1 of this dissertation. Figure 5.5(a) illustrates that, close to 90° azimuth, the angle of attack close to the blade tip ($z/b = 0.045$) is lower than that nearer to the mid-span of the blade. This effect is caused by the finite span of the blade and thus the

5.3 Angle of Attack and Blade Loading

influence of the tip vortices in inducing a strong component of flow, perpendicular to the blade surface, near the tips of the rotor blades. Close to 270° azimuth, a transient perturbation in the angle of attack is induced near to the tip of the blade. This impulsive perturbation is caused by interactions between the blade and the vortices that are trailed and shed from the blades in previous rotor revolutions. These blade-vortex interactions are visualised and discussed in more detail in Section 5.5 of this dissertation.

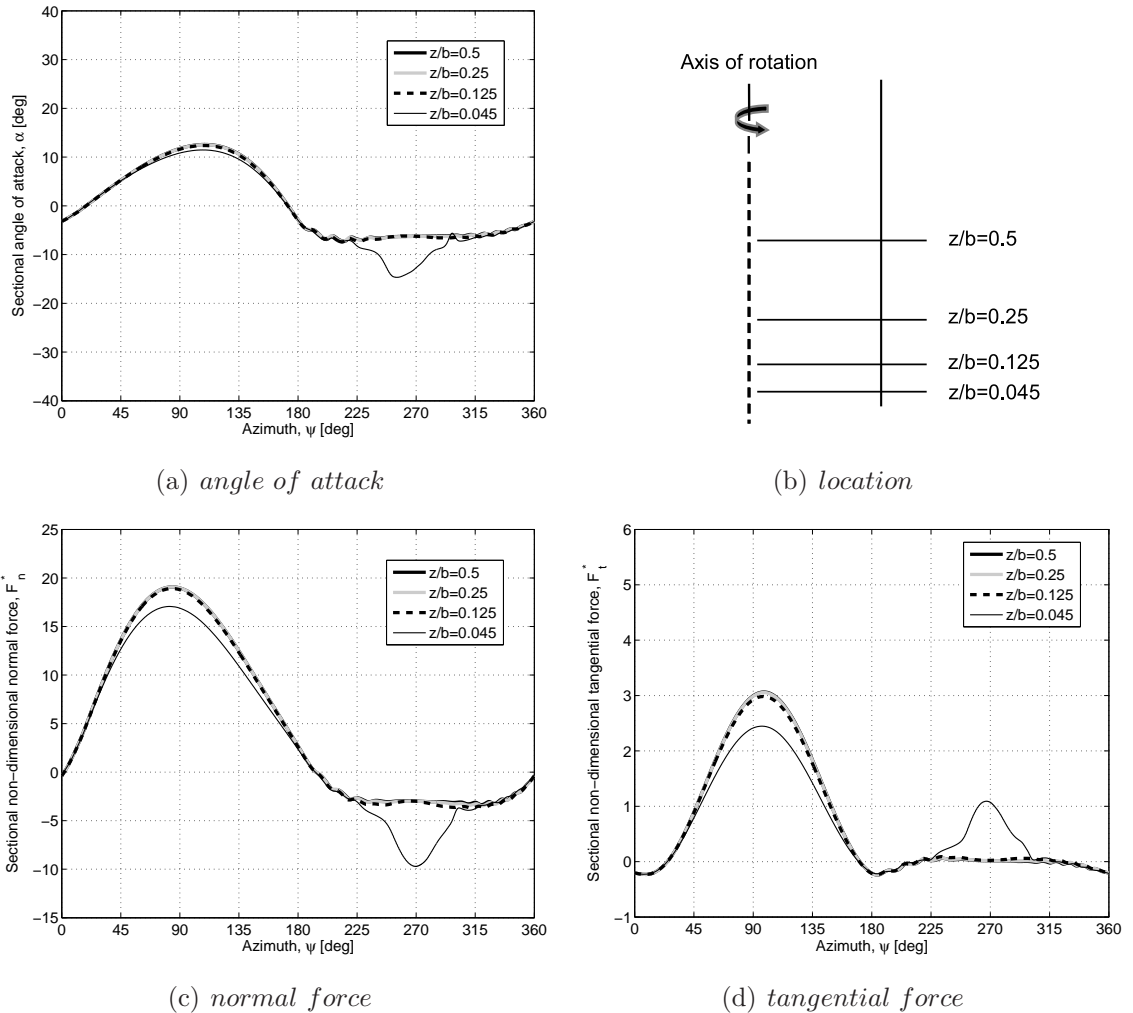


Figure 5.5: VTM-predicted forces and angle of attack distribution over one complete rotor revolution at four different spanwise stations along the blade of the straight-bladed turbine.

5.3 Angle of Attack and Blade Loading

Figure 5.6(a) shows the variation with azimuth of the angle of attack at four spanwise locations along the reference blade of the *curved-bladed* turbine, as defined in Figure 5.6(b). The variations with azimuth of the sectional non-dimensional normal and tangential forces are presented in Figures 5.6(c) and 5.6(d).

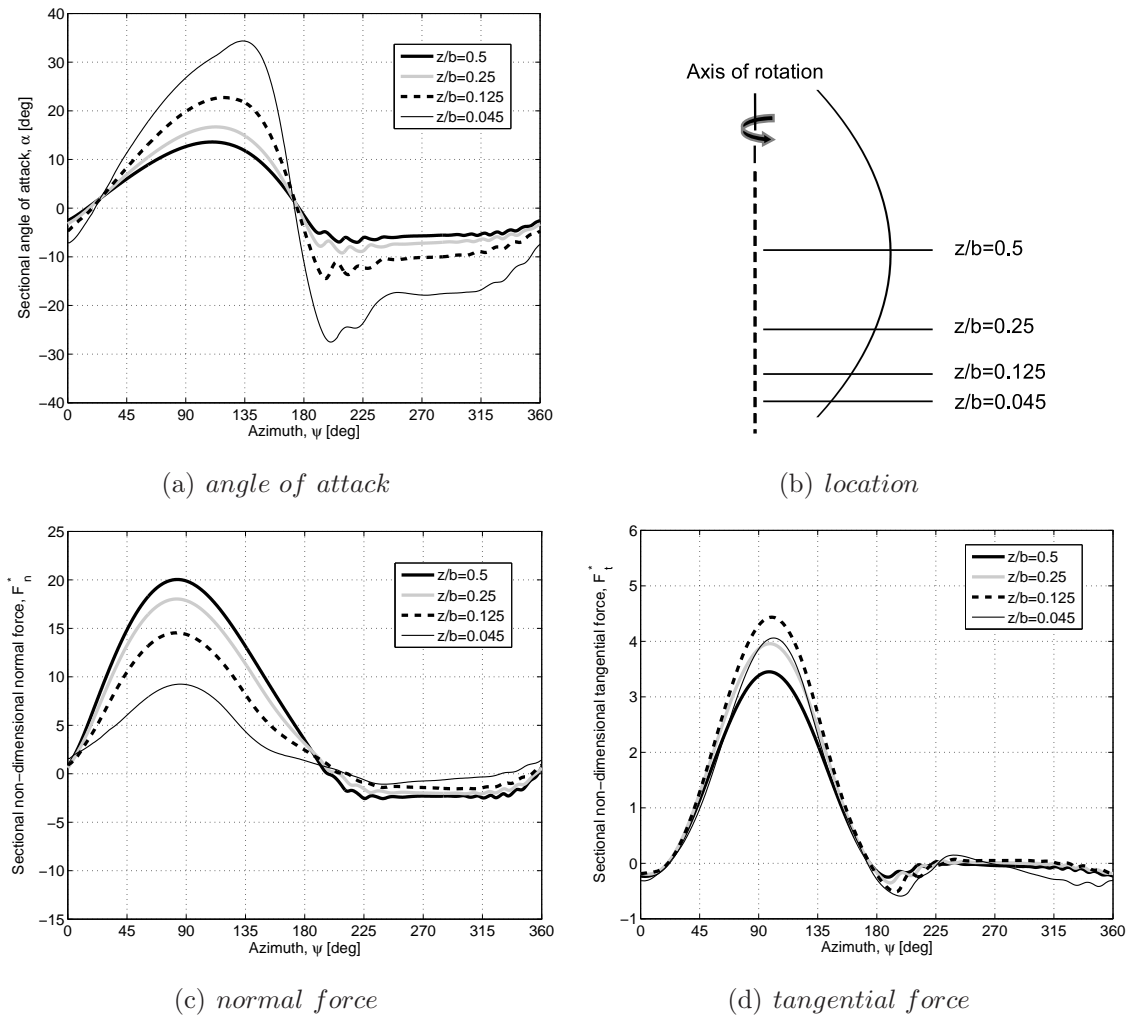


Figure 5.6: VTM-predicted forces and angle of attack distribution over one complete rotor revolution at four different spanwise stations along the blade of the curved-bladed turbine.

Figure 5.6 shows the cyclic variation with azimuth of the angle of attack and the blade aerodynamic loading for the curved-bladed turbine to resemble that of the straight-bladed turbine, with a similar peak close to 90° azimuth. The variation of the angle of attack along the blade span differs from that observed for the straight-

5.3 Angle of Attack and Blade Loading

bladed turbine, however, as the curvature of the blades results in a reduced radius, and, consequently, close to the blade tip, in a reduced circumferential component of velocity relative to the free stream. The amplitude of the oscillation of the local angle of attack close to the tip is thus significantly greater than that at the mid-span of the blade. This observation indicates that the static stall angle of the aerofoils within the curved-bladed configuration will be reached, and thus dynamic stall will be induced, at higher tip speed ratios than for a straight-bladed configuration.

Interestingly, Figure 5.6 illustrates that the blades of this turbine are not subject to the transient perturbations to the angle of attack, and thus to the blade loading, that are observed for the straight-bladed turbine close to the tips of its blades. This is most likely due to the effect of blade curvature, and thus of the reduced radius, close to the blade tips compared to the straight-bladed turbine. Since the local radius at the blade tip is small, blade-vortex interactions occur after the tip vortex has convected over a shorter distance compared to the situation for a less curved or a straight-bladed turbine. Consequently, the newly-created tip vortices interact with the blade well before the vortices have had time to convect any appreciable distance towards the horizontal centreline of the turbine. This effect is discussed in more detail in Section 5.5 of this dissertation.

Figure 5.7(a) shows the variation with azimuth of the angle of attack at four spanwise locations, as defined in Figure 5.7(b), along the *lower* portion of the reference blade of the turbine with *helically twisted* blades. Figure 5.8(a) shows the variation with azimuth of the angle of attack at four spanwise locations, as defined in Figure 5.8(b), along the *upper* portion of the reference blade of the same turbine. The variation with azimuth of the sectional non-dimensional normal and tangential forces produced by this turbine is presented in Figures 5.7(c), 5.7(d), 5.8(c) and 5.8(d). The distribution of the angle of attack and the blade aerodynamic loading is presented for both the upper and the lower portion of the blade in order to explain in more detail the asymmetry in the loading on the blade that is induced by helical twist.

Figure 5.7(a) indicates that, near to tip of the lower portion of the reference blade of the turbine with helically twisted blades, the maximum angle of attack is higher than at the mid-span. This is, again, a consequence of the reduced circumferential component of velocity relative to the free stream, and thus the reduced local tip speed ratio close to the tips of the blades compared to that at the mid-span.

5.3 Angle of Attack and Blade Loading

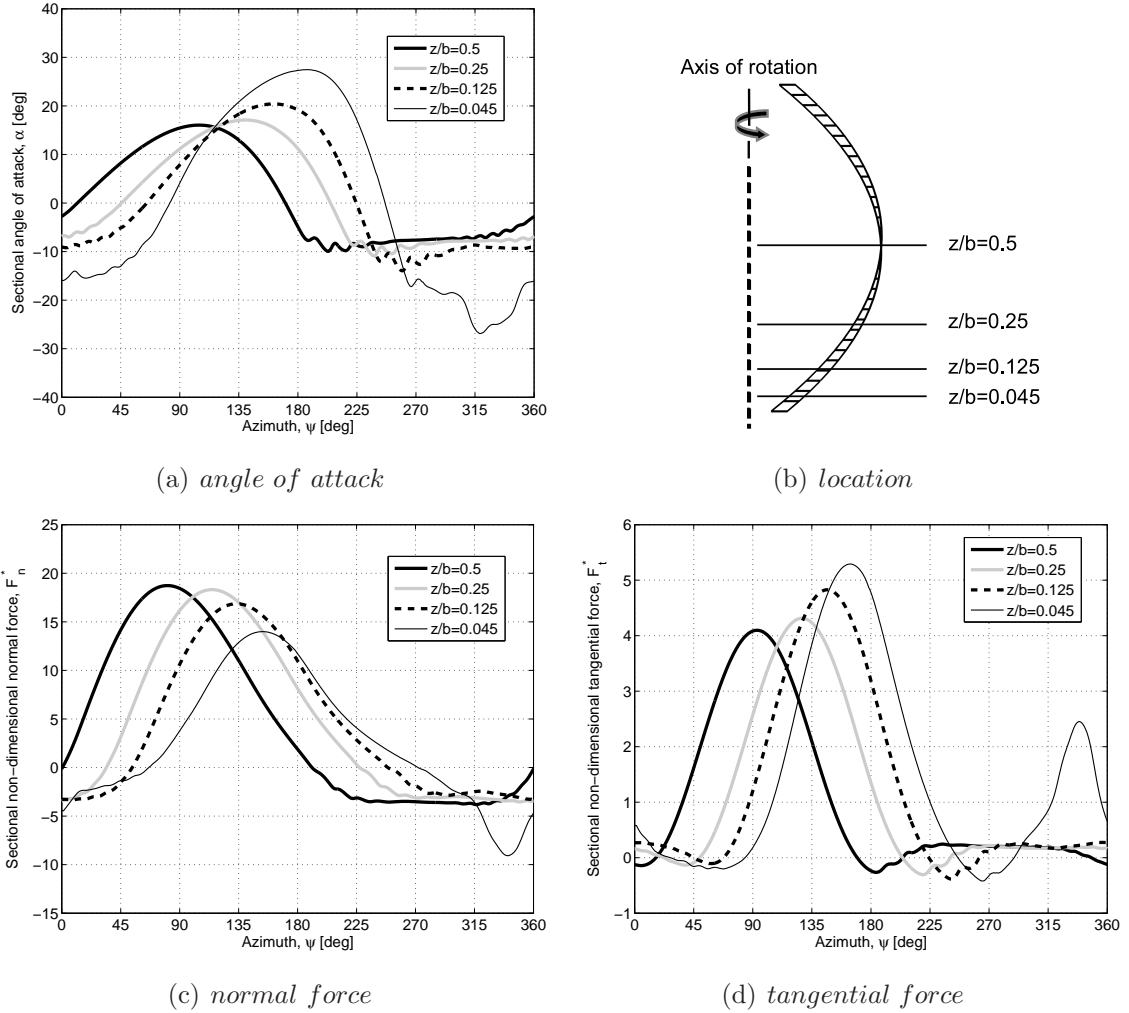


Figure 5.7: *VTM-predicted forces and angle of attack distribution over one complete rotor revolution at four different spanwise stations along the lower portion of the blade of the turbine with helically twisted blades. The azimuth ψ is with respect to the section at the mid-span of blade 1.*

Figure 5.8(a) shows that the maximum angle of attack close to the tip of the upper portion of the blade is only marginally greater than that at the mid-span. This asymmetry in the distribution of the angle of attack along the blade is a direct result of the helical blade twist. The sectional normal forces close to the blade tips of both the upper and the lower portion of the rotor are smaller than those experienced at the mid-span of the blade.

5.3 Angle of Attack and Blade Loading

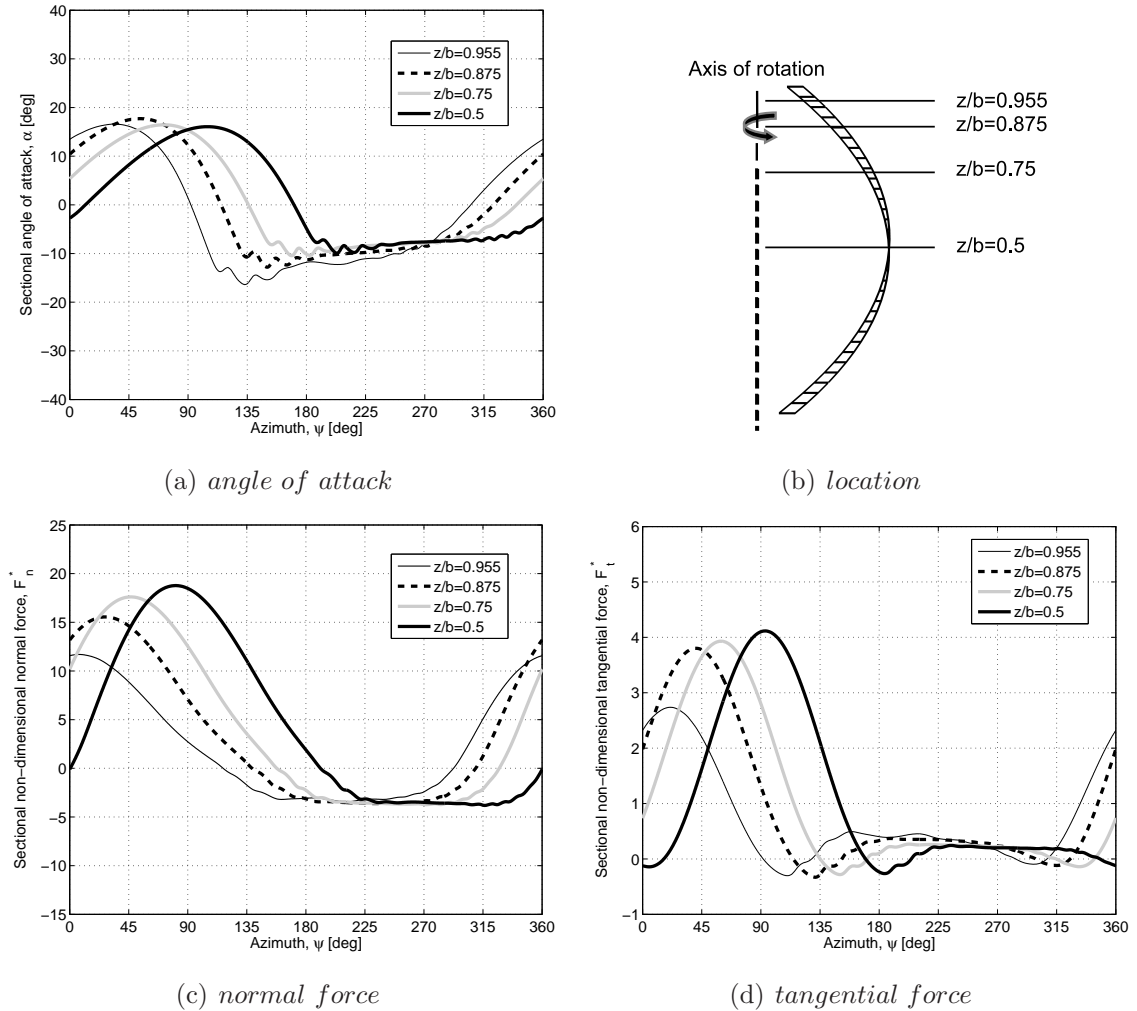


Figure 5.8: VTM-predicted forces and angle of attack distribution over one complete rotor revolution at four different spanwise stations along the **upper** portion of the blade of the turbine with helically twisted blades. The azimuth ψ is with respect to the section at the mid-span of blade 1.

Interestingly, the sectional tangential forces that are generated on the lower portions of the blade are slightly greater than those that are generated at the mid-span of the blade. The reduction in the local velocity, as a result of its smaller radius, that is experienced by the region close to the tips of the blade might lead one to the conclusion that the sectional tangential force close to the blade tip should also be lower than that at mid-span of the blade. The effect of the reduced radius is offset, however, by the higher angle of attack close to the tips of the blade, and this results in local tangential

5.4 Variation of Torque and Power with Azimuth

forces that are similar or even greater in magnitude than those experienced at the centre of the blade. The importance of this observation is discussed further in the following section, where the variation with azimuth of the torque and the power coefficient that is produced by each turbine configuration is analysed.

The primary consequence of the helical twist that is applied to the turbine is the phase lag in the angle of attack and, thus, in the loading along the length of the blades. The progressive phase shift in the variation of the angle of attack, and consequently in the blade loading along the length of the blade, is a result of the distribution of blade area over an azimuthal sector of the turbine, as seen in Figure 5.1(c). Figure 5.7 shows the occurrence of impulsive perturbations in the variation of the angle of attack and the blade loading close to the tip of the *lower* portion of the blade in the downwind part of rotor revolution, between 180° and 360° azimuth. Comparable perturbations are not apparent for the *upper* portion of the blade, as can be seen in Figure 5.8. The confinement of the interactions between the blades and the vortices within the wake to the lower portion of the blade is indicative of an asymmetry in the wake structure, and will be discussed in more detail in Section 5.5 of this dissertation.

5.4 Variation of Torque and Power with Azimuth

The variation with azimuth of the torque, and thus the power coefficient, of each turbine is analysed by investigating the sectional torque at different spanwise locations. The analysis of the sectional torque, which is the product of the sectional tangential force and the sectional radius, allows the contribution of the torque that is produced by a blade section to the torque that is produced by the entire turbine to be quantified. Figure 5.9 shows the sectional non-dimensional torque, Q^* , at four spanwise locations, as defined in Figures 5.5(b), 5.6(b), 5.7(b) and 5.8(b), along the reference blades of the three turbines. Figure 5.10 shows a three-dimensional visualisation of the distributions of sectional torque along the length of the entire reference blade of each turbine.

The angle of attack, and consequently the local tangential force coefficient, for those sections close to the lower tip of the helically twisted configuration is higher compared to that of those sections nearer to the mid-span of the blade. This can be understood once it is realised that blade curvature results in a smaller radius for the sections that are located close to the blade tip in comparison to those that are

5.4 Variation of Torque and Power with Azimuth

located towards the mid-span of the blade. It should be borne in mind though that the reduced radius of the sections close to the blade tip also results in a lower local velocity at those sections. Indeed, it is the combination of a lower local velocity and a higher force coefficient due to a higher angle of attack that results in a relatively uniform distribution of torque being developed along the length of the blades of this particular helically twisted turbine. This is reliant on the blades being designed so that blade curvature and helical blade twist are properly matched.

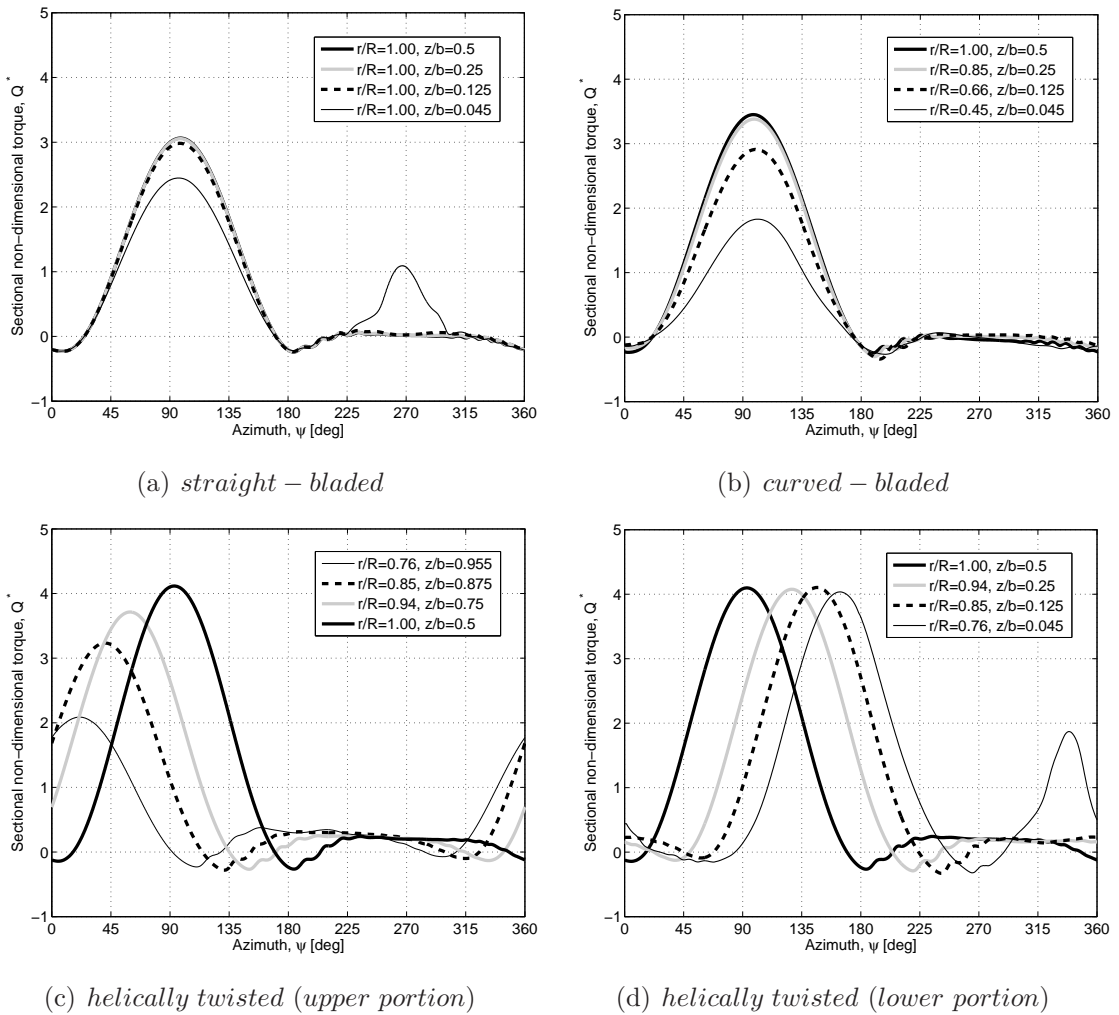


Figure 5.9: VTM-predicted variation with azimuth of the sectional non-dimensional torque at different blade sections for the three turbine configurations that were investigated.

5.4 Variation of Torque and Power with Azimuth

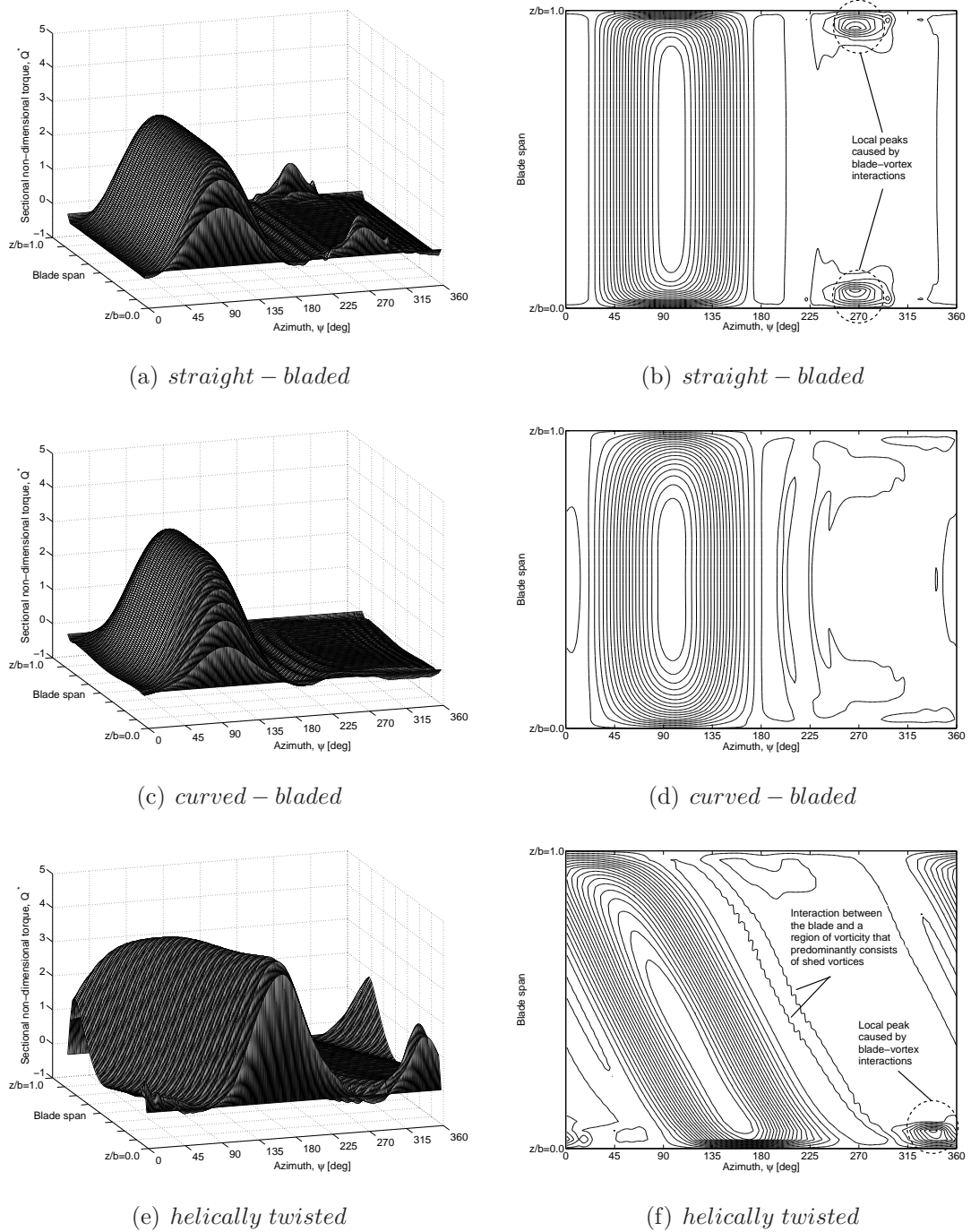


Figure 5.10: VTM-predicted variation with azimuth of the non-dimensional sectional torque along the blade spans of the straight- and curved-bladed turbines and the turbine with helically twisted blades.

5.4 Variation of Torque and Power with Azimuth

The azimuthal variation of the loading on the blades yields significant unsteadiness in the torque and hence the power that is produced by a vertical-axis wind turbine if its blades are not twisted. The introduction of helical blade twist together with blade curvature can reduce significantly the oscillations in torque and, thus, in the power output from the turbine. This is demonstrated in Figure 5.11, where the variation of the power coefficient, C_P , for one turbine revolution is presented for the three different turbine configurations at three different tip speed ratios. The tip speed ratios $\lambda = 2.0$, $\lambda = 3.5$ and $\lambda = 5.0$ were chosen to represent the behaviour of the turbines over their entire operating range.

The straight- and curved-bladed turbines exhibit significant unsteadiness in their power coefficients over the course of a single turbine revolution. The oscillations in the power coefficients of the straight- and curved-bladed turbines have three coherent peaks close to 90° , 210° and 330° azimuth; these reflect the peak in the variation of the torque of each single blade close to 90° azimuth, as shown in Figures 5.9(a) and 5.9(b). The power coefficient of the turbine with helically twisted blades, in contrast, is relatively steady. Despite each blade section of the helically twisted blade experiencing fluctuations in blade loading with azimuth, the more uniform distribution of its blade area around the azimuth of the turbine results in a significant reduction in the unsteadiness of the torque, and thus the power, that is transmitted through the shaft, when compared to the turbines with non-twisted blades.

The oscillations that are observed for the power coefficients of the straight- and curved-bladed configurations also manifest in oscillations of the rotor forces, as shown in Figures 5.12(a) and 5.12(b). In comparison with these, the oscillations in the side force, $F_{Y,Rotor}^*$, and the drag force, $F_{X,Rotor}^*$, of the rotor with the helically twisted blades are significantly reduced, as illustrated in Figure 5.12(c). The reduction in the amplitudes of the oscillations of the rotor forces on the helically twisted configuration could be very beneficial in practice since it might allow vibration and material fatigue on the tower and foundation of the turbine to be reduced, thus enhancing the design life of the system. The axial rotor forces, $F_{Z,Rotor}^*$, on the turbines with non-twisted blades are zero, whereas the asymmetric loading on the blades of the helically twisted turbine results in non-zero, but nevertheless very low, values for the axial rotor force, as discussed in Section 5.2 of this dissertation.

5.4 Variation of Torque and Power with Azimuth

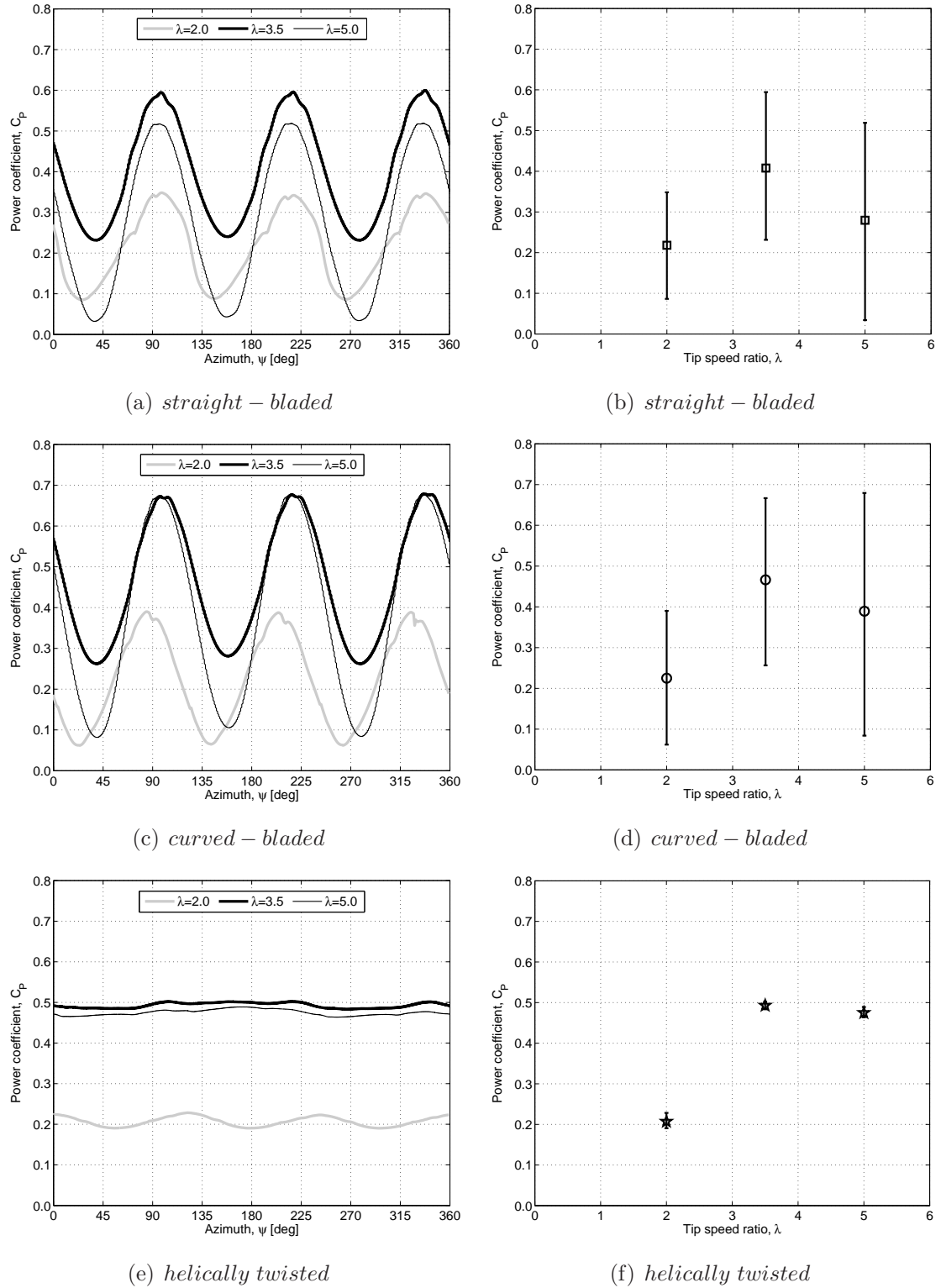


Figure 5.11: VTM-predicted variation of the power coefficients of the straight- and curved-bladed turbines and the turbine with helically twisted blades. Error bars in subfigures (b), (d) and (f) denote the variation of the power coefficient during one rotor revolution.

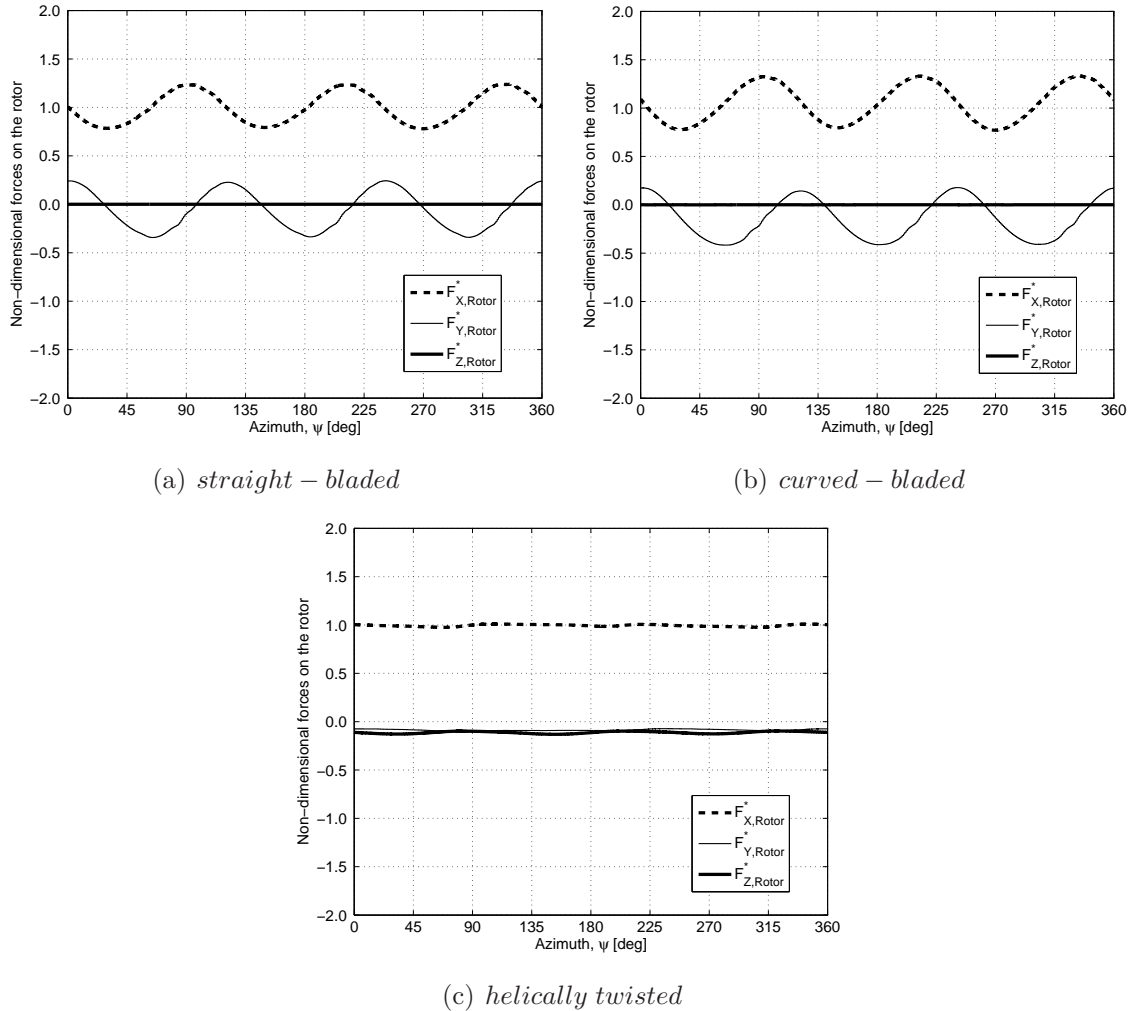


Figure 5.12: VTM-predicted variation with azimuth of the forces on the rotor of the straight- and curved-bladed turbines and the turbine with helically twisted blades when the rotors are operated at $\lambda = 3.5$.

5.5 Wake Structure

In the following, the structure of the wake that is generated by each configuration is analysed when the rotor is operated at a tip speed ratio of 3.5, in other words at a tip speed ratio in its mid-operating range. A three-dimensional representation of the wake that is produced by each of the three different turbine configurations is presented in Figure 5.13. Each wake is visualised as a surface within the flow on which the vorticity has constant magnitude. Figures 5.13(a), 5.13(c) and 5.13(e) illustrate the overall wake

structure that is developed by each of the three turbine configurations, whilst, in order to reveal the complexity of the vortical structure within the wake, in Figures 5.13(b), 5.13(d) and 5.13(f) separate shades are used to show the vorticity that is created by each of the three blades of the turbines.

Figure 5.14 shows the vorticity distribution on a plane through the centre of each of the three turbine configurations. This plane is oriented parallel to the axis of the rotor and is aligned with the wind direction. The vorticity distribution is depicted at the instant when blade 1 is located at 270° azimuth. The flow field is represented using contours of the component of vorticity perpendicular to the plane, thereby emphasising the vorticity that is trailed from the blades. The dark rendering corresponds to vorticity with a clockwise sense, and the light rendering to vorticity with a counter-clockwise sense of rotation.

Figures 5.14(a) and 5.14(b) illustrate that the non-twisted blades of the straight- and curved-bladed turbines result in a relatively symmetric distribution of vorticity in the wake downstream of the turbine. In contrast, the flow field of the turbine with helically twisted blades is characterised by a strong asymmetry in the distribution of vorticity between the upper and lower halves of the turbine, as is shown in Figure 5.14(c). It is apparent that their mutual induction causes the vortices that are produced by the blades of the turbine to convect towards the centreline of the rotor. The visualisation of the wake allows the origins to be identified of the localised impulsive perturbations that were observed in the variation of the angle of attack and the aerodynamic loading on the blades of the straight-bladed and the helically twisted configuration. Indeed, the transient perturbations in the variation of the angle of attack and the blade loading of the straight-bladed and helically twisted turbines that were observed in Figures 5.5 and 5.7 can be related directly to the interaction between the reference blade and the vortices that were generated by the blades in previous rotor revolutions. The interactions between the rotor blades and the vortices within the wake are visualised most clearly for the straight-bladed turbine and are depicted in Figure 5.14(a). It can also be seen why, in the absence of significant interactions with the tip vortices, the angle of attack, and consequently the blade loading, at the mid-span of the blade ($z/b = 0.5$) does not exhibit the same impulsive perturbations that are observed at sections closer to the tip of the blade. This observation is important as it implies that an appropriate three-dimensional representation of the wake is an essential component of any model

that is designed to capture accurately the aerodynamics of vertical-axis wind turbines. A more detailed analysis of interactions between the blades of a straight-bladed turbine and the vortices within the wake that is produced by its rotor was presented in Section 4.1.3 of this dissertation.

The vorticity distribution that is produced in the wake of the turbine with curved blades is shown in Figure 5.14(b). Compared to the extent of the blade-wake interactions that occur in the straight-bladed turbine system, no significant blade-wake interactions within the curved-bladed turbine system can be seen. This observation is consistent with Figure 5.6 which showed no significant transient perturbations in the angle of attack and the aerodynamic loading on the blades of the turbine. Since the amount of blade curvature is greater, and thus the radius close to the blade tips is smaller compared to the straight-bladed and helically twisted configuration, blade-vortex interactions occur after the tip vortices have convected in the z -direction over a shorter distance compared to the situation for a less curved or even a straight-bladed turbine. Consequently, the tip vortices interact with the blade before they have had time to convect any appreciable distance towards the horizontal centreline of the turbine.

Figure 5.15 shows the vorticity distribution on a horizontal plane through the centre of each of the three turbine configurations. The vorticity distribution is depicted at the instant when the mid-span of blade 1 is located at 270° azimuth. The flow field is represented using contours of vorticity magnitude. Since the planes are located at the centre of each configuration, the vorticity that is depicted in Figure 5.15 can, in the absence of any significant trailed vorticity at the location of this measurement plane, mainly be ascribed to the vorticity that is shed from the blades in response to the temporal variation of the bound vorticity on the blades. The three turbine configurations show comparable features in these particular visualisations of the flow fields. The vorticity that is shed during the part of the revolution when the leading edges of the blades face the wind, is somewhat smeared spatially. Much more compact vortical structures can be identified, in contrast, during the part of the revolution when the blades move with the wind. This is simply a consequence of the different rates of change of the vorticity that is bound to the rotor blades, and thus of the different strengths of the vortices that are shed into the wake, in these two parts of the rotor revolution.

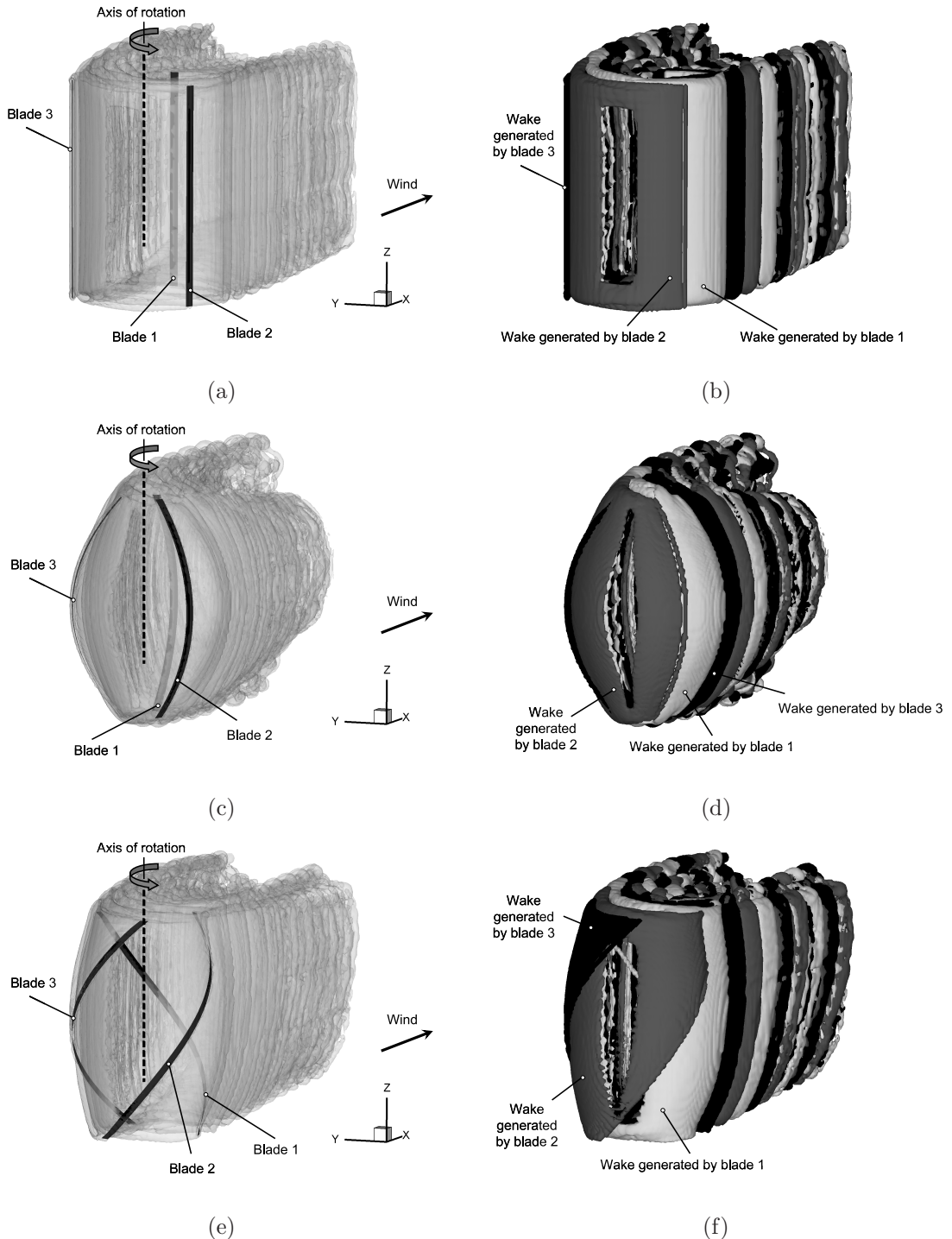


Figure 5.13: Three-dimensional graphical representation of the computed flow fields surrounding the turbine configurations with straight blades (a and b), curved blades (c and d), and helically twisted blades (e and f). The wake geometry is visualised by rendering a surface on which the vorticity has constant magnitude. The subfigures on the left show the entire vorticity field that is developed by each turbine, whereas the subfigures on the right show the vorticity that is developed by each individual blade.

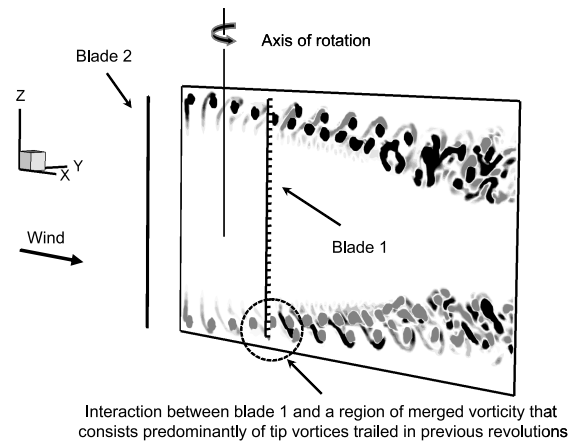
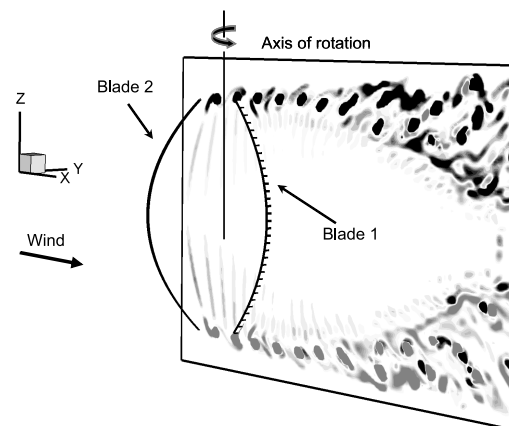
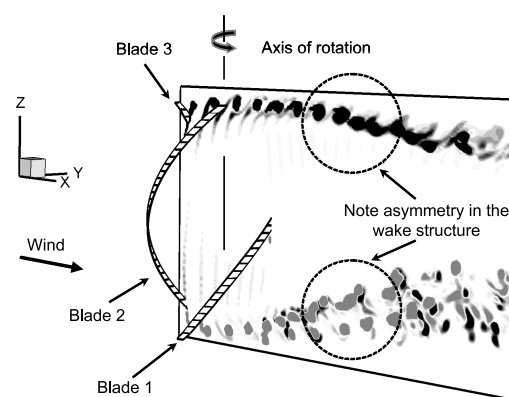
(a) *straight – bladed*(b) *curved – bladed*(c) *helically twisted*

Figure 5.14: Computed vorticity fields surrounding the (a) straight-bladed, (b) curved-bladed, and (c) helically twisted turbine, represented using contours of the component of vorticity that is perpendicular to a vertical plane that contains the axis of rotation of the turbine, and that is aligned with the wind direction. Mid-span of blade 1 at $\psi = 270^\circ$.

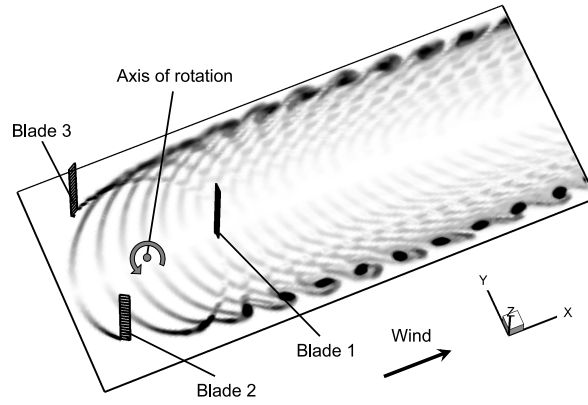
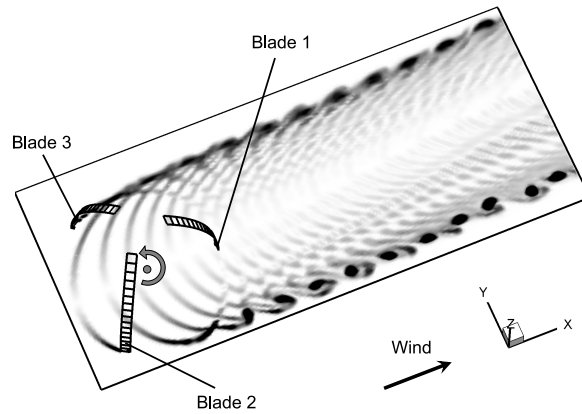
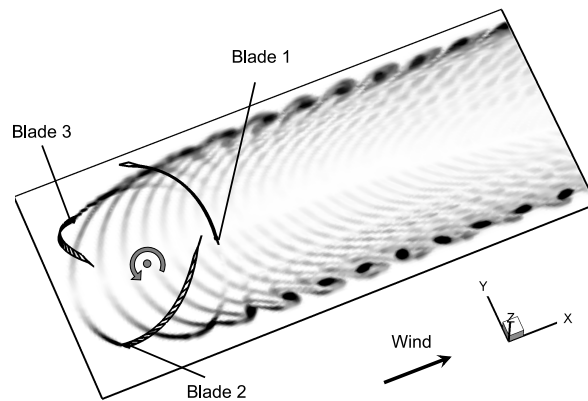
(a) *straight – bladed*(b) *curved – bladed*(c) *helically twisted*

Figure 5.15: Computed vorticity fields surrounding the (a) straight-bladed, (b) curved-bladed, and (c) helically twisted turbine, represented using contours of vorticity magnitude on horizontal planes that intersect with the mid-spans of the rotor blades. The mid-span of blade 1 is located at $\psi = 270^\circ$.

5.6 Summary

The aerodynamic performance and wake dynamics of three vertical-axis wind turbines, one with straight blades, another with curved blades and a third with a helically twisted blade configuration, have been investigated at different tip speed ratios using the VTM. The torque, and thus the power, that is produced by vertical-axis wind turbines with either straight or curved blades contains a substantial oscillatory component at the blade passage frequency of the turbine. The forces that act on the rotor in the stream-wise and the crosswind direction are also shown to produce a considerable oscillatory component to the overall forces on the turbine. These variations in the blade loading might contribute to fatigue of the rotor structure and reduce the design life of the turbine. By comparison, a turbine with helically twisted blades is shown to produce a relatively steady power coefficient if blade curvature and helical blade twist are properly matched. Despite the helically twisted blades still individually experiencing oscillations in blade loading with azimuth, a relatively steady overall force is achieved through an almost uniform distribution of blade area around the azimuth.

In contrast to non-twisted vertical-axis turbines, a configuration that comprises helically twisted blades produces a small, but notable, force in the direction of the rotational axis of the rotor. This axial force is caused by the effect of blade sweep that is introduced when the blades are helically twisted around the rotor axis. A swept blade produces a tangential force component that is non-parallel to the direction of the free stream and, if it is orientated to operate in a vertical-axis turbine configuration, consequently generates a force that acts in the direction of the rotor axis.

Blade curvature results in a reduced circumferential velocity relative to the free stream velocity, and thus a reduced local tip speed ratio, close to the blade tips compared to that at the mid-span of the blade. This is because the effective radius of the blade sections is smaller near to the blade tips than at the mid-span of the blade. The region close to the blade tip of the curved-bladed configuration therefore experiences oscillations in angle of attack that are of larger amplitude than those at the mid-span of the blade. This observation indicates that the static stall angle of an aerofoil within a curved-bladed configuration will be reached, and thus dynamic stall will be induced, at higher tip speed ratios than for a straight-bladed configuration.

5.7 Chapter Nomenclature

A	swept area
b	blade span
c	aerofoil chord length
C_P	power coefficient, $P/\frac{1}{2}\rho AV_\infty^3$
F_n	sectional force acting normal to the aerofoil chord
F_n^*	sectional non-dimensional normal force, $F_n/\frac{1}{2}\rho cV_\infty^2$
F_t	sectional force acting tangential to the aerofoil chord
F_t^*	sectional non-dimensional tangential force, $F_t/\frac{1}{2}\rho cV_\infty^2$
$F_{X,Rotor}$	x-component of force on the rotor (streamwise drag force)
$F_{X,Rotor}^*$	non-dimensional streamwise drag force, $F_{X,Rotor}/\frac{1}{2}\rho AV_\infty^2$
$F_{Y,Rotor}$	y-component of force on the rotor (crosswind side force)
$F_{Y,Rotor}^*$	non-dimensional crosswind side force, $F_{Y,Rotor}/\frac{1}{2}\rho AV_\infty^2$
$F_{Z,Rotor}$	z-component of force on the rotor (axial force)
$F_{Z,Rotor}^*$	non-dimensional axial force, $F_{Z,Rotor}/\frac{1}{2}\rho AV_\infty^2$
P	power
Q^*	sectional non-dimensional torque, F_t^*r/R
$r = r(b)$	sectional radius
R	radius of the rotor at blade mid-span
Re	blade Reynolds number, $\Omega Rc/\nu$
V_∞	wind speed/ free stream velocity
x, y, z	coordinates
α	angle of attack
λ	tip speed ratio, $\Omega R/V_\infty$
ν	kinematic viscosity
ψ	azimuth angle
ρ	air density
Ω	angular velocity of the rotor

Chapter 6

Influence of Operating Condition on Turbine Performance

Increasing interest is being shown in the application of vertical-axis wind turbines for decentralised electricity generation within cities. Particularly in the urban environment, vertical-axis turbines might offer several advantages over horizontal-axis configurations - as described in Chapter 1 of this dissertation. The aerodynamics of the urban environment are characterised by frequent and rapid changes in wind speed and direction. Historically, experimental and numerical studies of the aerodynamic performance of vertical-axis wind turbines have been conducted, almost exclusively, when the rotors are operated in *steady* wind and thus in somewhat artificial conditions. Most efficient use of the available space within the built environment may be achieved by the construction of clusters that consist of several individual turbines, as shown in Figure 6.1. Such clustering might, under certain wind directions, cause any one of the turbines to operate within the wake of one of the other turbines, possibly reducing the power output of the cluster. Another concern is that the local distortion to the air flow that is caused by the presence of buildings in the urban environment might, under certain conditions of wind speed and direction, cause vertical-axis wind turbines mounted on or near the buildings to operate in oblique flow - in other words in conditions in which the wind vector is non-perpendicular to the axis of rotation of the turbine.

Little is known about the effect on the operation of a vertical-axis wind turbine when the wind is perturbed from supposedly optimal conditions. The VTM has thus

been used to predict the performance of the three different vertical-axis wind turbines, that were introduced in the previous chapter of this dissertation, when their rotors are operated in three different conditions. These operating conditions were chosen to mimic the flow that a vertical-axis wind turbine is likely to encounter in the urban environment. Section 6.1 and Section 6.2 show the results of simulations for each of the three different turbine configurations when the rotor is operated in *oblique flow* and in an *unsteady wind*, respectively. The performance of the straight-bladed turbine when it is influenced by the *wake of another rotor* is discussed in Section 6.3.



(a) *City House, Croydon, UK*



(b) *Arena at Kings Dock, Liverpool, UK*



(c) *Cleveleys Promenade, Lancashire, UK*



(d) *ANZ Centre, Melbourne, Australia*

Figure 6.1: *Arrangement of vertical-axis wind turbines at four different urban sites. Courtesy of Quiet Revolution Ltd.*

6.1 Oblique Flow

The performance of each of the three different vertical-axis wind turbines that were introduced in Chapter 5 of this dissertation was studied in *oblique* flow, in other words in conditions in which the wind vector is non-perpendicular to the axis of rotation of the turbine. The performance of the turbines in *normal* flow, in other words in conditions in which the wind vector is perpendicular to the axis of rotation of the turbine, was treated as the baseline condition against which the turbine performance in oblique flow is compared.

Figure 6.2 shows the definition of the oblique flow angle, β , together with a representation of the wake that is produced by the turbine with helically twisted blades in oblique flow, as visualised by plotting one of the surfaces within the flow field surrounding the rotor on which the vorticity has a uniform magnitude.

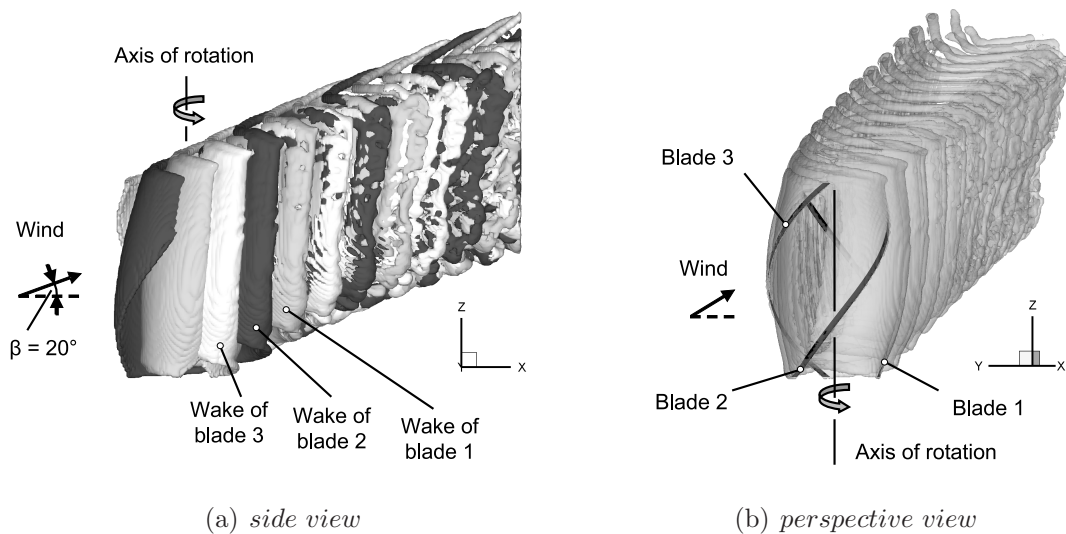


Figure 6.2: VTM-predicted flow field of the vertical-axis wind turbine with helically twisted blades at a tip speed ratio $\lambda = 3.5$ and at an oblique flow angle $\beta = 20^\circ$, visualised by plotting an isosurface of vorticity.

In what appears to be one of the only experimental measurements of the behaviour of vertical-axis wind turbines in oblique flow, Mertens *et al.* [83] and Simão Ferreira *et al.* [84] showed that their straight-bladed vertical-axis wind turbine produced a higher power coefficient when operated in oblique flow compared to when it was

operated in normal flow. The VTM predictions that are presented in this dissertation partly confirm these observations but also suggest that significantly higher power coefficients in oblique flow are obtained only at higher tip speed ratios and indeed only if the ratio between the height of the turbine and the radius of the rotor is sufficiently low. The results that are presented below also indicate that straight- and curved-bladed vertical-axis wind turbines produce power coefficients that vary significantly within one revolution of the rotor irrespective of whether the turbine is operated in normal flow or in oblique flow. A turbine with blades that are helically twisted around its rotational axis produces a relatively steady power coefficient, in contrast, under the same flow conditions.

The influence of the ratio between the height of the turbine and the radius of the rotor, henceforth called simply the height-to-radius ratio, on the performance of the straight-bladed turbine both in normal and in oblique flow will be discussed in the following section, whereas an analysis of the influence of blade curvature and helical blade twist on turbine performance is presented in Section 6.1.2.

6.1.1 Height-to-Radius Ratio

The power coefficient produced by straight-bladed vertical-axis wind turbines with three different height-to-radius ratios is shown in Figure 6.3 when the turbines are operated at different tip speed ratios in normal flow. The rotor radius was kept constant for all the turbine configurations that were investigated. Thus, a lower turbine height-to-radius ratio results in a lower aspect ratio of the blades, and consequently, in a lower aerodynamic efficiency of the turbine. This is the principal reason for the reduction in performance with decreasing height-to-radius ratio seen in Figure 6.3.

Figure 6.4 shows the power coefficient produced by straight-bladed vertical-axis wind turbines, as predicted by the VTM for the same three different height-to-radius ratios as shown in Figure 6.3, but when the turbines are operated with various angles of oblique flow. When the rotor is operated at the lowest tip speed ratio, the power coefficient of the turbine is slightly increased for all oblique flow angles that were investigated in the present study, irrespective of the height-to-radius ratio of the turbine. This is most likely because the component of velocity that is perpendicular to the blade is smaller in oblique flow than in normal flow, thereby causing the turbine to operate at a slightly higher effective tip speed ratio. Since the $C_P - \lambda$ curve has a steep, positive

gradient at low tip speed ratio, as shown in Figure 6.3, the turbine produces a higher power coefficient when it is operated in oblique flow, compared to when it is operated in normal flow, if the tip speed ratio is within the lower part of the operating range. Importantly, only the turbine with the smallest height-to-radius ratio develops a significantly higher power coefficient in oblique flow than when operated in normal flow, as shown in Figures 6.4(e) and (f). These results are consistent with the experimental studies carried out by Mertens *et al.* [83] and Simão Ferreira *et al.* [84]. When Figure 6.4 is taken in its entirety, however, it shows that the increase in the power output of the turbine in oblique flow that was observed in the experiments should by no means be taken as evidence of a general characteristic of vertical-axis wind turbines.

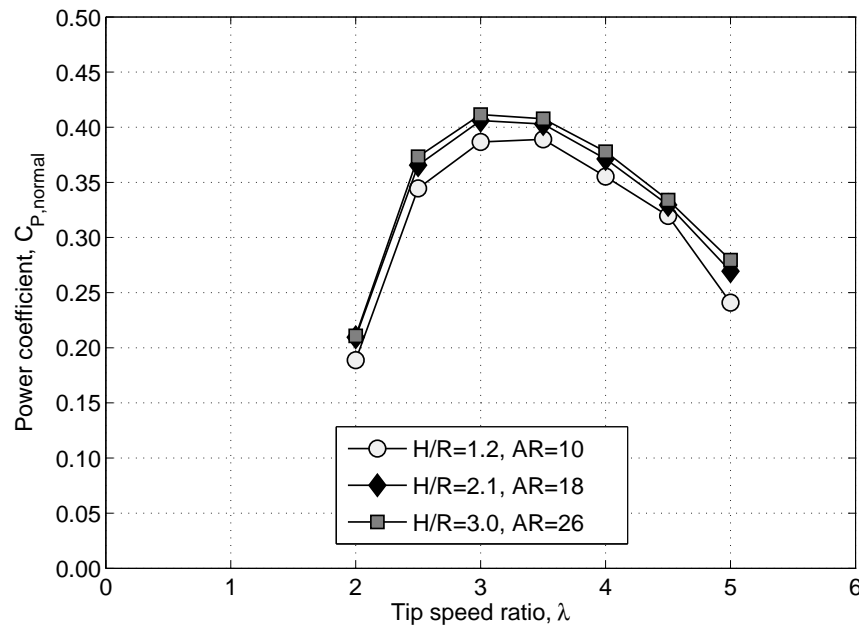


Figure 6.3: Influence of turbine height-to-radius ratio (H/R) on the VTM-predicted power coefficient of a straight-bladed vertical-axis wind turbine in normal flow.

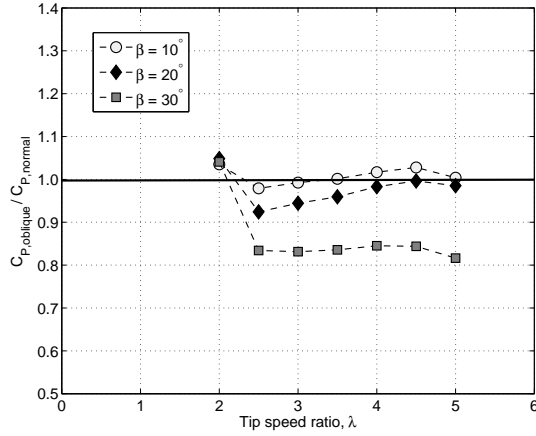
The reason why vertical-axis wind turbines with certain characteristics might produce higher power coefficients in oblique flow than in normal flow is revealed in Figure 6.5. This figure shows the VTM-predicted vorticity distribution on a plane that is immersed within the wake that is produced by the turbine with the smallest height-to-radius ratio that was simulated. This plane is aligned with the wind direction and contains the axis of rotation of the turbine. The vorticity distribution is depicted at

the instant when blade 1 is located at 270° azimuth (see Figure 5.2 for the definition of rotor azimuth). The flow field is represented using contours of the component of vorticity perpendicular to the plane, thereby emphasising the vorticity that is trailed by the blades. The dark rendering corresponds to vorticity with a clockwise sense of rotation, and the light rendering to vorticity with a counter-clockwise sense of rotation.

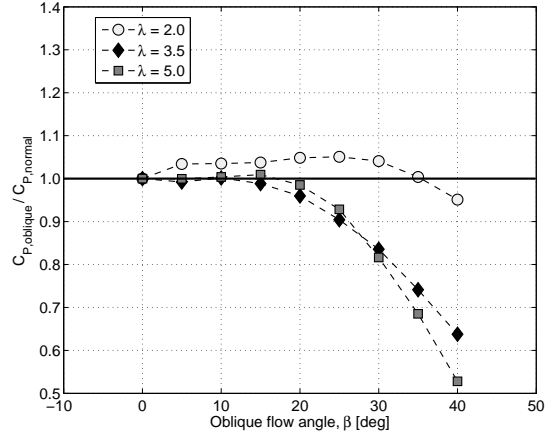
As the turbine rotates, its blades encounter the wake of the turbine as they traverse the downwind part of their azimuthal cycle - in other words between 180° and 360° azimuth. In normal flow, the entire length of each blade of the rotor is immersed in the wake of the turbine during the downwind portion of its cycle, as shown in Figure 6.5(a). In oblique flow, however, the convection of the wake is skewed, as shown in Figure 6.5(b), thereby allowing a portion of each blade to operate, over its entire azimuth, in a flow regime in which the influence of the wake is reduced significantly compared to the situation in normal flow. The resultant effect on the tangential force, and, consequently, on the power that is produced by the turbine, is illustrated in Figure 6.6.

In normal flow, the interaction between the wake and the blades acts effectively to suppress the loading on each blade during the downwind portion of its cycle, as shown in Figure 6.6(b), and hence the tangential force that is produced during the upwind segment of the blade cycle is the major contributor to the power that is produced by the turbine. In oblique flow, however, the contribution to the tangential force from the loading that is produced on the undisturbed portion of the blade during the downwind portion of its cycle contributes to an overall increase in the power that is produced by the turbine. This is despite the fact that the peak loading on the blades is reduced as a result of the reduction of the component of the wind vector that is perpendicular to the blade.

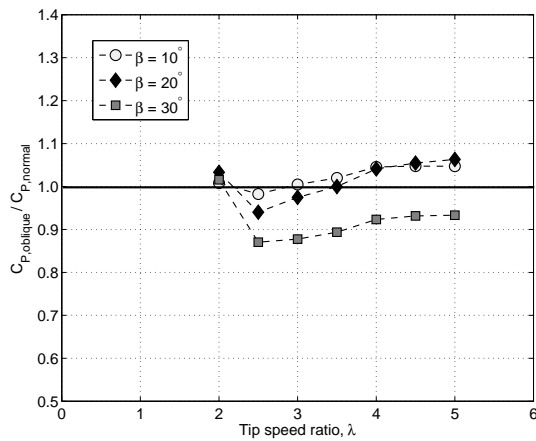
A simple geometric argument suggests then that the larger the height-to-radius ratio of the turbine, the smaller the proportion of the downwind blade that is exposed to relatively undisturbed flow by the effects of wake skew - and hence the smaller the proportion of the blade that develops significant tangential force during the downwind portion of its trajectory. This observation suggests thus that turbines with larger height-to-radius ratio should be less susceptible to the effects of wake skew than those with smaller height-to-radius ratio.



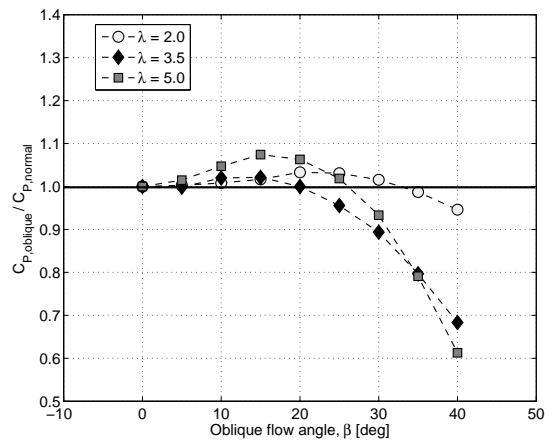
(a) $H/R = 3.0$



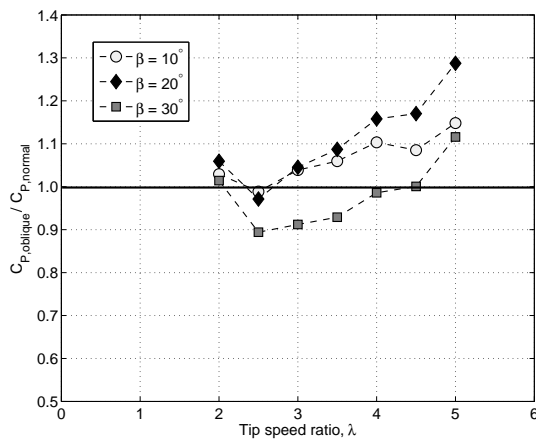
(b) $H/R = 3.0$



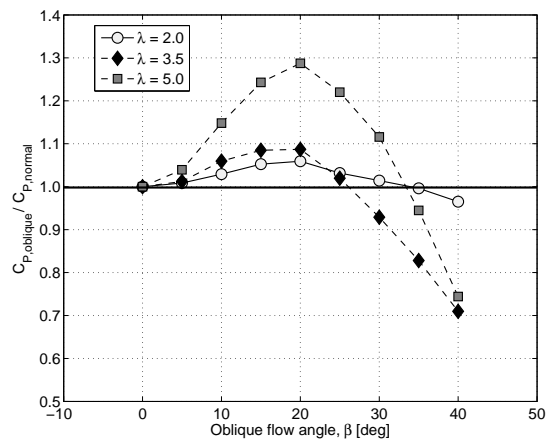
(c) $H/R = 2.1$



(d) $H/R = 2.1$



(e) $H/R = 1.2$



(f) $H/R = 1.2$

Figure 6.4: Influence of turbine height-to-radius ratio on the VTM-predicted power coefficient of a straight-bladed vertical-axis wind turbine at different oblique flow angles and at different tip speed ratios.

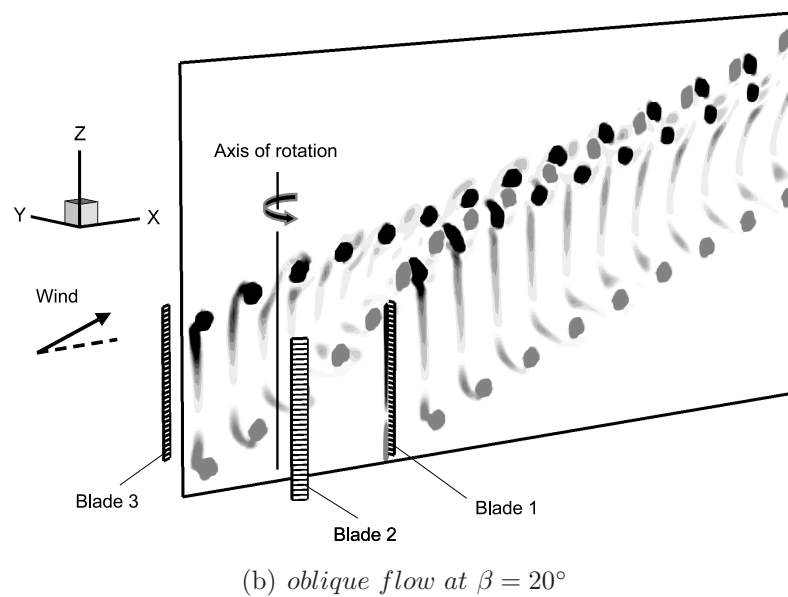
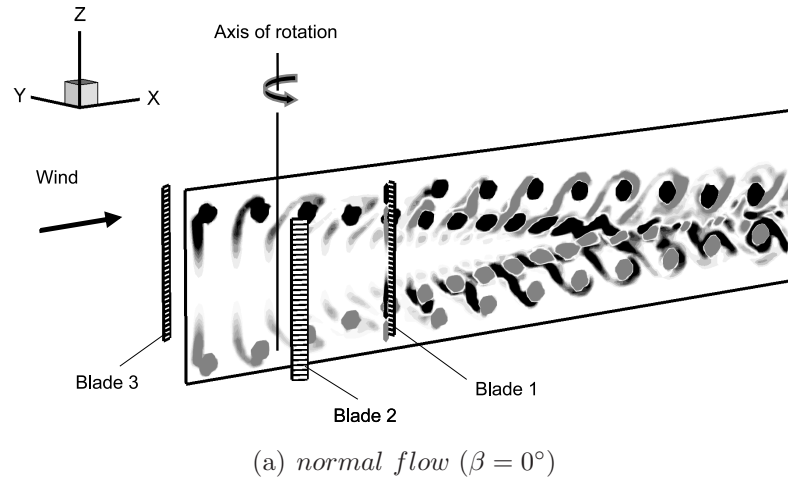


Figure 6.5: Computed vorticity field surrounding the straight-bladed vertical-axis wind turbine with $H/R = 1.2$ at $\lambda = 3.5$, represented using contours of the vorticity component that is perpendicular to a vertical plane that contains the axis of rotation of the turbine. Blade 1 is located at 270° azimuth.

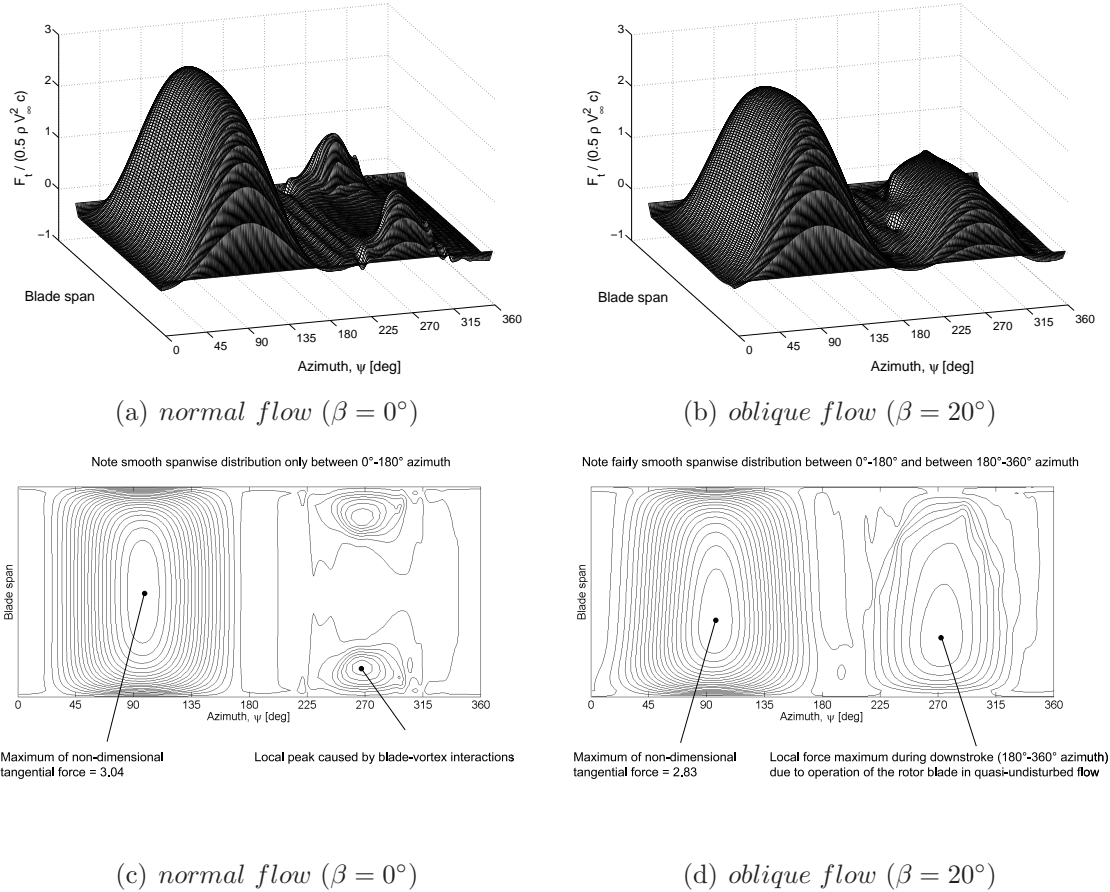


Figure 6.6: VTM-predicted variation with azimuth of the non-dimensional tangential force along the blade span of the straight-bladed vertical-axis wind turbine with $H/R = 1.2$ when operated at $\lambda = 3.5$ in normal flow ($\beta = 0^\circ$) and in oblique flow with $\beta = 20^\circ$.

The results presented in Figure 6.4 suggest also that the effect of wake skew on the power produced by the rotor becomes increasingly important the higher the tip speed ratio of the turbine. This can be explained in terms of the detailed mechanics of the vorticity distribution in the wake of the turbine. The vorticity that is produced by the rotor blades coalesces within the rotor area, as shown in Figure 4.6. At higher tip speed ratios, the vortical structures in the turbine wake convect more slowly downstream relative to the motion of the blades than at low tip speed ratios and the coalescence of the vorticity in the wake immediately behind the blades is more pronounced. Conversely, at lower tip speed ratios the wake is swept away from the rotational trajectory of the blades before significant coalescence can take place, and consequently the influence of

the wake on the loads produced on the blades is weaker compared to the situation at high tip speed ratio. The mutual interaction between the vortex filaments seems to be responsible for a nonlinearity in the trajectory of the wake that precludes overt use of a simple geometric model to account for the effects of wake skew on the performance of the turbine, however. This nonlinearity can be seen quite clearly in the trajectory of the vortices originating from the bottom of the rotor that are shown in Figure 6.5(b).

Importantly, the results presented in Figure 6.4 show that the efficiency of the vertical-axis wind turbines that were investigated in this study is not decreased significantly if the oblique flow angle is less than 20° - the power coefficient that is produced by the turbines in this range of oblique flow angles is even higher than in normal flow, particularly if they have a low height-to-radius ratio and are operated at high tip speed ratios. This is in distinct contrast to the performance of horizontal-axis configurations in off-design conditions. Indeed, a numerical study carried out by Coton and Wang [85] and experimental measurements taken by Ronsten *et al.* [86] showed that the performance of a horizontal-axis turbine always decreases when it is operated in yawed flow, in other words in conditions in which the wind vector is non-parallel to the axis of rotation of the rotor. Indeed, the horizontal-axis turbine that was investigated in these studies was 10% less efficient when operated at 20° yaw misalignment compared to when the wind was parallel to the rotor axis.

6.1.2 Blade Geometry

In normal flow, the power coefficients that are produced by both straight-bladed and curved-bladed vertical-axis turbines, as well as the forces that act on the rotor, vary cyclically within one revolution of the turbine, as shown in Chapter 5 of this dissertation. These cyclic loads cause vibrations that can generate noise and that can also lead to material fatigue of the turbine structure. The variation with azimuth of the power coefficient is reduced slightly in oblique flow conditions, as shown in Figures 6.7(a) and 6.7(b). This is because the larger second local peak in tangential force that is generated between 180° and 360° azimuth in oblique flow, as shown in Figure 6.6, results in a greater symmetry in the forces between the blades on the advancing and on the retreating sides of the rotor. The results presented in Figure 6.7(c) suggest that the power coefficient that is developed by the helically twisted configuration is relatively

steady over the entire azimuth, by comparison, irrespective of whether the turbine is operated in normal or oblique flow.

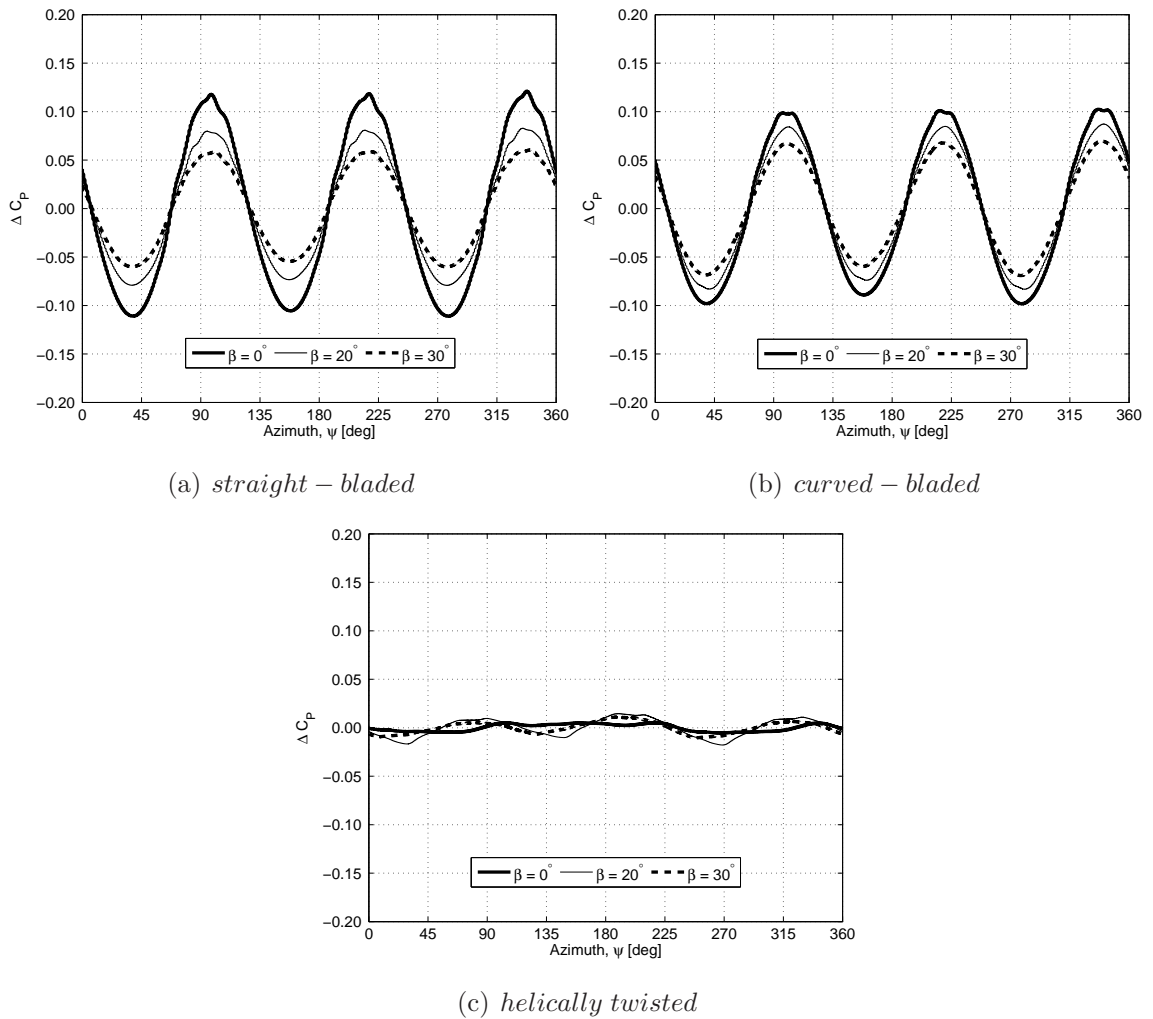


Figure 6.7: Influence of rotor geometry on the unsteady component of the VTM-predicted power coefficient of three different turbine configurations with $H/R = 3.0$ in normal flow and in oblique flow at $\lambda = 3.5$.

6.2 Unsteady Flow

Most experimental and numerical studies of the aerodynamic performance of vertical-axis wind turbines have been conducted with the rotors in *steady* wind conditions. This is either because of the inherent difficulties of wind tunnel experiments under unsteady wind conditions or because of the significant challenge that accurate simulation of the aerodynamics of vertical-axis wind turbines - in either steady or unsteady wind conditions - poses to numerical modelling techniques. Field tests of full-scale turbine configurations are only partially instructive since they do not allow the various mechanisms that cause any unsteadiness in turbine behaviour to be isolated and studied independently. Detailed analyses of the blade aerodynamic loading and the performance of vertical-axis wind turbines when operated in an *unsteady* wind, and thus in conditions that are more representative of real-world operation, are therefore scarce in the literature. Nevertheless Kang et al. [87] and Kooiman and Tullis [88] have conducted experimental studies of vertical-axis wind turbines in varying wind conditions and McIntosh [7] has performed a numerical investigation of the two-dimensional aerodynamics of an aerofoil in a planar, cyclic motion designed to emulate that of the mid-section of the blade of a vertical-axis wind turbine when exposed to unsteady onset flow. These studies suggest that the vertical-axis wind turbine is, potentially, well suited to operate in sites where wind conditions are characterised by frequent and rapid changes in direction and speed.

An ‘ideal’ vertical-axis wind turbine would always operate at the tip speed ratio for which the maximum efficiency is obtained. This would be done by adjusting the rotational speed of the rotor, when the wind speed changes, in order to keep a constant tip speed ratio. This control strategy is generally very difficult to implement in practice because of the inertia of the rotor and the response time that is associated with any practical control system. In all the simulations that are presented in this section, the rotational speed of the rotors was kept constant in order to isolate the aerodynamic effects that are introduced by the fluctuation in wind speed from the additional unsteady aerodynamic effects that will be introduced when the rotor accelerates or decelerates. This is consistent, in practical terms, with the behaviour of full-size rotors where the rotational speed cannot be made to respond rapidly to changes in wind speed.

By adopting the notation that was used by McIntosh [7], the variation in wind speed that is experienced by a vertical-axis wind turbine during a gust can be expressed in terms of a gust length

$$D_g = \frac{V_\infty}{f_c} \quad (6.1)$$

where V_∞ is the mean free stream velocity and f_c is the characteristic fluctuation frequency of the gust. The gust-induced unsteady aerodynamic effects that are encountered by a vertical-axis wind turbine with rotor radius, R , can then be characterised by a reduced gust frequency

$$k_g = \frac{2R}{D_g} = \frac{2Rf_c}{V_\infty} \quad (6.2)$$

Using the definition of the mean tip speed ratio, $\lambda_{mean} = \Omega R/V_\infty$, an expression for the number of rotor revolutions per gust can consequently be derived as

$$R_g = \frac{\lambda_{mean}}{\pi k_g} \quad (6.3)$$

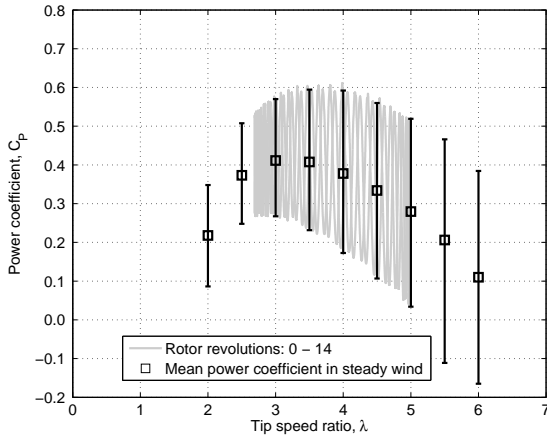
Based on experimental measurements in an urban area, Bertényi *et al.* [89] estimated that the highest frequency of the fluctuations with meaningful energy content in urban wind conditions is of the order of 1Hz. In the present dissertation, results are presented for reduced gust frequencies $k_g = 0.08$ and $k_g = 0.74$. A reduced gust frequency of $k_g = 0.74$ would correspond, for example, to conditions in which a generic urban wind turbine with radius 2m was operated at a mean wind speed of 5.4m/s and encountered a gust with a characteristic fluctuation frequency of 1Hz. This would thus correspond to the severest operating conditions that this turbine would be likely to encounter in the urban environment.

In the VTM simulations presented below, the free stream velocity was varied sinusoidally around a mean velocity that gives a tip speed ratio of $\lambda_{mean} = 3.5$. The reduced gust frequencies $k_g = 0.08$ and $k_g = 0.74$ give $R_g = 14$ and $R_g = 1.5$, respectively. The behaviour of each of the three different turbines is compared when the sinusoidal variation of the free stream velocity has two different amplitudes: $\Delta V/V_\infty = \pm 0.1$ and $\Delta V/V_\infty = \pm 0.3$. The assumption is made, within all the simulations presented below, that the gust field has infinite spatial extent.

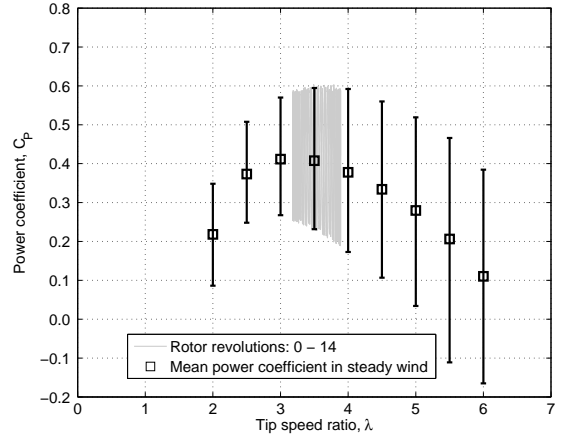
6.2.1 Power Coefficient

Figure 6.8 shows the variation of the power coefficients that are produced by the three different turbines in unsteady wind conditions with $R_g = 14$. Data is presented for fourteen rotor revolutions in order to show the behaviour of the turbine over one complete gust period. The instantaneous power coefficient is based on the instantaneous wind speed and is presented for the corresponding instantaneous tip speed ratio. The mean power coefficient that is produced by each turbine configuration in steady wind conditions is shown for comparison along with ‘error bars’ that denote the variation of the power coefficient over each turbine revolution in a steady wind, as described in Chapter 5 of this dissertation. The variation of the power coefficients produced by the turbines when subjected to the gust with $k_g = 0.08$ is almost identical to that which would be produced in equivalent steady wind conditions. Indeed, it can be inferred from the data that when the turbine is exposed to a gust with such a low reduced frequency, its response is essentially quasi-steady.

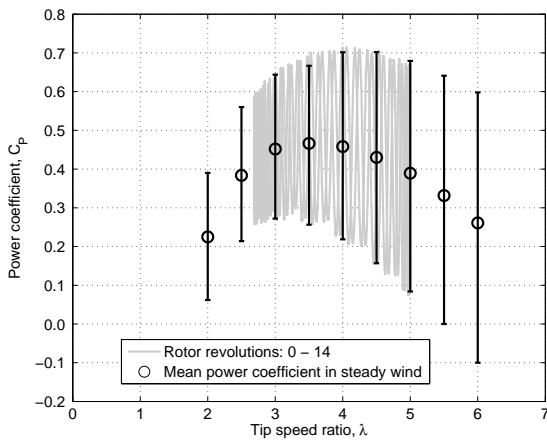
Figure 6.9 shows the variation of the power coefficients that are produced by the turbines in unsteady wind conditions with $R_g = 1.5$. Although the period of the gust, under these conditions, is equal to 1.5 rotor revolutions, data is presented for three rotor revolutions - this is the number of rotor revolutions that must elapse in order for the turbine and the gust to return into phase. For $\Delta V/V_\infty = \pm 0.1$, the aerodynamic behaviour of the turbines can again be inferred to be essentially quasi-steady since no significant deviation is apparent from the range of variations of the power coefficients that are produced by the turbines under steady wind conditions at the same tip speed ratio. Increasing the amplitude of the sinusoidal variation of the free stream velocity, however, results in small but notable deviations from the quasi-steady behaviour of each turbine. Importantly, the variation of the power coefficients that is caused by the continuous change in angle of attack on the blades as they revolve is far more significant than that which is induced by the unsteadiness in the wind conditions. This important inference is examined in more detail below.



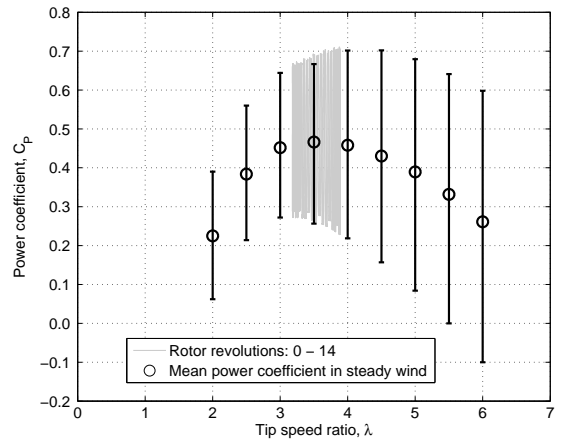
(a) *straight-bladed*, $\Delta V/V_\infty = \pm 0.3$



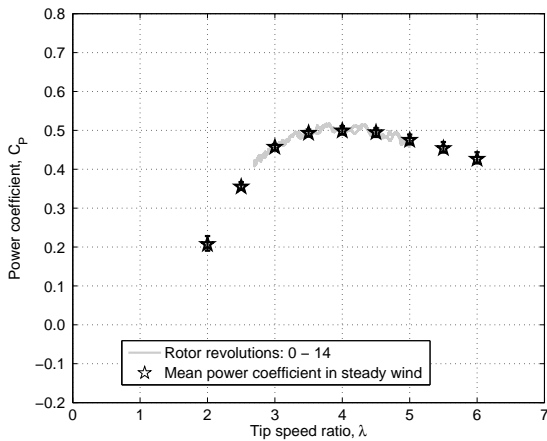
(b) *straight-bladed*, $\Delta V/V_\infty = \pm 0.1$



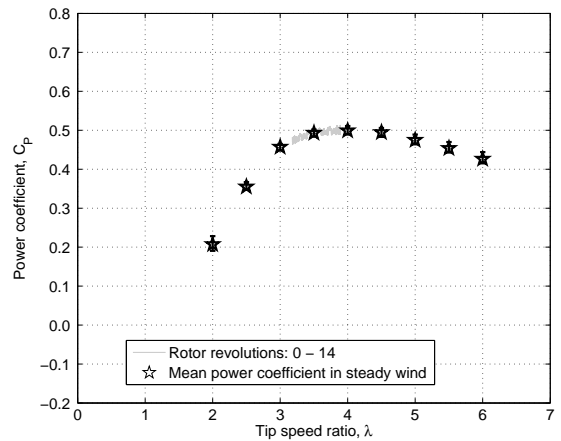
(c) *curved-bladed*, $\Delta V/V_\infty = \pm 0.3$



(d) *curved-bladed*, $\Delta V/V_\infty = \pm 0.1$

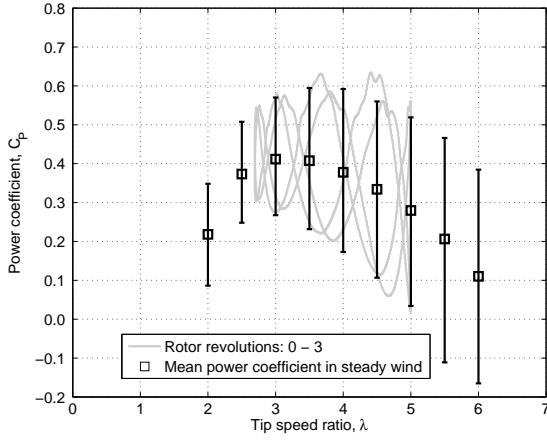


(e) *helically twisted*, $\Delta V/V_\infty = \pm 0.3$

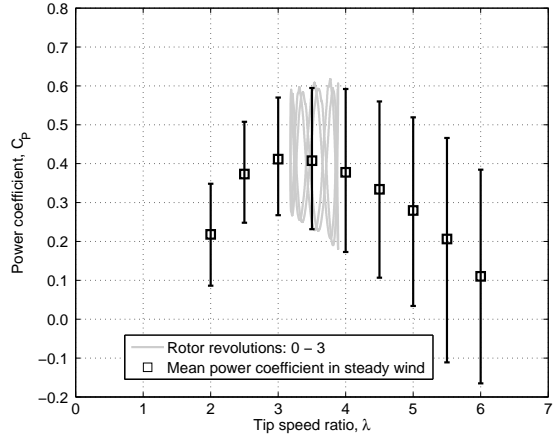


(f) *helically twisted*, $\Delta V/V_\infty = \pm 0.1$

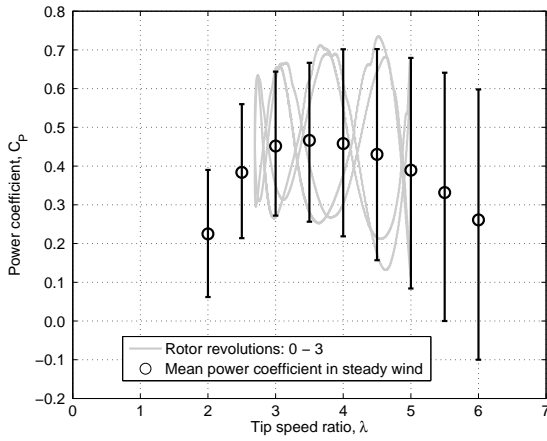
Figure 6.8: VTM-predicted variation of the power coefficients of three different turbine configurations when the rotors are operated at $R_q = 14$. Error bars denote the variation of the power coefficient during one rotor revolution in steady wind conditions.



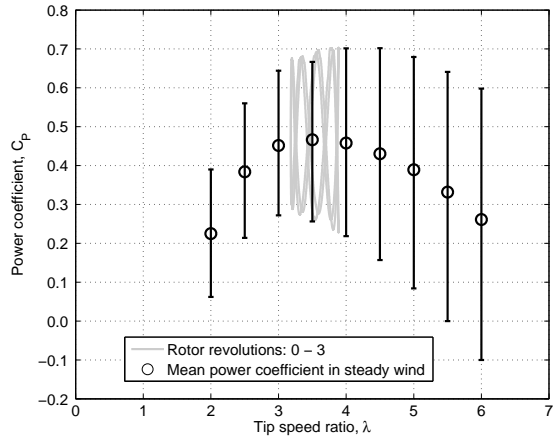
(a) *straight – bladed, $\Delta V/V_\infty = \pm 0.3$*



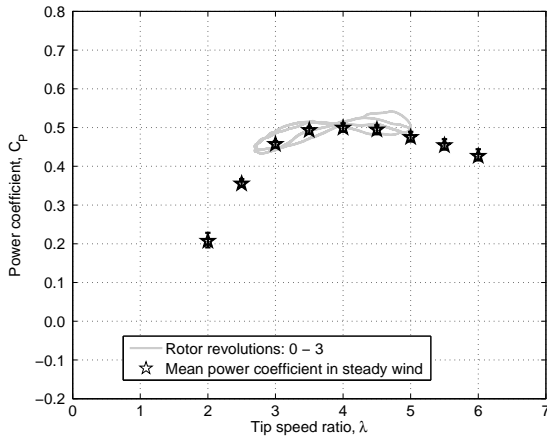
(b) *straight – bladed, $\Delta V/V_\infty = \pm 0.1$*



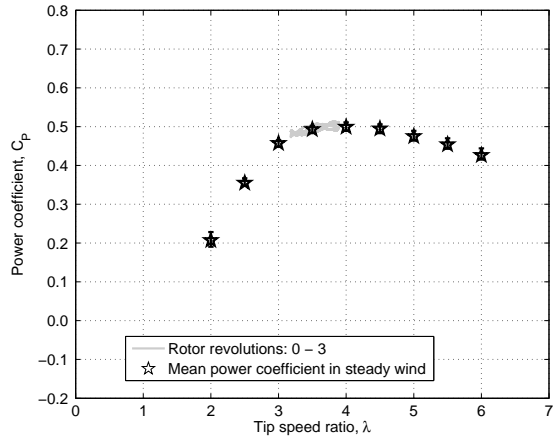
(c) *curved – bladed, $\Delta V/V_\infty = \pm 0.3$*



(d) *curved – bladed, $\Delta V/V_\infty = \pm 0.1$*



(e) *helically twisted, $\Delta V/V_\infty = \pm 0.3$*



(f) *helically twisted, $\Delta V/V_\infty = \pm 0.1$*

Figure 6.9: *VTM-predicted variation of the power coefficients of three different turbine configurations when the rotors are operated at $R_g = 1.5$. Error bars denote the variation of the power coefficient during one rotor revolution in steady wind conditions.*

A close-up of the variation of the power coefficient of each rotor when operated in unsteady wind conditions with $R_g = 1.5$ and for $\Delta V/V_\infty = \pm 0.3$ is shown in Figure 6.10 along with the temporal variation of the wind speed. The behaviour of the power coefficients in unsteady wind conditions is characterised by a hysteresis loop, indicated by the arrows in Figures 6.10(a), (b) and (c). The three dominant peaks per rotor revolution that characterise the variation of the power coefficients in steady wind conditions are still apparent, however. Interestingly, of the three turbines, the helically twisted configuration exhibits the highest relative deviation of the power coefficient in unsteady wind conditions from that in steady wind conditions. The amplitude of the variation of the power coefficient produced by the helically twisted configuration in unsteady wind conditions is much smaller, however, than that produced by either the straight- or the curved-bladed turbines.

As alluded to earlier, the ‘ideal’ vertical-axis wind turbine would maintain its tip speed ratio at that for maximum power by adjusting its rotational speed to match any changes in wind speed. Since the rotational speed of the turbines in this study was kept constant as the wind speed was varied, the mean power coefficients that they produce can be expected to be smaller than those obtained at their optimum tip speed ratio. Figure 6.11 shows the mean power coefficient that is produced by each turbine in unsteady wind conditions as a percentage of that generated by an ‘ideal’ turbine operating at constant tip speed ratio. In other words, the figure indicates the loss that would be experienced by a ‘real’ turbine that has an inertia that is too high or a response time that is too long to adjust the rotational speed of the rotor to variations in the wind speed. The gust frequency has only a very small effect on the deviation of the power coefficient from the optimum value. Interestingly, Figure 6.11 shows that, at the lower amplitude of the sinusoidal variation of the wind speed that was investigated, almost 100% of the mean power coefficient of the ‘ideal’ turbine is obtained. Only at higher amplitudes of the sinusoidally varying wind speed do notable reductions in the mean power coefficients occur.

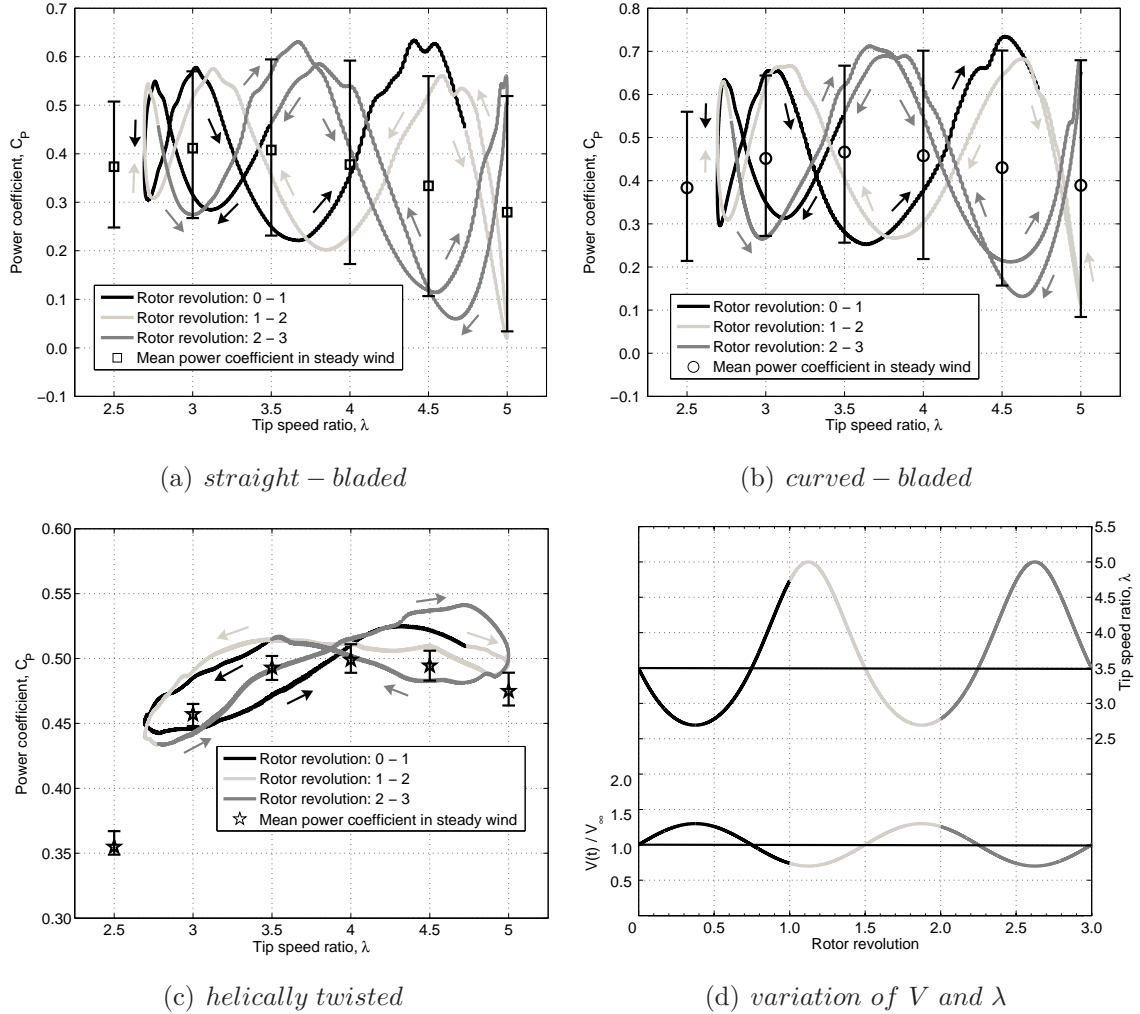


Figure 6.10: VTM-predicted variation of the power coefficients for the straight-bladed and curved-bladed turbines and the turbine with helically twisted blades when the rotors are operated in unsteady wind conditions with $\Delta V/V_\infty = \pm 0.3$ and $R_g = 1.5$ (which corresponds to $k_g = 0.74$ at $\lambda = 3.5$). Error bars denote the variation of the power coefficient during one rotor revolution in steady wind conditions.

Interestingly, the straight- and curved-bladed configurations exhibit greater losses in performance than does the helically twisted configuration. This can be explained once it is realised that the variation of the power coefficient with tip speed ratio of either the straight- or curved-bladed turbines has a steeper gradient than the helically twisted configuration at mid-operating range, as shown in Figures 6.8 and 6.9 for steady wind conditions. Although the key rotor parameters of the three turbines are identical, the difference in their aerodynamic design leads, naturally, to different shapes of the power curves even if they are operated at the same tip speed ratio, as explained in more detail

in Chapter 5 of this dissertation. It can thus be concluded that a turbine that features a steep gradient in its variation of power coefficient with tip speed ratio is more prone to power losses if the rotor speed is kept constant in unsteady wind conditions than a turbine that features a shallower gradient in its $C_P - \lambda$ curve.

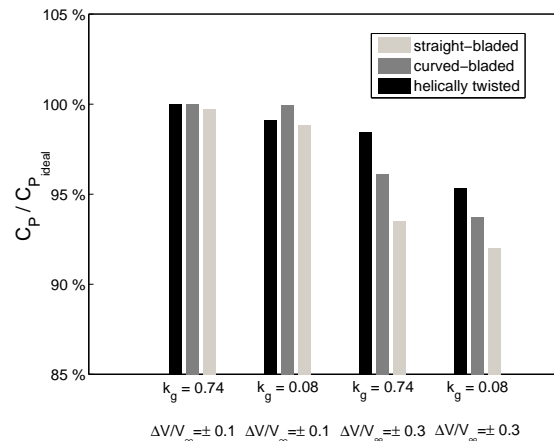
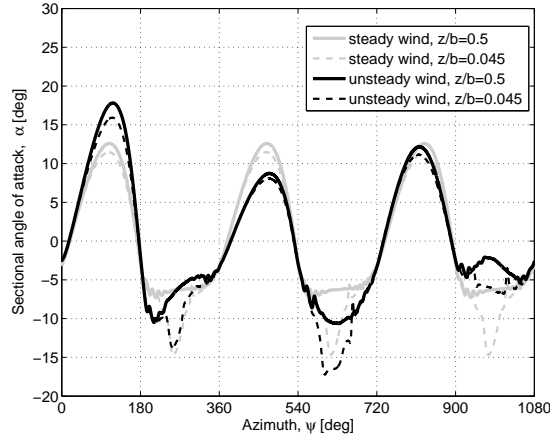


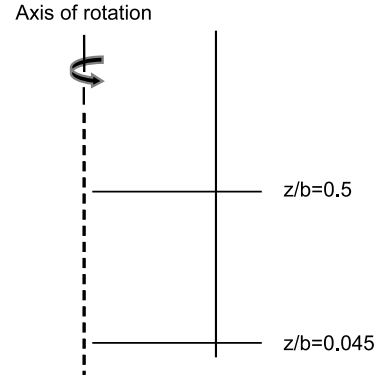
Figure 6.11: Mean power coefficient produced by the turbine configurations in unsteady wind conditions - as a percentage of that generated by an ‘ideal’ turbine with constant tip speed ratio.

6.2.2 Blade Aerodynamic Loading

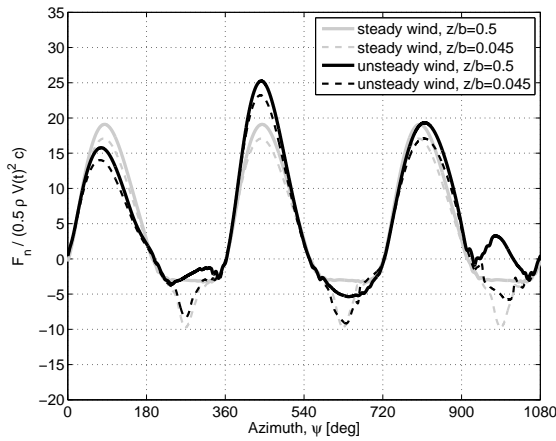
The effect of unsteady wind conditions on the performance of the three different vertical-axis wind turbines is revealed in more detail by analysing the aerodynamic loading on the blades of the rotors. Figure 6.12 shows the aerodynamic angle of attack and the sectional normal and tangential forces that are generated at two different locations along the reference blade of the straight-bladed vertical-axis wind turbine during the three rotor revolutions that correspond to a single gust cycle. The figure shows a comparison between the angle of attack and the sectional forces that are produced in unsteady wind conditions and those generated in steady wind conditions. The forces are non-dimensionalised by the instantaneous wind speed in Figures 6.12(c) and (d), whereas Figures 6.12(e) and (f) show forces that are non-dimensionalised by the mean wind speed. The first set of curves are useful in order to compare qualitatively the blade aerodynamic loading produced in unsteady wind conditions to that produced in steady wind conditions, while the second set of curves provides a better gauge of the loads that are transmitted into the structure of the turbine.



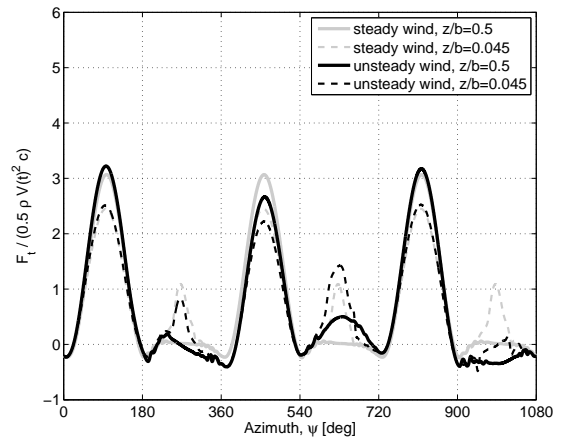
(a) angle of attack



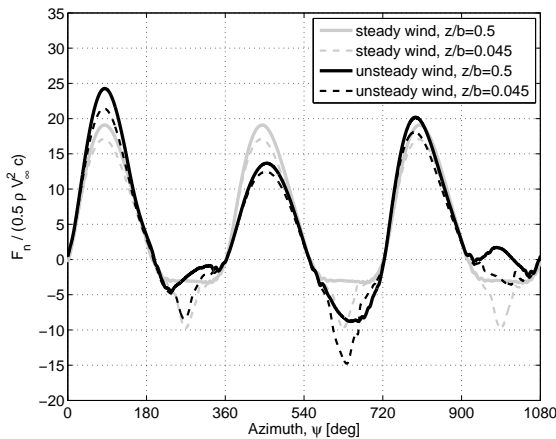
(b) location



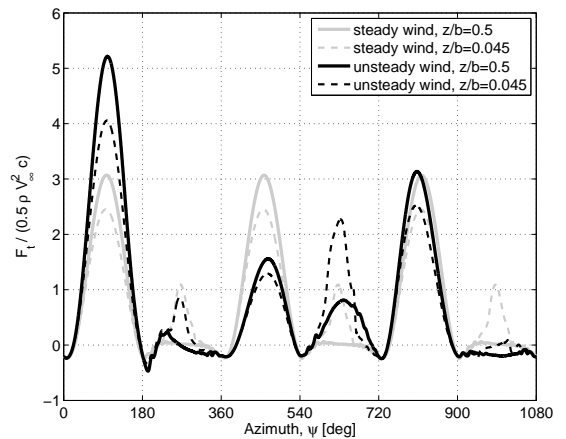
(c) normal force, nondim. by $V = V(t)$



(d) tangential force, nondim. by $V = V(t)$



(e) normal force, nondim. by V_∞



(f) tangential force, nondim. by V_∞

Figure 6.12: VTM-predicted aerodynamic angle of attack and sectional forces in steady and unsteady wind conditions (with $k_g = 0.74$ and $\Delta V/V_\infty = \pm 0.3$) over three complete rotor revolutions at two different spanwise locations along the reference blade of the straight-bladed turbine.

In steady wind conditions, the variation of the angle of attack, and thus the variation of the sectional aerodynamic loading, features a peak close to 90° azimuth during each rotor revolution. These peaks are the origin of the distinct peaks in the variation of the power coefficient that were shown in Figure 5.11(a). When the rotor is operated in steady wind conditions, both the angle of attack and the sectional forces show impulsive perturbations near to the tip of the blade as they rotate past 270° azimuth. These impulsive perturbations are induced by interactions between the blade and a region of concentrated vorticity in the wake of the turbine that consists, predominantly, of vorticity that was trailed in previous revolutions, as shown in Figure 5.14.

In unsteady wind conditions, the sectional angle of attack and the sectional loading show comparable features to those observed in steady wind conditions - for instance, the dominant peak close to 90° azimuth during each revolution and the perturbations due to blade-vortex interactions are still evident. As one might expect, the variation with azimuth of the sectional forces and the angle of attack differs from rotor revolution to rotor revolution when the turbine is operated in unsteady conditions. Interestingly, interactions of different strength between the blade and the tip vortices, reflected in different magnitudes of the blade aerodynamic loading close to 270° and 630° azimuth, occur within the first two rotor revolutions when the turbine is operated in unsteady wind conditions. Any significant perturbations to the angle of attack and the sectional aerodynamic loading on the blade are absent during the third revolution, close to 990° azimuth, however. These characteristics are explained in the following section in terms of the vorticity distribution within the wake that is produced by the rotor in unsteady wind conditions.

6.2.3 Wake Structure

The flow field that surrounds the straight-bladed turbine in steady wind conditions was shown in Figures 5.14(a) and 5.15(a) by visualising the vorticity distribution on vertical and horizontal planes that are immersed within the wake of the rotor. Following the same approach, the wake that is generated by the straight-bladed turbine in unsteady wind conditions is shown in Figures 6.13 and 6.14. The evolution of the wake is illustrated over the three rotor revolutions that correspond to a single gust period. The period is shown over a sequence of azimuth positions that are 90° apart. Figure 6.15

shows the three-dimensional flow field that surrounds the rotor, over a sequence of azimuth positions that are one rotor revolution apart, by plotting a surface within the wake on which the vorticity has constant magnitude.

The behaviour of the wake reflects the periodic variation of the wind speed that was applied to the turbine. As a result of the oscillations in the onset wind speed, the distances between the individual tip vortices within the wake vary along its length, as can be seen clearly in Figures 6.13(a), (e) and (i). The reason for the presence of significant perturbations to the sectional angle of attack and the sectional loading on the blade during the first and second rotor revolution, but not during the third revolution (see Figure 6.12), is revealed in the vorticity distribution in the wake that is depicted in Figures 6.13(d), (h) and (l). The uneven spacing between the tip vortices that is induced by the variation of onset wind speed allows the blade, within the third revolution, to pass through the wake without significant interaction with any of the tip vortices. This is not the case during the first and second revolutions, where the more dense distribution of tip vortices within the wake inevitably results in stronger blade-vortex interactions. Downstream of the rotor, the effects of the mutual interactions between the tip vortices that are trailed in the upwind portion of the rotor revolution and those that are trailed in the downwind portion of the revolution are apparent. These interactions yield patches of merged vorticity within the wake, and these features grow in spatial extent as they convect further downstream. Although similar regions of merged vorticity can also be observed within the flow field in steady wind conditions, as shown in Figure 5.14(a), the vorticity distribution within the wake that is produced by the rotor in unsteady wind conditions is somewhat more disordered. Comparable structures within the wake to those seen in the vertical plane can also be seen on the horizontal plane through the wake shown in Figure 6.14. Interestingly, Figure 6.14 shows the wake structure to possess significant lateral asymmetry - the regions of clumped vorticity exist predominantly on the side of the turbine on which the leading edges of the blades face the wind. This asymmetry results primarily because the vorticity that is shed during the portion of the rotor revolution when the leading edges of the blades face the wind, is stronger than that which is shed when the blade moves with the wind. This results in a stronger mutual interaction between the vortices during the portion of the rotor revolution when the leading edges of the blades face the wind and hence in a tendency for these vortices to clump into larger structures more

quickly. The complexity of the three-dimensional wake that is generated by the rotor is clearly apparent in Figure 6.15 where the mutual interaction between the shed and the trailed vorticity from the blades causes the individual vortices to break up to form a complex system of interwoven vortex filaments several rotor diameters downstream of the turbine.

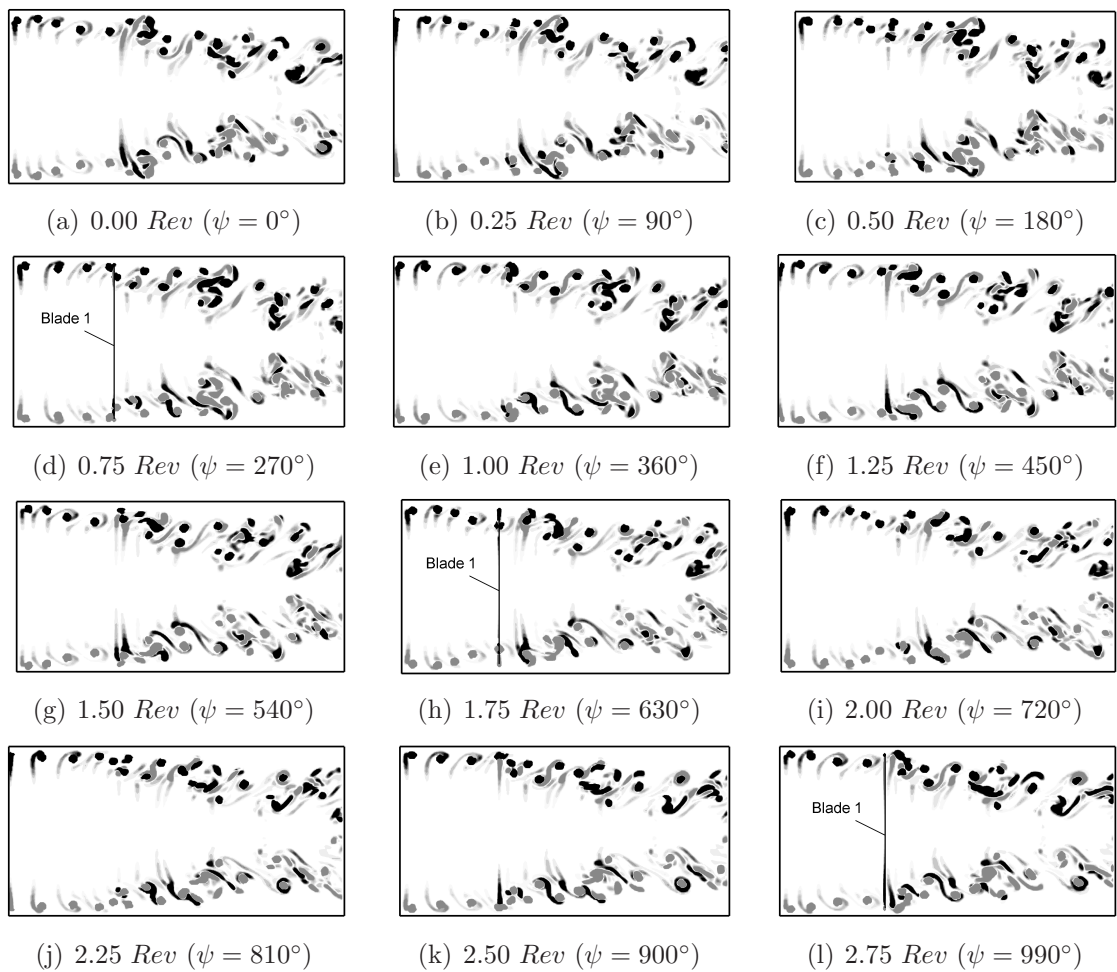


Figure 6.13: Computed vorticity field surrounding the straight-bladed turbine in unsteady wind conditions (with $k_g = 0.74$ and $\Delta V/V_\infty = \pm 0.3$), represented using contours of vorticity on a vertical plane that contains the axis of rotation of the turbine and that is aligned with the wind direction.

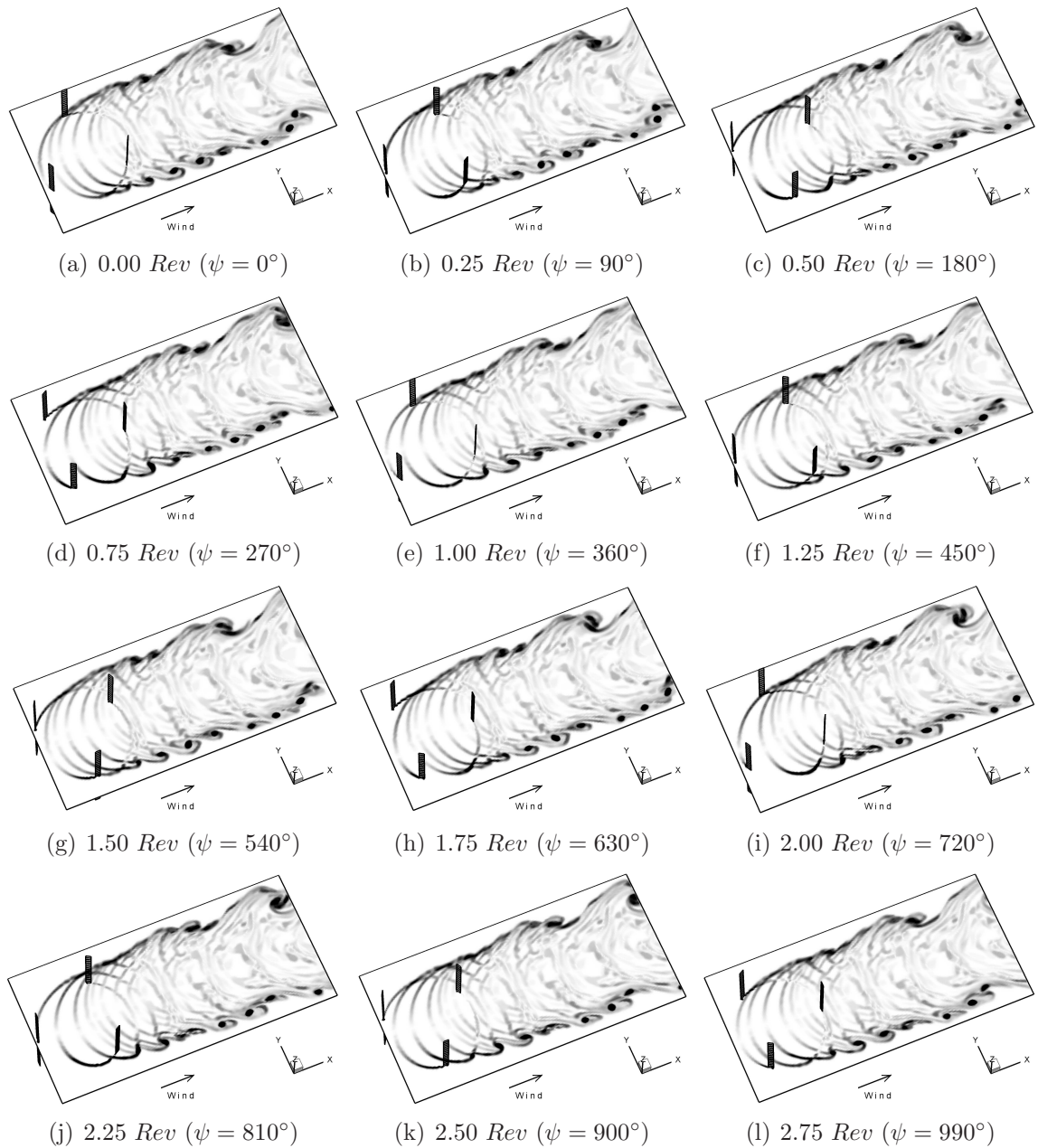


Figure 6.14: *Computed vorticity field surrounding the straight-bladed turbine in unsteady wind conditions (with $k_g = 0.74$ and $\Delta V/V_\infty = \pm 0.3$), represented using contours of vorticity on a horizontal plane that intersects with the mid-spans of the rotor blades.*

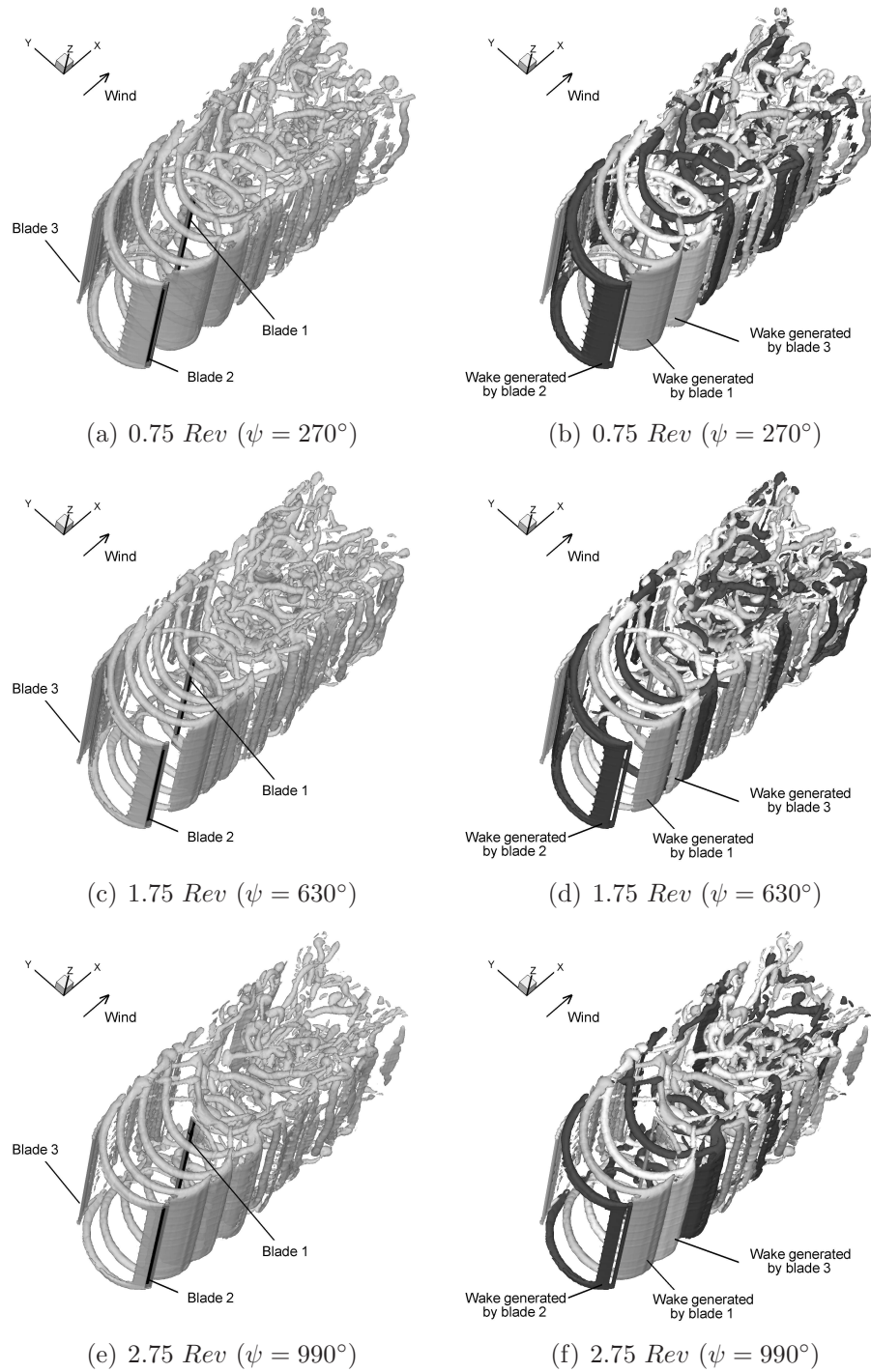


Figure 6.15: Computed vorticity field surrounding the straight-bladed turbine in unsteady wind conditions (with $k_g = 0.74$ and $\Delta V/V_\infty = \pm 0.3$), represented by an isosurface of vorticity. The subfigures on the left show the entire wake that is generated by the rotor, whereas the different colours in the subfigures on the right represent the vorticity that is developed by the individual blades of the turbine.

6.3 Turbine-Turbine-Interaction

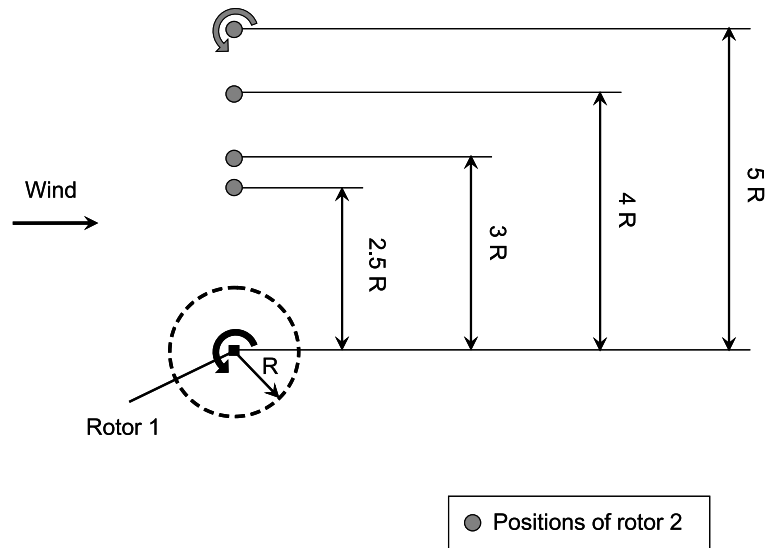
Mertens [90] discussed several concepts for the most efficient use of vertical-axis wind turbines in the built environment - including the integration of vertical-axis rotors into buildings and the construction of clusters that consist of several individual turbines. Such clustering might, under certain wind directions, lead to any one of the turbines operating within the wake of one of the other turbines. Little is known about the aerodynamic effect of wake impingement on the blade aerodynamic loading and performance of a vertical-axis wind turbine, and hence there is little information available that can help planners decide on optimal layout of multiple turbines in any given scenario.

Historically, several computational methods have been used to study the aerodynamic interference between two or more vertical-axis wind turbines. Schatzle *et al.* [91] used a modification of the vortex model developed by Strickland *et al.* [26] in order to study the aerodynamic interaction between two curved-bladed vertical-axis wind turbines. Rajagopalan *et al.* [92], McIntosh [7] and Durrani *et al.* [93] analysed interactions between individual rotors that were represented by two-dimensional aerofoils in a planar, cyclic motion designed to emulate that of the mid-section of the blade of a vertical-axis wind turbine. These studies showed that the performance of a vertical-axis turbine is, not surprisingly, reduced when it is operated in the wake that is produced by another rotor. These investigations also indicated, however, that a rotor that is located downwind or parallel to another rotor might, under certain conditions, produce a higher power coefficient than a single, isolated rotor.

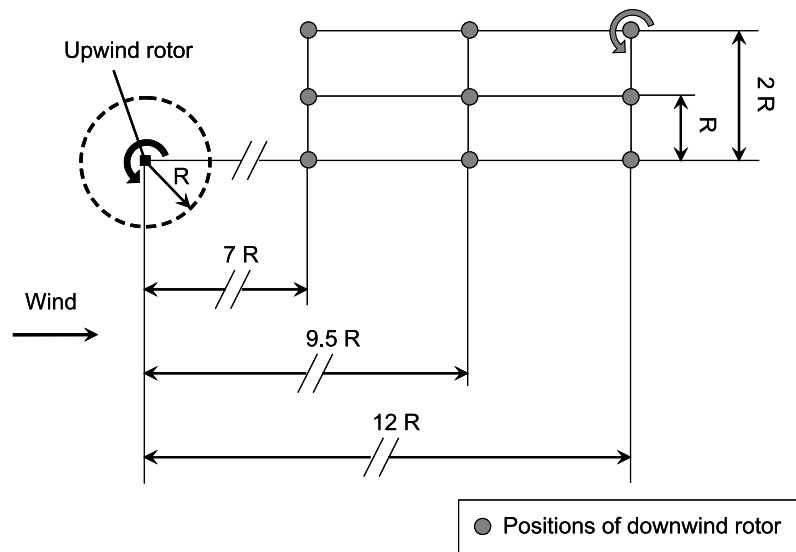
According to the author's knowledge, there have been no publications in the literature in which the full three-dimensional flow field surrounding two vertical-axis wind turbines has been modelled accurately from first principles. This is most likely because many CFD-based techniques suffer from the adverse effects of numerical dissipation, rendering these computations very difficult. Indeed, numerical dissipation is an inherent feature of many computational approaches that are based on the primitive variable formulation of the Navier-Stokes equation. As a result, the vorticity within the wake dissipates 'artificially' rather than through the proper physical process of vortical instability. Several methods can be used to alleviate the adverse effects of numerical dissipation in these computations, such as refinement of the computational grid or

higher-order discretisation of the governing equations. Yet the very large number of cells that is necessary to model accurately the aerodynamic interaction between two or more rotors, or the computational overhead associated with higher-order methods, usually results in very high computational costs when following this strategy. The accurate prediction of the dynamics of the wake that is produced by a vertical-axis turbine is essential if the aerodynamic interference between two rotors, and in particular the effect of wake impingement on rotor performance, is to be properly captured in numerical simulations. One of the prime features of the VTM is its ability to portray accurately the evolution of the turbine wake as it develops well downstream of its origin on the blades of the rotor. The VTM has thus been used to study the performance of two straight-bladed turbines, the design of which was described in Chapter 5 of this dissertation, when they are operated both in a *parallel* arrangement, in which the rotors are only separated from each other in crosswind direction, and in an *upwind-downwind* arrangement, in which they are separated from each other in the streamwise and crosswind directions, as shown in Figure 6.16. In order for the underlying physics of the mutual aerodynamic interference between vertical-axis wind turbines to be most readily understood, the problem is simplified by studying the interactions between only two turbines.

Passola Parcerissa [94] showed in a parametric study, using the VTM, that the various different possible combinations of rotational direction of two vertical-axis rotors that are operated in either a parallel or in an upwind-downwind arrangement only marginally affect the performance of each individual rotor. In the present dissertation, results are thus only shown for rotors that have the same rotational direction (counterclockwise when viewed from above in all cases). All the rotors were operated at a tip speed ratio of 3.5. In all parallel and upwind-downwind arrangements, the reference blades of the rotors were at identical azimuth positions at all times - in other words, all the rotors were in phase. The distance between the rotors is defined as the distance between their axes of rotation. The aerodynamics and wake dynamics of the rotors when operated in a parallel arrangement are described in the following section, whereas Section 6.3.2 shows results for the rotors when they are operated in an upwind-downwind arrangement. VTM predictions are also presented for an isolated, single rotor - this rotor is identical to the straight-bladed turbine described in Chapter 5 of this dissertation and is used as the reference rotor against which the performance of the rotors in the various interacting configurations is compared.



(a) parallel arrangement



(b) upwind – downwind arrangement

Figure 6.16: Relative locations of the straight-bladed vertical-axis wind turbines (a) in a parallel and (b) in an upwind-downwind arrangement.

6.3.1 Parallel Arrangement

Figure 6.17 shows the ratio of the power coefficient that is produced by each of the two rotors, when operated in a parallel arrangement, to the power coefficient that is produced by the single, isolated reference rotor. A small but notable increase in power coefficient is produced by each of the two rotors, compared to that which is produced by the reference rotor. This is irrespective of the crosswind separation between the rotors. As might be expected from very simple aerodynamic considerations, the increase in power coefficient is most pronounced when the distance between the rotors is smallest.

Figure 6.18 shows the variation with azimuth of the power coefficients that are produced by rotor 1, rotor 2 and the reference rotor for the smallest and the largest crosswind separations between the rotors. The figure shows that the oscillations in the power coefficient that are produced by rotor 1 and rotor 2 are somewhat reduced compared to those produced by the reference rotor. Furthermore, Figure 6.18(a) indicates that the variation of the power coefficient that is produced by each of the two rotors in a parallel arrangement is slightly phase-shifted compared to that of the reference rotor. Not surprisingly, the influence of each rotor on the performance of the other rotor becomes weaker as the crosswind separation between the rotors is increased, as shown in Figure 6.18(b). Indeed, the variation of the power coefficient with azimuth is almost the same as that of the reference rotor when the rotors are separated from each other by the largest distance at which simulations were carried out in the present study.

The reasons for the difference in the variation with azimuth of the power coefficient, and the associated higher efficiency, produced by a rotor when operated in parallel with another, compared to that of the same rotor when operated in isolation, is revealed in the figures below. Figure 6.19 shows the flow fields surrounding two rotors, as visualised by plotting contours of vorticity on a horizontal plane through the rotor centres. The flow fields are shown for two different crosswind separations between the rotors. Figure 6.20 depicts the three-dimensional flow fields surrounding the same configurations, as visualised by plotting an isosurface of vorticity in the flow.

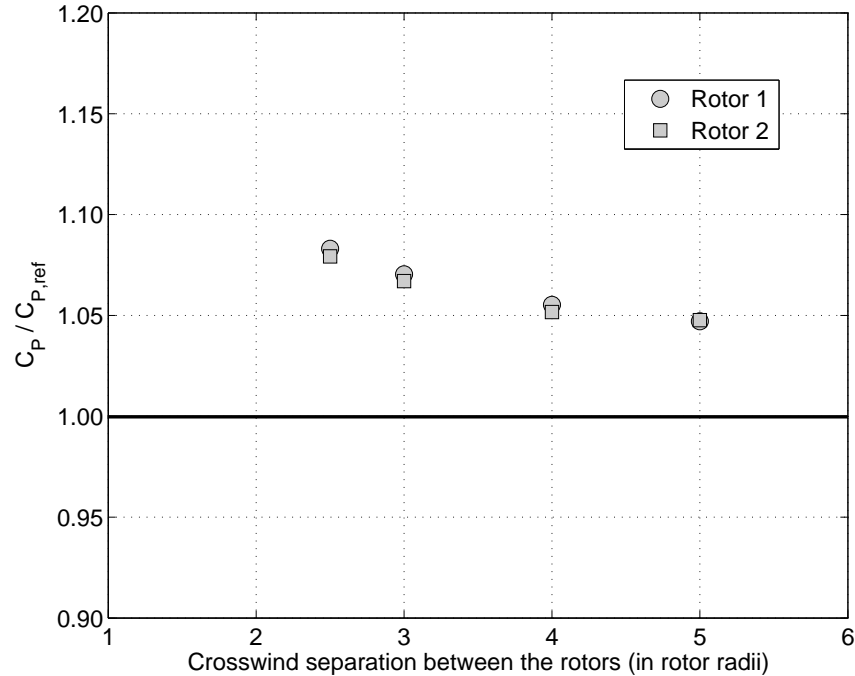


Figure 6.17: *VTM-predicted ratio of the power coefficient that is produced by each of the rotors in a parallel arrangement to the power coefficient that is produced by one of the rotors in isolation.*

The shed vorticity that is produced by a vertical-axis wind turbine causes a slight lateral divergence of the wake that is generated by the rotor, as shown in Figure 5.15(a) for a single, isolated straight-bladed turbine. Figure 6.19(a) shows that the presence of a second rotor results in the wake that is produced by the first to be somewhat constrained in its lateral expansion compared to the situation for a single, isolated rotor. This suggests that higher local velocities are present in the wake of the rotors, particularly in the constrained flow field in the region where the wakes of the two rotors are closest to each other. This effect is comparable to that created when a single vertical-axis rotor is operated close to the walls of a wind tunnel or a tow tank, as described by Alidadi and Calisal [95], amongst others, or when a vertical-axis rotor is operated within a duct.

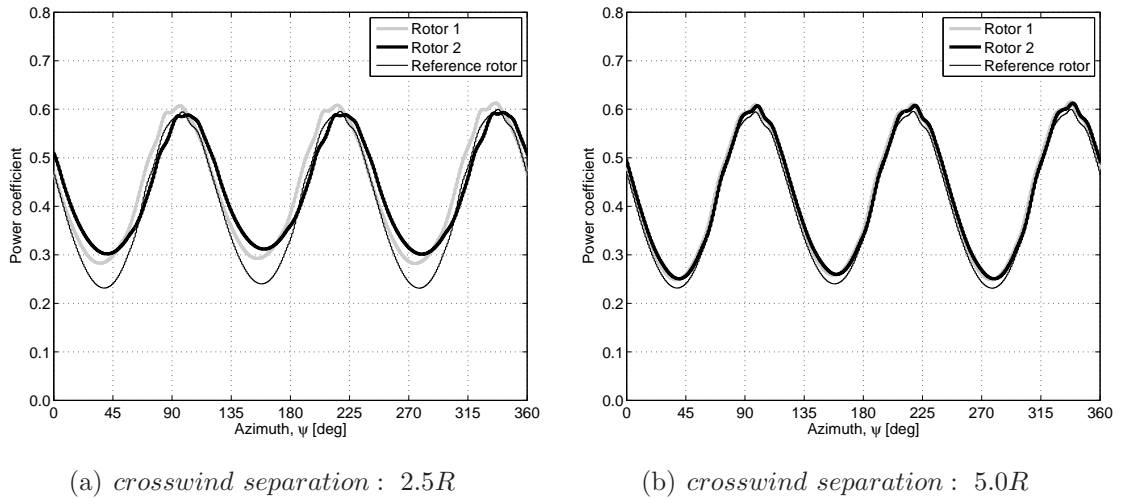


Figure 6.18: VTM-predicted variation with azimuth of the power coefficient that is produced by the reference rotor and those produced by the rotors in a parallel arrangement at two different crosswind separations.

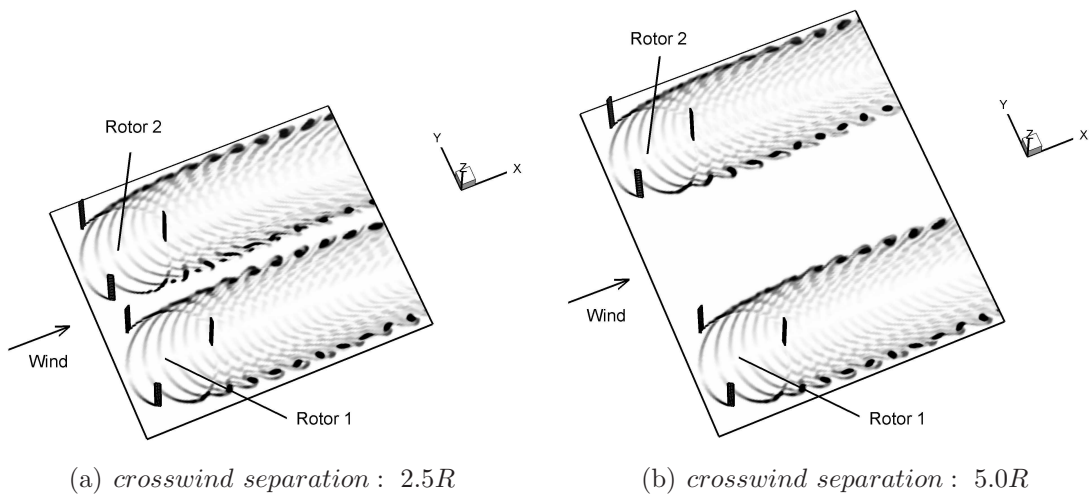


Figure 6.19: VTM-predicted flow fields surrounding the straight-bladed turbines when they are operated in a parallel arrangement at two different crosswind separations, represented using contours of vorticity on a horizontal plane that intersects with the mid-spans of the rotor blades.

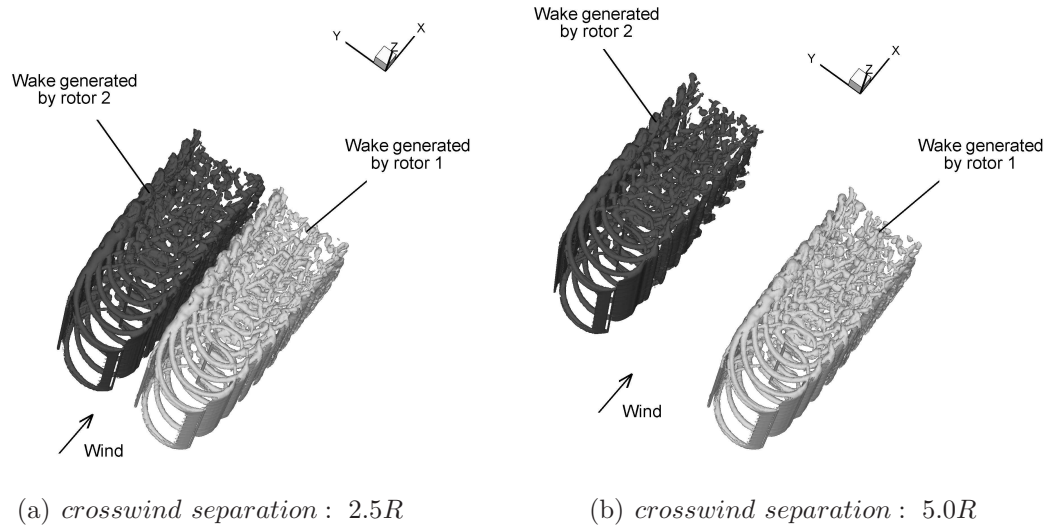
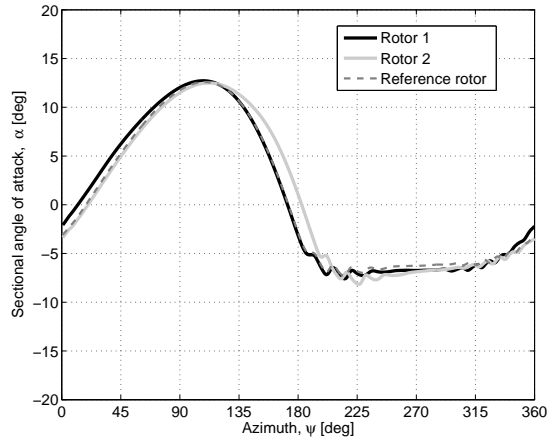


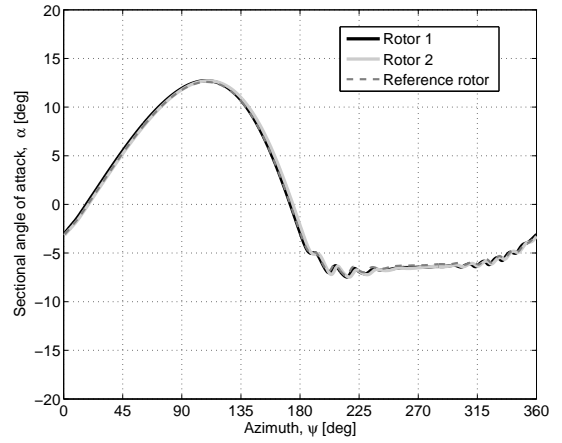
Figure 6.20: VTM-predicted flow fields surrounding the straight-bladed turbines when they are operated in a parallel arrangement at two different crosswind separations, visualised by plotting an isosurface of vorticity.

Figure 6.21 compares the VTM-predicted variation with azimuth of the blade aerodynamic loading and the aerodynamic angle of attack at the mid-spans of the reference blades of the two rotors in a parallel arrangement to those of the reference rotor. Figures 6.21(a), (c) and (e) show that the angle of attack and the aerodynamic loading that are generated on the blades of rotor 1 are increased slightly between 0° and 90° azimuth compared to those produced by the reference rotor. The angle of attack and the aerodynamic loading generated on the blades of rotor 2, in contrast, are higher between 90° and 180° azimuth. This is simply because the influence of rotor 2 is strongest, and thus the increase in the local velocity, compared to the situation for an isolated rotor, is highest, when the blades of rotor 1 are closest to rotor 2 - this is the case when the blade passes between 0° and 90° azimuth. In contrast, the blades of rotor 2 are closest to the wake that is produced by rotor 1 when they are between 90° and 180° azimuth.

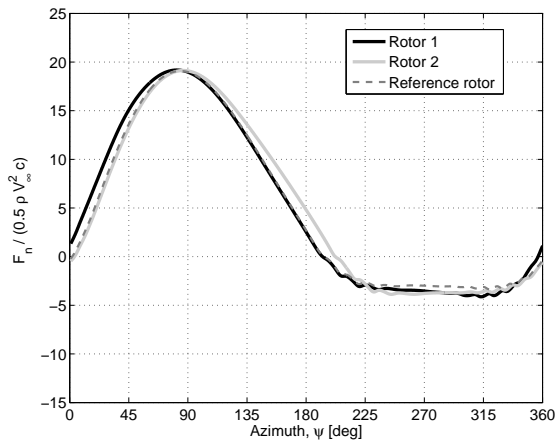
6.3 Turbine-Turbine-Interaction



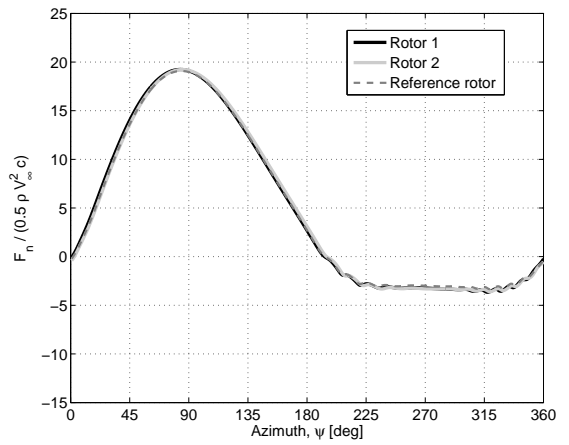
(a) angle of attack, crossw. sep. : $2.5R$



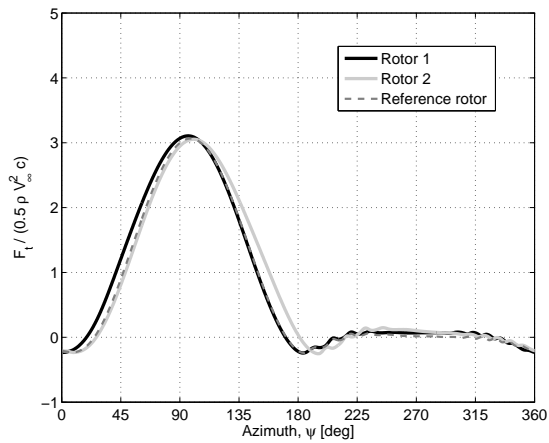
(b) angle of attack, crossw. sep. : $5.0R$



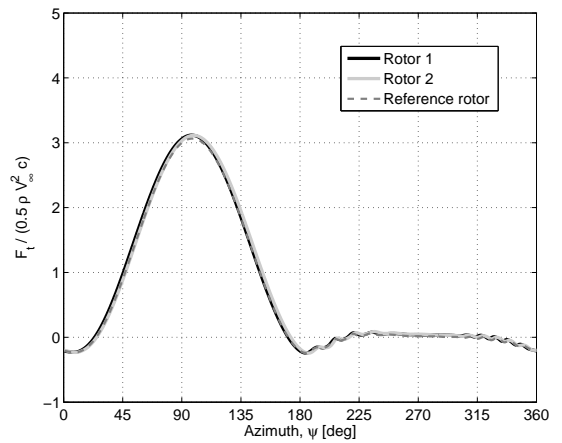
(c) normal force, crossw. sep. : $2.5R$



(d) normal force, crossw. sep. : $5.0R$



(e) tangential force, crossw. sep. : $2.5R$



(f) tangential force, crossw. sep. : $5.0R$

Figure 6.21: VTM-predicted variation with azimuth of the aerodynamic angle of attack and the loading at the mid-span of the blade of the reference rotor and those produced by the rotors in a parallel arrangement.

This observation is important since it suggests that the increase in efficiency of a vertical-axis wind turbine that is operated in a parallel arrangement is a result of two interrelated effects. Firstly, each rotor operates - at least partially - in a flow with higher local velocity, and thus in a flow with higher kinetic energy content, than that of the free stream. Secondly, the velocity component that is induced by the presence of the wake of another rotor results in an increase in angle of attack on the blades, and consequently in an increase in the non-dimensional forces on the blades and thus in the blade aerodynamic loading. It should also be noted that the small increase in local velocity yields a small decrease in effective tip speed ratio. It is thus not surprising that the tip speed ratio at which the maximum power coefficient is produced by a vertical-axis wind turbine is somewhat different when it is operated in parallel with another rotor compared to when it is operated in isolation. Indeed, McIntosh [7] showed that the tip speed ratio at which the maximum power coefficient is produced by a vertical-axis rotor is higher when it is operated in a parallel arrangement than when it is operated in isolation.

6.3.2 Upwind-Downwind Arrangement

Figure 6.22 shows the ratio of the power coefficients that are produced by the downwind rotor in an upwind-downwind arrangement to the power coefficient that is produced by the single, isolated reference rotor. It is clear that the downwind rotor, when it is fully immersed within the wake that is generated by the upwind rotor, produces a much lower power coefficient (squares in Figure 6.22) than that of the reference rotor. This is simply because of the reduced effective wind velocity that is encountered by the downwind turbine in this arrangement. Figure 6.23 shows the flow fields surrounding the two straight-bladed turbines in an upwind-downwind arrangement when at various streamwise and crosswind separations. The flow fields are visualised by plotting a surface within the flow on which the vorticity has constant magnitude. Figure 6.23(a) shows the wake that impinges on the downwind turbine, when it is a small distance downstream of the upwind rotor, to consist of a system of structured, interwoven vortex filaments. The wake that impinges on the downwind turbine, when it is a large distance downstream of the the upwind rotor, comprises a much larger number of small regions of clumped and disordered vorticity, as shown in Figure 6.23(b), rather than a

system of densely intermeshed vortical structures as in the case when the streamwise separation between the rotors is small. This is simply because the self-induced velocity of the trailed and shed vorticity produced by the rotor blades of the upwind rotor act to distort and break up the individual vortical filaments as the wake convects further downstream. The dissipation of the wake due to this inherent natural instability of the vortices results in a recovery of the velocity, and thus of the power coefficient produced by the downwind turbine, as the separation between the two turbines is increased. A similar trend in the variation of power coefficient of the downwind turbine with streamwise separation between the upwind and downwind rotors is apparent when the downwind rotor is operated only partially within the wake that is produced by the upwind rotor (circles in Figure 6.22).

Higher power coefficients are produced by the downwind turbine when it is only partially immersed within the wake that is generated by the upwind turbine compared to the situation when it is fully immersed within the wake of the upwind rotor. Importantly, the power coefficient that is produced by the downwind turbine, no matter whether it is fully or partially immersed within the wake that is produced by the upwind rotor, is always smaller than that which is produced by the single, isolated reference rotor. In contrast, the downwind turbine is shown to produce a higher power coefficient than the reference rotor when it is separated from the upwind turbine by one rotor diameter in the crosswind direction (triangles in Figure 6.22). The most likely cause of this phenomenon is that the downwind turbine encounters a somewhat higher effective local velocity outside of the wake of the upwind turbine in this configuration. This effect is thus comparable to that when the turbines are operated in a parallel arrangement, as described above. Indeed, Figure 6.25(c) and, particularly, Figure 6.24(c) show the contraction of the wake of the upwind rotor as it is constrained in its lateral expansion as it passes by the downwind rotor. This suggests that a higher local velocity than the undisturbed free stream velocity is present in this region of the flow field. It can therefore be concluded that a higher power coefficient can be produced by the downwind turbine when the crosswind separation between the two turbines is just large enough to avoid direct impingement on the downwind turbine of the wake that is produced by the upwind rotor.

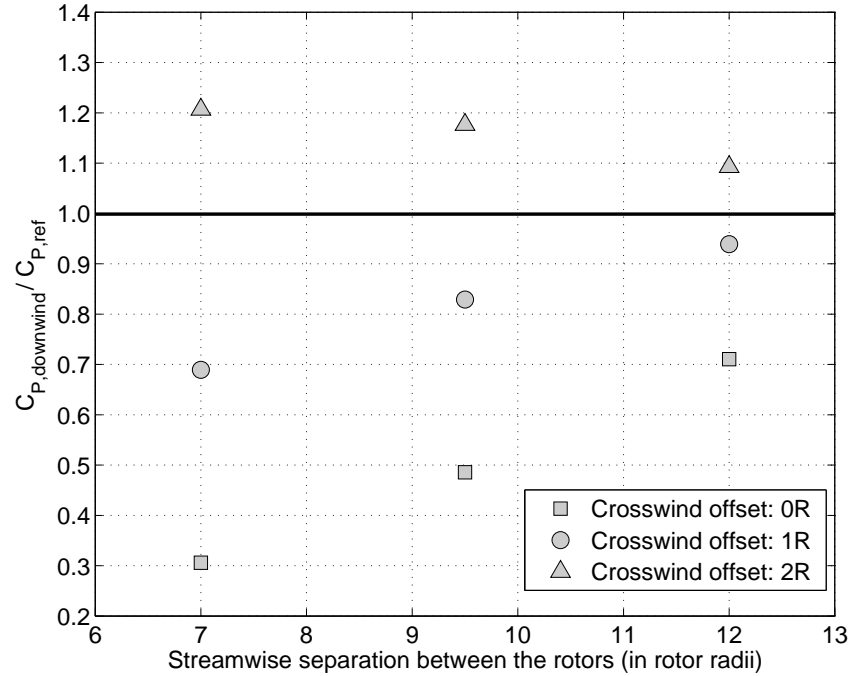


Figure 6.22: *VTM-predicted ratio of the power coefficient that is produced by the downwind rotor in an upwind-downwind arrangement to the power coefficient that is produced by one of the rotors when operated in isolation.*

Figure 6.26 shows the variation with azimuth of the aerodynamic angle of attack and the tangential force along the blades of the downwind and reference rotors, when the turbines are operated at the closest streamwise separation that was simulated in the present study. The angle of attack and the associated force are shown at two different locations along the reference blade: at the mid-span, denoted $z/b = 0.5$, and close to the tip of the blade, denoted $z/b = 0.045$. At a crosswind separation of $2R$, the aerodynamic angle of attack and the loading on the blades are higher than on the blades of the reference rotor, as shown in Figures 6.26(e) and (f). This increase in angle of attack, and the associated increase in blade aerodynamic loading, is a direct consequence of the increased effective flow velocity that is induced by the wake of the upwind rotor, and thus of the decreased effective tip speed ratio that is experienced by the downstream turbine, as described earlier in this section.

6.3 Turbine-Turbine-Interaction

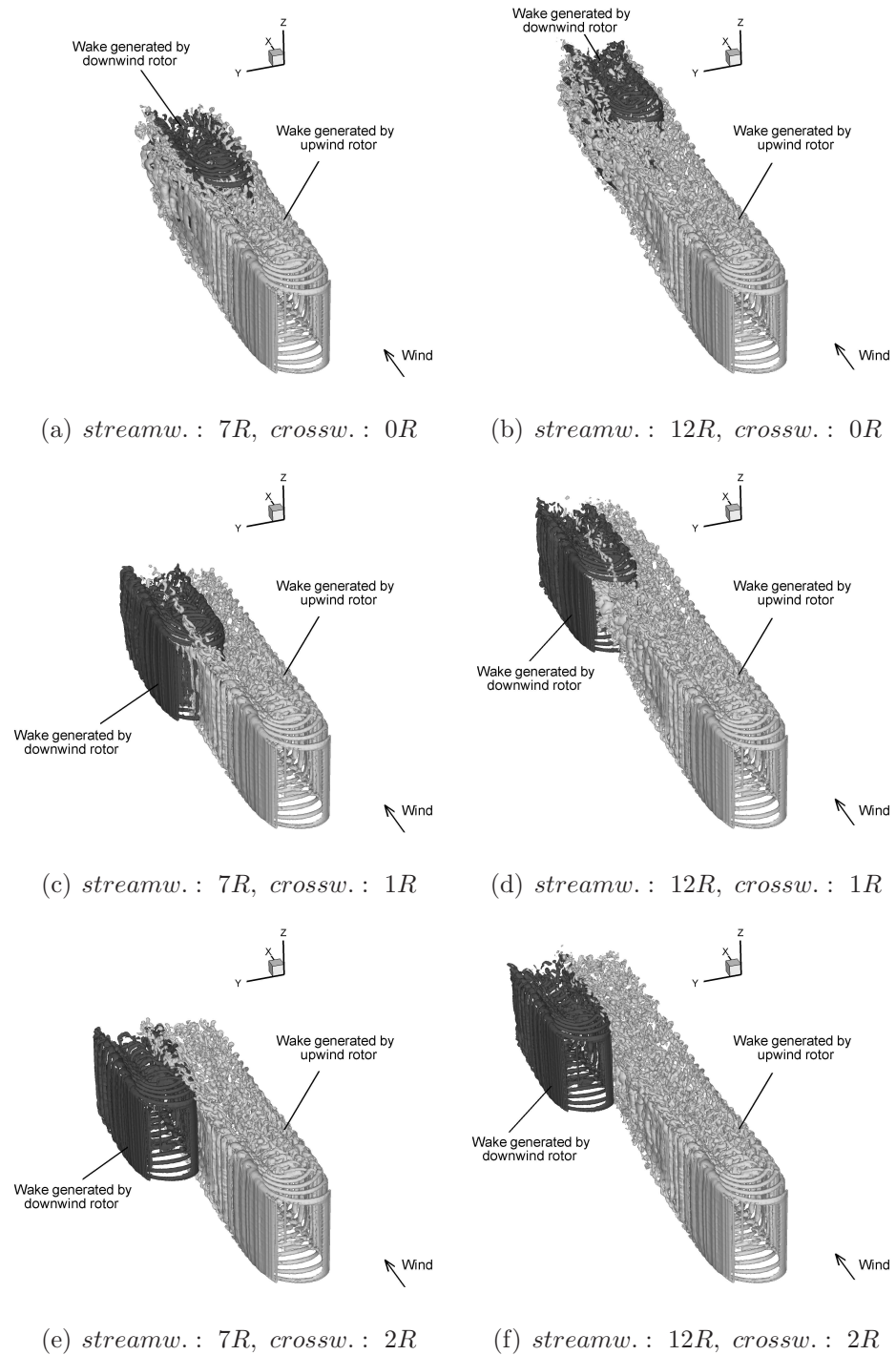


Figure 6.23: VTM-predicted flow fields surrounding the straight-bladed turbines when they are operated at different streamwise and crosswind separations from each other, visualised by plotting an isosurface of vorticity.

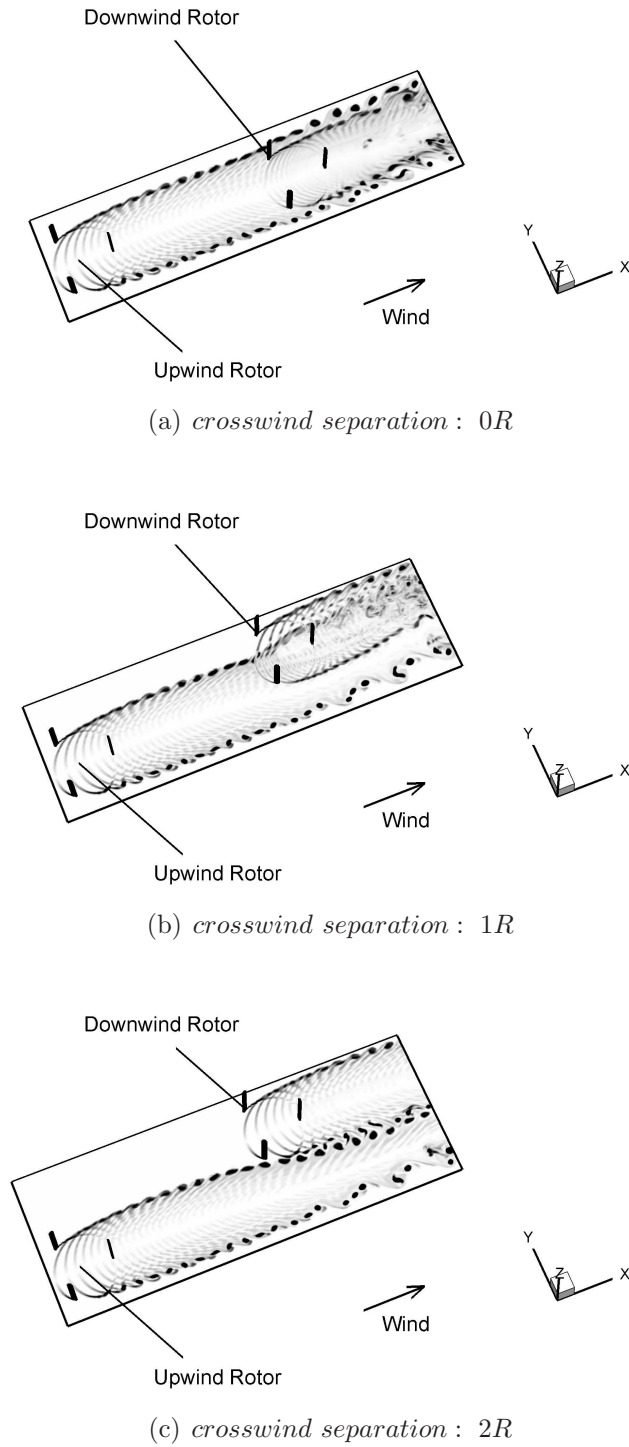


Figure 6.24: VTM-predicted flow fields surrounding the straight-bladed turbines when they are operated at a streamwise separation of $7R$, represented using contours of vorticity on a horizontal plane that intersects with the mid-spans of the rotor blades.

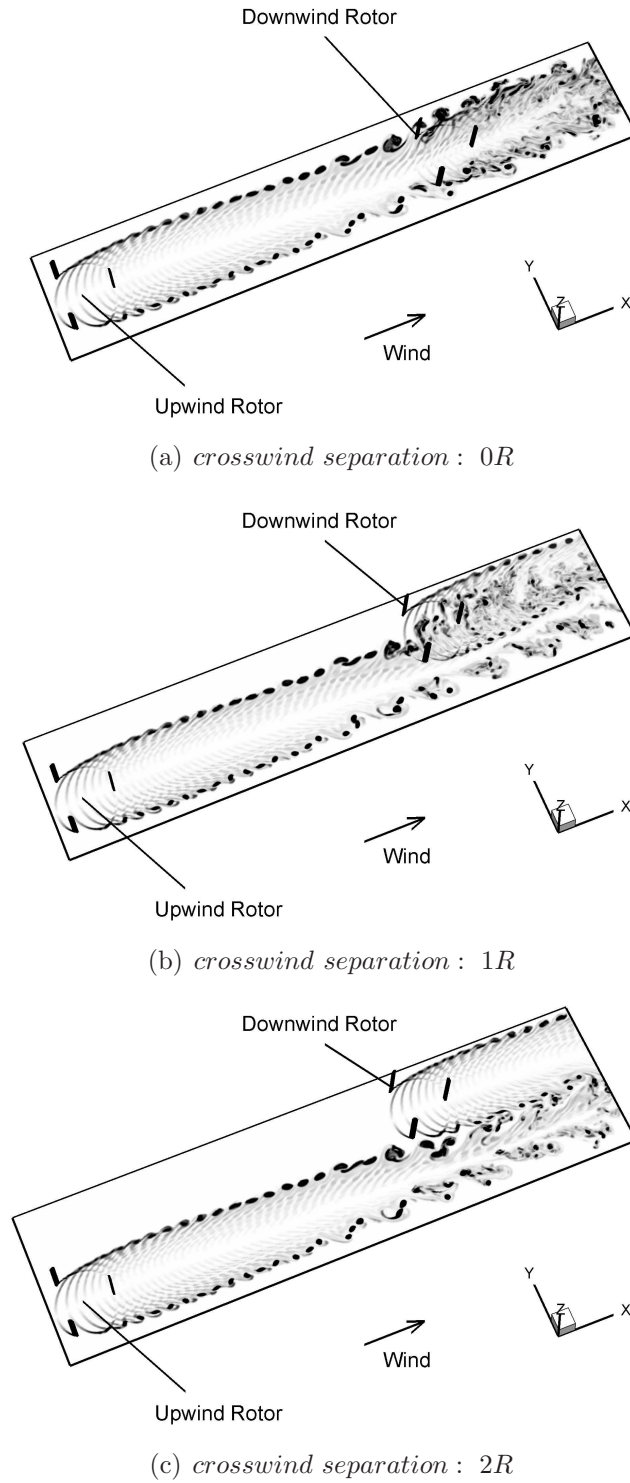


Figure 6.25: VTM-predicted flow fields surrounding the straight-bladed turbines when they are operated at a streamwise separation of $12R$, represented using contours of vorticity on a horizontal plane that intersects with the mid-spans of the rotor blades.

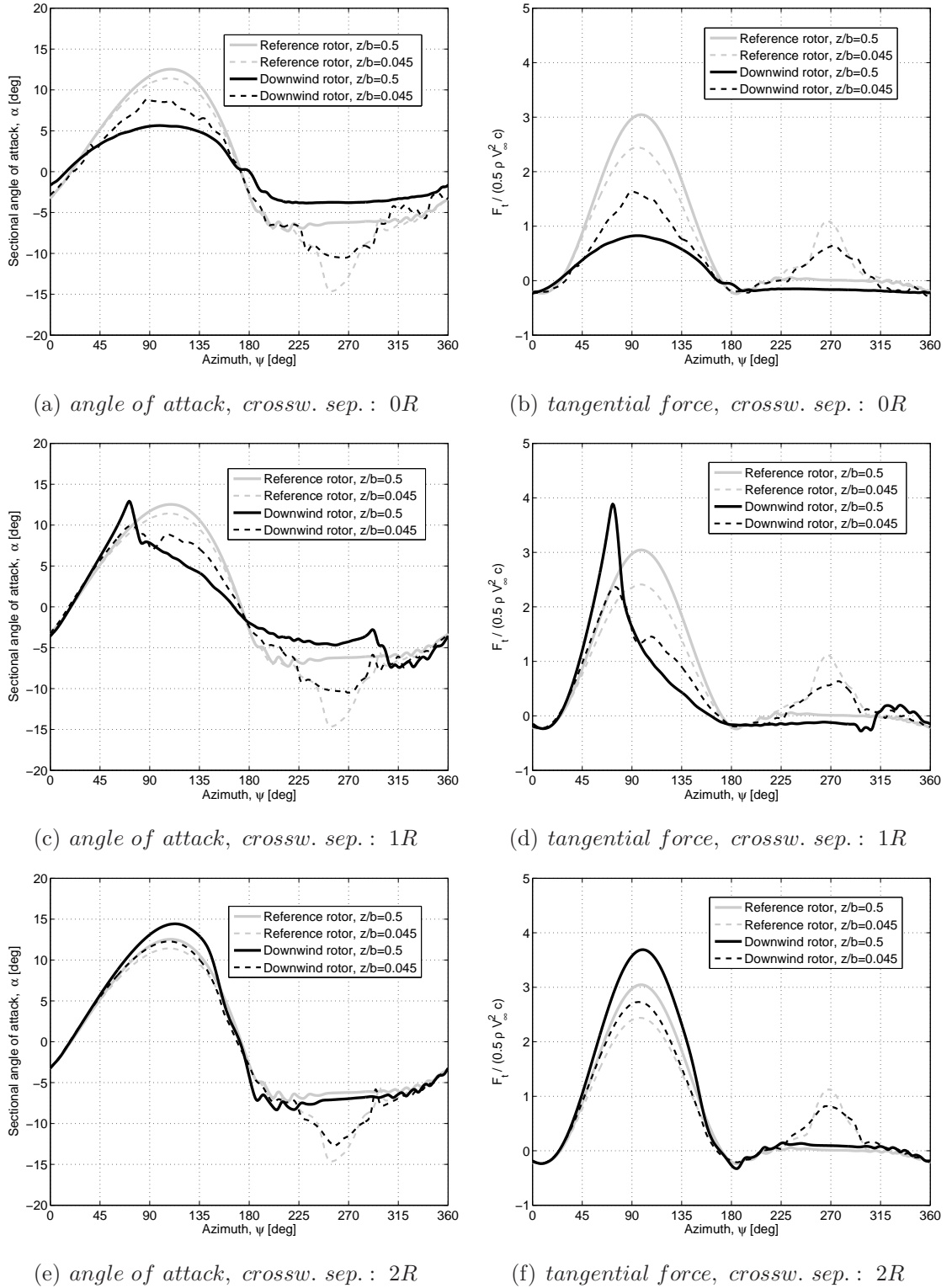


Figure 6.26: VTM-predicted variations with azimuth of aerodynamic angle of attack and tangential force at two different spanwise locations along the blades of the reference rotor and the downwind rotors, when the turbines are operated in an upwind-downwind arrangement with a streamwise separation of $7R$.

When the crosswind separation between the upwind and downwind rotors is one radius, the blades of the downwind turbine operate, for most of the rotor revolution, within the wake that is produced by the upwind turbine, as shown in Figures 6.26(c) and (d). Indeed, the aerodynamic angle of attack and the tangential force generated on the blades of the downwind turbine are, almost exclusively, smaller than those on the blades of the reference rotor. Interestingly, the angle of attack and the tangential force on the blades of the downwind rotor are considerably higher than those on the blades of the reference rotor between 0° and 70° azimuth. This indicates that the partial wake impingement results in the blades of the downwind rotor operating, between 0° and 70° azimuth, in a region in which the wake produced by the upwind rotor induces a higher local velocity than the free stream.

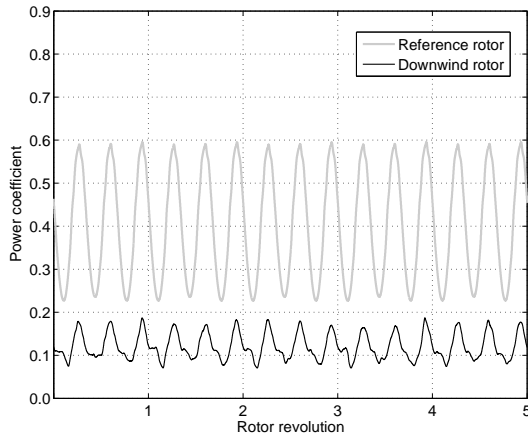
Compared to the situation at the isolated reference rotor, it is clear that the angle of attack and the blade aerodynamic loading that are produced on the blades of the downwind rotor are significantly reduced when the downwind turbine is fully immersed within the wake of the upwind rotor, as shown in Figures 6.26(a) and (b). Interestingly, these figures also indicate that the blade tips of the downwind rotor experience higher angles of attack, and thus generate higher tangential forces, than the mid-span of the blade. This suggests that a region of concentrated vorticity is apparent close to the centre of the downwind rotor, whereas the influence of the wake produced by the upwind rotor on the blade tips of the downwind rotor is weak, by comparison. Indeed, Figure 5.14, introduced earlier in Chapter 5 of this dissertation, shows that the vorticity that is trailed from the blades of the turbine convects towards the centreline of the rotor. The vorticity is thus distributed inhomogeneously within the rotor wake - with an apparent concentration of vorticity in the region close to the horizontal centreline of the rotor. When the wake that is produced by the upwind rotor impinges on the downwind rotor, it has a stronger effect on the mid-span of the blade of the downwind rotor than on its tips. This observation is important since it emphasises the need for a three-dimensional representation of the flow field if the aerodynamic interference between vertical-axis wind turbines is to be modelled with any degree of fidelity.

Figure 6.27 shows the variations with time of the power coefficients that are produced by the reference and the downwind rotors. The variation of the power coefficient is presented for five complete rotor revolutions in order to show the small variability from revolution to revolution of the power coefficient that is produced by the downwind

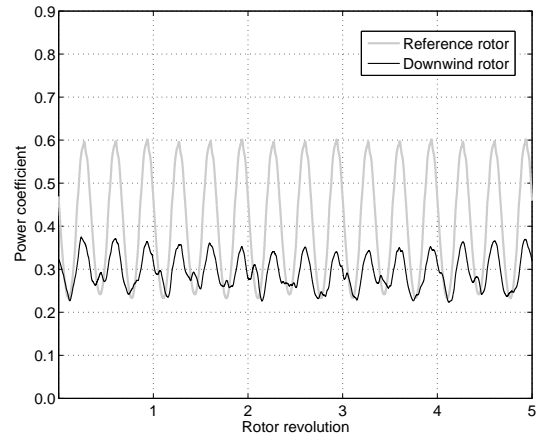
turbine, particularly when it is fully immersed within the wake that is produced by the upwind rotor. This small variability is caused by the impingement of the individual vortical structures that are contained within the wake that is produced by the upwind rotor.

When the downwind rotor is fully immersed within the wake that is produced by the upwind rotor, not only its mean power coefficient, but also the variation in power coefficient in each rotor revolution, is significantly reduced, compared to that of the reference rotor, as shown in Figures 6.27(a) and (b). By contrast, the variation with azimuth of the power coefficient that is produced by the downwind turbine is increased when the upwind and downwind turbines are not aligned parallel with the wind direction, as shown in Figures 6.27(c), (d), (e) and (f). As described in Chapter 1 of this dissertation, unsteadiness in the power coefficient, and thus in the associated blade aerodynamic loading, can cause material fatigue and is thus detrimental to the design life of the turbine. Importantly, however, the variation of the power coefficient that is caused by the continuous change in angle of attack on the blades as they revolve is far more significant than the additional variation that is induced by the full or partial impingement of the wake on the turbine. This is in distinct contrast to the aerodynamic behaviour of a horizontal-axis turbine. Indeed, Fletcher and Brown [96] investigated the aerodynamic interference of horizontal-axis wind turbines, using the VTM, and showed that the power coefficient of a horizontal-axis turbine has a significant unsteady component when it is operated within the wake of another turbine. They also showed, however, that the variation with rotor revolution of the power coefficient that is produced by a single, isolated horizontal-axis wind turbine is very small, by comparison. In contrast to the situation for a vertical-axis wind turbine, the variation with azimuth of the power coefficient that is produced by a horizontal-axis configuration is thus considerably different when the horizontal-axis rotor is operated in off-design conditions compared to when it is operated in isolation. This suggests that the vertical-axis wind turbine configuration has somewhat more favourable characteristics in supposedly off-design operating conditions when compared to the horizontal-axis turbine configuration.

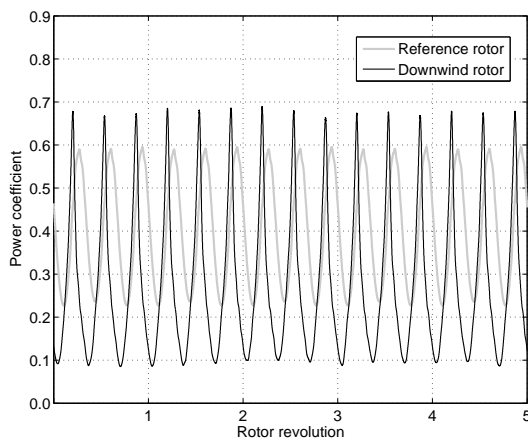
6.3 Turbine-Turbine-Interaction



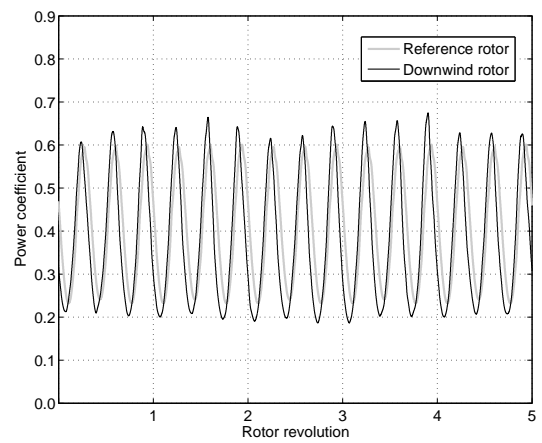
(a) $streamw.: 7R, crossw.: 0R$



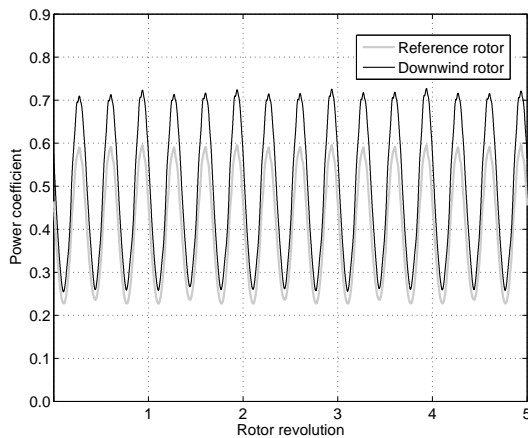
(b) $streamw.: 12R, crossw.: 0R$



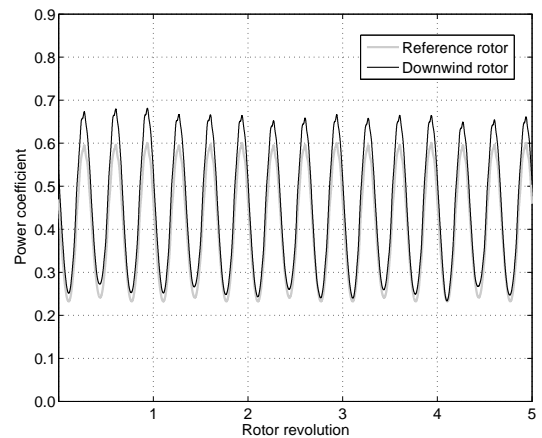
(c) $streamw.: 7R, crossw.: 1R$



(d) $streamw.: 12R, crossw.: 1R$



(e) $streamw.: 7R, crossw.: 2R$



(f) $streamw.: 12R, crossw.: 2R$

Figure 6.27: VTM-predicted variation with time (in rotor revolutions) of the power coefficient that is produced by the reference rotor and those which are produced by the downwind rotors in an upwind-downwind arrangement.

6.4 Summary

The Vorticity Transport Model has been used to investigate the aerodynamic behaviour of three different vertical-axis wind turbines in three different operating conditions. Indeed, the performance of each turbine was analysed in oblique flow and in unsteady wind conditions and the performance of the straight-bladed turbine was studied when its rotor was operated in the wake produced by another rotor.

A vertical-axis wind turbine can generate a higher power coefficient in oblique flow, compared to that developed in normal flow, if its height-to-radius ratio is sufficiently small. This is because oblique flow skews the convection of the wake, thereby allowing a significant portion of the blade to operate, over its entire azimuth, in a flow region in which the influence of the wake is significantly reduced compared to the situation in normal flow. This effect becomes increasingly dominant at higher tip speed ratios since in oblique flow the vortical structures in the turbine wake, which otherwise would convect relatively slowly downstream, are swept away more efficiently from the rotational trajectory of the blades than at lower tip speed ratios. The variation of the power coefficient within one revolution of the rotor that is observed both for straight- and for curved-bladed vertical-axis wind turbines in normal flow is shown to be reduced, to some extent, in oblique flow. The power coefficient that is produced by a vertical-axis wind turbine with helically twisted blades is fairly steady over the entire azimuth, by comparison, irrespective of whether the turbine is operated in normal or in oblique flow.

The instantaneous tip speed ratio of a rotor that is operated at a constant rotational speed in unsteady wind conditions changes according to the varying free stream velocity and, consequently, deviates from the tip speed ratio at which the highest aerodynamic efficiency is obtained. The associated power loss becomes significant only when the amplitude of the oscillations in wind speed is high, whereas the frequency of the variation in wind speed is shown to have a minor effect for all practical urban wind conditions. In steady wind conditions, the power coefficients that are produced by both the straight- and the curved-bladed turbines vary considerably within one rotor revolution because of the continuous variation of the angle of attack on the blades and, thus, the inherent unsteadiness in the blade aerodynamic loading. These variations are shown to be larger, and thus far more significant, than those that are induced by the unsteadiness in the wind conditions.

Not surprisingly, a vertical-axis wind turbine produces a much lower power coefficient when it is fully immersed within the wake that is generated by a rotor that is located upwind of it, compared to the power coefficient that is produced by a single, isolated turbine that is operated in an undisturbed free stream. This is simply because of the reduced effective wind velocity that is encountered by the downwind turbine in this arrangement. A vertical-axis wind turbine that is operated downwind of another turbine can generate a higher power coefficient than that which is produced by a single, isolated turbine, when the crosswind separation between the two turbines is sufficiently large to avoid direct impingement on the downwind turbine of the wake that is produced by the upwind rotor. This is because the presence of the wake that is generated by the upwind rotor constrains the lateral expansion of the wake that is produced by the downwind turbine. The increase in efficiency of the downwind rotor when it is operated in this configuration is a result of two interrelated effects. Firstly, the downwind rotor operates - at least partially - in a flow with higher local velocity, and thus in a flow with higher kinetic energy content, than that of the free stream. Secondly, the velocity component that is induced by the presence of the wake of another rotor results in an increase in angle of attack on the blades, and consequently in an increase in the non-dimensional forces on the blades and thus in the blade aerodynamic loading. The temporal variation of the power coefficient that is produced by the downwind rotor is somewhat increased compared to that produced by a single, isolated rotor, except when it is fully immersed within the wake that is produced by the upwind rotor. Importantly, however, the variation of the power coefficient that is caused by the inherent continuous change in angle of attack on the blades as they revolve is far more significant than the additional variation that is induced by the full or partial impingement of the wake on the turbine.

6.5 Chapter Nomenclature

A	swept area
AR	aspect ratio, b/c
b	blade span
c	aerofoil chord length
C_P	power coefficient, $P/\frac{1}{2}\rho AV_\infty^3$

$C_{P,downwind}$	power coefficient of the downwind turbine
$C_{P,mean}$	mean power coefficient for one rotor revolution
$C_{P,normal}$	power coefficient in normal flow
$C_{P,oblique}$	power coefficient in oblique flow
$C_{P,ref}$	power coefficient of the isolated reference rotor in steady, normal flow
ΔC_P	unsteady component of the power coefficient, $C_P - C_{P,mean}$
D_g	gust length, V_∞/f_c
f_c	characteristic fluctuation frequency
F_n	sectional force acting normal to the aerofoil chord
F_t	sectional force acting tangential to the aerofoil chord
H	turbine height
k_g	reduced gust frequency, $2R/D_g$
P	power
R	radius of the rotor at blade mid-span
R_g	Number of rotor revolutions per gust, $\lambda_{mean}/\pi k_g$
V	(unsteady) wind speed, $V = V(t)$ $V = V_\infty = constant$ in <i>oblique flow</i> and for <i>turbine-turbine interactions</i>
V_∞	(steady) wind speed/ (mean) free stream velocity
ΔV	unsteady component of the wind velocity, $V(t) - V_\infty$
z	coordinate; the z-axis is aligned with the rotational axis of the rotor
α	angle of attack
β	oblique flow angle, i.e. angle between wind vector and horizon
λ	tip speed ratio, $\Omega R/V$
λ_{mean}	mean tip speed ratio, $\Omega R/V_\infty$
ψ	azimuth angle
ρ	air density
Ω	angular velocity of the rotor

Chapter 7

Conclusions and Outlook

7.1 Conclusions

The accurate modelling of the aerodynamics of vertical-axis wind turbines poses a significant challenge. The cyclic motion of the turbine induces large variations in the angle of attack on the blades of the rotor that result in significant unsteadiness in the blade aerodynamic loading and can manifest as dynamic stall. In addition, aerodynamic interactions occur between the turbine blades and the wake that is generated by the rotor. Interactions between the blades of the turbine and, in particular, tip vortices that were trailed in previous revolutions produce impulsive variations in the blade aerodynamic loading, but these interactions are notoriously difficult to simulate accurately. These aerodynamic characteristics of vertical-axis wind turbines are somewhat more complex compared to those of horizontal-axis configurations, and are partially responsible for the fact that industrial and academic research has focused primarily on horizontal-axis turbines in the past decades. This has had the result that vertical-axis wind turbines are still relatively poorly understood compared to horizontal-axis wind turbines.

The main objectives of this research have been to increase the understanding of the flow field surrounding vertical-axis turbines and to understand some of the aerodynamic factors that influence the performance of different vertical-axis turbine configurations under different, practically relevant, operating conditions. A simulation tool, the Vorticity Transport Model (VTM), has been used to carry out a computational study to achieve these aims. The VTM is based on the vorticity-velocity form of the unsteady,

incompressible Navier-Stokes equation. The numerical diffusion of vorticity within the flow field surrounding the turbine is kept at a very low level by using a Riemann solver that is based on Toro's Weighted Average Flux method. This approach permits many rotor revolutions to be captured without significant spatial smearing of the wake structure and thus renders the VTM well suited to the study of the aerodynamic performance and wake dynamics of vertical-axis wind turbines.

The VTM consists of an outer model, in which the dynamics of the wake that is generated by the rotor are calculated based on basic fluid dynamics principles, and an inner model, in which the blade aerodynamic loading is determined based on a lifting-line approach. The blade aerodynamic model within the VTM has been enhanced by a semi-empirical dynamic stall model that was implemented in the course of this research in order to account for the effects of large, transient variations of the angle of attack on the aerodynamic loading on the turbine blades. In order to validate the VTM and its dynamic stall model, VTM predictions were compared to experimental measurements of the performance of an aerofoil in a dynamic stall test and to experimental measurements of the performance of two different vertical-axis turbines that were operated at different tip speed ratios.

The VTM-predicted variations of the normal and tangential force coefficients agree reasonably well with experimental measurements of dynamic stall when the VTM is used in conjunction with its dynamic stall model. Not surprisingly, large discrepancies occur between the experimental measurements and VTM predictions that are based on static aerofoil data, particularly at low tip speed ratios. This indicates that the use of a model that is based on static aerofoil data is insufficient to predict reliably the aerodynamics of vertical-axis wind turbines. Although some discrepancies between experimental measurements and the VTM predictions that include the dynamic stall model are apparent, the variations with angle of attack of the VTM-predicted coefficients agree reasonably well, overall, with experimental measurements in terms of the shapes and sizes of the dynamic stall hysteresis loops. These comparisons provide confidence that the effect of dynamic stall is satisfactorily accounted for in the VTM when its dynamic stall model is used to represent the blade aerodynamics.

The VTM-predicted sectional force for an aerofoil at the mid-span of a straight blade of a vertical-axis rotor agrees well with previous computations that are documented in the literature of the two-dimensional aerodynamics of the same aerofoil in

an equivalent planar, cyclic motion. In the downstream part of the revolution of the turbine, aerodynamic interactions occur between the blades of the rotor and vortices in the wake. These blade-wake interactions cause transient excursions in the angle of attack on the blade beyond the static stall angle, leading to localised dynamic stall near the tips of the blades. Indeed, the conclusion that local dynamic stall is induced by blade-wake interactions is supported by the improved correlation between experimental measurements made by Strickland *et al.* [47] and VTM predictions that results when the dynamic stall model is employed within the VTM to represent the blade aerodynamics compared to when only a quasi-steady model was used. It is suggested, thus, that the disagreement between these experimental measurements and computational data that has been presented in previous studies arises because three-dimensional aerodynamic effects, such as interactions between the blades of the turbine and the vortices in the wake, were not modelled with sufficient fidelity.

The VTM has further been used to simulate the three-dimensional flow field surrounding a commercial vertical-axis wind turbine. This turbine consists of three blades that are helically twisted around the rotational axis of its rotor. The predicted variation of the power coefficient agrees very favourably with experimental measurements of the rotor performance. It was demonstrated that an appropriate implementation of a dynamic stall model is essential if the performance of the turbine is to be predicted reliably over its entire operating range.

When these results are taken together, they provide significant confidence in the ability of the VTM to predict accurately the aerodynamics of vertical-axis wind turbines.

The aerodynamic performance and wake dynamics of three vertical-axis wind turbines, one with straight blades, another with curved blades and a third with a helically twisted blade configuration, have been investigated when their rotors were operated at different tip speed ratios.

The power coefficient that is produced by vertical-axis wind turbines with either straight or curved blades contains a substantial oscillatory component at the blade passage frequency of the turbine. The forces that act on the rotor in streamwise and crosswind direction are also shown to produce a considerable oscillatory component to the overall forces on the turbine. The variations in the blade loading can fatigue the rotor structure and reduce the design life of the turbine. By comparison, a turbine with

helically twisted blades is shown to produce a relatively steady power coefficient. In contrast to non-twisted vertical-axis turbines, a configuration that comprises helically twisted blades produces a small, but notable, force in direction of the rotational axis of the rotor. This axial force is caused by the effect of blade sweep that is introduced when the blades are helically twisted around the rotor axis.

Blade curvature results in a reduced circumferential velocity relative to the free stream velocity, and thus a reduced local tip speed ratio, close to the blade tips compared to that at the mid-span of the blade. This is because the effective radius of the blade sections is smaller near to the blade tips than at the mid-span of the blade. The regions close to the blade tips of the curved-bladed configuration therefore experience a lower effective tip speed ratio and thus oscillations in angle of attack that are of larger amplitude than those at the mid-span of the blade. This observation indicates that the static stall angle of an aerofoil within a curved-bladed configuration will be reached, and thus dynamic stall will be induced, at higher tip speed ratios than for a straight-bladed configuration.

The simulations presented in this dissertation suggest that a helically twisted configuration has an advantage over turbines that have non-twisted blades since the oscillations in the variation of the power coefficient and the rotor forces are shown to be significantly reduced when the blades are helically twisted around the rotational axis of the rotor. Helical blade twist might thus potentially increase the design life of a vertical-axis rotor and its components.

The aerodynamic behaviour of the straight-bladed, the curved-bladed and the helically twisted configuration was also studied when their rotors were operated in three different operating conditions. These conditions were chosen to mimic the flow conditions a vertical-axis wind turbine is likely to encounter in the urban environment and thus represent somewhat more realistic flow conditions compared to the steady, uniform flow in which rotors have been typically investigated in previous studies that are documented in the literature. Indeed, in the present research, the performance of each turbine was analysed in unsteady wind, when its rotor was operated in the wake produced by another rotor, and in oblique flow - in other words when the wind vector was non-perpendicular to the axis of rotation of the rotor.

Compared to the power coefficient that is generated by a vertical-axis wind turbine in normal flow, in other words in conditions in which the wind vector is perpendicular

to the axis of rotation of the turbine, a vertical-axis turbine can generate a higher power coefficient in oblique flow if the ratio between the height of the turbine and its rotor radius is sufficiently small. This is because oblique flow skews the convection of the wake, thereby allowing a significant portion of the blade to operate, over its entire azimuth, in a flow region in which the influence of the wake is significantly reduced compared to the situation in normal flow. This effect becomes increasingly dominant at higher tip speed ratios since in oblique flow the vortical structures in the turbine wake, which otherwise would convect relatively slowly downstream, are swept away more efficiently from the rotational trajectory of the blades than at lower tip speed ratios. The variation of the power coefficient within one revolution of the rotor that is observed both for straight- and for curved-bladed vertical-axis wind turbines in normal flow is shown to be reduced, to some extent, in oblique flow. The power coefficient that is produced by a vertical-axis wind turbine with helically twisted blades is fairly steady over the entire azimuth, by comparison, irrespective of whether the turbine is operated in normal flow or in oblique flow.

The instantaneous tip speed ratio of a rotor that is operated at a constant rotational speed in unsteady wind conditions varies according to the instantaneous free stream velocity and, consequently, deviates from the tip speed ratio at which the highest aerodynamic efficiency is obtained. The associated power loss becomes significant only when the amplitude of the oscillations in wind speed is high, whereas the frequency of the variation in wind speed is shown to have a minor effect for all practical urban wind conditions. In steady wind conditions, the power coefficients that are produced by both the straight- and the curved-bladed turbines vary considerably within one rotor revolution because of the continuous variation of the angle of attack on the blades, and thus the inherent unsteadiness in the blade aerodynamic loading. These variations are shown to be larger, and thus far more practically significant, than those that are induced by the unsteadiness in the wind conditions.

Not surprisingly, a vertical-axis wind turbine produces a much lower power coefficient when it is fully immersed within the wake that is generated by a rotor that is located upwind of it, compared to the power coefficient that is produced by a single, isolated turbine that is operated in undisturbed free stream. This is simply because of the reduced effective wind velocity that is encountered by the downwind turbine

in this arrangement. A vertical-axis wind turbine that is operated downwind of another turbine can generate a higher power coefficient than that which is produced by a single, isolated turbine, when the crosswind separation between the two turbines is just large enough to avoid direct impingement on the downwind turbine of the wake that is produced by the upwind rotor. This is because the presence of the wake that is generated by the upwind rotor constrains the lateral expansion of the wake that is produced by the downwind turbine. The increase in efficiency of the downwind rotor when it is operated in this configuration is a result of two interrelated effects. Firstly, the downwind rotor operates - at least partially - in a flow with higher local velocity, and thus in a flow with higher kinetic energy content, than that of the free stream. Secondly, the velocity component that is induced by the presence of the wake of another rotor results in an increase in angle of attack on the blades, and consequently in an increase in the non-dimensional forces on the blades and thus in the blade aerodynamic loading. The temporal variation of the power coefficient that is produced by the downwind rotor is somewhat increased compared to that produced by a single, isolated rotor, except when it is fully immersed within the wake that is produced by the upwind rotor. Importantly, however, the variation of the power coefficient that is caused by the continuous change in angle of attack on the blades as they revolve is far more significant than the additional variation that is induced by either full or partial impingement of the wake on the turbine.

7.2 Outlook

In the simulations presented in this dissertation, some of the characteristics of the flow environment that a vertical-axis wind turbine might encounter in practice were modelled. Several aspects of the real flow environment, such as atmospheric turbulence or the influence of the atmospheric boundary layer and thus more complicated onset flow, were not accounted for in these simulations. Nevertheless, the approach that was documented in this dissertation is useful and informative since it increases the understanding of the flow field surrounding vertical-axis wind turbines by allowing the various mechanisms that influence their aerodynamic behaviour to be isolated and studied independently. It is clear that confidence in the simulations and thus in the applicability of the model as a simulation tool for the design of vertical-axis wind

turbines could be increased further if appropriate models are incorporated into the VTM that account for more of the characteristics of the real flow field.

The ability to compare computational results with experimental measurements is crucial in order to establish confidence in any numerical simulation tool. Detailed experimental measurements of the performance of vertical-axis wind turbines, particularly of its blade aerodynamic loading, for Reynolds and Mach numbers that represent flow conditions that an urban wind turbine encounters in practice, are scarce in the literature at present. This is, to some extent, in contrast to the situation for horizontal-axis wind turbines and simply reflects the focus of academic and industrial research in the past decades. An extensive set of experimental measurements, provided by using latest measurement equipment, of the variation with tip speed ratio of the power coefficient, of the variation with azimuth of the blade aerodynamic loading and of the dynamics of the wake that are produced by straight-bladed vertical axis wind turbines and helically twisted configurations would thus be very useful in order to generate a benchmark database against which numerical predictions could be compared. This would help to further the development of computational models and to increase confidence in their predictions. The development of simulation tools that can more accurately portray the physics of the flow field surrounding vertical-axis rotors will, in conjunction with experimental measurements, further enhance our understanding of the aerodynamic characteristics of vertical-axis wind turbines and, consequently, help to improve the design of these devices.

A Leishman-Beddoes-type dynamic stall model has been implemented into the VTM within the course of this research. In doing so, some of the modifications to the original dynamic stall model that have been proposed in recent publications in the literature were not considered. This was because these modifications introduce additional semi-empirical coefficients that require extensive experimental measurements which were very scarce at the time of implementation of the model. The predictive capability of such a modified model for aerofoil performance at operating conditions that differ from the test conditions can be called into question in the absence of comprehensive data for these coefficients. Any future increase in availability of experimental measurements of dynamic stall, for conditions that are typical to the flow environment in which urban wind turbines operate, could provide data that can be used to refine the version of the dynamic stall model that is currently implemented within the VTM.

Although VTM predictions of the performance of an aerofoil in a dynamic stall test were shown to agree reasonably well with experimental measurements, it is clear that the dynamic stall model that is currently employed within the VTM could, potentially, be enhanced further, with possibly beneficial effect on the quality of the simulations.

An approach that would overcome the need for explicit modelling of dynamic stall by semi-empirical models, and that would arguably increase the fidelity of the prediction of the flow in vicinity of the rotor blades, is to couple the (outer) wake model of the VTM to a conventional CFD method and thus to replace the lifting-line approach to which the wake model is coupled in the version of the VTM that has been used to produce all the simulations that are described in this dissertation. Indeed, promising results for a model that couples a conventional CFD method and the VTM wake model have recently been reported in the literature (Ref. 44). Although the computational costs of this approach are significantly higher than those of the version of the VTM that was used to produce the results that are documented in the present dissertation, it is expected that this method will become increasingly attractive in the light of the increasing availability of high-performance computing in the future.

It is hoped that the results presented in this dissertation concerning the effect of the geometric configuration of the rotor blades on the performance of vertical-axis wind turbines might be useful for the designers of these devices. Furthermore, the study of the effect of the operating condition on turbine performance showed that the vertical-axis wind turbine configuration has favourable characteristics in supposedly off-design operating conditions. This is in distinct contrast to the horizontal-axis configuration. These findings contribute to the discussion about the most appropriate turbine configuration in the urban environment and suggest that the vertical-axis wind turbine is potentially better suited to the flow conditions that are typical to the built environment than the horizontal-axis configuration.

References

- [1] Global Wind Energy Council (GWEC), *Global Wind Report 2009*. March 2010.
- [2] BP plc, *Statistical Review of World Energy*. June 2010.
- [3] International Energy Agency (IEA), *Energy Technology Perspectives - Scenarios & Strategies to 2050*. July 2010.
- [4] M. L. Parry, O. F. Canziani, J. P. Palutikof, P. J. van der Linden, and C. E. Hanson (Editors), *Climate Change 2007: Impacts, Adaptation and Vulnerability. Contribution of Working Group II to the Fourth Assessment Report of the Intergovernmental Panel on Climate Change*. Intergovernmental Panel on Climate Change (IPCC), Cambridge University Press, Cambridge, United Kingdom and New York, NY, USA, 2007.
- [5] B. Metz, O. R. Davidson, P. R. Bosch, R. Dave, and L. A. Meyer (Editors), *Climate Change 2007: Mitigation of Climate Change. Contribution of Working Group III to the Fourth Assessment Report of the Intergovernmental Panel on Climate Change*. Intergovernmental Panel on Climate Change (IPCC), Cambridge University Press, Cambridge, United Kingdom and New York, NY, USA, 2007.
- [6] Energy Technologies Institute (ETI), *Energy Technologies Institute unveils first projects to benefit from £1.1 billion initiative*. Press Release, Loughborough, UK, 13 January 2009.
- [7] S. McIntosh, *Wind energy for the built environment*. PhD Thesis, University of Cambridge, Cambridge, UK, 2009.

REFERENCES

- [8] G. J. M. Darrieus, *Turbine having its rotating shaft transverse to the flow of the current*. US Patent 1,835,018, 1931.
- [9] S. J. Savonius, “The S-rotor and its applications,” *Mechanical Engineering*, vol. 53, no. 5, pp. 333–338, 1931.
- [10] R. Gasch and J. Twele, *Windkraftanlagen*. 5th edition, Teubner Verlag, Wiesbaden, Germany, 2007.
- [11] F. Scheurich, T. M. Fletcher, and R. E. Brown, “Simulating the aerodynamic performance and wake dynamics of a vertical-axis wind turbine,” *Wind Energy*, vol. 14, no. 2, pp. 159–177, 2011.
- [12] F. Scheurich, T. M. Fletcher, and R. E. Brown, “The influence of blade curvature and helical blade twist on the aerodynamic performance of a vertical-axis wind turbine,” in *Proceedings of the 48th AIAA Aerospace Sciences Meeting including the New Horizons Forum and Aerospace Exposition, AIAA-2010-1579*, Orlando, FL, USA, 4-7th January 2010.
- [13] F. Scheurich, T. M. Fletcher, and R. E. Brown, “Effect of blade geometry on the aerodynamic loads produced by vertical-axis wind turbines,” *Journal of Power and Energy*, vol. 225, no. 3, pp. 327–341, 2011.
- [14] F. Scheurich, “Small-scale wind turbines for sustainable energy supply in urban environments,” in *Proceedings of the Universitas 21 International Conference for Graduate Research Students: Sustainable Cities for the Future*, University of Melbourne, Melbourne, and University of Queensland, Brisbane, Australia, 29th November - 5th December 2009.
- [15] F. Scheurich and R. E. Brown, “Vertical-axis wind turbines in oblique flow: sensitivity to rotor geometry,” in *Proceedings of the European Wind Energy Association (EWEA) Annual Event*, Brussels, Belgium, 14-17th March 2011.
- [16] F. Scheurich, “Modelling the aerodynamics of vertical-axis wind turbines in urban wind conditions,” in *Proceedings of the 6th PhD Seminar on Wind Energy in Europe organised by the European Academy of Wind Energy (EAWE)*, Norwegian

REFERENCES

- University of Science and Technology, Trondheim, Norway, 30th September - 1st October 2010.
- [17] F. Scheurich and R. E. Brown, “Modelling the aerodynamics of vertical-axis wind turbines in unsteady wind conditions,” *Wind Energy*, in print.
- [18] F. Scheurich, A. Passola Parcerissa, and R. E. Brown, “Simulating wake interactions of vertical-axis wind turbines,” in *Book of Abstracts of the Wake Conference*, Visby, Gotland, Sweden, 8-9th June 2011.
- [19] F. Scheurich and R. E. Brown, “The effect of dynamic stall on the aerodynamics of vertical-axis wind turbines,” in *Proceedings of the 29th AIAA Applied Aerodynamics Conference, AIAA-2011-3369*, Honolulu, HI, USA, 27-30th June 2011.
- [20] F. Scheurich and R. E. Brown, “Effect of dynamic stall on the aerodynamics of vertical-axis wind turbines,” *AIAA Journal*, in print.
- [21] P. C. Klimas, “Darrieus rotor aerodynamics,” *Transactions of the ASME. Journal of Solar Energy Engineering*, vol. 104, pp. 102–105, 1982.
- [22] H. Glauert, *The Elements of Aerofoil and Airscrew Theory*. 2nd edition, Cambridge University Press, 1948.
- [23] R. J. Templin, *Aerodynamic performance theory for the NRC vertical-axis wind turbine*. National Research Council Canada, LTR LA 160, 1974.
- [24] J. H. Strickland, *The Darrieus turbine: a performance prediction model using multiple streamtubes*. Sandia, SAND75-0431, 1975.
- [25] I. Paraschivoiu, “Double-multiple streamtube model for studying vertical-axis wind turbines,” *Journal of Propulsion and Power*, vol. 4, pp. 370–377, 1988.
- [26] J. H. Strickland, B. T. Webster, and T. Nguyen, “A vortex model of the Darrieus turbine: an analytical and experimental study,” *Transactions of the ASME. Journal of Fluids Engineering*, vol. 101, pp. 500–505, 1979.

REFERENCES

- [27] F. N. Coton, D. Jiang, and R. A. McD. Galbraith, “An unsteady prescribed wake model for vertical axis wind turbines,” *Journal of Power and Energy*, vol. 208, pp. 13–20, 1994.
- [28] M. O. L. Hansen and D. N. Sørensen, “CFD model for vertical axis wind turbine,” in *Proceedings of the European Wind Energy Conference*, Copenhagen, Denmark, 2nd-6th July 2001.
- [29] C. J. Simão Ferreira, H. Bijl, G. van Bussel, and G. van Kuik, “Simulating dynamic stall in a 2D VAWT: modeling strategy, verification and validation with particle image velocimetry data,” *Journal of Physics: Conference Series*, vol. 75, p. 012023, 2007.
- [30] K. Horiuchi, I. Ushiyama, and K. Seki, “Straight wing vertical axis wind turbines: a flow analysis,” *Wind Engineering*, vol. 29, pp. 243–252, 2005.
- [31] R. E. Brown, “Rotor wake modelling for flight dynamic simulation of helicopters,” *AIAA Journal*, vol. 38, no. 1, pp. 57–63, 2000.
- [32] R. E. Brown and A. J. Line, “Efficient high-resolution wake modelling using the vorticity transport equation,” *AIAA Journal*, vol. 43, no. 7, pp. 1434–1443, 2005.
- [33] I. G. Currie, *Fundamental Mechanics of Fluids*. 2nd edition, McGraw-Hill, 1993.
- [34] E. F. Toro, “A weighted average flux method for hyperbolic conservation laws,” *Proceedings of the Royal Society of London, Series A: Mathematical and Physical Sciences*, vol. 423, no. 1865, pp. 401–418, 1989.
- [35] G. Strang, “On the construction and comparison of finite difference schemes,” *Journal of Numerical Analysis*, vol. 5, pp. 995–1011, 1968.
- [36] E. F. Toro, *Some aspects of shock capturing methods for gas dynamics*. College of Aeronautics, Cranfield Institute of Technology, COA-9112, 1991.
- [37] S. K. Godunov, *Different methods for shock waves*. PhD Thesis, Moscow State University, USSR, 1954.

REFERENCES

- [38] E. F. Toro, *Riemann Solvers and Numerical Methods for Fluid Dynamics*. 3rd edition, Springer Verlag, Berlin, 2006.
- [39] K. Karamcheti, *Principles of Ideal-Fluid Aerodynamics*. 2nd edition, R. E. Krieger Publishing Co., 1980.
- [40] L. Rosenhead, “The spread of vorticity in the wake behind a cylinder,” *Proceedings of the Royal Society of London, Series A*, vol. 127, no. 806, pp. 590–612, 1930.
- [41] D. W. Moore, “Finite amplitude waves on aircraft trailing vortices,” *Aeronautical Quarterly*, vol. 23, pp. 307–314, 1972.
- [42] A. J. Line, *Computational modelling of helicopter high-frequency dynamics*. PhD Thesis, Imperial College (University of London), London, UK, 2005.
- [43] L. Greengard and V. Rokhlin, “A fast algorithm for particle simulations,” *Journal of Computational Physics*, vol. 135, no. 2, pp. 280–292, 1997.
- [44] G. R. Whitehouse, A. H. Boschitsch, M. J. Smith, C. E. Lynch, and R. E. Brown, “Investigation of mixed element hybrid grid-based CFD methods for rotorcraft flow analysis,” in *Proceedings of the 66th American Helicopter Society Annual Forum*, Phoenix, AZ, USA, 11-13th May 2010.
- [45] L. Prandtl, “Tragflügeltheorie,” *I. Mitteilung. Nachrichten der Königlichen Gesellschaft der Wissenschaften Göttingen, Math.-Phys. Klasse*, pp. 451–477, 1918.
- [46] L. Prandtl, “Tragflügeltheorie,” *II. Mitteilung. Nachrichten der Königlichen Gesellschaft der Wissenschaften Göttingen, Math.-Phys. Klasse*, pp. 107–137, 1919.
- [47] J. H. Strickland, T. Smith, and K. Sun, *A vortex model of the Darrieus turbine: an analytical and experimental study*. Sandia, SAND81-7017, 1981.
- [48] J. K. Harvey and F. J. Perry, “Flowfield produced by trailing vortices in the vicinity of the ground,” *AIAA Journal*, vol. 9, no. 8, pp. 1659–1660, 1971.

REFERENCES

- [49] G. R. Whitehouse, *Helicopter response to vortex encounters in the near-airfield environment*. PhD Thesis, Imperial College (University of London), London, UK, 2004.
- [50] J. Weissinger, *The lift distribution of swept-back wings*. NACA TM-1120, 1947.
- [51] I. H. Abbott and A. E. von Doenhoff, *Theory of Wing Sections: including a Summary of Airfoil Data*. Dover Publications, New York, 1959.
- [52] W. J. McCroskey, K. W. McAlister, L. W. Carr, and S. L. Pucci, *An experimental study on dynamic stall on advanced airfoil sections*. NASA TM-84245, 1982.
- [53] L. W. Carr, K. W. McAlister, and W. J. McCroskey, *Analysis of the development of dynamic stall based on oscillating airfoil measurements*. NASA TN D-8382, 1977.
- [54] M. S. Chandrasekhara and L. W. Carr, “Flow visualization studies of the Mach number effects on the dynamic stall of oscillating airfoils,” *Journal of Aircraft*, vol. 27, no. 6, pp. 516–522, 1990.
- [55] M. H. Akbari and S. J. Price, “Simulation of dynamic stall for a NACA 0012 airfoil using a vortex method,” *Journal of Fluids and Structures*, vol. 17, no. 6, pp. 855–874, 2003.
- [56] A. Spentzos, G. N. Barakos, K. J. Badcock, B. E. Richards, F. N. Coton, R. A. McD. Galbraith, E. Berton, and D. Favier, “Computational fluid dynamics study of three-dimensional dynamic stall of various planform shapes,” *Journal of Aircraft*, vol. 44, no. 4, pp. 1118–1128, 2007.
- [57] J. G. Leishman, *Principles of Helicopter Aerodynamics*. 2nd Edition, Cambridge University Press, Cambridge, UK, 2006.
- [58] R. B. Green, R. A. McD. Galbraith, and A. J. Niven, “Measurements of dynamic stall vortex convection speed,” *Aeronautical Journal*, vol. 96, no. 958, pp. 319–325, 1992.
- [59] J. G. Leishman and T. S. Beddoes, “A semi-empirical model for dynamic stall,” *Journal of the American Helicopter Society*, vol. 34, no. 3, pp. 3–17, 1989.

REFERENCES

- [60] S. Gupta and J. G. Leishman, “Dynamic stall modelling of the S809 aerofoil and comparison with experiments,” *Wind Energy*, vol. 9, no. 6, pp. 521–547, 2006.
- [61] T. Theodorsen, *General theory of aerodynamic instability and the mechanism of flutter*. NACA 496, 1935.
- [62] T. von Kármán and W. R. Sears, “Airfoil theory for non-uniform motion,” *Journal of the Aeronautical Sciences*, vol. 5, pp. 379–390, 1938.
- [63] B. Thwaites, *Incompressible Aerodynamics*. Oxford University Press, UK, 1960.
- [64] R. K. Angell, P. J. Musgrove, and R. A. McD. Galbraith, *Collected data for tests on a NACA 0015 - volume III: pressure data relevant to the study of large scale vertical axis wind turbines*. Department of Aerospace Engineering, University of Glasgow, Glasgow, UK, GU-AERO-8803, 1988.
- [65] W. Sheng, R. A. McD. Galbraith, and F. N. Coton, “A modified dynamic stall model for low Mach numbers,” *Journal of Solar Energy Engineering*, vol. 130, pp. 031013/1–10, 2008.
- [66] W. T. Evans and K. W. Mort, *Analysis of computed flow parameters for a set of suddenly stalls in low speed two-dimensional flow*. NACA TND-85, 1959.
- [67] T. S. Beddoes, “Onset of leading edge separation effects under dynamic conditions and low Mach number,” in *Proceedings of the 34th Annual Forum of the American Helicopter Society*, Washington, DC, USA, 15-17th May 1978.
- [68] T. S. Beddoes, “Representation of aerofoil behaviour,” *Vertica*, vol. 7, pp. 183–197, 1983.
- [69] A. J. Niven and R. A. McD. Galbraith, “Modelling dynamic stall vortex inception at low Mach numbers,” *Aeronautical Journal*, vol. 101, no. 2163, pp. 67–76, 1997.
- [70] T. S. Beddoes, *A third generation model for unsteady aerodynamics and dynamic stall*. Westland Helicopters Ltd., RP-908, 1993.

-
- [71] G. Gobbi, *Analysis and reconstruction of dynamic-stall data from nominally two-dimensional aerofoil tests in two different wind tunnels*. PhD Thesis, University of Glasgow, Glasgow, UK, 2010.
- [72] J. W. Larsen, S. R. K. Nielsen, and S. Krenk, “Dynamic stall model for wind turbine airfoils,” *Journal of Fluids and Structures*, vol. 23, no. 7, pp. 959–982, 2007.
- [73] J. G. Leishman, *A semi-empirical model for dynamic stall*. University of Maryland, USA, UM-AERO-87-24, 1987.
- [74] W. Sheng, R. A. McD. Galbraith, and F. N. Coton, “A new stall-onset criterion for low speed dynamic-stall,” *Journal of Solar Energy Engineering*, vol. 128, no. 4, pp. 461–471, 2006.
- [75] R. B. Green and R. A. McD. Galbraith, “Phenomena observed during aerofoil ramp-down motions from the fully separated state,” *Aeronautical Journal*, vol. 98, no. 979, pp. 349–356, 1994.
- [76] R. B. Green and R. A. McD. Galbraith, “Dynamic recovery to fully attached aerofoil flow from deep stall,” *AIAA Journal*, vol. 33, no. 8, pp. 1433–1440, 1995.
- [77] W. Sheng, R. A. McD. Galbraith, and F. N. Coton, “Return from airfoil stall during ramp-down pitching motions,” *Journal of Aircraft*, vol. 44, no. 6, pp. 1856–1864, 2007.
- [78] P. J. Penna, *Wind tunnel tests of the Quiet Revolution Ltd. QR5 vertical axis wind turbine*. Institute for Aerospace Research, National Research Council Canada, LTR-AL-2008-0004, 2008.
- [79] F. L. Ponta and P. M. Jacovkis, “A vortex model for Darrieus turbine using finite element techniques,” *Renewable Energy*, vol. 24, pp. 1–18, 2001.
- [80] P. Vittecoq and A. Laneville, “The aerodynamic forces for a Darrieus rotor with straight blades: wind tunnel measurements,” *Journal of Wind Engineering and Industrial Aerodynamics*, vol. 15, pp. 381–388, 1983.

-
- [81] I. Paraschivoiu, *Wind turbine design: with emphasis on Darrieus concept*. Polytechnic International Press, 2002.
- [82] M. Raciti Castelli and E. Benini, “Effect of blade inclination angle on a Darrieus wind turbine,” in *Proceedings of the ASME Turbo Expo 2010: Power for Land, Sea, and Air, GT2010-23332*, Glasgow, UK, 14-18th June 2010.
- [83] S. Mertens, G. van Kuik, and G. van Bussel, “Performance of an H-Darrieus in the skewed flow on a roof,” *Journal of Solar Energy Engineering*, vol. 125, pp. 433–440, 2003.
- [84] C. J. Simão Ferreira, K. Dixon, C. Hofemann, G. van Kuik, and G. van Bussel, “The VAWT in skew: Stereo-PIV and vortex modelling,” in *Proceedings of the 47th AIAA Aerospace Sciences Meeting including the New Horizons Forum and Aerospace Exposition, AIAA-2009-1219*, Orlando, FL, USA, 5-8th January 2009.
- [85] F. N. Coton and T. Wang, “The prediction of horizontal axis wind turbine performance in yawed flow using an unsteady prescribed wake model,” *Journal of Power and Energy*, vol. 213, no. 1, pp. 33–43, 1999.
- [86] G. Ronsten, J. A. Dahlberg, G. Jiang, and D. He, *An experimental investigation of the performance and wind tunnel wall interference for a wind turbine operating in yaw*. The Aeronautical Research Institute of Sweden, FFA-TN-1994-13, 1994.
- [87] I. S. Kang, K. Ariyasu, Y. Hara, T. Hayashi, and I. Paraschivoiu, “Characteristics of a straight-bladed vertical axis wind turbine in periodically varying wind,” in *EXPO World Conference on Wind Energy, Renewable Energy, Fuel Cell (WCWRF 2005)*, Hamamatsu, Japan, 2005.
- [88] S. J. Kooiman and S. W. Tullis, “Response of a vertical axis wind turbine to time varying wind conditions found within the urban environment,” *Wind Engineering*, vol. 34, no. 4, pp. 389–401, 2005.
- [89] T. Bertényi, C. Wickins, and S. McIntosh, “Enhanced energy capture through gust-tracking in the urban wind environment,” in *Proceedings of the 48th AIAA Aerospace Sciences Meeting including the New Horizons Forum and Aerospace Exposition, AIAA-2010-1376*, Orlando, FL, USA, 4-7th January 2010.

REFERENCES

- [90] S. Mertens, *Wind energy in the built environment*. Multi-Science Publishing Co. Ltd, Brentwood, UK, 2006.
- [91] P. R. Schatzle, P. C. Klimas, and H. R. Spahr, “Aerodynamic interference between two Darrieus wind turbines,” in *Proceedings of the AIAA/ SERI Wind Energy Conference, AIAA paper 80-0606*, Boulder, CL, USA, 9-11th April 1980.
- [92] R. G. Rajagopalan, T. L. Rickerl, and P. C. Klimas, “Aerodynamic interference of vertical axis wind turbines,” *Journal of Propulsion and Power*, vol. 6, no. 5, pp. 645–653, 1990.
- [93] N. Durrani, N. Qin, H. Hameed, and S. Khushnood, “2D Numerical analysis of a VAWT wind farm for different configurations,” in *Proceedings of the 49th AIAA Aerospace Sciences Meeting including the New Horizons Forum and Aerospace Exhibition, AIAA-2011-461*, Orlando, FL, USA, 4-7th January 2011.
- [94] A. Passola Parcerissa, *The effect of helical blade twist and wake interaction on the aerodynamics of vertical-axis wind turbines*. Final Year Project Report, University of Glasgow, Glasgow, UK, 2011.
- [95] M. Alidadi and S. Calisal, “Effects of towing tank walls on the performance of a vertical axis turbine,” in *Proceedings of the Oceans MTS/IEEE Conference*, Vancouver, BC, Canada, 29th September - 4th October 2007.
- [96] T. M. Fletcher and R. E. Brown, “Simulation of wind turbine wake interaction using the vorticity transport model,” *Wind Energy*, vol. 13, no. 7, pp. 587–602, 2010.

Appendix A

Coefficients of Dynamic Stall Model

Table A.1: *Coefficients that are used within the dynamic stall model and that are deduced from static aerofoil data for the NACA 0015 aerofoil.*

S_1	S_2	α_1	C_{n_1}	C_{n_α}	K	C_{d_0}
4.00	1.75	14.0°	1.294	0.10	0.23	0.0074

Table A.2: *Time constants used in the dynamic stall model.*

T_p	T_b	T_f	T_v	T_{VL}
1.7	4.0	3.0	6.0	7.0

Appendix B

Rotor Parameters

Table B.1: *Rotor parameters for the straight-bladed turbine used in the experiment conducted by Strickland et al. [47].*

Number of blades	2
Aerofoil section	NACA 0012
Average blade Reynolds number	40,000
Aerofoil chord length	9.14 <i>cm</i>
Rotor tip speed	45.7 <i>cm/s</i>
Chord-to-radius ratio	0.15
Tip speed ratios	7.5, 5.0 and 2.5

Table B.2: *Geometric properties of the straight-bladed, the curved-bladed and the helically twisted turbine configurations.*

	straight-bladed	curved-bladed	helically twisted
Height-to-radius ratio	3.00	3.00	3.00
r/R at mid-span	1.00	1.00	1.00
r/R at blade tips	1.00	0.33	0.73
Helical twist of blade tips*	0.00	0.00	$\pm 82^\circ$
Swept area [†] (in $[R^2]$)	6.00	4.58	5.41

*i.e. azimuth positions of blade tips compared to mid-span.

[†]The swept area is defined as the intersection between a cylinder of which the surface is described by the trajectory of the rotor blades and a vertical plane through the turbine that contains the axis of rotation of the rotor.

Table B.3: *Rotor parameters of the straight-bladed, the curved-bladed and the helically twisted turbine configurations.*

Number of blades	3
Aerofoil section	NACA 0015
Average blade Reynolds number at mid-span	800,000
Chord-to-radius ratio at mid-span	0.115
Aspect ratio	26

Appendix C

Grid Parameters

Table C.1: *Grid parameters used within the study of the effect of grid resolution.*

	coarse	fine
Cells per rotor radius	22	44
Cells per blades span (AR=15)	50	100
Time steps per rotor revolution	180	360
Number of cells after 12 rotor revolutions [‡]	400,000	2,700,000
Time for completion of 12 rotor revolutions [§]	42 hours	390 hours

[‡]Note: the rotor revolutions that are required within the VTM to obtain a converged solution depend on several parameters, such as tip speed ratio and number of rotor blades. A converged solution for a rotor that comprises two straight blades and that is operated at a tip speed ratio of five is typically obtained after ten complete rotor revolutions.

[§]Wall clock time. Each simulation was run on a single machine with processor Intel® Xeon® X3363 (2.83GHz).